THE ROLE OF SURFACE IN HYDRIDE FORMATION PROCESSES[†]

Viktor O. Litvinov, Ivan I. Okseniuk, Dmytro I. Shevchenko, Valentyn V. Bobkov

V.N. Karazin Kharkiv National University, Kharkiv, Ukraine
Corresponding Author e-mail: vlitvinov9206@gmail.com

Several $LaNi_5$-based hydrogen storage alloys were studied using secondary ion mass spectrometry (SIMS) technique. Ar^+ ions with the energy of 10 - 18 keV were used as primary ions. The study of the initial stages of the processes of $LaNi_5$-based alloys interaction with hydrogen under the experimental conditions showed that on the areas of clean surface, hydrogen formed chemical compounds with the both of the main components of the alloy: nickel and lanthanum. As hydrogen accumulates on the surface and in the near-surface region, a hydrogen-containing structure is formed, which is characterized by a certain stoichiometric ratio of components. Nickel in this structure has strong chemical bonds with two hydrogen atoms, and lanthanum – with two or more hydrogen atoms. Along with such compounds, some structures with lower hydrogen content are also formed. The formed hydrogen-containing structure includes both main alloy components, La and Ni for all the studied samples, even though only lanthanum is generally accepted to be the hydride-forming element in such alloys. The SIMS studies of the chemical composition of the surface monolayers of the intermetallic alloy $LaNi_5$, in the process of its interaction with oxygen, showed the following. As a result of the oxygen interaction with the alloy, a complex chemical structure including oxygen, lanthanum and nickel is formed on the surface and in the near-surface region of $LaNi_5$. Oxygen in such a structure, similarly to hydrogen, forms strong chemical bonds with both components of the alloy. This is indicated by the presence in the mass spectra of a large set of oxygen-containing emissions of positive and negative secondary ions with lanthanum and nickel, as well as oxygen-containing lanthanum-nickel cluster secondary ions. The formed oxide compounds have a three-dimensional structure and occupy tens of monolayers. Oxygen poisoning of the surface of the hydride-forming alloy $LaNi_5$ can occur regardless of whether the surface of the alloy was clean from the very beginning or it was covered with a layer of hydrogen-containing chemical compounds.

Keywords: *SIMS; surface; intermetallic alloy; lanthanum alloy; LaNi₅; hydrogen; metal hydride; oxygen; oxides*
PACS: 34.35.+a, 79.20.Rf, 88.30

INTRODUCTION

The energy supply independence is currently an integral part of the sovereignty of every state. One of the promising directions for solving the problem of the energy supply independence and ensuring sustainable development is the development of the field of hydrogen energy, that is, the field of energy, which is based on the use of hydrogen as a means for the energy production, accumulation, transportation and consumption. Hydrogen energy has turned into a direction, along with some other ones, with which the leading countries of the world associate the prospects of their national economics. The needs of various branches of hydrogen energy, which are necessary for the production and utilization of hydrogen as a renewable, ecological and safe energy carrier, require the introduction and development of various types of metal hydride technologies, that is, the technologies, based on the ability of a number of hydride-forming intermetallic alloys reversibly react with gaseous hydrogen to form metal hydrides.

The ability of a number of metals and alloys to reversibly absorb significant amount of hydrogen with the formation of metal hydrides has given rise to a number of technical solutions for the practical use of this phenomenon. The basis for this is the unique combination of the metal-hydrogen systems properties, namely, the possibility to achieve extremely high volumetric densities of hydrogen atoms in metal lattices (up to 0.09-0.1 g cm⁻³), a wide range of operating temperatures and pressures, selectivity of the hydrogen absorption process, significant changes in the physical properties of the metal, when it is saturated with hydrogen, catalytic activity and a number of other features [1-4].

The reversible reaction of metal hydride formation can occur either as a result of direct interaction of the hydride-forming metal (or alloy) with gaseous hydrogen, or as a result of an electrochemical process. The process of direct interaction includes the following stages: transport of hydrogen molecules to the metal surface; physical adsorption, dissociation of adsorbed H_2 molecules and the transfer of hydrogen atoms into the material volume with the formation of an interstitial solid solution (α-phase) and then – hydride (β-phase). The concentration of hydrogen atoms in the α-phase is small; they are statistically distributed in the interstitial voids of the metal matrix, which retains the original structure with a small (up to 5%) increase in the volume. On the contrary, the hydride is characterized by a high content of hydrogen atoms and their ordered arrangement.

The reaction of interaction with hydrogen takes place with the release of heat during the formation of the hydride and the absorption of heat during hydride dissociation. The reaction is reversible, the process can be turned to one direction or the other and its speed can be controlled by changing only the temperature and (or) pressure. An increase in the pressure of gaseous hydrogen and a decrease in temperature shift the equilibrium of the reaction to the side of hydride formation, while a decrease in pressure and an increase in temperature cause decomposition of the hydride [5,6].

Among the large number of metal hydrides known to date, the hydrides of intermetallic compounds occupy a special place. Such hydrides are represented by the general formula $A_mB_nH_x$, where A_mB_n is an intermetallic compound of two or more metals, at least one component (A) of which has a high affinity for hydrogen, i.e. forms a highly stable binary hydride, and the other one (B) does not interact directly with hydrogen under normal conditions. It is customary to classify the hydride-forming intermetallics according to the ratio of hydride-forming (A) and non-hydride-forming (B) components. Among the large number of types of hydride-forming intermetallics, such compounds as AB_5, AB_2, AB and A_2B are of the greatest practical importance. In the compounds AB_5, rare earth elements and/or calcium are used as the component A; in the compounds AB_2 and AB, the elements of the titanium subgroup are used; in the compounds A_2B, mainly magnesium is used. The component B in all the intermetallics mainly includes transition metals (Fe, Co, Ni, V, Mn, Cg, etc.). The formation of hydrides of intermetallic compounds is accompanied by the expansion of crystal lattices. Typical values of the increase in the volume of the unit cell vary from 10 - 15 to 20 - 25%. In this case, the symmetry of the original metal matrix is usually preserved.

The technologies based on the use of metal hydrides, the so-called metal hydride technologies, include the accumulation, compact and safe storage and transportation of hydrogen, thermosorption compression, separation of hydrogen from gas mixtures, its purification, distribution of isotopes, as well as ensuring the operation of various physical and technical devices, such as injectors of thermonuclear facilities, ion sources of accelerators, gas supply systems of vacuum-plasma facilities, etc. [2, 7, 8].

Accumulation, compact and safe storage, and transportation of hydrogen
The reversible storage of hydrogen in the form of intermetallic hydride has a number of advantages as compared to the conventional storage methods using gas cylinders or cryogenic equipment. The intermetallic hydrides have clearly defined volumetric advantages as compared to the compressed or liquefied gas. In fact, the density of hydrogen in hydrides approaches that of liquid hydrogen, since the packing density of H in the hydride crystal lattice is usually much higher than that of liquid hydrogen. This method of storage can be implemented at relatively low temperatures and pressures, which provides a high degree of fire and explosion safety, without the use of cryogenic technology and expensive and highly insulated containers, which are necessary to minimize the losses caused by liquid hydrogen evaporation. Furthermore, the method is characterized by compactness and low energy costs for the hydrides formation as compared to the liquefaction and compression of hydrogen [6].

Thermosorption compression
The concept of hydrogen compression by using intermetallic hydrides is based on the fact that the process of hydrogen absorption, accompanied by the formation of a metal hydride, occurs with the release of heat (exothermic reaction); in the course of the hydride decomposition with the hydrogen release, the heat absorption occurs (an endothermic process). The absorption occurs at a rather low pressure of hydrogen, and the release – at high pressure, similar to the processes of suction and discharge in a mechanical compressor. This makes it possible to carry out the process of low-pressure hydrogen absorbing at a lower temperature, and to desorb higher-pressure hydrogen when the appropriate heat is delivered to the metal hydride. This method is called thermosorption (or thermochemical) hydrogen compression, and the devices implementing it are the metal hydride thermosorption compressors (MH TSC) [9]. The metal hydride thermosorption compressor has a number of advantages as compared to traditional mechanical compressors. Such a compressor has no moving parts, pistons, membranes, or bellows. This provides a simplified design and high reliability, thus reducing the probability of explosive hydrogen leakage.

By applying the thermosorption compressors, it is possible to solve the problem of utilization of low-potential (unusable) heat in various industries, converting it into highly organized energy of compressed gas.

Hydrogen purification, hydrogen separation from gas mixtures
The selectivity of the intermetallics reaction with hydrogen allows for the realization of the processes of hydrogen purification from gaseous impurities, as long as the reactive species, such as O_2, H_2O, CO, etc., tend to be absorbed by hydride, and the inert species, such as N_2, CH_4, etc., can be removed at the initial stages of the dehydrogenation process. Thus, the devices based on the intermetallic hydrides are often used in specialized applications, where H_2 "ultra-high purity" is required (for example, as a gas-carrier of gas chromatograph). The selectivity of the reaction also allows using the devices based on intermetallic hydrides to extract hydrogen from the gas mixtures without application of expensive devices, such as palladium filters.

The intermetallic hydrides can also be used to separate different isotopes of hydrogen: protium (H), deuterium (D), and tritium (T), for example, the separation of D from natural hydrogen (0.016% of D, residual H), or the removal of radioactive T from non-radioactive D and/or H. For example, zirconium-based getter alloys are used in a number of nuclear energy technologies, as well as in the fuel cycle research and development of thermonuclear reactors. Zirconium-based (Zr_2Fe) non-evaporable getters are used to solve the rather urgent task of purifying gas streams from hydrogen tritium isotope [10-12]. The advantage of using Zr_2Fe (SAES Getters ST198) instead of traditional methods of tritium collection and removal [13] is simplicity and possibility to avoid the production of tritium water, which makes a greater biological hazard. The gas absorption method is a non-oxidation process, in which the tritium water vapor is

never produced in the process line. In getters, tritium is stored more safely than in derivative products of the conventional oxidation-adsorption process. Also, the hydrogen isotopes, captured by the metal hydride getters, can be later extracted in their elemental form.

Ensuring the operation of various physical and technical devices.

The ability to control the pressure of desorbed hydrogen by means of a directed thermal effect on the metal hydride allows using the metal hydrides for high-precision regulated supply of hydrogen to the consumer. Some metal hydrides with fast dynamics of low-pressure hydrogen absorption (hydrogen getters) formed the basis of efficient hydrogen removal systems and systems of regulated supply of low-pressure hydrogen to the vacuum-plasma installations.

A distinctive feature of getter hydride-forming intermetallics is the low equilibrium pressure of hydrogen sorption-desorption at the temperatures close to the room ones. This feature allows using them in various devices operating at sub-atmospheric pressures, in particular, to ensure the operation of various physical and technical devices, such as injectors of thermonuclear installations, ion sources of accelerators, gas power systems of vacuum-plasma installations, gas lasers and other devices using hydrogen as a working medium [[14], **Error! Reference source not found.**].

THE ROLE OF IMPURITY GASES IN HYDROGEN IN THE PROCESSES OF INTERACTION WITH HYDRIDE-FORMING ALLOYS

The impurity gases that are present in hydrogen have different effects on the absorption capacity of hydride-forming alloys, in some cases, they can significantly change the kinetic parameters of the sorption-desorption processes and the hydrogen capacity of the alloy [16]. The impurity gases can be conventionally divided into four groups according to the nature of their influence on the alloy and its hydrogen-sorption characteristics [17, 18].

The first group is the impurities that lead to surface poisoning. The impurity gas molecules, contacting the surface, form a strong chemical bond with the surface metal atoms, which cease participating in the processes of dissociative chemisorption of hydrogen. In general, a monolayer coating is sufficient for complete deactivation of the material. Such a deactivated surface efficiently blocks the area of the underlying material from interaction with hydrogen. Thus, the surface poisoning lies in the formation of a surface structure that prevents the rapid dissociation of hydrogen on the surface $H_2 \rightarrow 2H$ and/or the penetration of hydrogen into the volume, what is equally necessary for the practical use of reversible hydrides. In the process of cycling, the poisoning causes a rapid decrease in hydrogen capacity. However, as long as the impurity molecules are localized only on the surface, the poisoned samples can often be reactivated (for example, by cycling and/or heating in pure H_2). An example of poisoning is exposure to the surface (at certain temperatures) of CO carbon monoxide, which forms a chemisorbed monolayer on the surface of $LaNi_5$ with a heat of adsorption comparable to the heat of nickel carbonyl formation. This makes the nickel atoms, on which the catalytic dissociation of hydrogen takes place, inactive. CH_3SH (methyl mercaptan) and H_2S produce a similar effect.

The second group are the impurities that slow down the processes of interaction with hydrogen, in particular, lead to some decrease of the hydrogen absorption kinetics, but not to the detriment of the hydrogen capacity. This group includes the impurities that are characterized by much softer and more homogeneous form of interaction with hydride-forming materials, than the interactions categorized as poisoning. The influence of CO_2, NH_3 is an example.

The third group are the impurities that have a reactive effect, i.e., initiate a chemical reaction causing the alloy volume corrosion and, as a result, an irreversible decrease in hydrogen capacity. This situation occurs when hydrogen is contaminated with oxygen (in some situations, oxygen has a poisonous effect). In the case with the lanthanum-nickel alloys, the effect of oxygen lies in the formation of compounds with lanthanum: La_2O_3 or various hydrates or hydroxides. Some oxygen compounds with nickel atoms are also formed. At the room temperature, this process is quite slow. H_2O has a similar effect. In this case, the H_2O molecule dissociates on the surface, thus resulting in the surface efficient oxidizing (hydrolysis). The rate of the oxidation reaction can be slightly slowed down by the presence of a certain amount of physisorbed H_2O molecules on the surface. The reaction usually causes the formation of very stable chemical compounds that are hydrogenated irreversibly and cannot be easily regenerated to the original state.

And the fourth group are the impurities chemically inert to the alloys, which do not form chemical compounds with the alloy material and do not transform the surface, but slow down the kinetics of sorption due to the formation of an inert layer of the impurity components on the surface. This effect is caused by CH_4, C_2H_4 or N_2.

It should be noted that the nature of the impurities influence can change significantly with temperature, time and, possibly, concentration.

THE SURFACE ROLE IN HYDRIDE FORMATION PROCESSES

As a result of the researchers' serious efforts, a large number of hydride-forming alloys for the application in various fields have been synthesized. At the same time, for a long period, the properties of such alloys had been optimized mainly by changing their component composition or the method of their preparation. A large number of publications have been devoted to these problems over the past ten to twenty years. Much less attention was paid to the study of the role of the materials surface in the processes of their interaction with hydrogen, as well as the role of gaseous impurities in hydrogen during interaction with the surface. Such processes can play a decisive role in the processes of hydride formation. Therefore, the progress of the practical development of metal hydride technologies requires careful research at the monolayer level of both the actual elementary processes of hydrogen interaction with the

surface of materials that form hydrides, and the influence of gas impurities. Such studies will allow solving a number of problems related to the dynamics of sorption - desorption and surface poisoning.

It is generally accepted that the surface of a solid body contains not only the upper atomic layer, but also several upper monolayers, which differ in composition from the bulk. In the case of a pure single-crystal sample, there may be three or four such monolayers. For the polycrystalline metals or multiphase alloys, the surface or surface layer can be as thick as 10 nm. The formation of the surface layer of chemical compounds is caused by interaction with the gas phase. The composition of such compounds, in addition to the bulk impurities, includes the elements: C, O, H, and N. This surface layer is formed naturally on an initially clean and reactive metal surface. In some cases, it completely passivates the metal surface. The passivation is quite desirable in some respects, for example for corrosion protection, but plays a negative role in cases, where the surface must remain reactive, for example for catalysts, getters or hydride-forming metals and alloys. The surface properties are especially important in the absorption of hydrogen by intermetallic hydride-forming compounds, since the first stage of absorption is physical adsorption followed by dissociation (atomization) of the adsorbed hydrogen molecules on the transition metal atoms.

Among the intermetallic compounds of the system, such as AB, AB_2, AB_5 and A_2B (where A is a metal forming a stable hydride, B is, mainly, a transition metal that does not interact with hydrogen under normal conditions) have gained interest as potential materials for technological applications. So, AB_5 alloys, based on lanthanum, attract considerable attention due to their ability to store large amount of hydrogen, ease of activation, and ability to react quickly and reversibly at ambient temperature and moderate pressures [19]. The alloys such as TiFe and Mg_2Ni, have been recognized as H_2 carriers for vehicles, mainly due to their convenient pressure-composition-temperature (PCT) relations, high H_2 content, favorable kinetics, and lower cost as compared to some other suitable alloys. However, a serious problem for all these materials in technological applications is their poor resistance to poisoning by gaseous impurities such as O_2, H_2O vapor, CO, CO_2, etc., which are present in the supplied H_2 gas and in atmospheric sources [18]. As a result, the alloys frequently require activation procedures before they accept hydrogen. Applicability of intermetallics for storage, transportation, purification of hydrogen, its separation from gas mixtures, etc. depends mainly on their cyclic stability, H-capacity, absorption and desorption kinetics.

While the cyclic stability and hydrogen capacity are determined by the volumetric properties of intermetallic compounds, namely: parameters of the crystal lattice, electronic band structure, the kinetics of sorption-desorption largely depends on the properties of the surface. Despite numerous studies of bulk characteristics, the nature and properties of the surface of these materials have so far attracted little attention, although the activated intermetallics, which disperse during hydrogenation, are a fine powder, and therefore their surface is an important factor in the hydrogenation process [20, 21].

The studies of surface properties in relation to the kinetics of sorption-desorption processes, as well as in relation to the activation, deactivation and reactivation of materials, are absolutely necessary, especially given the urgency of developing activation procedures, as well as to improve the properties of metal hydride systems in terms of hydrogenation using commercial H_2 sources, for example, hydrogen from steam reforming of hydrocarbons, etc.

The knowledge of the chemical composition of the surface outer monolayers is quite important when studying the kinetics of hydrogen sorption-desorption processes, since the surface of any metal material, subject to the experimental conditions, is always covered with a greater or lesser amount of chemical compounds, what is due to the interaction with the gas phase [22]. Such compounds largely determine the parameters of further interaction with the gas phase. A clean surface can be obtained only due to some special measures, which are often difficult to implement.

Although there are many studies in the literature on the interaction of hydrogen with metals, not all the publications consider the influence of the material surface on the characteristics of the hydrogen sorption-desorption process. There are few experimental studies (e.g. [23, 24]) of the influence of the surface coatings chemical composition on the processes kinetics. The nature of such studies is fragmentary, as they do not provide an opportunity to form a general idea of the patterns of such influence. One of the reasons for this is that the detection of hydrogen using the most common analytical methods of surface investigation is very problematic. The electronic spectral methods (such as AES and XPS) cannot always detect hydrogen and its compounds. One of the unique features of the mass spectrometric methods SIMS (secondary ion mass spectrometry) and SNMS (secondary neutral mass spectrometry) is the ability to detect hydrogen.

Thus, the study of the composition of chemical compounds on the surface is of great importance. The studies of this kind are very important for understanding the initial stages of the processes that develop on the surface, such as the initial accumulation of hydrogen, poisoning of the reaction due to the presence of impurities in the gas phase, activation or passivation of hydrogenation, etc. [25]. Such studies attract considerable attention of scientists engaged in various disciplines from both fundamental and applied viewpoint.

APPLICATION OF SECONDARY ION MASS SPECTROMETRY (SIMS) METHOD FOR STUDYING THE SURFACE OF SOLIDS AND THEIR OUTER ATOMIC LAYERS

The SIMS method is based on the analysis of the characteristics of the ionic component of the products of solids sputtering with a beam of accelerated primary ions (or atoms). When interacting with the surface of a solid, the primary ion can undergo elastic or inelastic scattering, be recharged, adsorbed, or penetrate deep into the solid. In the latter case, as a result of the repeated collisions with atoms of a solid (cascade of collisions), the ion losses energy, is

neutralized and can either be implanted into the lattice or fly-off into vacuum as a result of scattering. At the same time, a part of the atoms located on the surface and near the surface receive the energy exceeding that of the interatomic bond in the lattice, and when moving towards the surface, this part of the atoms can leave the surface, thus resulting in the "cathode sputtering" (emission of neutral atoms) and in the secondary ion emission (emission of secondary positive and negative ions) [22, 26-29].

Among the distinguishing features of the SIMS method are: the possibility of analyzing any solid substances without any special preparation (metals and alloys, semiconductors, dielectrics); possibility of detection of all the elements from hydrogen to transuranic elements; high sensitivity of the analysis corresponding to the trace atoms concentration: $\sim 10^{-4} - 10^{-7}$ % (or corresponding to the substance consumption: $\sim 10^{-6}$ of a monolayer); the possibility of performing depth profiling analysis of materials with high depth resolution: $\sim 30 - 100$ Å; the possibility of identifying not only individual elements and isotopes, but also their chemical compounds.

When conducting the surface analysis, SIMS method is mainly used for the identification of surface atoms and molecules, as well as for studying the dynamics of the surface phenomena, various physical and chemical processes at the interface between a solid and a gas. Such surface phenomena as catalysis, corrosion, adsorption, and diffusion are investigated by the SIMS method.

The information about the elemental and isotopic composition, about the composition of chemical compounds on the surface is usually provided by the mass spectra of sputtered positive and negative secondary ions. The information about the physical and chemical processes on the surface of solids under different experimental conditions can be obtained by analyzing the dependences of the emission intensity of characteristic secondary ions on the temperature of the sample, the partial pressure of the gas in the target chamber, the current density of primary ions, and kinetic dependences.

Along with high sensitivity, the SIMS method has a unique ability not only to detect hydrogen, but also to determine the presence of hydrogen chemical compounds on the surface and in the near-surface layer, as well as to detect changes in the composition of such compounds, subject to the experimental conditions. This makes the method quite an effective tool for studying the characteristics of hydrogen sorption-desorption processes by materials used in metal hydride technologies [30].

The following content of this article is an overview of the works studying the metal hydrides surface by the SIMS method.

SIMS INVESTIGATION OF THE LaNi$_5$ ALLOY SURFACE AND A NUMBER OF LANTHANUM-BASED ALLOYS DURING THEIR INTERACTION WITH HYDROGEN

In 1970, when studying the intermetallic compounds AB$_5$ (where A is a rare earth metal, B is nickel or cobalt), it was found that the intermetallic LaNi$_5$ is capable to absorb and release a large amount of hydrogen at temperatures close to the room one and at relatively low pressures [19]. Thus, as a result of hydrogen sorption at the room temperature and the pressure of 0.2-0.5 MPa, the LaNi$_5$H$_{6,7}$ hydride was formed, in this case the volume of the crystal lattice unit cell increased by 25% with maintaining hexagonal symmetry. The hydrogen content in the hydride was 1.4 wt. %: If calculated per unit volume, this is one and a half times greater than the amount of hydrogen contained in liquid hydrogen.

The subsequent studies of AB$_5$ intermetallic compounds determined their main properties and parameters. The hydrides of AB$_5$H$_x$ composition, where x, subject to the nature of A and B, varies from 3 to 8, are characterized by moderate dissociation pressures (from 0.01 to 1 MPa) at the room temperature and low enthalpy of hydrogen absorption $(30 - 40$ kJ·mol^{-1}). In practice, of greatest interest is the intermetallic LaNi$_5$ hydride, whose absorption capacity and kinetics of hydrogen absorption can be considered as a comparison standard for the preparation of other materials for hydrogen batteries operating at low temperatures. LaNi$_5$ alloy is a vivid example of hydride-forming materials used in metal hydride technologies. Due to high hydrogen capacity, high cyclic stability and ease of activation, the materials based on it occupy one of the central places in metal hydride energy technologies.

Fig. 1 shows the pressure-composition-temperature diagram for the LaNi$_5$/H system. The results of numerous studies on LaNi$_5$ are presented in a vast number of original works and reviews [1-3, 31, 32]. In general, according to the published data, the hydrogen sorption characteristics of the LaNi$_5$ alloy can be characterized as follows. The intermetallic has a hexagonal structure of the CaCu$_5$ type. The equilibrium saturation of LaNi$_5$ with hydrogen is achieved in ~ 10 minutes, and most of the hydrogen (up to 90%) is absorbed or desorbed in the first few minutes. The absorption rate depends weakly on the temperature and pressure, what indicates a low activation energy of this process. The desorption of hydrogen occurs with some hysteresis, that is, the pressure of hydrogen required for the formation of a hydride is greater than that at which the hydride decomposes (pressure hysteresis). The value of hysteresis decreases as the number of cycles of the absorption - desorption process increases.

The absorption capacity of the intermetallic LaNi$_5$ increases markedly with a decrease in temperature with an almost unchanged absorption rate. The LaNi$_5$ hydride formation enthalpy is 15.7 kJ mol^{-1}H, decomposition enthalpy is 15.1 kJ mol^{-1}H [33].

As it was noted earlier, there is a large number of works studying hydrogen absorption in metals and alloys, especially in hydride-forming materials. At the same time, the number of works devoted to the influence of the surface itself on the initial stages of hydride formation is quite limited.
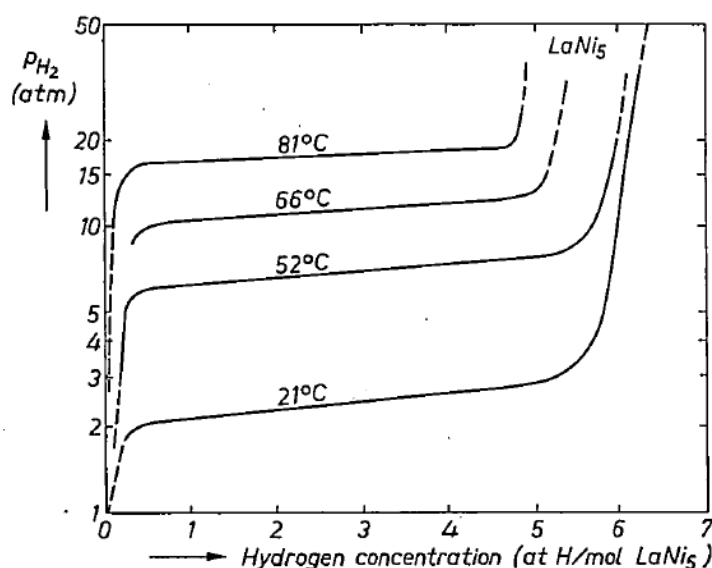
Figure 1. Pressure-composition isotherms for the LaNi$_5$/H system [19]

Among the works devoted to the study of the surface of hydrogen-storing alloys by the SIMS method, we should mention the works [34, 35], which present the results of studying the hydrogen-containing samples of the LaNi$_5$ alloy. In [36] the characteristics of chemical bonds in hydrogen (deuterium)-saturated LaNi$_5$ alloys, as well as in the alloy, in which nickel is partially replaced by Al or Ag, were investigated by SIMS and X-ray photoelectron spectroscopy. In addition to AB$_5$ hydrogen storage alloys based on La, the alloys based on Nd and Sm were also studied with SIMS. In [37], the characteristics of the components of Nd$_2$Co$_{14}$B and Nd$_2$Fe$_{14}$B alloys interaction with hydrogen and their function during hydrogenation were studied with SIMS. The information about the metal-hydrogen bonds in the SmCo$_5$D$_n$ system was presented in [38].

Below are presented the results of studying with SIMS the initial stages of the interaction of hydrogen with the surface of the hydrogen-storing alloy LaNi$_5$, as well as a number of lanthanum-based alloys when interacting with hydrogen [39-41].

The measurements were carried out in the following way. The monolithic samples, or tablets, compressed from finely dispersed alloy material, were bombarded with a beam of Ar$^+$ ions with the energy of 8 keV when analyzing the positive secondary ions, and 16 keV when analyzing the negative secondary ions. The residual vacuum in the target chamber was ~ 4 10^{-6} Pa, the current density of the primary beam was 1.2-12.0 μA cm^{-2}, what corresponded to the SIMS dynamic mode. The SIMS instrument was equipped with an energy filter, which allowed measuring the emission intensities of only low-energy (in a narrow range of energies) secondary ions, which largely characterize the presence and composition of chemical compounds on the surface under study [42]. The intensities of secondary ion emissions were measured in the dynamic range of at least 6 orders of magnitude. Before the measurements, the samples were annealed in the residual vacuum at the temperature of 750-1000 K in order to partially clean the surface from the chemical compounds that are either desorbed or dissolved in the volume of the material during the annealing process. After annealing, the surface was cleaned with a beam of primary ions until the composition of the mass spectra and intensity of secondary ion emissions were completely stabilized. The composition of the gas phase was monitored using a gas mass spectrometer. With the help of the same mass spectrometer, after the necessary calibrations, small partial pressures of gases in the vacuum chamber were measured. The studied alloy samples were the tablets pressed from finely dispersed material.

In the case, when the emissions of polyatomic secondary ions, which characterize the composition of chemical compounds on the surface, overlap in a complex manner by mass, their specific contributions were divided according to the usual procedure, utilizing the known natural distribution of isotopes.

Generally, the data of the SIMS experiments were analyzed to determine the functions of various components of the alloy in relation to its interaction with hydrogen, that is, adsorption on the surface and its subsequent binding in the alloy.

The mass spectra analysis of positive and negative secondary ions sputtered from the surface of the investigated LaNi$_5$ samples, measured before and during the annealing process, showed the presence of a vast number of various emissions related to the alloy material and its impurities, as well as the objects introduced from the gas phase. During the samples annealing, in addition to the emissions of positive and negative secondary ions, the emission of positive thermoions was observed (in the absence of the primary beam bombardment). Namely, emission of positive thermoions of alkali metals Na$^+$, K$^+$, Rb$^+$, Cs$^+$, which, in principle, are typical for metals and alloys of technical purity, as well as emission of thermoions La$^+$, LaO$^+$ were observed. The emission of such La-containing thermal ions is explained by the decomposition and desorption of oxides, which are on the surface from the very beginning and which, as a rule, must be removed to achieve high reactivity of the surface. The oxides removal is essentially the purpose of the samples activation.

As an example, Fig. 2 shows the dependence of the emission intensity of thermoions La^+, LaO^+ on the sample temperature. Fig. 3 shows the time dependence of the emission intensity of the same thermoions at the temperature of 880 K. It is obvious that in a few minutes the intensity of the oxygen-containing lanthanum ions emission, and therefore the amount of oxygen-containing compounds of lanthanum on the surface, decreases several times.
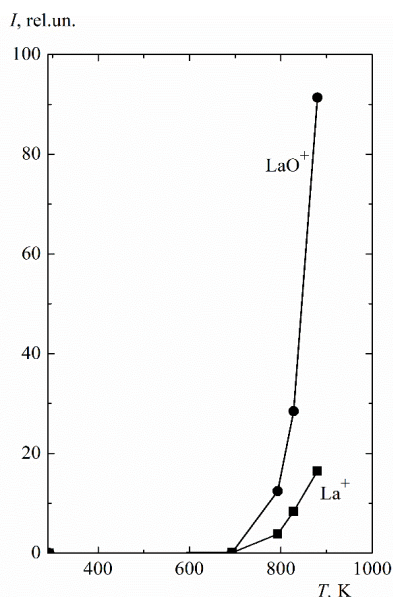
Figure 2. Temperature dependence of the emission intensity of thermoions La^+, LaO^+ from the surface of the LaNi$_5$ sample
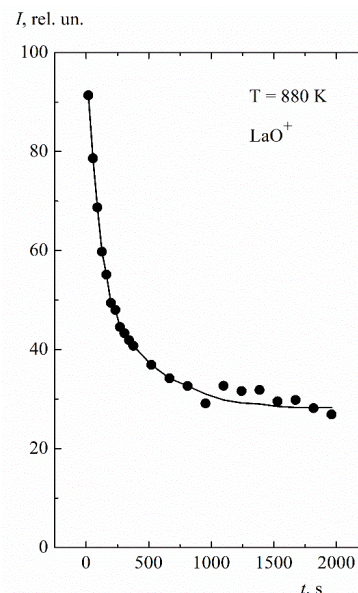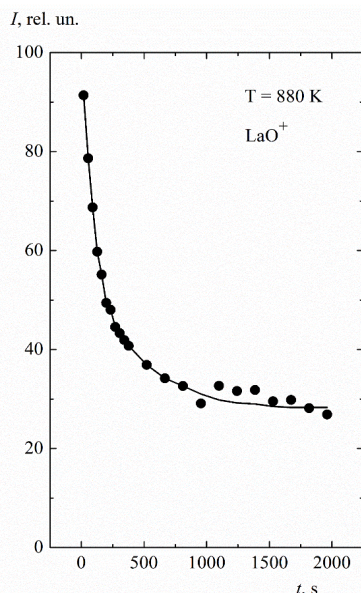
Figure 3. Time dependence of the emission intensity of La^+, LaO^+ thermionic ions from the surface of the LaNi$_5$ sample at the temperature of 880 K

The mass spectra measured after annealing and cleaning of the surface with the primary beam are much cleaner. Figs. 4, 5 are the examples of such a spectra. The spectra of positive secondary ions contain emissions of atomic and cluster ions of lanthanum and nickel, intermetallic ions of lanthanum and nickel, the emissions, which are attributed to the compounds of these ions with hydrogen, oxygen, and carbon (what is typical for metals and alloys). . Moreover, the emissions related to lanthanum predominate, and the most intense emission is the emission of lanthanum oxide ions, whereas the nickel oxide emission is almost absent. The spectra of negative secondary ions, in contrast to the positive ones, contain for the most part, nickel-related emissions, including nickel oxides.

This composition of mass spectra indicates that even after annealing and cleaning with the primary beam, the surface of the studied samples is, to a certain extent, covered with chemical compounds, which include hydrides, oxides, hydroxides, and carbides. In this case, judging by the presence in the emission spectra of cluster ions, such as $Ni_4^\pm$ or $LaNi_2^\pm$, this coating is not continuous, that is, the surface of the samples has areas free of chemical compounds.
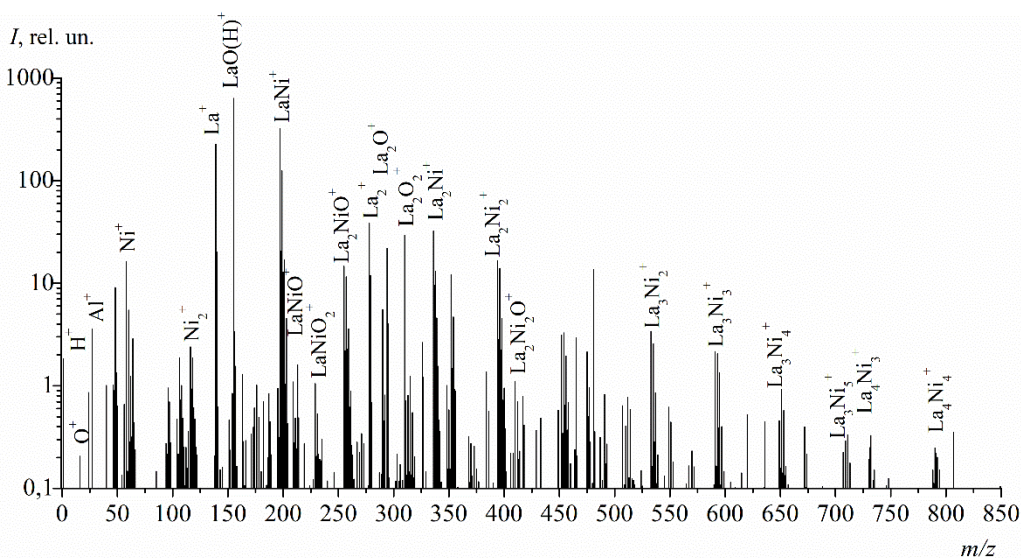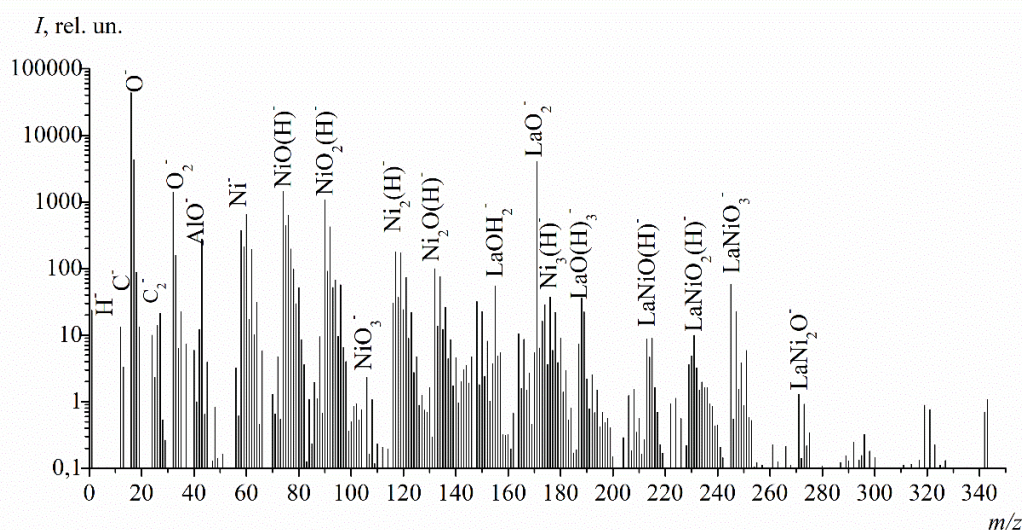
Figure 4. Section of the mass spectrum of positive secondary ions, sputtered from the surface of the LaNi$_5$ alloy sample at the room temperature, in a residual vacuum and with a primary ion current density of j=4.5 $\mu A \cdot cm^{-2}$

Figure 5. Section of the mass spectrum of negative secondary ions, sputtered from the surface of the LaNi$_5$ alloy sample at the room temperature, in a residual vacuum and with a primary ion current density of j=4.5 μA ·cm^{-2}

It is known that the equilibrium pressure of the processes of hydride formation (and hydride decomposition) at the temperatures >300K for the LaNi$_5$ alloy is much higher (close to atmospheric) than that in the vacuum chamber during SIMS experiments. The hydrogen-saturated samples placed in the chamber are degassed as a result of vacuum pumping, here not only the β-phase, in which the hydrogen in the alloy is in the form of a hydride, decomposes, but also little remains of the α-phase, i.e. of the solid solution of hydrogen in the lattice, especially since the samples are annealed before the measurements. Under the indicated conditions of the experiment, the hydrogen molecules colliding with the surface, as in the case with a number of other metals and alloys, interact only with the surface atoms and, in the best case, hydrogen saturates only the near-surface region, without diffusing in a noticeable amount into the volume. Such a situation does not allow carrying out the SIMS study of the LaNi$_5$ samples surface whose volume concentrations of hydrogen are substantial.

In order to verify the assumption that, under the specified experimental conditions, the hydrogen, upon reaching the surface, interacts only with the surface and near-surface metal atoms, without diffusing in significant quantities into the volume, the following experiment was conducted. The surface of the LaNi$_5$ sample was cleaned with the primary beam with the density of 6 μA cm^{-2} in a residual vacuum, then the primary beam was turned off and hydrogen was supplied into the chamber settling within few seconds to a partial pressure of ~ 3.5·10^{-3} Pa. At this pressure, the sample was exposed for a certain period, then the hydrogen was pumped out (the major mass of hydrogen was pumped out in a few seconds), the primary beam was turned on (with the current density of 0.3 μA cm^{-2}), and the dependence of the emission intensity of the secondary ions Ni$_2$H$^-$ (Ni$_2$H$^-$ are characteristic of the hydrogen compounds), on the time of sputtering was measured. That is the depth profiling analysis was carried out. However, the exact calculation of the number of sputtered monolayers is not possible, since the sputtering coefficient of the material under study is unknown, so only an estimate of the number of sputtered monolayers was calculated for the sputtering coefficient equal to 4 (bombardment of the sample at the angle of 60° to the normal). The measurements were made for several hydrogen exposure duration values. The results of the measurements are shown in Fig. 6.

The analysis shows that about 12 monolayers are sputtered in ~ 300 s, while the emission intensity of Ni$_2$H$^-$ ions decreases several times, which indicates to a decrease in the amount of hydrogen-containing chemical compounds. This fully agrees with the assumption that the processes of interaction with hydrogen for this sample are limited only to the near-surface region at the given experimental conditions. At the same time, of course, one should not forget about the effects introduced by the primary beam, namely, the implantation of recoil atoms (hydrogen atoms located on the surface) and ion mixing. As a result of such influence, the hydrogen can be detected even at the depth of several tens of monolayers, but such hydrogen is not an object that characterizes the actual processes of interaction with the alloy surface.

Thus, under the specified experimental conditions, it is indeed possible to study only the initial stages of hydrogen accumulation (hydrogenation), namely, the interaction of hydrogen with the surface of the specified alloys, without taking into account its diffusion into the volume, as one of the channels for changing the surface composition. In this case, of course, the influence of the primary beam must be taken into account. Taking this in mind, the studies of changes in the quantitative and qualitative composition of the mass spectra of secondary ions, sputtered from the surface of the samples, subject to the partial pressure of hydrogen in the sample chamber, were conducted. Figs. 7,8 show the examples of such dependences for hydrogen-related emissions of positive and negative secondary ions, sputtered from the surface of the LaNi$_5$ sample. Fig. 9 also shows the dependence for the hydrogen-containing complex lanthanum nickel ions.
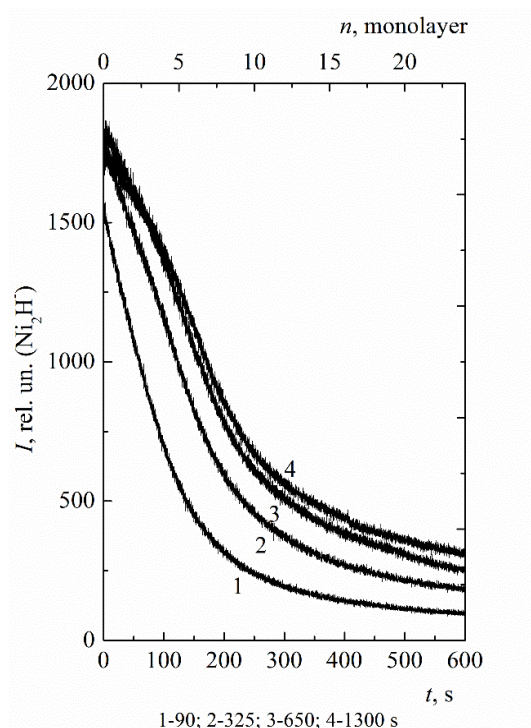
Figure 6. Time dependence of the emission intensity of negative secondary Ni_2H^- ions, sputtered from the surface of $LaNi_5$ at the room temperature, for different exposure doses at a hydrogen partial pressure of $3.5 \cdot 10^{-3}$ Pa
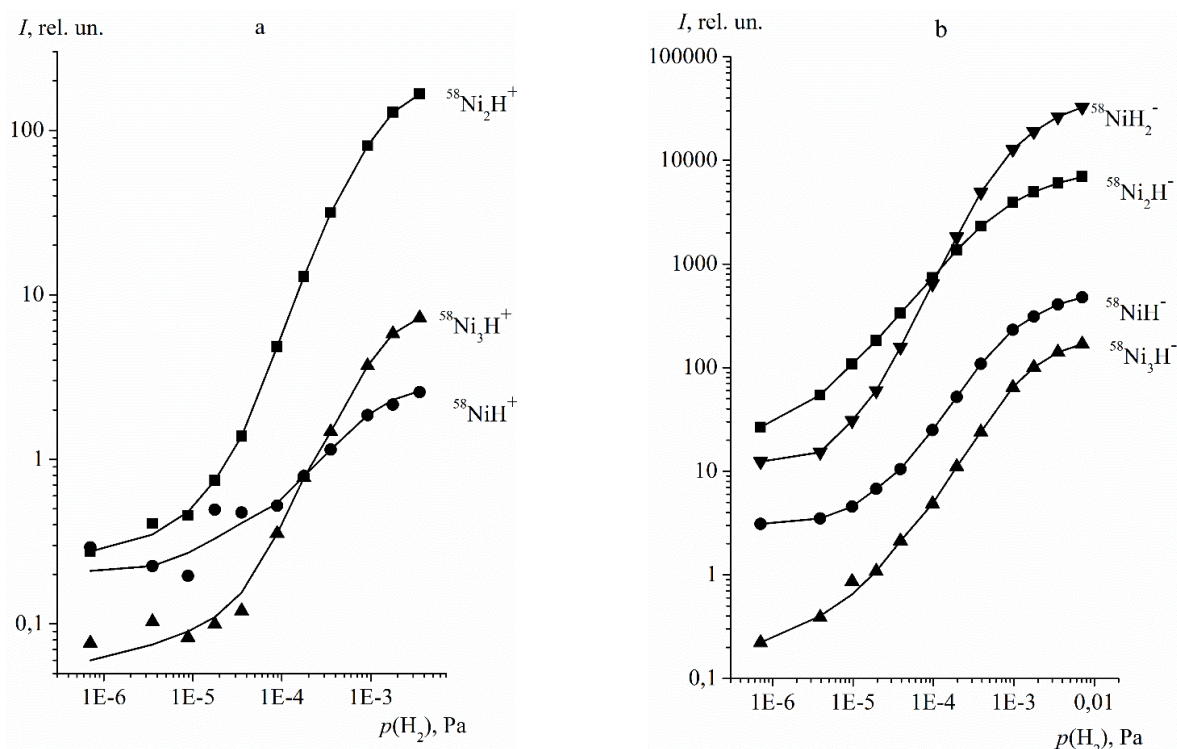

Figure 7. Dependence of the emission intensity of positive (a) and negative (b) hydrogen-containing secondary ions with nickel, sputtered from the surface of $LaNi_5$ at the room temperature, on the partial pressure of hydrogen.

As the analysis shows, when the partial pressure of hydrogen increases from residual $\sim 7 \cdot 10^{-7}$ to $\sim 3\text{-}7 \cdot 10^{-3}$ Pa, the intensity of both positive and negative hydrogen-containing secondary ions, which are observed, increases by two orders of magnitude. In the spectrum of positive ions, the hydrogen-containing ions with lanthanum are the most intensive, in the spectrum of negative ions the most intensive are those with nickel (what is explained by the different electron affinity energy of 0.5 eV for lanthanum and 1.15 eV for nickel).

The presence of the emissions of hydrogen-containing ions with lanthanum and with nickel and complex lanthanum-nickel ions ($LaNi^-$, $LaNi_2H^-$), as well as the increase in the intensity of such emissions, indicates that

hydrogen, impacting the surface, forms chemical bonds with both components of the alloy. The increase in the intensity of these emissions with the increase in the flow of hydrogen on the surface indicates an increase in the number of hydrogen-containing chemical compounds, which include nickel and lanthanum, on the surface.
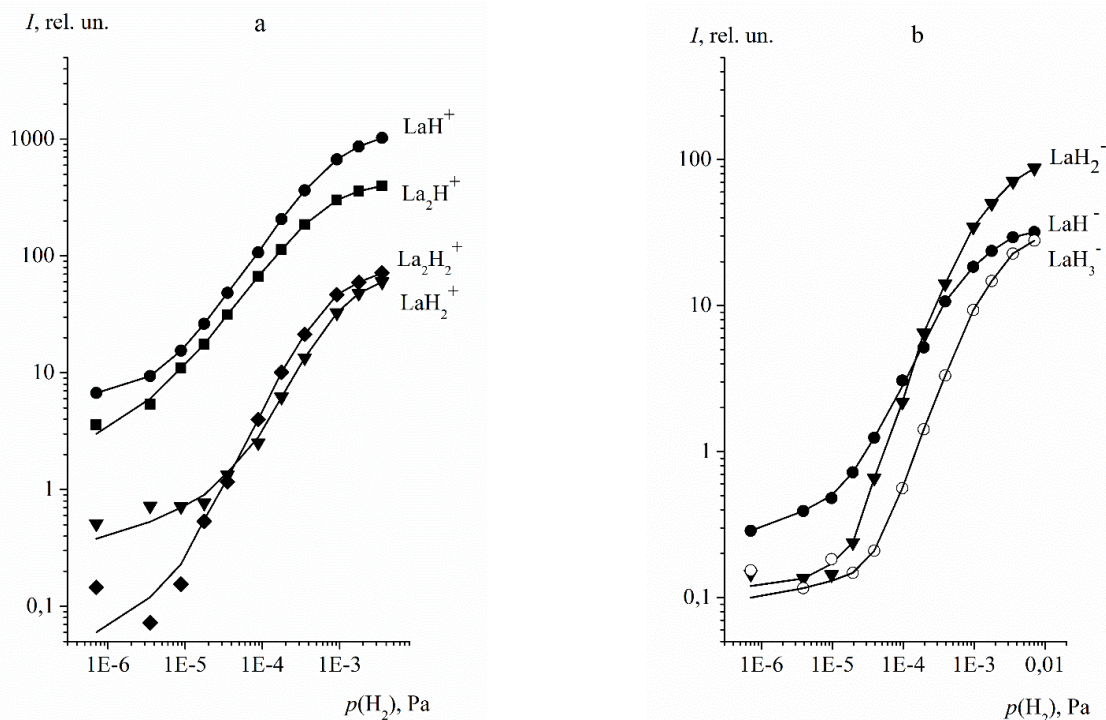

Figure 8. Dependence of the emission intensity of positive (a) and negative (b) hydrogen-containing secondary ions with lanthanum, sputtered from the surface of LaNi$_5$ at the room temperature, on the partial pressure of hydrogen

Regarding the kind of compounds which are formed on the surface, the following can be said. The emission of some ions stands out slightly from the general picture of the growth of the hydrogen-containing ions intensity. The emission intensity of NiH$_2^-$ ions increases more rapidly with the increase of the hydrogen partial pressure, than that for the other hydrogen-containing secondary ions, and increases by more than three orders of magnitude. For the maximum pressure values, the emission of NiH$_2^-$ ions becomes predominant. It is logical to assume that at the partial pressures higher than $\sim 10^{-5}$ Pa, a hydrogen-containing structure begins to form actively on the surface, the characteristic fragment of which is the NiH$_2^-$ ion. As long as nickel is divalent in most chemical compounds, it is also logical to assume that as the partial pressure of hydrogen increases, nickel hydride NiH$_2$ is formed on the surface and in the near-surface region, and NiH$_2^-$ ions are the fragments of this compound. A similar picture occurs with the emission of LaH$_2^-$ and LaH$_3^-$ ions. The emission intensity of these ions also increases at a faster rate, and it also increases by more than two orders of magnitude (for LaH$_2^-$ – by three orders of magnitude). It can be assumed that lanthanum hydride LaH$_2$ and LaH$_3$ are formed on the surface along with nickel hydride NiH$_2$, and the ions LaH$_2^-$, LaH$_3^-$, LaH$_2^+$ and La$_2$H$_2^+$ are characteristic fragments of these chemical compounds.

The tendency of the curves in Figs. 7-9 to reach the plateau is, apparently, due to the fact that at hydrogen partial pressures greater than $\sim 7 \cdot 10^{-3}$ Pa (at the room temperature) on the surface and in the near-surface region a hydride structure is completely formed, whose composition does not undergo qualitative or quantitative changes at further hydrogen pressure increase.

The dependences of the emission intensity of the oxygen-containing secondary ions on the partial pressure of hydrogen were also measured. The examples of such dependencies are shown in Fig. 10.

As Fig. 10 shows, an increase in the partial pressure of hydrogen leads to an increase in the intensity of the emission of hydroxide ions (both lanthanum and nickel) and practically does not affect the emission of oxide ions. The lack of influence of oxide ions on the emission can be explained by the fact that the oxide structure (which includes both lanthanum and nickel atoms), from which the oxygen-containing ions are sputtered, does not undergo significant changes, neither quantitative nor qualitative, as the hydrogen pressure increases. Earlier, a number of arguments were proposed in favor of a certain picture of hydride formation; however, such a picture makes sense only for a relatively clean surface. It is difficult to assume that the same processes of hydride formation take place on the surface covered with oxides; at least, the obtained experimental data do not support such an interpretation. A logical explanation of such a situation can be the assumption that the surface is only partially covered with oxides; along with islands of oxides, there is also a clean surface, on which the interaction with hydrogen actually takes place. The oxides on the surface have an island structure, whose size is hardly affected by hydrogen. The effect of hydrogen on oxides lies only in the formation of a certain amount of hydroxides.

The analysis of the results shows that a group of ions, containing more than one hydrogen atom, stands out from an overall large number of hydrogen-containing secondary ions that are sputtered. For NiH_2^-, $La_2H_2^+$, LaH_2^+, LaH_2^-, LaH_3^-, $LaNiH_2^-$, $LaNiH_3$, the dependence of the emission intensity on the partial pressure of hydrogen within the pressure range from $\sim 10^{-5}$ to $\sim 10^{-3}$ Pa allows for approximation by a power function with the exponent greater than one. For the other numerous group of hydrogen-containing ions, such as La_2H^+, $LaH^\pm$, Ni_nH^- (n = 1, 2, 3, 4), as well as complex ions $LaNiH^\pm$, $LaNi_2H^\pm$ such an approximation is also possible, however, in all the cases with different exponents that are smaller than one.
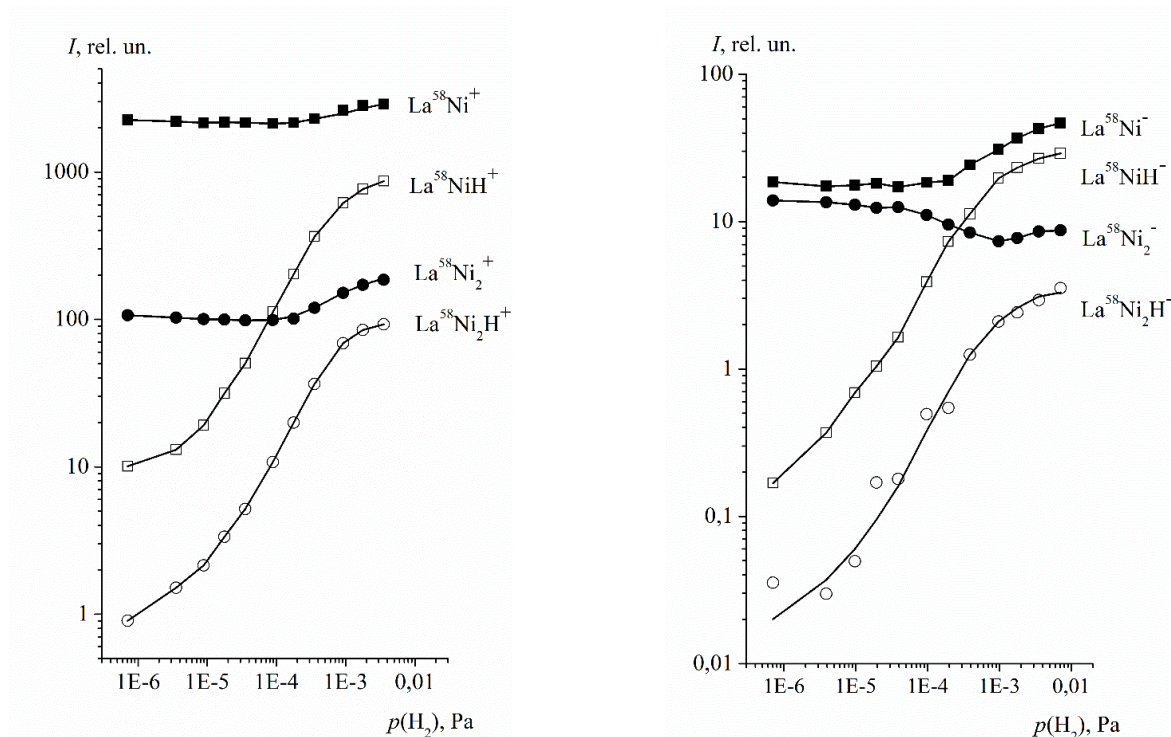
Figure 9. Dependence of the emission intensity of hydrogen-containing complex secondary ions (with lanthanum and nickel), sputtered from the surface of $LaNi_5$, on the partial pressure of hydrogen, at the room temperature
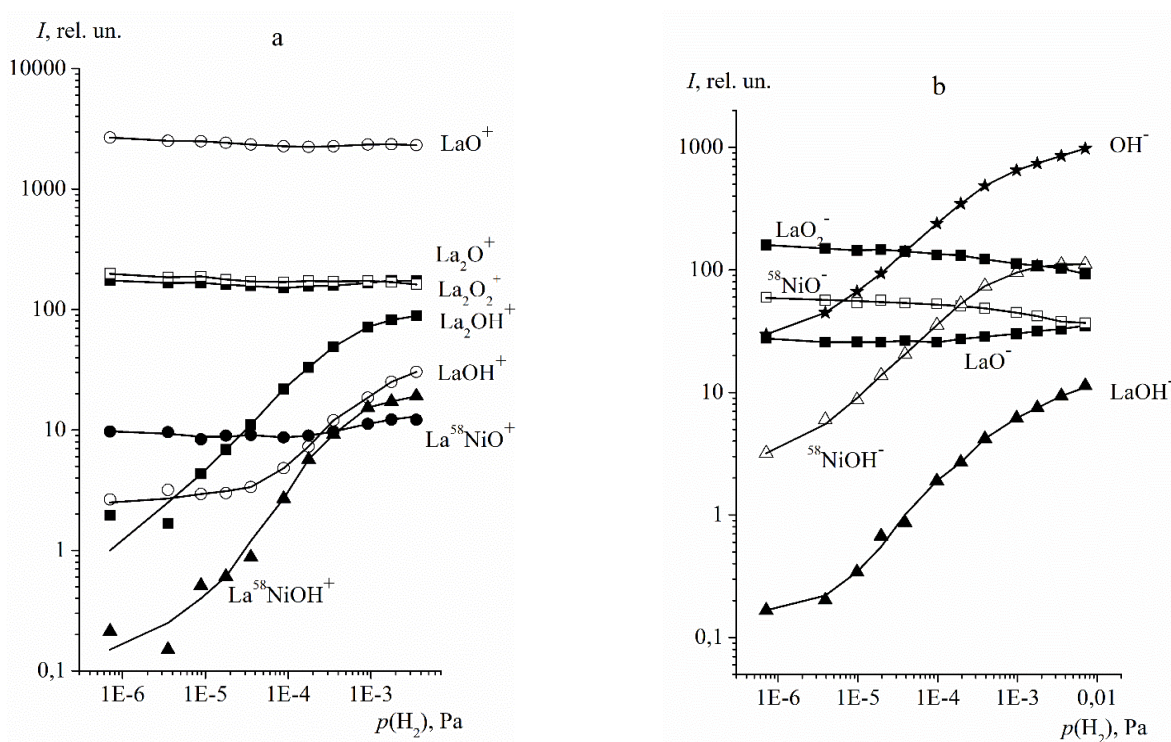

Figure 10. Dependence of the emission intensity of oxygen-containing positive (a) and negative (b) secondary ions, sputtered from the surface of $LaNi_5$ at the room temperature, on the partial pressure of hydrogen

The presence of the group of secondary ions containing more than one hydrogen atom and differing in the value of the exponent of the degree of the power function, which approximates the dependence of the emission intensity on the partial pressure of hydrogen, gives reason to assume the following. As hydrogen accumulates on the surface and in the near-surface region of the samples, a parent hydrogen-containing structure, whose characteristic fragments are secondary ions containing more than one hydrogen atom, is formed. This compound is characterized by the fact that nickel, which is divalent in most chemical compounds, has strong bonds with two hydrogen atoms, and trivalent lanthanum has such bonds with more than two hydrogen atoms. The fact that the set of characteristic ions for this compound includes the complex $LaNiH_2^-$ ion indicates that the formed hydrogen-containing structure includes the both main components of the alloy. Thus, it can be assumed that under the specified conditions of the experiment, a hydrogen-containing intermetallic compound, characterized by a certain stoichiometric ratio, is formed on the surface and in the near-surface region. Such a compound cannot be identified with the bulk hydride phase of the alloy (β-phase), which is formed in the volume of the sample at significantly higher pressures and is characterized by a number of thermodynamic and crystallographic parameters.

The emission of the secondary ions, containing less than two hydrogen atoms, is the result of the fragmentation of the hydrogen-containing surface-structures, in which the alloy components do not exhibit their valence limits. The increase in the intensity of such emissions represents only an increase in the number of such structures or, in fact, an increase in the amount of hydrogen, which formed a bond with the alloy components, in various atomic combinations.

In the processes of intermetallic alloys hydrogenation, the temperature is an equally important parameter as the hydrogen pressure, therefore, when carrying out the work, the dependence of the emission intensity of hydrogen-containing secondary ions on the samples temperature was measured. The measurements were carried out at the residual pressure and, for a greater clarity, at an increased partial pressure of hydrogen $P_{H2}=3.54\cdot10^{-4}$ Pa. As it was in the case of dependences on the partial pressure of hydrogen, the temperature dependences for the secondary ions, which include the alloys main components, that is, lanthanum and nickel, are similar. As an example, Fig. 11 shows a series of such dependencies for the secondary ions sputtered from the surface of the $LaNi_5$ sample.
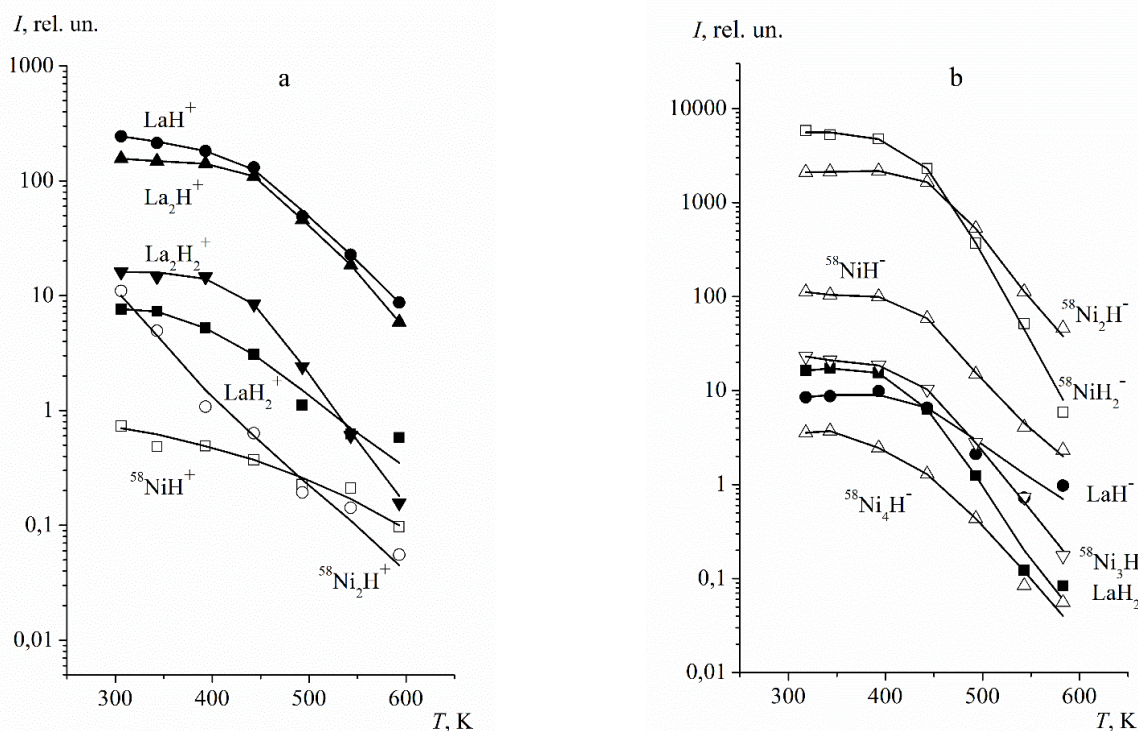

Figure 11. Dependence of the emission intensity of positive (a) and negative (b) hydrogen-containing secondary ions, sputtered from the surface of $LaNi_5$, on the temperature at the hydrogen pressure increased to $p(H_2)=3.54\cdot10^{-4}$ Pa, and at the current density of primary ions $j=4,5$ μA·cm^{-2}

The main characteristic feature of the temperature dependences, measured at an increased hydrogen partial pressure, is a significant decrease in the emission intensity of almost all the positive and negative hydrogen-containing ions as the temperature increases. The emission intensity of such ions correlates with the amount of hydrogen-containing compounds on the surface; therefore, a decrease in the intensity of these emissions indicates a decrease in the amount of hydrogen-containing chemical compounds.

The steady state coverage of the surface by the adsorbed particles and the products of chemical reactions of these particles with the surface atoms of a solid is determined by the dynamic balance between several processes. These are the adsorption-desorption processes, since the steady state coverage is realized at adsorption-desorption equilibrium

between the gas phase and the surface, as well as the processes of sputtering by the primary beam and diffusion processes of adsorbed particles into the volume. The parameters of sputtering processes, in the first approximation, do not change with temperature in the studied temperature range and, therefore, sputtering affects the steady state coverage in the same way at different temperatures. The parameters of the diffusion processes, as a rule, can significantly depend on the temperature, especially for hydride-forming alloys. In order to find out the role of the diffusion processes in our experimental conditions, the following experiment was conducted.

The surface of the sample ($LaNi_5$) was pre-cleaned with the high-density primary beam. Then hydrogen was supplied into the chamber, settling within 1-2 seconds to a pressure of $1.8 \cdot 10^{-4}$ Pa, simultaneously, the time dependence of the emission intensity of the Ni_2H^- ions, which is characteristic of hydrogen-containing compounds, was measured. During this measurement the primary current density was reduced to $j=1.13$ µA cm^{-2}. A lower density, than that at measuring the temperature dependences, was used to reduce the sputtering effect of the primary beam. The exposure duration at the increased hydrogen pressure was 150 seconds. The results of measuring the time dependence of the characteristic ion emission intensity during the exposure are presented in Fig. 12. After the exposure for 150 c, the hydrogen was pumped out within ~1 s. The density of the primary beam was increased to $j=4.5$ µA·cm^{-2}, and the time dependence of the emission intensity was measured, i.e. in the process of sputtering of the formed layer of hydrogen-containing compounds. This procedure was repeated for various sample temperatures. These data are presented in Fig. 13.
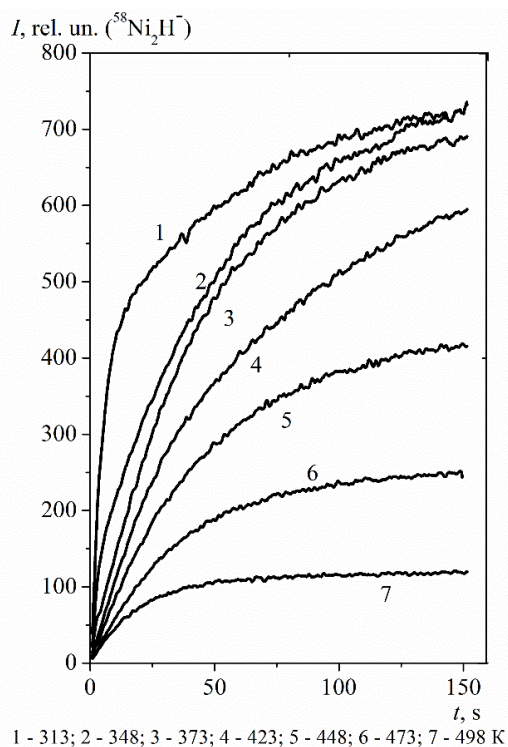

Figure 12. Time dependence of the emission intensity of secondary ions Ni_2H^-, sputtered from the $LaNi_5$ surface, for different temperatures of the sample at the current density of primary ions $j=1.13$ µA·cm^{-2} and the partial pressure of hydrogen $p(H_2)=1.8 \cdot 10^{-4}$ Pa
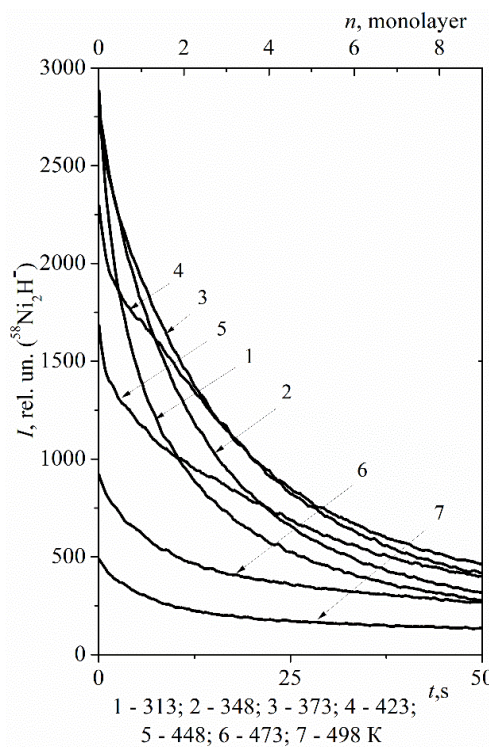
Figure 13. Dependence of the emission intensity of secondary ions Ni_2H^- on the time of sputtering after exposure at hydrogen partial pressure $p(H_2)=1.8 \cdot 10^{-4}$ Pa at different temperatures and primary ion current density $j=4.5$ µA·cm^{-2}

From the data shown in Fig. 12 the following is evident. First, the emission intensity of secondary ions, characteristic of the hydrogen-containing compounds, increases with time, what is quite natural. All the curves tend to rich the plateau. Since the registered ions are sputtered from the upper monolayers, the increase of their emission intensity indicates an increase in the amount of hydrogen-containing compounds on the surface, the fragment of which is Ni_2H^- ion. Secondly, the emission intensity of the characteristic ions decreases with an increase of the temperature, at which the exposure was realized. Such a decrease, by the same logic, can be explained by the fact that at a fixed partial pressure of hydrogen, an increase in the temperature of the sample leads to the formation of a smaller number of hydrogen-containing compounds on the surface. In this case, the dynamic equilibrium between the processes of adsorption, desorption, diffusion and sputtering is realized faster; the curves reach the plateau faster.

An approximate estimate of the number of sputtered monolayers was made as a function of time for the sputtering coefficient equal to 4. The analysis of the data (Fig. 13) allows concluding that during the exposure at the specified partial pressure in the studied temperature range, the hydrogen diffuses with the formation of chemical bonds in noticeable quantities only to the depth of ~ 10 monolayers.

In addition to the above, the following should be noted. In the process of sputtering, the amount of the hydrogen-containing compounds for different stages of sputtering changes in a complex manner. Considering that in this case the sputtering itself is the process that determines the composition of the surface compounds, that is, without taking into account the hydrogen diffusion in the process of measurements, then it can be assumed that the data, obtained in the sputtering process, actually represent the results of the depth profiling analysis. This allows tracing the dependence of the amount of hydrogen-containing compounds on the temperature, at which the exposure was realized, for different stages of sputtering. Fig. 14 presents the following data.
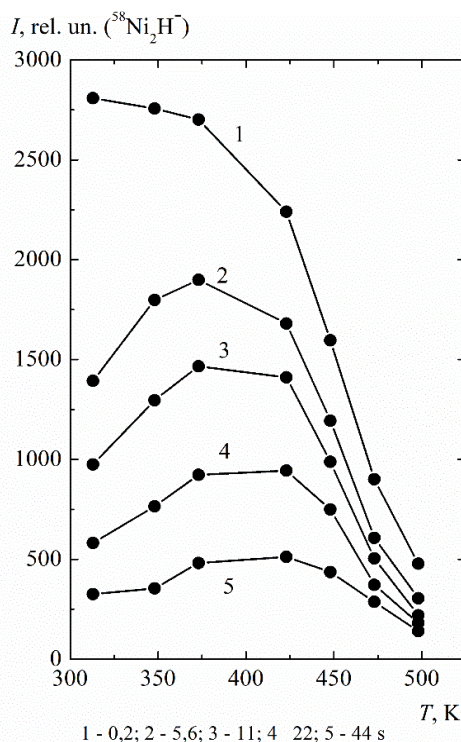

Figure 14. Dependence of the emission intensity of secondary ions Ni₂H⁻, sputtered from the surface of LaNi₅, on the exposure temperature for different stages of sputtering

The analysis of the dependences presented in Fig. 14 shows, that in the first monolayer at the beginning of sputtering for ~ 0.2 s, the number of hydrogen-containing compounds decreases monotonically with the increase of the exposure temperature, i.e., the curve monotonically decreases. For the subsequent monolayers, there is a tendency for reaching the maximum emission intensity at the temperatures higher than the initial one. Thus, in the second monolayer (after ~ 5,6 s of sputtering) and, similarly, in the third and fourth monolayers (after ~ 11 and 17 s of sputtering), the amount of hydrogen-containing compounds increases with the increase of the exposure temperature from 313 K to 373 K. In the fifth and deeper monolayers, the number of hydrogen-containing compounds increases with the increase of the exposure temperature up to 423 K. At the higher exposure temperatures, the number of compounds decreases for all the monolayers. Thus, in the region from the fifth monolayer and deeper, the maximum emission intensity, and therefore the amount of hydrogen-containing compounds, is in the temperature range of 373-423 K. At the same time, a general decrease in the emission intensity is observed for each subsequent monolayer.

The given results allow for the following conclusions. After the exposure for 150 s, at the hydrogen partial pressure of ~ 10^{-4} Pa, the number of chemical compounds on the surface monotonically decreases several times as the exposure temperature increases ~ to 500 K. In the deeper monolayers, the amount of hydrogen-containing compounds increases at the beginning with the increase in the temperature, at which the exposure is realized, and only after reaching ~ 423 K it begins to decrease. The maximum number of compounds at the depth of more than ~ 5 monolayers is formed in the temperature range of 373-423 K.

Thus, there are additional reasons to believe that under experimental conditions, realized in this study, the processes of hydrogen interaction with the investigated alloys take place only, mainly, on the surface and in the nearest near-surface region. This, in turn, allows to interpret the obtained results as the initial stages of hydrogen accumulation (hydrogenation) processes, namely, as the interaction of hydrogen with the surface of these alloys, without taking into account its significant diffusion into the volume, as one of the channels for changing the surface composition.

In addition to the temperature dependences of the emission intensity of hydrogen-containing secondary ions the temperature dependences of the oxygen-containing ions of the main components of the alloys under investigation and carbon-containing ones, were measured. As an example, Figs. 15, 16 show the temperature dependences for such secondary ions, sputtered from the LaNi₅ surface, which were measured at the residual partial pressure of hydrogen.
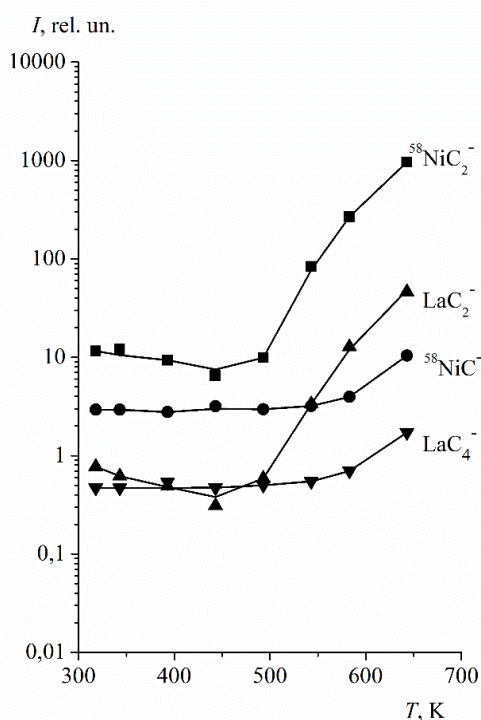
Figure 15. Temperature dependence of the emission intensity of carbon-containing negative secondary ions, sputtered from the surface of LaNi₅, at the residual partial pressure of hydrogen, and the current density of primary ions j=4.5 µA·cm⁻²
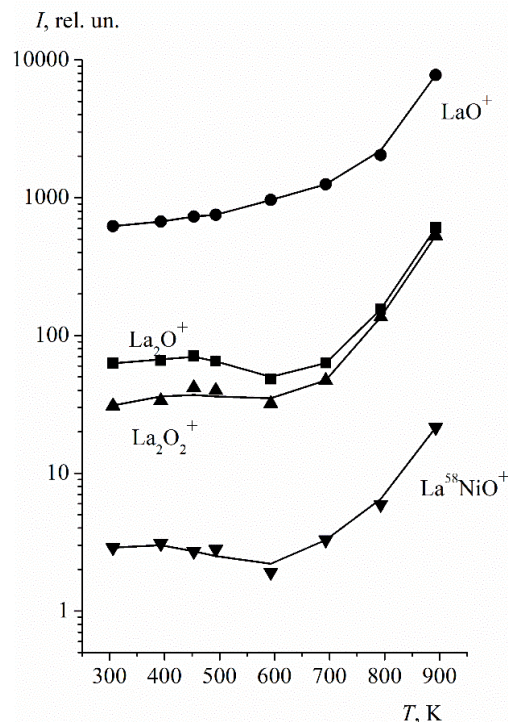
Figure 16. Temperature dependence of the emission intensity of positive secondary ions containing oxygen, which are sputtered from the surface of LaNi₅ at the residual partial pressure of hydrogen and the current density of primary ions j = 4.5 µA·cm⁻²

The presence of the emissions of carbon-containing ions is due to the fact that carbon is present in the volume of polycrystalline samples as an impurity. A common feature of all the temperature dependences of carbon-containing ions emissions is a greater or lesser increase in the emission intensities at an increase of the temperature (Fig. 15). Especially intensive growth is observed at the temperatures above ~ 450 K ($^{58}NiC_2^-$, LaC_2^-). This, most likely, is due to the fact, that at these temperatures carbon begins to diffuse from the volume to the surface, where it forms chemical bonds with the alloy components.

The presence of oxygen-containing ions in the mass spectra of secondary ion emissions is a consequence of both the presence of oxides in the samples volume as a bulk impurity, and, to a lesser extent, the result of oxygen sorption from the gas phase. As Fig. 16 shows, the emission intensity of oxide ions at the temperatures above ~600 K has a general tendency to increase with the temperature rise. The observed increase in the emission intensities of oxygen-containing ions is logically to be associated with the intensification of the oxide formation processes at these temperatures.

Next, the results of the investigation of the surface of intermetallic alloys $LaNi_{4.75}Al_{0.25}$ and $LaNi_{4.5}Mn_{0.5}$ by SIMS are presented. That is, the LaNi₅-based alloys, in which a part of the nickel atoms were replaced by aluminum or manganese atoms, were studied [41].

It is known, that the properties of the intermetallic LaNi₅ can be changed within wide range by replacing lanthanum or nickel completely or partially with some other metals. As long as lanthanum has a rather high cost, it is replaced by the mixed metal Mm, which contains La, Ce, Pr, Nd, Sm Gd in different percentage ratios. This significantly reduces the cost of the intermetallic without significant change in its properties. In order to change the hydrogen sorption characteristics of alloys of the LaNi₅ (MmNi₅) type, reduce the number of activation cycles, increase the stability of characteristics in the process of operation, and reduce the cost, they are alloyed by replacing the nickel atoms by various elements (Mg, Al, Ti, Zr, Mn, Mo, Cr, V, Fe, Co, Si, Zn, Sn). [4, 5, 43, 44]. Different options of Mm(Ni, Co, Mn, Al)₅ alloys are the basis of most up-to-date commercial anodes of nickel-metal hydride (NiMH) batteries.

Various hydrogen sorption characteristics of such doped alloys have been extensively studied experimentally. However, despite the considerable efforts by experimentalists, the mechanisms causing doping effects still remain insufficiently determined.

Summarizing the results of a large number of works devoted to the study of the influence of alloying with aluminum and manganese, the following conclusions can be drawn. Partial replacement of Ni atoms in the intermetallic LaNi₅ by Al or Mn atoms causes significant reduction of the equilibrium pressure in the plateau region, reducing the absorption/desorption pressure hysteresis with a slight decrease in the hydrogen capacity. The kinetics of sorption processes also does not change significantly, although the data on the kinetics are contradictory [5, 45-48].

It was established that the alloy with aluminum has a higher cyclic stability than $LaNi_5$, and is also characterized by a greater resistance to the presence of an oxygen admixture in hydrogen. The partial replacement of nickel atoms by aluminum increases the resistance to both internal and external degradation of the material [49-52].

The study of Al influence on the hydrogen diffusion in the alloy hydride doped with aluminum showed a significant increase of the activation energy of hydrogen diffusion at the room temperature, and, accordingly, a decrease in the rate of diffusion by more than two orders of magnitude as compared to the base alloy hydride [53, 54].

When discussing the reasons for the decrease in equilibrium pressure, corresponding to the plateau on the sorption/desorption isotherm, when nickel is replaced by aluminum or manganese, many authors, for example, in [47, 55, 56] agree that the main reason is an increase in the size of the elementary crystal cell of the alloy, since the atomic radius of Al and Mn exceeds that of Ni. In [55] it is shown that the plateau pressure on the pressure-composition-temperature diagram is inversely proportional to the interstitial hole size in the crystal lattice, in which the hydrogen is accommodated. As a result of the increase of interstitial hole size, the hydrogen atoms are more easily embedded in the crystal lattices, forming thermodynamically more stable hydrides, which leads to an increase in the enthalpy of hydride decomposition and a decrease in the equilibrium potential of hydride formation.

Therefore, the replacement of nickel atoms in $LaNi_5$ by larger atoms stabilizes the hydride phase of these materials and leads to the formation of more stable hydrides. From the technological point of view, this replacement is a convenient option for expanding the working temperature range of these materials. Unfortunately, the replacement of nickel with larger atoms is usually accompanied by a slight decrease in the hydrogen capacity [57, 58].

Generally, the data of SIMS experiments were analyzed in order to determine the functions of different components of the alloy related to the interaction with hydrogen, that is, the adsorption on the surface and its subsequent binding in the alloy.

The analysis of the mass spectra of positive and negative secondary ions, sputtered from the surface of the investigated samples $LaNi_{4.75}Al_{0.25}$ and $LaNi_{4.5}Mn_{0.5}$, which were measured before and in the process of annealing, as in the case with $LaNi_5$, showed the presence of a vast number of various emissions. These emissions are atomic and cluster ions of lanthanum, nickel, aluminum, manganese and also ions which combine the alloy components and the impurities that are present in the samples. In the mass spectra, there are also emissions caused by interaction with the gas phase, that is, the emissions corresponding to the compounds with hydrogen and oxygen. The spectra of positive secondary ions are dominated by the emissions related to lanthanum. The most intensive emission in the spectra of positive ions for all the samples was the emission of lanthanum oxide ions. The spectra of negative secondary ions contain intensive emissions related to nickel, including nickel oxides.

Besides, at the temperatures of more than 700 K, the emission of La^+ and LaO^+ thermionic ions was observed for all the samples; for the samples $LaNi_{4.75}Al_{0.25}$ and $LaNi_{4.5}Mn_{0.5}$ the emission of Al^+ and Mn^+ thermionic ions, respectively, was observed. The emission of such thermoions can be the result of the decomposition and desorption of the oxides that are on the surface from the very beginning.

The mass spectra measured after annealing and cleaning with the primary beam is much cleaner. In Figs. 17, 18 the examples of spectra of positive ions for $LaNi_{4.75}Al_{0.25}$ and $LaNi_{4.5}Mn_{0.5}$ are presented. Like with $LaNi_5$, the spectra of positive secondary ions contain emissions of atomic and cluster ions of lanthanum and nickel, intermetallic ions of lanthanum and nickel, emissions related to the compounds of these ions with hydrogen, oxygen, carbon (which, in general, is typical for metals and alloys). Moreover, the emissions related to lanthanum predominate, and the most intensive emission was that of lanthanum oxide ions, but the emission of nickel oxide was virtually absent. The spectra of negative secondary ions, in contrast to the positive ones, contain mostly nickel-related emissions, including nickel oxides.
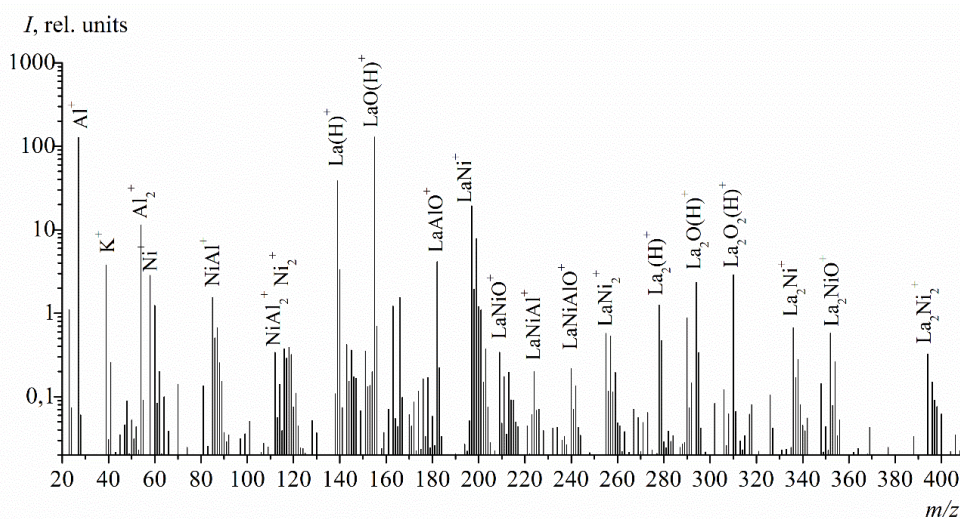

Figure 17. Section of the mass spectrum of positive secondary ions, sputtered from the surface of the $LaNi_{4.75}Al_{0.25}$ alloy sample at the room temperature, in the residual vacuum
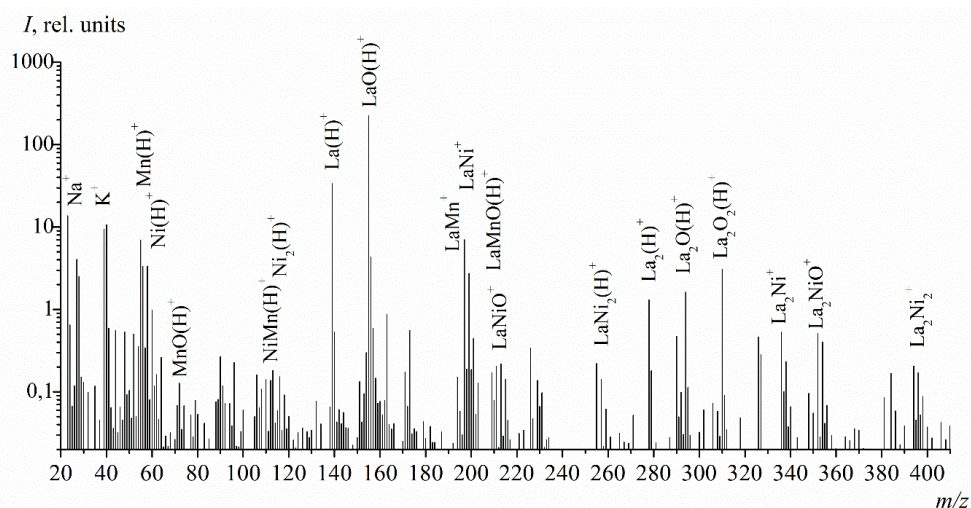
Figure 18. Section of the mass spectrum of positive secondary ions, sputtered from the surface of the LaNi$_{4.5}$Mn$_{0.5}$ alloy sample at the room temperature, in the residual vacuum

As long as the alloys under study are of main interest concerning the interaction with hydrogen, the dependences of the emission intensity of various hydrogen-containing secondary ions, which were sputtered from the surface of the samples, on the partial pressure of hydrogen in the sample chamber, were measured first of all. It is such emissions that allow drawing a conclusion about the presence and composition of chemical compounds containing hydrogen on the surface. The mass spectra obtained at the increased hydrogen partial pressures, as in the case with LaNi$_5$, contain a large set of hydrogen-containing emissions of both positive and negative secondary ions. In the spectra of positive ions, the emissions of hydrogen-containing ions containing lanthanum atoms are the most intensive. In the spectra of negative ions, there are ions containing nickel atoms. The electron affinity energy for lanthanum is 0.5 eV, for nickel it is 1.15 eV [59].

The analysis of the results has shown that for all the samples under study, as in the case of LaNi$_5$, the composition of the mass spectra and the dependence of the emission intensity of the secondary ions, containing lanthanum and nickel, on the partial pressure of hydrogen, are similar. The mass spectra contain emissions of hydrogen-containing positive ions LaH$_n^+$, La$_2$H$_n^+$ (n=1, 2), Ni$_m$H$^+$ (m=1, 2, 3), negative ions LaH$_n^-$, (n=1, 2, 3, 4), NiH$_m^-$ (m=1, 2), Ni$_n$H$^-$ (n=2, 3, 4) and a number of other ions with low intensity.

The specific character of the Mn/Al-doped alloys is the presence of a number of additional emissions related to manganese or aluminum. In the mass spectra of the secondary ions, sputtered from the surface of the LaNi$_{4.5}$Mn$_{0.5}$ alloy, in addition to the ions comprising the main components of the alloy, there is an emission of secondary ions containing Mn. These are positive ions Mn$_n^+$, Mn$_n$H$^+$ (n=1, 2), NiMn$^+$, NiMnH$^+$, LaMn$^+$, LaMnH$^+$ and negative ions MnH$^-$, MnH$_2^-$, MnNiH$^-$, MnNiH$_2^-$. Besides, the emission of manganese ions with oxygen MnO$^-$, MnOH$^-$ is also observed. This indicates that the composition of chemical compounds on the surface of this sample, including oxygen-containing ones, under the specified conditions of the experiment includes all the components of the alloy, including manganese.

In the mass spectra of secondary ions, sputtered from the surface of the alloy dopped with aluminum LaNi$_{4.75}$Al$_{0.25}$, additional emissions of Al$^+$, NiAl$^+$, LaAl$^+$, LaAlO$^+$, Ni$_2$Al$^-$, as well as hydrogen-containing emissions of complex nickel-aluminum and lanthanum-aluminum ions NiAlH$^+$, LaAlH$^+$, LaAlOH$^+$, NiAlH$^-$, NiAlH$_2^-$, Ni$_2$AlH$^-$, are observed. At the same time, there are no emissions corresponding to compounds of aluminum directly with hydrogen (namely Al$_n$H$_m^\pm$), at least in the amount that allows for their unambiguous interpretation in the mass spectra. Since the complex hydrogen-containing ions of aluminum with nickel or with lanthanum are the fragments of the surface chemical compounds, the absence of Al$_n$H$_m^\pm$ ions allows to conclude that at the increased pressures, the hydrogen on the surface is not bound to aluminum, but bound to nickel or lanthanum atoms. This is a notable difference from the alloy with manganese, where the presence of emissions of secondary manganese ions directly with hydrogen (Mn$_n$H$^\pm$) gives reason to believe that manganese, along with nickel and lanthanum, takes a direct part in the processes of hydride formation. Fig. 19 presents the examples of the dependence of the emission intensity of hydrogen-containing ions with manganese and with aluminum on the partial pressure of hydrogen.

The measured dependences of the emission intensities on the partial pressure of hydrogen for all the alloys under study show the following. As the partial pressure of hydrogen increases, the intensity of most of the observed positive and negative hydrogen-containing secondary ions increases substantially. The growing nature of these dependences indicates an increase in the number of hydrogen-containing compounds on the surface and in the near-surface region of the samples, which include all the alloy components. The specific feature of the alloy dopped with aluminum, as noted earlier, is that under the given experimental conditions, hydrogen does not form chemical bonds directly with aluminum, unlike with nickel, lanthanum, and manganese.

The temperature dependences for the hydrogen-containing secondary ions, which include the dopant atoms sputtered from LaNi$_{4.5}$Mn$_{0.5}$ and LaNi$_{4.75}$Al$_{0.25}$ alloys, have mainly the same decreasing character.
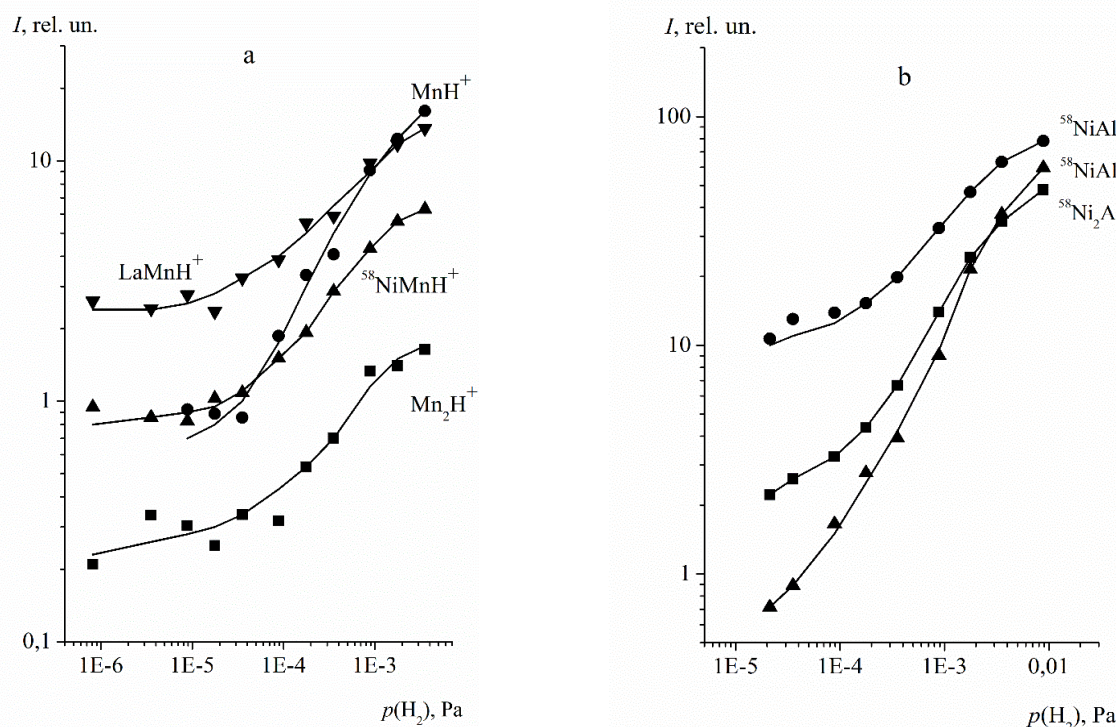
Figure 19. Dependence of the emission intensity of the positive hydrogen-containing secondary ions with manganese, sputtered from the surface of $LaNi_{4,5}Mn_{0,5}$ (a), and negative hydrogen-containing secondary ions with aluminum, sputtered from the surface of $LaNi_{4,75}Al_{0,25}$ (b), on the partial pressure of hydrogen at the room temperature and current density of primary ions $j=4.5\ \mu A\cdot cm^{-2}$

SIMS INVESTIGATION OF CHEMICAL COMPOSITION OF THE COMPOUNDS ON THE SURFACE OF $LaNi_5$ ALLOY DURING ITS INTERACTION WITH OXYGEN

In the following section we present the results of the SIMS studies of the surface monolayers chemical composition of the intermetallic alloy $LaNi_5$ in the process of its interaction with oxygen [60, 61].

The practical use of the intermetallic alloys in various areas of hydrogen energy, such as compact and safe storage of hydrogen, purification, its separation from gas mixtures, and ensuring the operation of various devices using hydrogen as a working medium, requires the solution of a number of problems, one of the main of which is the problem of resistance to gaseous impurities. The impurity gases, which are present in hydrogen, as was indicated earlier, can significantly affect the absorption capacity of intermetallic alloys. In some cases, they can significantly change the kinetic parameters of the sorption-desorption processes and the hydrogen capacity of the alloy [16-18].

The impurity gases, adsorbed on the intermetallic alloy surface, can form a strong chemical bond with the surface metal atoms, as a result these atoms cease participating in the processes of dissociative chemisorption of hydrogen. Such a deactivated surface effectively blocks the underlying region of the material from interacting with hydrogen. If the impurity gas is oxygen, then the high activation energy between the physisorbed and chemisorbed states of hydrogen on the oxidized surface prevents dissociative chemisorption and associative desorption, since most metal oxides do not have valence electronic states for hydrogen chemisorption. The sticking coefficient of hydrogen becomes practically zero. Molecular hydrogen cannot penetrate through the protective surface layer in order to dissociate on the metal surface under the oxide.

On the other hand, the hydrogen dissolved in the alloy cannot leave the surface because the associative desorption is prevented [58]. The removal of the surface oxides lowers the activation energy and causes an increase in the hydrogen sticking coefficient, as well as an increase in the rate of dissociative chemisorption and associative desorption.

The intermetallic alloy $LaNi_5$ has a set of parameters that are very attractive for the practical needs. The alloy is characterized by high hydrogen capacity, excellent sorption–desorption kinetics, relatively low sensitivity to impurities in gaseous hydrogen, and the ability to be easily reactivated after poisoning. At the same time, if the study of the specific character of the alloy bulk properties attracted and continues to attract the attention of many researchers, much less attention was paid to the analysis of the surface properties and its influence on the parameters of hydrogen sorption–desorption processes [62]. Based on this, studies of the surface properties of intermetallic alloys, in general, and the $LaNi_5$ alloy, in particular, remain relevant even nowadays. The study of the surface chemical composition, at the initial stages of interaction with reactive gases, can provide useful information that will allow not only to expand the general understanding of the processes of hydride formation, but also is of undoubted interest for the improvement of activation technologies applied in the processes of interaction with hydrogen, which has gaseous impurities.

A number of works investigated the influence of oxygen on the processes of the intermetallic alloy $LaNi_5$ interaction with hydrogen. At the same time, the published results show some contradictions regarding the nature of the compounds, which are present on the surface.

Thus, in papers [17, 20, 21, 49, 58, 64-66] dedicated to the study of the influence of impurities in gaseous hydrogen and the state of the metal surface on the sorption characteristics of intermetallic alloys, it is considered that the oxygen influence on the properties of the intermetallic alloy $LaNi_5$ involves the processes of the components segregation on the surface. In these works, a model of surface segregation of $LaNi_5$ is proposed. This model is based on the analysis with X-ray photoelectron spectroscopy, low-energy electron diffraction and Auger electron spectroscopy, as well as the magnetic susceptibility measurements.

The essence of the model is as follows. On a freshly prepared $LaNi_5$ sample, the component composition of the surface is the same as in the volume. As long as the surface energy of lanthanum is lower than that of nickel, when reaching the state of thermodynamic equilibrium, the surface is enriched with lanthanum. Selective oxidation of lanthanum on the surface additionally lowers its surface energy. Since the surface segregation is usually driven by the difference in the surface energy of the alloy components, the oxidation of lanthanum promotes the prerequisites for its segregation. Lanthanum diffuses to the surface and binds with oxygen. In the presence of hydrogen, the surface of the alloy is largely covered with La_2O_3 or $La(OH)_3$. The surface oxide is formed as a result of the reaction with oxygen from the gas phase and with the bulk oxygen diffused to the surface.

The authors of these works believe that, as lanthanum segregates and oxidizes, the nickel atoms group together, forming large clusters, which in some cases cross the surface, resulting in a mixture of Ni and La_2O_3 on the surface. Dissociative chemisorption and associative desorption of hydrogen in this case can occur on metallic nickel particles or on the lower $LaNi_5$ metallic layer. The lanthanum oxide and nickel form a protective coating over $LaNi_5$, and therefore, this alloy is rather little affected by impurities such as CO_2, H_2O or O_2, which are present in hydrogen.

In [67], at the investigation of $LaNi_5$ using X-ray photoelectron spectroscopy, it was shown that, when it was exposed to oxygen, the lanthanum atoms, but not nickel ones, were oxidized. The nickel segregation occurs in each hydrogen sorption-desorption cycle. Lanthanum in this model actually serves as a gas absorber, thus ensuring the formation of pure nickel clusters. This process is a mechanism of self-regeneration of the $LaNi_5$ alloy active surface. A similar model was proposed in [68].

Thus, an essential feature of the considered model is the oxygen-induced separation of the alloy components into lanthanum oxidation products (oxides or hydroxides) and nickel clusters. The nickel clusters provide the necessary active centers for dissociative chemisorption of hydrogen before its penetration into the metal lattice.

In contrast to the model described above, in works [69, 70], on the bases of the photoelectron studies, the effect of oxygen is believed to be more complex than that assumed in the above model. Although the rare earth components (lanthanum) are oxidized rather quickly when being exposed to oxygen, however, the experiments have shown that nickel oxide is present in the first few surface monolayers along with the lanthanum oxide. Moreover, the magnetic susceptibility measurements show that primary clustering of nickel occurs during hydrogen desorption but not during its absorption. Thus, it appears that the lanthanum-rich oxide layer is important not because it provides large clusters of nickel on the surface, but rather because it protects the underlying material. In the course of hydrogen sorption-desorption processes, nickel remains unoxidized not due to the self-regeneration mechanism, but, most likely, due to the reducing hydrogen atmosphere [68].

In [62, 71, 72], in the frame of the discussion of the processes of intermetallic alloys activation, in particular $LaNi_5$, the following is proposed. The metal surface, under the influence of air, is enriched with lanthanum and is completely oxidized, mainly to La_2O_3. Actually, oxides, hydroxides and carbides are present on the surface. The nickel, which is on the surface, is completely oxidized. It consists of NiO, $Ni(OH)_2$, and Ni_2O_3, but the latter two components exist only in the upper few monolayers. The La_2O_3 layer extends to a greater depth as compared to NiO, the latter being present only in the form of thin oxide layers. Thus, it is believed that NiO oxide is distributed over the surface of La_2O_3 and, in fact, behaves as a system on a metal carrier, which has a higher catalytic activity as to hydrogen. The NiO, formed on the surface, can be easily reduced by hydrogen even at the room temperature to form active nickel clusters. In other words, after activation, NiO is reduced to the metallic state and forms the Ni/La_2O_3 system. This, in turn, intensifies the hydrogen adsorption and increases the reaction rate.

From the overview of the processes models of the of $LaNi_5$ interaction with the components of the gaseous medium it follows, that until now there is no doubt that the chemical composition of the surface of intermetallic alloys is one of the most important parameters, which controls many surface phenomena, including the processes of hydrogen sorption-desorption, heterogeneous catalysis, etc. At the same time, there is no consensus on what the surface actually represents, and what chemical compounds are present on it, when impurities are present in hydrogen, in particular, oxygen. This circumstance provides grounds for further research.

Next we present the experimental results of the SIMS study of the surface monolayers chemical composition of the intermetallic alloy $LaNi_5$ in the process of its interaction with oxygen. The studied samples were tablets pressed from the fine-grained $LaNi_5$ alloy. Before the measurements, the samples were annealed in a residual vacuum at the temperature of ~1000 K. After annealing, the surface was cleaned with the beam of primary ions until the composition of the mass spectrum and the emission intensity of various secondary ions were fully stabilized.

As mentioned earlier, after annealing and cleaning the sample with the primary beam, the measured mass spectra of both positive and negative secondary ions contain numerous emissions of atomic and cluster ions of the alloy components, as well as the emissions caused by interaction with the gas phase and bulk impurities, i.e. the emissions related to the compounds of lanthanum and nickel with hydrogen, oxygen, and carbon.

The mass spectra of positive and negative secondary ions, sputtered from the surface of the alloy, were measured in the range of oxygen partial pressures $6.6 \cdot 10^{-7}$–$8.8 \cdot 10^{-4}$ Pa and the residual hydrogen partial pressure. The mass spectra contain a large set of oxygen-containing emissions of both positive and negative secondary ions. In the spectra of positive ions, the emissions of oxygen-containing ions, which include lanthanum atoms, turned out to be most intensive. This is, obviously, due to the electropositive nature of lanthanum.

In the spectra of negative ions, there is a large set of oxygen-containing ion emissions, which include nickel atoms. There are also a vast number of oxygen-containing emissions of the complex secondary ions, which include atoms of lanthanum, nickel and oxygen in various combinations. Despite the fact that in the operating mode the residual partial pressure of hydrogen is 4-$5 \cdot 10^{-6}$ Pa, the spectra along with the emission of the oxide ions have corresponding emissions of hydroxide ions.

The dependences of the intensities of a number of oxygen-containing emissions on the partial pressure of oxygen in the sample chamber at the residual partial pressure of hydrogen and the room temperature were measured. The spectra of positive secondary ions were measured at the current density of the primary beam of 9 μA cm^{-2}, and the spectra of secondary negative ions were measured at the current density of the primary beam of 17 μA cm^{-2}. Figs 20-22 present the examples of the measured most specific dependences of the intensities for some positive and negative secondary ions with lanthanum, nickel and intermetallic lanthanum-nickel ions.
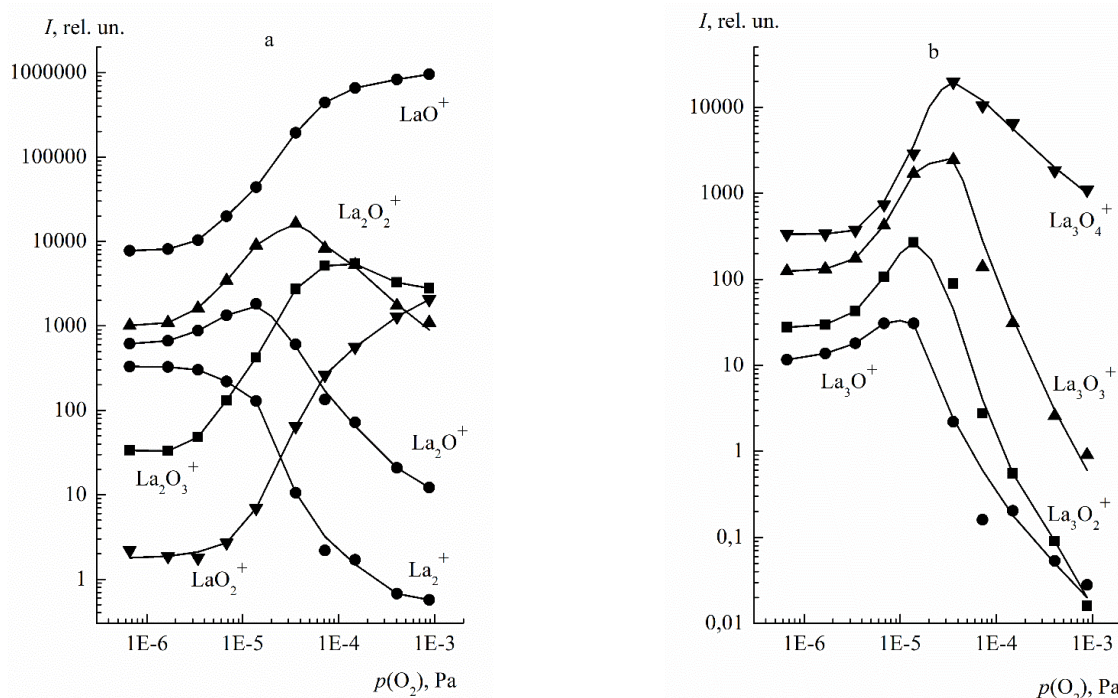

Figure 20. Dependence of the emission intensities of positive secondary ions with lanthanum, sputtered from the surface of LaNi$_5$, on the partial pressure of the oxygen at the room temperature and primary ion current density of 9.0 μA cm^{-2}

The sputtering of the surface of a solid, as is known, occurs when a sufficiently energetic cascade (initiated by primary ions) of paired collisions of target atoms approaches the surface [73]. In the sputtering process, along with monatomic or diatomic particles, the polyatomic complexes, as a part of the surface and near-surface region, are sputtered. Such complexes can escape from the surface if the binding energy of the atoms in it is greater or just under the binding energy of the corresponding complex with the surface. At the stage of separation from the surface, the fragmentation processes of these complexes can continue, as a result of which only stable fragments or only atomic particles remain. Also, at the stage of escape, as a result of electron exchange processes between the escaping complex and the surface, as well as between the complex fragments, a charge state and an excited state of stable fragments are formed. This is the basis of the secondary ion emission and SIMS method, and that, ultimately, allows drawing a conclusion about the state of the surface based on the analysis of the measured mass spectra.

It should be noted that, in contrast to the above mechanism, a model of the polyatomic secondary ions formation due to the recombination of atoms and molecules, sputtered independently in the same cascade of collisions from non-adjacent sites, as a result of interaction in the region near the surface, is also considered [74-77]. If such a model is correct, then the sputtered polyatomic ions will certainly not completely depict the composition of chemical compounds on the surface.
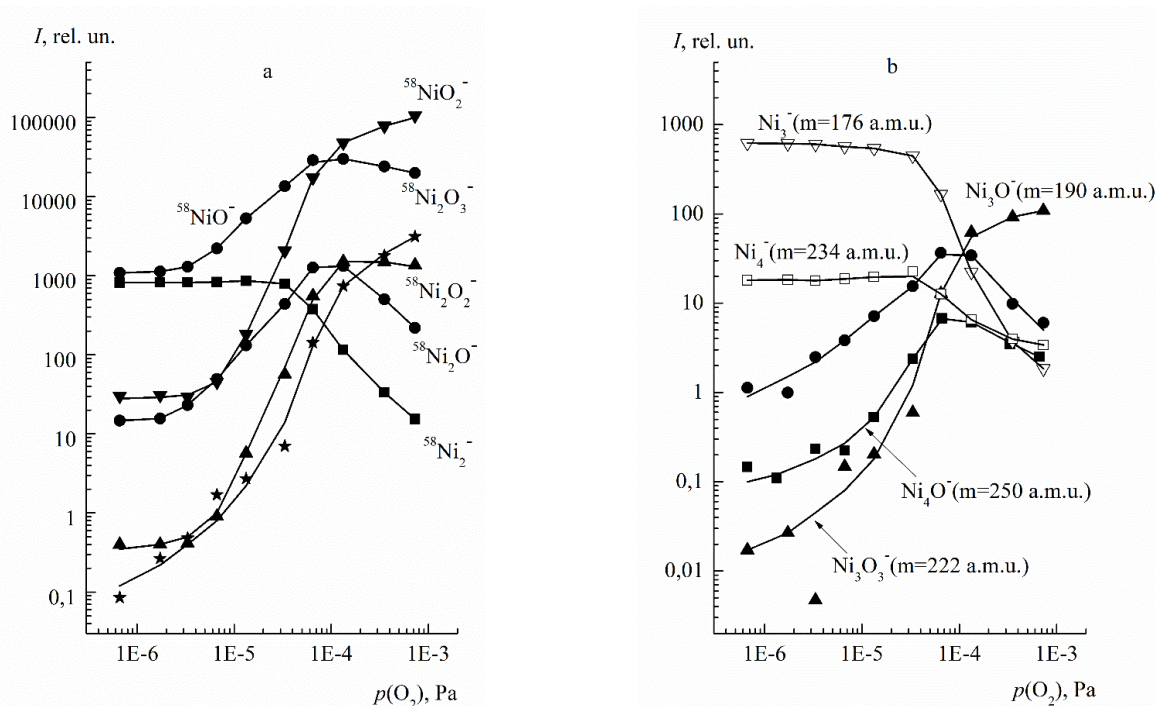
Figure 21. Dependence of the emission intensities of negative secondary ions with nickel, sputtered from the surface of LaNi$_5$, on the partial pressure of oxygen at the room temperature and primary ion current density of 17.0 μA cm^{-2}
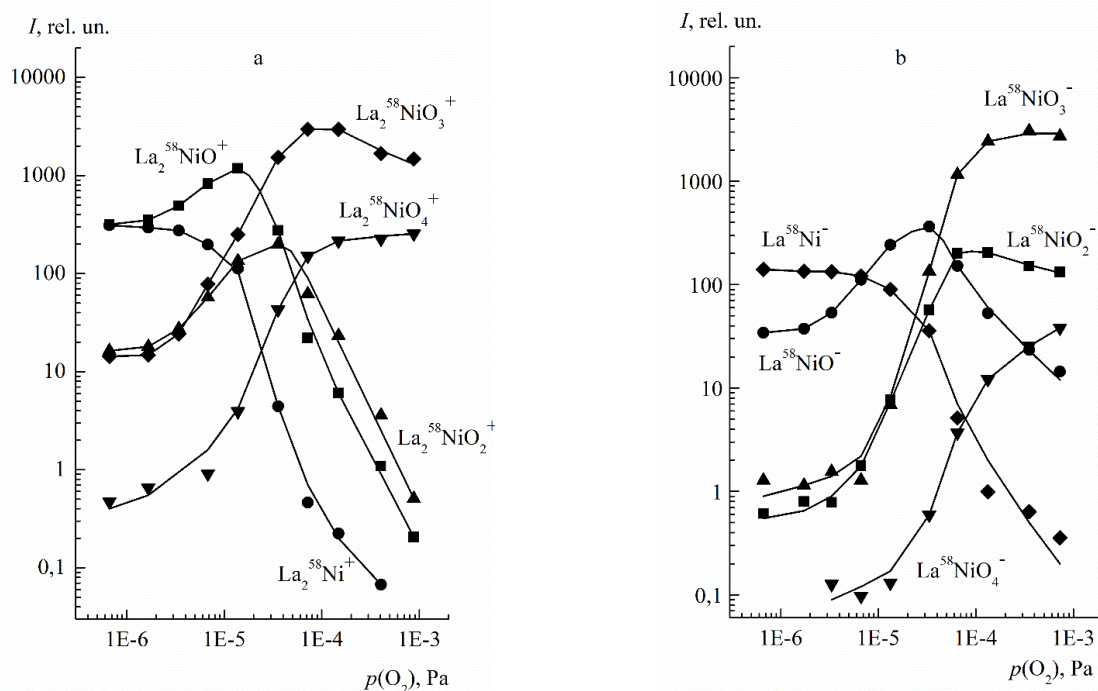

Figure 22. Dependences of the emission intensities of complex secondary ions with lanthanum and nickel, sputtered from the surface of LaNi$_5$, on the partial pressure of oxygen at the room temperature

First, such a model is proposed on the basis of theoretical calculations and has a very limited comparison with the experiment. Secondly, even if in some cases the model is valid for diatomic clusters, it is difficult to assume that up to 6-8 atoms, sputtered in one cascade from non-adjacent sites, recombine above the surface. But in our experiments, the emissions of such secondary ions (for example, $Ni_4O_4^-$, $LaNi_3O^+$, $La_3Ni_2O^+$) are observed, although with low intensity.

Of course, matching of the composition of various secondary ions with specific chemical compounds on the surface must be approached with caution, since, to a much greater extent, the composition of the compounds on the surface corresponds to that of the neutral (not ionic) component of the sputter products. It should be kept in mind that the processes of a charge acquisition and preservation can affect the composition of the sputtered polyatomic ions.

The above said gives reasons to believe that the diversity of the composition of both positive and negative secondary ions, and even the behavior of the dependences of these ions emission intensity on the partial pressure of oxygen, observed in our experiments, are determined exclusively by the composition of the surface and near-surface monolayers, from which the sputtering takes place.

The analysis of the results allows concluding that oxygen forms strong chemical bonds with the both components of the alloy, when it impacts the surface of the $LaNi_5$ sample. This is evidenced by the presence of a large set of secondary ions of $La_nO_m^{\pm}$, $Ni_nO_m^{\pm}$ type, and the presence of secondary ions of $La_nNi_mO_k^{\pm}$ type (where n, m and k take different values in the case of positive and negative ions).

When discussing the mass spectra composition, the following must be kept in mind. Although all the sputtered ions are the fragments of the surface and near-surface monolayers of a solid, the emission of atomic and even diatomic secondary ions, as a rule, is not sufficiently informative. Such ions can be fragments of the chemical compounds having the most diverse composition. At the same time, the emission of complex ions, containing several atoms, largely characterizes the parent structure, from which its ionized fragments are knocked out.

The information about the composition and state of the surface, obtained on the basis of the analysis of such polyatomic emissions, can be more reliable. From this point of view, the most interesting are the emissions of $La_nNi_mO_k^{\pm}$ ions. The presence of such emissions in the spectrum gives reasons to believe that upon the oxygen sorption on the surface of $LaNi_5$, it not only forms strong chemical bonds with both components of the alloy, but forms a general structure of lanthanum, nickel, and oxygen. Moreover, judging by the diversity of the observed secondary ions composition, such an oxide structure in the investigated pressure range is not homogeneous, but is a superposition of structures with different stoichiometric ratios of the components.

With the increase of the oxygen pressure, the emission intensities of most oxygen-containing secondary ions (Figs. 20-22) pass through a maximum. Moreover, the more oxygen atoms in the composition of the secondary ion are per metal atom, the higher is the oxygen pressure, at which the maximum is observed. There are also secondary ions, the emission intensity of which with the increase of the oxygen partial pressure only tends to rich the plateau. Thus, the course of the observed oxygen dependences represents the process of increase in the number of oxygen atoms per number of metal atoms in the oxygen-containing structure, which is formed on the surface and in the near-surface region. As the partial pressure of oxygen increases, an oxide structure is realized on the surface of the $LaNi_5$ sample, in which the number of oxygen atoms per number of the matrix atoms increases.

As is noted above, the mass spectra contain a large number of the emissions of secondary hydroxide ions of the alloy components. In most cases, the intensity of these emissions is small as compared to that of the oxide ion emissions. The presence of such emissions is due to both the residual hydrogen in the sample volume and the interaction of the gas phase with the residual hydrogen. The dependences of the emission intensity of such ions on the partial pressure of oxygen generally correlate with those of the oxide ions. In most cases, the dependencies pass through a maximum or tend to reach the plateau. As an example, Fig. 23 shows the oxygen dependencies for some secondary ions of hydroxides.
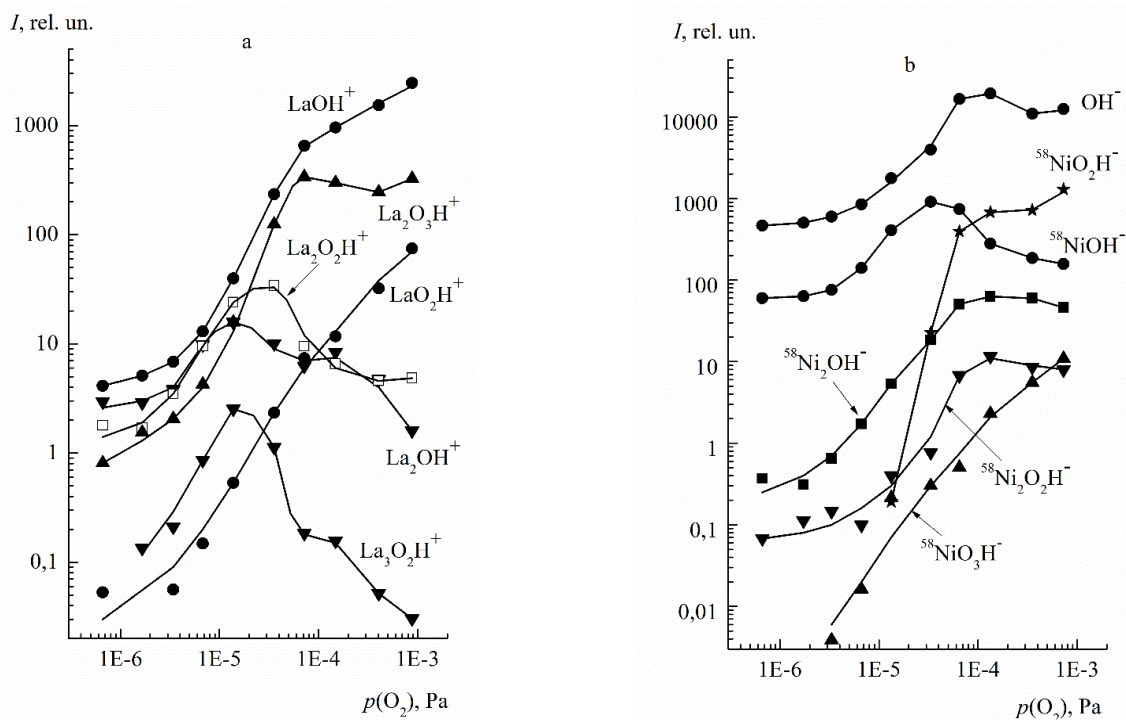

Figure 23. Dependence of the emission intensities of hydroxide secondary ions, sputtered from the surface of $LaNi_5$, at the room temperature, on the partial pressure of oxygen

It should be emphasized, that the concentration of oxygen on the surface, and therefore, the steady state coverage of the surface with oxygen-containing chemical compounds, under our experimental conditions at the room temperature, is determined by the dynamic equilibrium between the processes of oxygen adsorption from the gas phase and sputtering by the primary beam. Also, the effects of the ionic mixing should be taken into account.

Here the following should be noted. It cannot be excluded that under certain experimental conditions, the oxygen-containing secondary ions can be formed at the stage of the escape in the process of the escaping fragment interaction with the gas phase; in our case, as the result of association with oxygen. In this case, the composition of the sputtered ions will not completely characterize the surface structure. In order to check such a possibility, the following experiments were conducted.

After cleaning the surface of the sample with the primary beam at continuous recording of the emission intensity of the selected ion, oxygen was supplied into the sample chamber up to the pressure of $\sim 3.3 \cdot 10^{-4}$ Pa. After 44-46 seconds, the supply of the oxygen was shut off, and then the dependences of the intensity of secondary ion emission and the oxygen pressure in the sample chamber on time were measured. Fig. 24 presents the results of measurements at the sputtering stage after shutting off the supply of oxygen for the oxygen-containing positive ions with lanthanum La_2^+, La_2O^+, $La_2O_3^+$, Fig. 24a, and for the negative ions with nickel NiO_2^-, $Ni_2O_3^-$, Ni_2O^-, Fig. 24b.
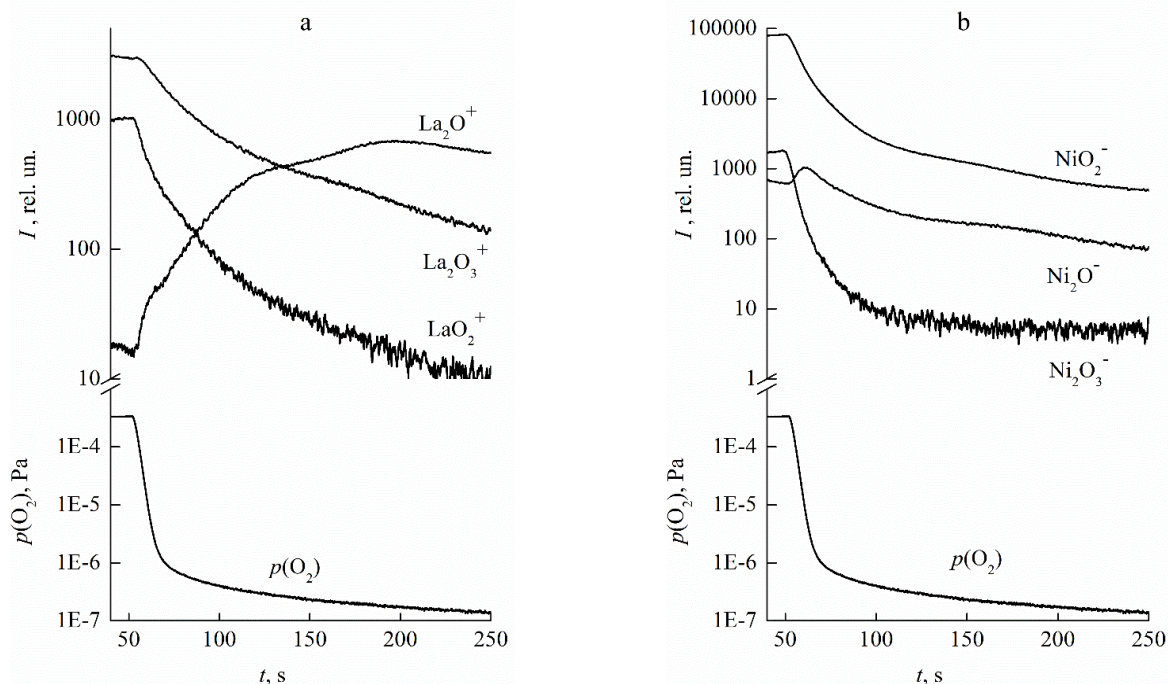

Figure 24. Time dependence of the emission intensities of the oxygen-containing secondary ions and of the partial pressure of oxygen in the sample chamber: a – positive ions, b – negative ions

The analysis of the obtained dependencies shows that the partial pressure of oxygen $p(O_2)$ in the sample chamber, after shutting off its supply, drops by two orders of magnitude in ~ 10 seconds. The emission intensity of secondary ions falls much more slowly. The emission intensity of La_2^+ ions during the same 10 seconds decreases only by 3.3 times, that of $La_2O_3^+$ ions by 1.4 times, in contrast, the emission intensity of $La_2O_2^+$ ions begin to grow and passes through a maximum. The situation with the emissions of oxygen-containing negative ions NiO_2^-, $Ni_2O_3^-$, Ni_2O^-, is similar. The emission intensity of NiO_2^-, $Ni_2O_3^-$ ions decreases to a much lesser degree than the oxygen pressure, and the emission intensity of Ni_2O^- ions passes through a maximum.

Thus, the results of the experiments show that there is no direct correlation between the change in the partial pressure of oxygen and the change in the emission intensity of the secondary ions. This gives reasons to believe that the secondary ions are formed not as a result of association with oxygen of the gas phase, but as a result of sputtering of the oxides formed on the surface.

The behavior of the dependences of the emission intensity on time for the selected ions correlates well with the oxygen pressure dependences for these ions, which are shown in Fig. 20a, 22a. I.e. the curve for La_2O^+ (Fig. 20a) and the curve for Ni_2O^- (Fig. 21a) passes through a maximum as the oxygen partial pressure increases. The dependencies for these ions in Fig. 24a and Fig. 24b qualitatively repeat this trend but in the reverse order. The results, obtained for LaO_2^+, $La_2O_3^+$, NiO_2^-, $Ni_2O_3^-$, in this sense, also correlate with the oxygen dependencies for these ions: these dependencies are shown in Fig. 20a and Fig. 21a. The oxygen dependencies for these ions only tend to rich the plateau. The curves for LaO_2^+, $La_2O_3^+$, $Ni_2O_3^-$, NiO_2^- in Fig. 24, which correspond to sputtering, also qualitatively repeat this trend in the reverse order.

As a continuation of this type of experiments, a study of the dependences of the emission intensities of a wider range of secondary ions on the time of their sputtering after exposure of the sample to oxygen was carried out [78]. An oxide structure was created on the surface of the sample at an increased partial pressure of oxygen, what, as noted

above, is characterized by a set of oxygen-containing secondary ions and by the ratio of their emission intensities. Then this structure was sputtered with the primary beam. As the sputtering progressed, a change in the emission intensity of the observed secondary ions was recorded.

These experiments were carried out in the following way. After cleaning the surface of the sample with the primary beam in the residual vacuum, during the continuous recording of the emission intensity of the selected ion, oxygen was supplied into the chamber up to the pressure of $\sim 3.3 \cdot 10^{-4}$ Pa. After 46-48 seconds, the supply of the oxygen was shut off and the time-dependences of the secondary ion emission intensity and the oxygen pressure in the target chamber were further measured. The oxygen pressure was recorded using a gas mass spectrometer. The results of the measurements are presented in Figs. 25-28.
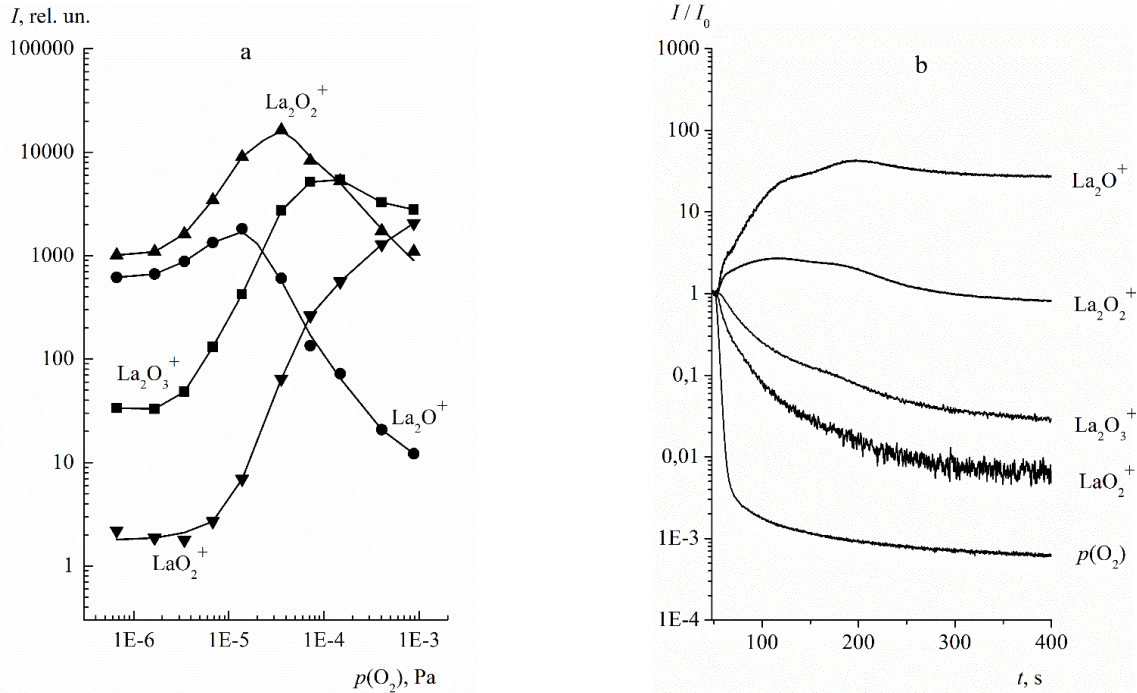

Figure 25. Dependences of the emission intensities of positive secondary ions with two lanthanum atoms on the oxygen partial pressure (a) and dependencies of the emission intensities of positive secondary ions with lanthanum on the sputtering time after exposure to oxygen (b)
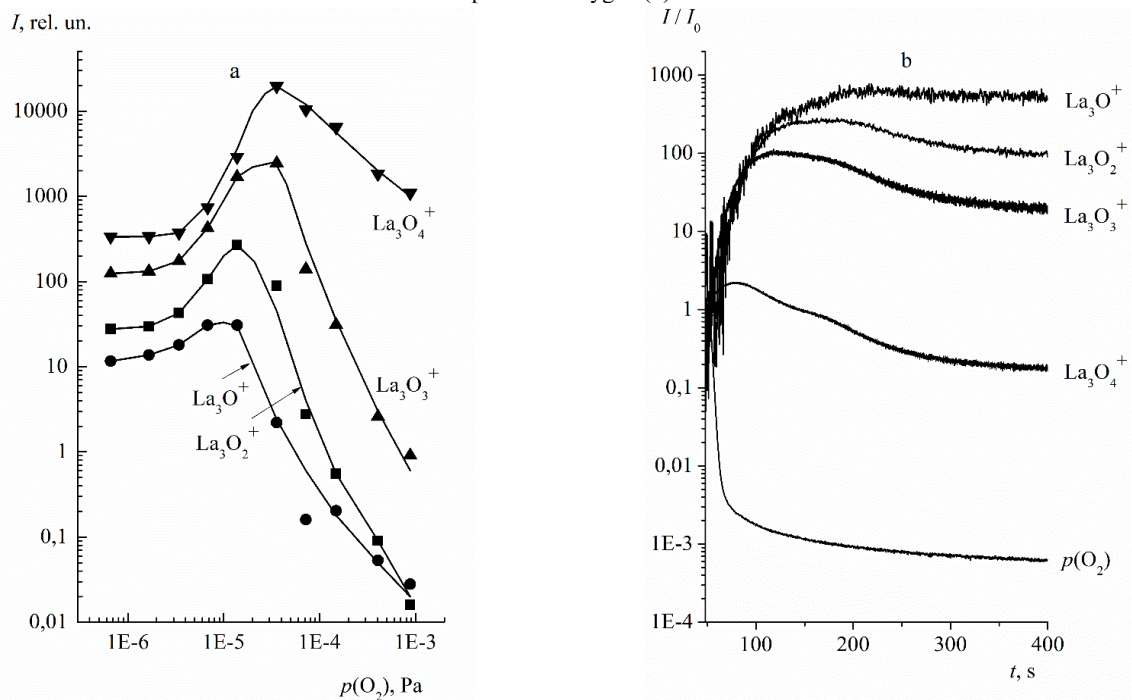

Figure 26. Dependences of the emission intensities of positive secondary ions with three lanthanum atoms on the oxygen partial pressure (a) and dependences of the emission intensities of positive secondary ions with lanthanum on the sputtering time after the exposure to oxygen (b)
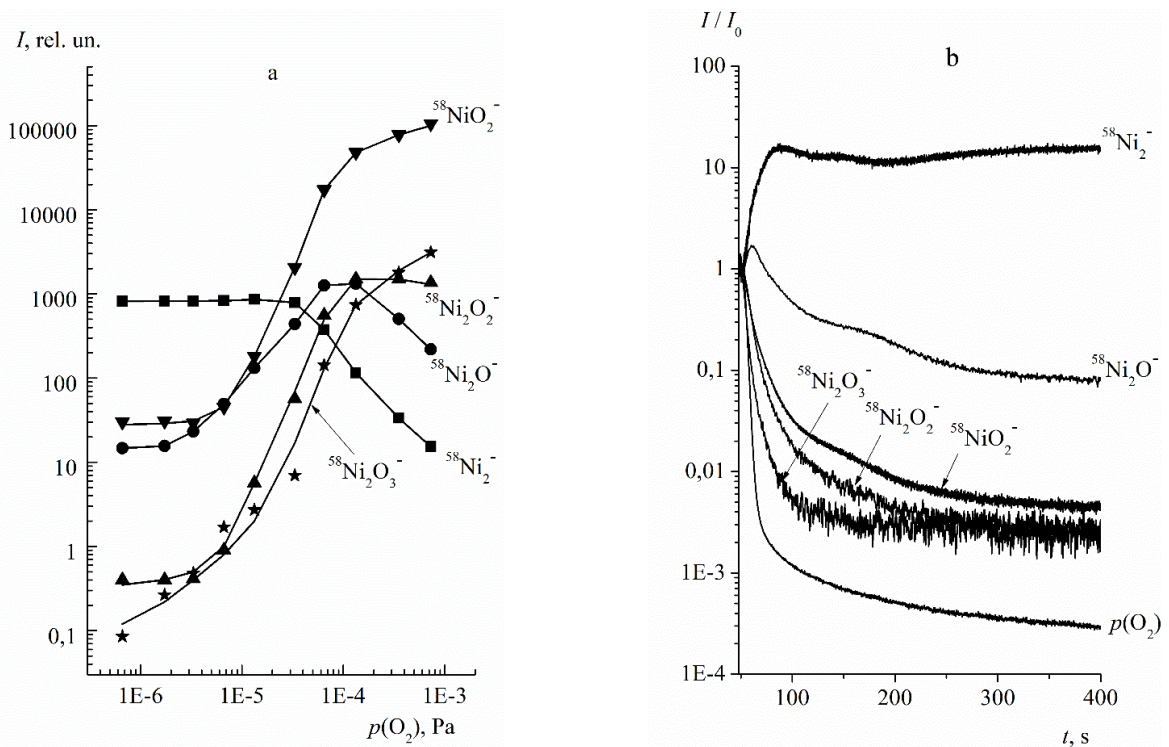
Figure 27. Dependences of the emission intensities of negative secondary ions with nickel on the oxygen partial pressure (a) and dependences of the emission intensities of negative secondary ions with nickel on the sputtering time after the exposure to oxygen (b)
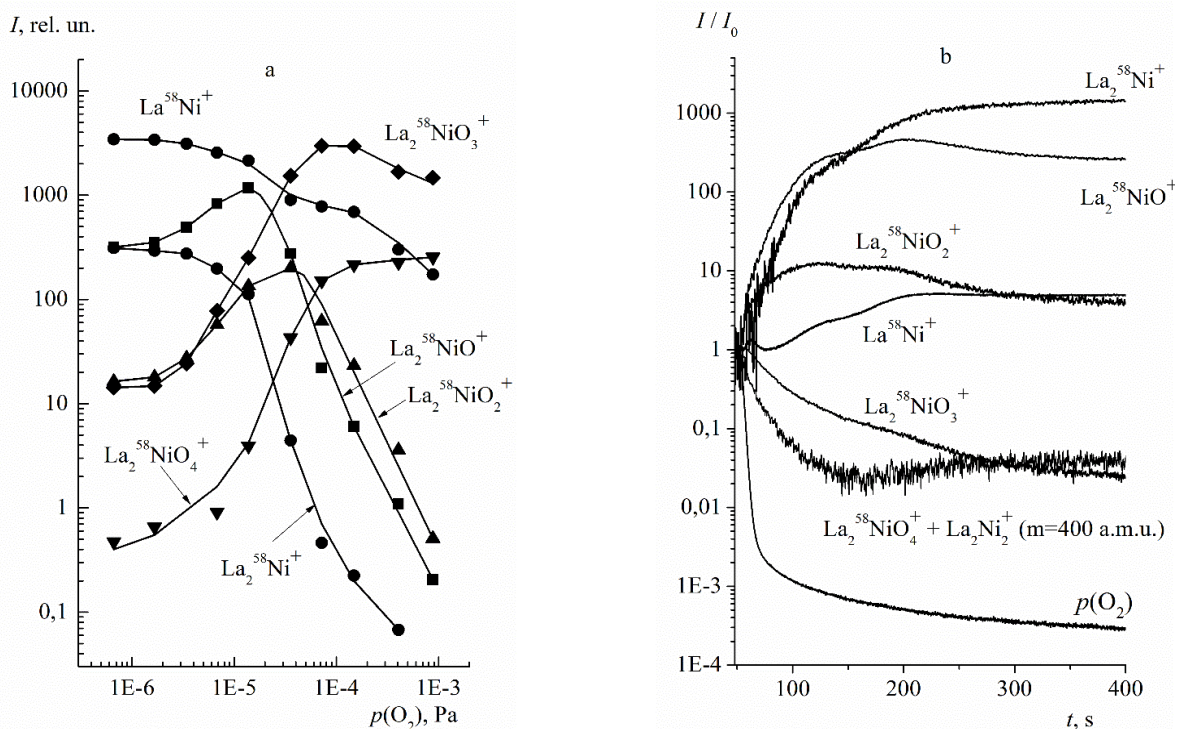

Figure 28. Dependences of the emission intensities of complex secondary ions with lanthanum and nickel on the partial pressure of oxygen (a) and dependences of the emission intensities of complex secondary ions with lanthanum and nickel on the sputtering time after the exposure to oxygen (b)

For clarity, these figures also present both the results of changes in the emission intensity of a number of oxygen-containing emissions (Figs. 25a, 26a, 27a, 28a), obtained at the increase in the partial pressure of oxygen, and the results of the measurements at the sputtering stage (Figs. 25b, 26b, 27b, 28b) after shutting off the supply of oxygen, for the oxygen-containing positive ions with lanthanum and for the negative ions with nickel. For the convenience of comparison, the actual emission intensities, shown in the figures concerning the sputtering, are normalized to their

intensity at the moment, which corresponds to the shutting off the supply of oxygen. Thus, the curves in Figs. 25b, 26b, 27b, 28b show how many times the emission intensity changes during the time of sputtering in relation to the starting point. The same figures present the dependences of the oxygen partial pressure in the chamber, also normalized to their initial value.

The curve marked in Fig. 28b as $La_2^{58}NiO_4^+ + La_2Ni_2^+$, represents the sum of the emissions of secondary ions $La_2^{58}NiO_4^+$ and $La_2Ni_2^+$ (400 a.m.u.), the separation of their specific contributions was not carried out, since the signal was recorded in a continuous mode (unlike the curve for $La_2^{58}NiO_4^+$ in Fig. 28a).

The analysis of the results obtained during the sputtering of oxides shows the following. The oxygen partial pressure $p(O_2)$ in the target chamber, after shutting off the supply, drops by two orders of magnitude in 10 seconds. At the same time, the intensity of the secondary ions emission changes much more slowly. For some secondary ions the emission intensity increases during the sputtering, for the others it decreases, and for a number of ions passes through a maximum. This applies both to the ions with lanthanum, and to those with nickel, as well as to the complex nickel-lanthanum ions (Figs. 24b-28b). Such a behavior of the emission intensity dependences on sputtering time for the selected ions correlates well with the oxygen dependences of these ions, shown in Figs. 24a-28a. The course of dependences of the ion emission intensity on the sputtering time qualitatively repeats in the reverse order the course of the corresponding dependences, obtained with the increase of the oxygen partial pressure.

Such a correlation allows to state that in the sputtering experiments, after the oxygen is pumped out of the sample chamber, as the oxides formed on the surface are sputtered, the situation is realized opposite to that, which occurs at the increase of the partial pressure of oxygen, when the number of oxygen atoms per atom of the matrix in the surface structure increases. That is, as the oxygen-containing structure (formed at the maximum oxygen partial pressures in these experiments) is sputtered, the number of oxygen atoms per number of matrix atoms decreases.

The data, presented in Figs. 24b-27b, indicate that the sputtering of the formed oxides continues during hundreds of seconds. This indicates that the formed oxide compounds have a three-dimensional structure and occupy dozens of monolayers. In such a three-dimensional oxide structure, the outer monolayers are characterized by the highest concentration of oxygen. The oxygen concentration decreases in the deeper lying monolayers.

The sputtering results, obtained during the sample exposure in oxygen under the action of the primary beam and the exposure with primary beam turned off (Fig. 27b) allow making a qualitative similar interpretation. This gives reasons to believe that the primary beam, while introducing the factor of sputtering and ion mixing, does not significantly affect the oxidation processes of $LaNi_5$.

In addition to the above, the results of the sputtering experiments show that there is no direct correlation between the change with time in the partial pressure of oxygen and the change with time in the emission intensities of the secondary oxygen ions. This is a direct indication that the observed secondary ions are not a product of the association of the sputtered surface fragments with the oxygen of the gas phase at the fly-off stage, but are the products of the oxide compounds sputtering, and characterize the composition of the surface and near-surface regions.

SIMS INVESTIGATIONS OF THE OXYGEN EFFECT ON KINETICS OF HYDROGEN SORPTION-DESORPTION PROCESSES BY LaNi₅ HYDRIDE-FORMING ALLOY

Previously, the results of the study of the processes of hydrogen interaction with $LaNi_5$ alloy surface were presented. According to these data, as hydrogen accumulates on the surface (at an increase of hydrogen partial pressure), a hydrogen-containing structure, which is characterized by a certain stoichiometric ratio of components, is formed on the surface and in the near-surface region of the sample. For the SIMS experiments, this structure is characterized both by a certain set of hydrogen-containing secondary ions (positive and negative), sputtered from the surface by the primary beam, and also by the ratio of emission intensities of these ions. One of the secondary ions, which have one of the highest emission intensities at relatively low hydrogen partial pressures, is the Ni_2H^- secondary ion. The emission intensity of such ions depends almost linearly on the partial pressure of hydrogen and can be taken as a measure of the amount of hydrogen that has a chemical bond with the alloy components on the surface and near-surface region. The same applies to the secondary ion La_2H^+. When analyzing the processes of hydrogen sorption-desorption on the surface of $LaNi_5$, these secondary ions were chosen to monitor the amount of hydrogen on the surface.

When studying the effect of the composition of surface chemical compounds on the kinetics of hydrogen sorption processes, the experiments were carried out in the following way. The surface of the sample ($LaNi_5$) was cleaned with the high-density primary beam, next, oxygen was supplied into the chamber up to a certain pressure, so that a certain steady state coverage with oxygen-containing compounds was formed on the surface. Then, hydrogen was supplied into the chamber (within 2-3 seconds) up to a given pressure, and an increase in the number of hydrogen-containing compounds on the surface was observed; the number of compounds was monitored by the emission intensity of the specific secondary ions (Ni_2H^-). After the emission intensity reached the plateau, hydrogen was pumped out (within 2-3 seconds) from the sample chamber, and again, the process of sputtering of the hydrogen-containing compounds was observed by monitoring the emission intensity of the secondary ions Ni_2H^-. Next, the partial pressure of oxygen was increased stepwise, therefore increasing the steady state coverage with oxygen-containing compounds, and the procedure with hydrogen was repeated. Here, it is considered that the steady state surface coverage by adsorbed particles and the products of chemical reactions of these particles with the surface atoms of a solid (in our case, oxides

and hydrides), with the diffusion being not taken into account, is determined by the dynamic equilibrium between the processes of adsorption from the gas phase and the processes of sputtering by the primary beam. All the experiments were performed at the constant primary ion current density (j=14 µA cm^{-2}). In Figs. 29-31 the examples of the measured dependences for several values of the hydrogen partial pressure at different oxygen coatings are presented.
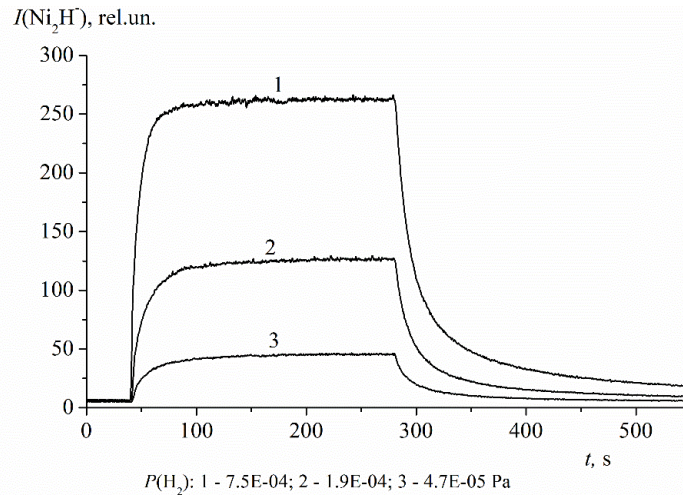
I(Ni$_2$H$^-$), rel.un.

P(H$_2$): 1 - 7.5E-04; 2 - 1.9E-04; 3 - 4.7E-05 Pa

Figure 29. Time dependence of the emission intensity of Ni$_2$H$^-$ ions from the LaNi$_5$ surface at the residual surface pre-coverage with oxygen (at P(O$_2$) residual) and at different values of hydrogen partial pressure
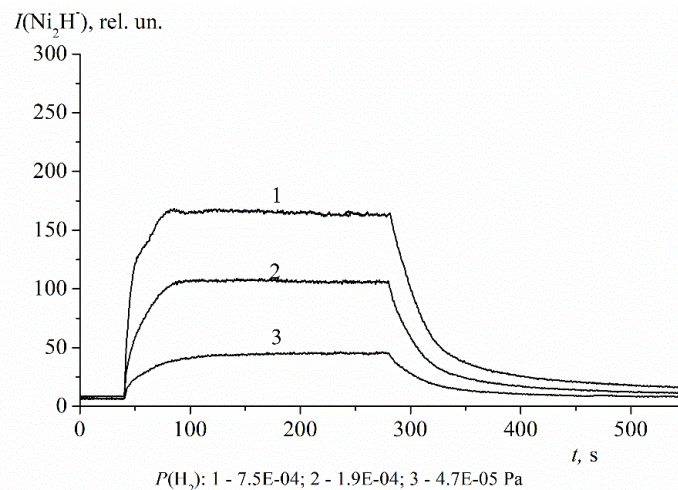
I(Ni$_2$H$^-$), rel. un.

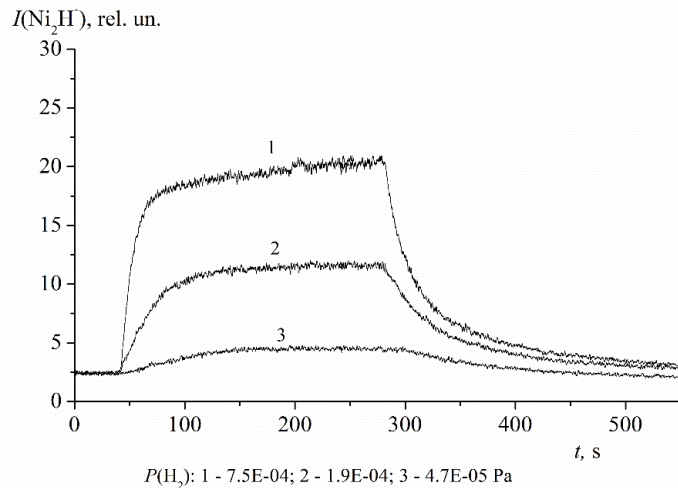P(H$_2$): 1 - 7.5E-04; 2 - 1.9E-04; 3 - 4.7E-05 Pa

Figure 30. Time dependence of the emission intensity of Ni$_2$H$^-$ ions from the LaNi$_5$ surface for the surface pre-coverage with oxygen (at P(O$_2$) 4·10^{-5} Pa) and at different values of the hydrogen partial pressure

I(Ni$_2$H$^-$), rel. un.

P(H$_2$): 1 - 7.5E-04; 2 - 1.9E-04; 3 - 4.7E-05 Pa

Figure 31. Time dependence of the emission intensity of Ni$_2$H$^-$ ions from the LaNi$_5$ surface for the surface pre-coverage with oxygen (at P(O$_2$) 1·10^{-4} Pa) and at different values of the hydrogen partial pressure

The analysis shows that the emission intensity of Ni_2H^- ions and, therefore, the amount of hydrogen-containing compounds on the surface decreases as the partial pressure of oxygen increases, that is, as the surface oxidizes. An increase in oxygen pressure (above $\sim 4\cdot10^{-4}$ Pa) results in a decrease in the emission of Ni_2H^- ions down to the background level, that is, with such oxygen coatings, the hydrogen ceases to interact with the surface. It is evident, that under such experimental conditions, the surface is completely covered by the layer of oxygen-containing chemical compounds, which prevent the hydrogen chemisorption. On the other hand, at the fixed oxygen pressure, the higher the pressure of hydrogen supplied to the chamber is, the greater is the number of hydrogen-containing compounds. Since at the sorption stage all the curves reach the plateau, this means that a steady state coverage of hydrogen-containing compounds is formed on the surface rather quickly, according to the balance between the processes of adsorption of hydrogen from the gas phase and the processes of sputtering. The lack of saturation of the emission intensity as to the hydrogen pressure indicates that all the hydrogen supplied to the chamber (in the applied pressure range) participates in the reaction and, potentially, the surface still has a sufficient resource for the formation of hydrogen-containing compounds either locally or stoichiometrically.

In order to present more clearly the kinetics of the hydrogen sorption process, the data obtained for the sorption stage were normalized to the maximum intensity; the results are given in Fig. 32.
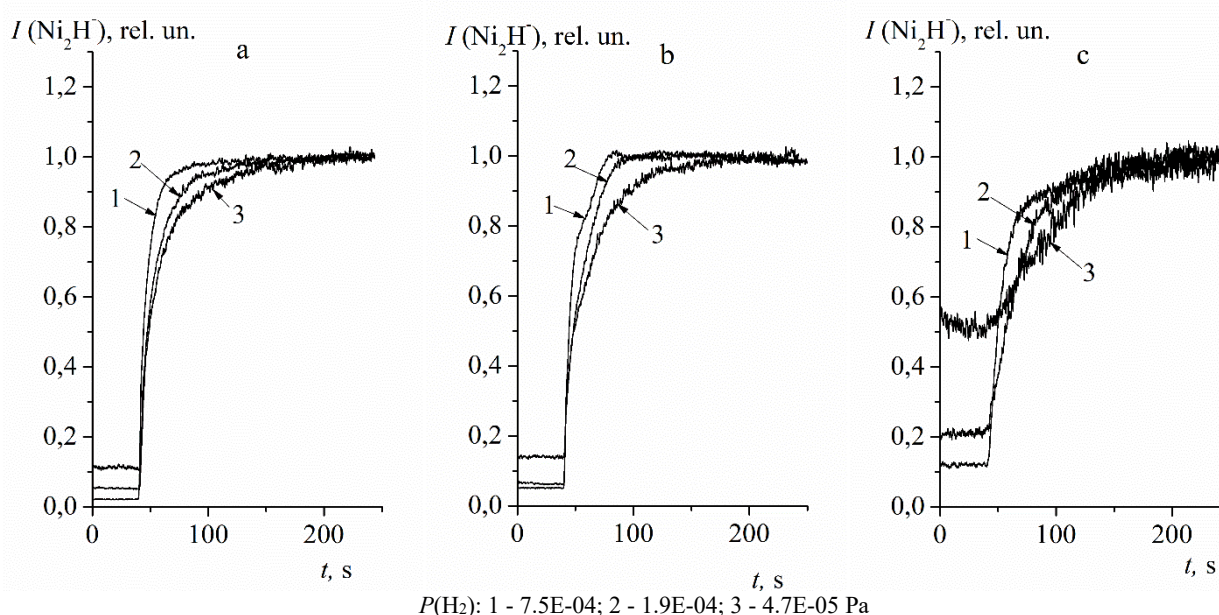

$P(H_2)$: 1 - 7.5E-04; 2 - 1.9E-04; 3 - 4.7E-05 Pa

Figure 32. The normalized time dependence of the emission intensity of Ni_2H^- ions from the $LaNi_5$ surface for different oxygen-precovered surfaces and different values of hydrogen partial pressure: a) residual oxygen pressure; b) $P(O_2) = 4\cdot10^{-5}$; c) $P(O_2) = 1\cdot10^{-4}$ Pa.

From Fig. 32 it follows that the oxygen coating has a weak effect on the formation rate of the maximum possible coverage with hydrogen-containing compounds for this combination of parameters. To a greater extent, the rate is affected by the pressure of the hydrogen supplied to the chamber; the higher is the pressure, the higher is the rate of the compounds formation.

Similar experiments were performed for the case, when La_2H^+ ions were used as characteristic secondary ions. The analysis of their results allows drawing similar conclusions.

When studying the effect of the composition of chemical compounds, which are present on the surface (in our case, the effect of surface oxidation), on the kinetics of hydrogen desorption processes, the experiments were performed in the following way. The surface of the sample was cleaned with the primary beam, then the primary ion current density $j=0.14$ $\mu A\cdot cm^{-2}$ was set (a lower density than that in other experiments was used to minimize the decrease of the amount of chemical compounds on the surface by sputtering); the sample chamber was supplied with oxygen and various oxygen pre-coatings were created on the clean surface of the sample, next, the oxygen was pumped out and the chamber was supplied with hydrogen, which created its own coverage on the partially oxidized surface. After the formation of the specified coverage, hydrogen was pumped out and the sample was heated up linearly with at the rate of 1.62 K sec^{-1}, simultaneously, the emission intensity of the characteristic ions Ni_2H^- was recorded. After the experiment was over, the surface was cleaned with the primary beam to the initial state. The measurements were repeated for different values of the exposure both in oxygen and in hydrogen. The results are presented in Fig. 33.

The increase of the sample exposure in oxygen at the same unchanged exposure in hydrogen leads to a decrease in the number of hydrogen-containing chemical compounds on the surface. This, in fact, confirms the results of the experiments on sorption. (Figs. 29-31). After small exposures in hydrogen (Fig. 33a), that is, with a small amount of hydrogen-containing compounds on the surface, the hydrogen desorption is noticeable with an increase in temperature, and therefore the decrease in the number of hydrogen-containing chemical compounds for all the investigated oxygen

pre-exposures begins only at the temperatures above ~ 450 K. After relatively larger exposures in hydrogen (Fig. 33b), that is, with a relatively large number of hydrogen-containing compounds on the surface, the hydrogen desorption begins almost immediately after the onset of heating for all the investigated oxygen pre-exposures. In each case, however, at the temperature of ~ 575 K, the emission of characteristic ions becomes negligible, so the surface becomes free of hydrogen-containing chemical compounds; in this case, such a situation occurs for all the oxygen pre-exposures.
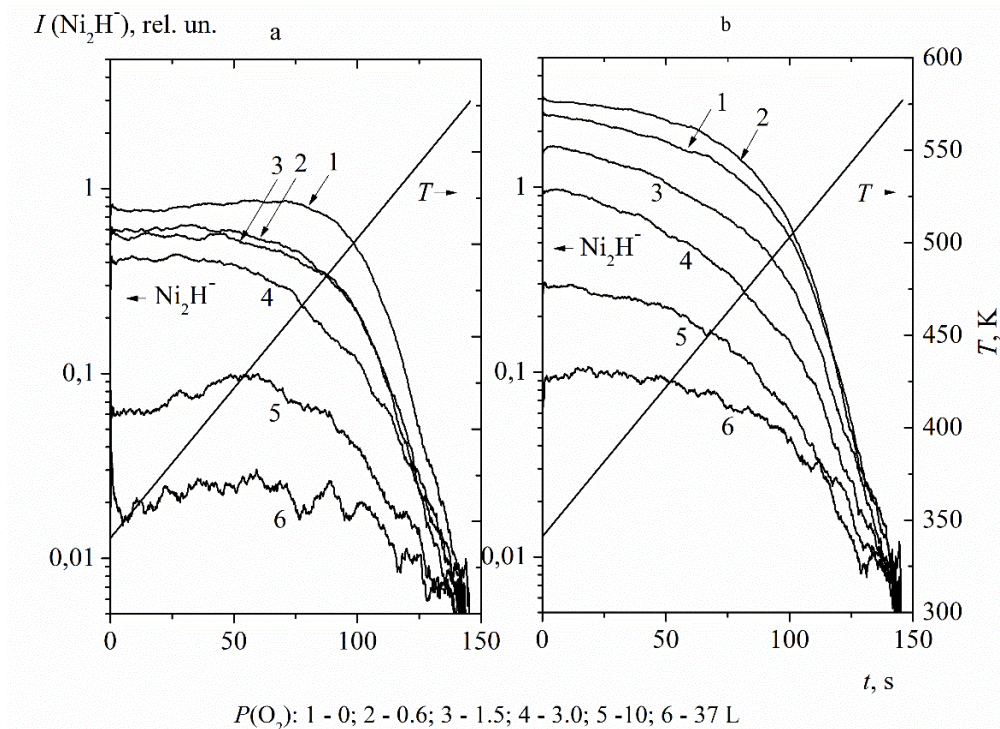

$P(O_2)$: 1 - 0; 2 - 0.6; 3 - 1.5; 4 - 3.0; 5 -10; 6 - 37 L

Figure 33. Time dependence of the Ni_2H^- ions emission intensity from the $LaNi_5$ surface at a linear increase in temperature after different values of pre-exposure in oxygen for the exposure in hydrogen: a) – 4 L; b) – 60 L
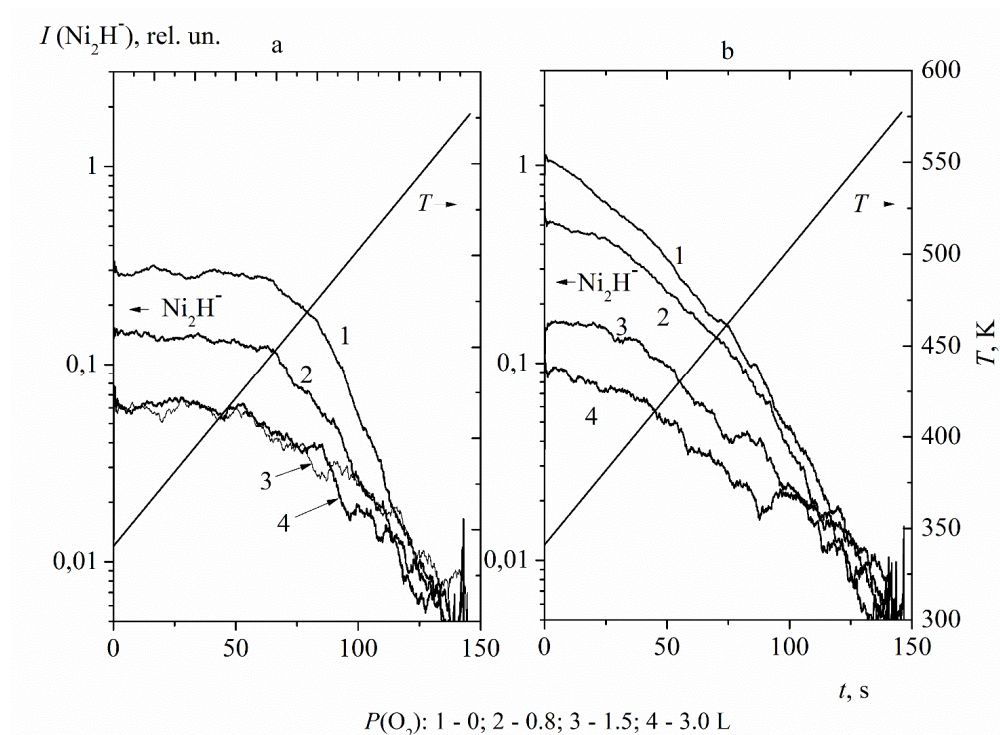

$P(O_2)$: 1 - 0; 2 - 0.8; 3 - 1.5; 4 - 3.0 L

Figure 34. Time dependence of the Ni_2H^- ions emission intensity from the $LaNi_5$ surface with a linear increase in temperature after the sample exposure in hydrogen: a residual pre-coverage; b – 60 L, for several values of exposure in oxygen (1-4)

Next, the conditions for the desorption experiment, in contrast to the above, were slightly changed. First, a hydrogen coverage was formed on a clean surface, and then the effect of oxygen was investigated. The surface of the sample was cleaned with a primary beam, after that the primary current density j=0.14 μA·cm^{-2} was set; the chamber was supplied with hydrogen (instead of oxygen, as in the first case), and a certain hydrogen pre-coverage was formed on the sample surface (the experiment was carried out for the residual hydrogen pre-coverage and for the pre-coverage corresponding to the exposure of 60 L); then hydrogen was pumped out and the chamber was supplied with oxygen (instead of hydrogen, as in the first case), which interacted with the hydrogen-precovered surface. After the specified oxygen exposure was reached, the oxygen was pumped out and the sample was heated up linearly (in time) at the rate of 1.62 K·sec^{-1}, while, just as in the first case, the emission intensity of the characteristic Ni_2H^- ion was recorded. When the experiment was over, the surface was cleaned with the primary beam to the initial state. The measurements were repeated for different exposure values in both hydrogen and oxygen. Fig. 34 presents the measured dependences for the residual surface pre-coverage with hydrogen and for the hydrogen exposure of 60 L at several values of the oxygen exposure.

The analysis shows that the conclusions drawn when considering the results of the first experiment (Fig. 33) are fully valid for the experiment, when the coverage with hydrogen-containing compounds was formed before the exposure to oxygen. This allows concluding that both in the first and second cases, an increase in temperature causes the decomposition of similar chemical compounds on the surface. Therefore, regardless of what comes first to the clean surface, hydrogen or oxygen, the chemical compounds similar in composition will be formed, as Fig. 3 shows, the compounds are, likely, hydroxides. Thus, the oxygen poisoning of the surface of the hydride-forming alloy $LaNi_5$ can occur regardless of whether the alloy surface was clean from the very beginning or was covered with a layer of hydrides.

CONCLUSION

The studies of the lanthanum-based alloys performed by the SIMS method showed that under normal conditions the surface of $LaNi_5$, $LaNi_{4.75}Al_{0.25}$ and $LaNi_{4.5}Mn_{0.5}$ samples, which are used mainly as the hydrogen storage materials, is, to a certain extent, covered with a layer of chemical compounds including oxides, hydrides, hydroxides, carbides of the alloy components. Moreover, judging by the presence of lanthanum cluster ions in the emission spectra, this coverage is not continuous, that is, the surface of the samples has some regions free of chemical compounds. The annealing and bombardment with the primary beam, although reducing the amount of these compounds, does not lead to complete cleaning of the surface.

The study of the time dependences of the emission intensity for the secondary ions characterizing the presence of hydrogen-containing compounds on the surface, measured in the process of hydrogen adsorption and then in the process of sputtering of the formed surface compounds, which was performed at different temperatures of the sample, showed the following. The processes of the alloys interaction with hydrogen under experimental conditions (at the room temperature and hydrogen pressure in the sample chamber $1\cdot10^{-6}$-$7\cdot10^{-2}$ Pa) are limited only to the near-surface region, i.e. the hydrogen, reaching the surface, interacts only with the surface and near-surface atoms of the alloy components and, in the best case, saturates only the near-surface region without diffusing in a noticeable amount into the alloy volume.

In the process of the hydrogen adsorption, the amount of the hydrogen-containing compounds, formed on the surface and in the near-surface region, monotonically decreases with the increase of temperature; the steady state coverage with the compounds is also realized faster. In the investigated temperature range, the hydrogen diffuses in noticeable quantities to the depth of ~ 10 monolayers. Thus, the processes of hydrogen interaction with the alloys in the given experimental conditions take place only on the surface and in the near-surface region. This, in turn, allows interpreting the obtained results as the initial stages of hydrogenation processes, and not taking into account the diffusion of hydrogen into the volume, as one of the channels for changing the surface composition.

The study of the initial stages of the processes of these alloys interaction with hydrogen under experimental conditions showed, that on the regions of the clean surface, hydrogen forms chemical compounds with the both main components of the alloy, nickel and lanthanum. As the hydrogen accumulates on the surface and in the near-surface region, a hydrogen-containing structure is formed, which is characterized by a certain stoichiometric ratio of components. Nickel in this structure has strong chemical bonds with two hydrogen atoms, and lanthanum with two or more hydrogen atoms. Along with such a compound, the structures with lower hydrogen content are also formed. The formed hydrogen-containing structure includes the both main components of the alloy La and Ni for all the studied samples, even only lanthanum is generally believed to be the hydride-forming element in such alloys.

The hydrogen sorption from the gas phase to the alloys surface causes a significant change in the emission properties of the alloy, in terms of secondary ion emission. The yield of the positive secondary ions increases and the yield of negative secondary ions increases especially greatly, first of all, due to the hydrogen-containing ion emissions. Such an increase is due to the processes of formation on the surface and in the near-surface area of the structures, whose sputtering by the primary beam is characterized by significantly higher coefficients of secondary ion emission as compared to the clean metal surface.

In the case of the $LaNi_{4.5}Mn_{0.5}$ alloy, the manganese, as an additional alloy component, is also a part of the forming hydrogen-containing structure and, therefore, takes a direct part in the processes of hydride formation. In the case of the $LaNi_{4.75}Al_{0.25}$ sample, unlike the manganese, the aluminum does not form direct chemical bonds in

significant quantities with hydrogen. That is, the aluminum atoms themselves in this alloy do not take participation in the processes of hydride formation, in the sense of the formation of chemical bonds. Their main role of aluminum is in the crystal lattice reconstruction.

The studies of the temperature influence on the emission intensity of hydrogen-containing secondary ions have shown that with the increase of temperature, the number of hydrogen-containing compounds on the surface and in the near-surface region decreases. Such a decrease is, primarily, related to a decrease in the sticking coefficient of the hydrogen molecules.

The SIMS studies of the chemical composition of the surface monolayers of the intermetallic alloy $LaNi_5$ in the process of interaction with oxygen showed the following. As consequence of the oxygen interaction with the alloy, a complex chemical structure including oxygen, lanthanum and nickel is formed on the surface and in the near-surface region of $LaNi_5$. Both oxygen and hydrogen in such a structure form strong chemical bonds with the both components of the alloy. This is evidenced by the presence in the mass spectra of a large set of oxygen-containing emissions of positive and negative secondary ions with lanthanum and nickel, as well as cluster oxygen-containing lanthanum-nickel secondary ions. The formed oxide compounds have a three-dimensional structure and occupy dozens of monolayers. In such a three-dimensional oxide structure, the outer monolayers are characterized by the highest ratio of the number of oxygen atoms to the number of matrix atoms. This ratio decreases in the deeper lying monolayers.

The quantitative and qualitative ratio of the elements in the resulting oxide structure mainly depends on the partial pressure of oxygen and, to a much lesser extent, on the sputtering action of the primary beam.

The observed secondary ions are not the product of the association of the surface sputtered fragments with oxygen of the gas phase at the fly-off stage, but are the products of the oxide compounds sputtering, therefore the secondary ions characterize the composition of the surface and near-surface region.

The study of the effect of oxygen on the kinetics of hydrogen-sorption processes by the hydride-forming alloy $LaNi_5$ showed the following. With a fixed number of oxygen-containing compounds on the surface, the higher is the pressure of hydrogen above the surface, the greater is the number of the formed hydrogen-containing compounds. The oxygen coating has a weak effect on the formation rate of the maximum possible (at the specific combination of the parameters) coverage with hydrogen-containing compounds. The greater is the hydrogen pressure above the surface, the higher is the rate of the compounds formation.

The study of the oxygen influence on the kinetics of desorption processes showed that for all the investigated oxygen exposures, at a small amount of hydrogen-containing compounds on the surface, a noticeable decrease in their amount begins only at the temperatures above ~ 450 K. At a relatively large amount of the hydrogen-containing compounds on the surface, the decrease starts almost immediately after the beginning of heating from 300 K. At the temperature of ~ 575 K, the emission of characteristic ions becomes negligible, so the surface becomes free of hydrogen-containing chemical compounds.

Poisoning of the surface of the hydride-forming alloy $LaNi_5$ with oxygen can occur regardless of whether the surface of the alloy was clean from the very beginning or was covered with a layer of hydrogen-containing chemical compounds.

ORCID
Viktor O. Litvinov, https://orcid.org/0000-0003-2311-2817; **Ivan I. Okseniuk**, https://orcid.org/0000-0002-8139-961X
Dmytro I. Shevchenko, https://orcid.org/0000-0002-4556-039X; **Valentyn V. Bobkov**, https://orcid.org/0000-0002-6772-624X

REFERENCES
[1]   B.P. Tarasov, M.V. Lototsky, V.A. Yartys, Russian Chem. J. **L**(6), 34-48 (206). (In Russian).
[2]   G. Sandrock, J. Alloy Compd. **293–295**, 877 (1999), https://doi.org/10.1016/S0925-8388(99)00384-9.
[3]   P. Dantzer, in: *Hydrogen in Metals. III. Properties and Applications*, (Springer-Verlag, Berlin – Heidelberg, 1997), pp. 279-340, https://doi.org/10.1007/bfb0103405
[4]   V.M. Azhazha, M.A. Tikhonovsky, A.G. Shepelev, Yu.P. Kurilo, T.A. Ponomarenko, and D.V. Vinogradov, PAST, **1**, 145-152 (2006), https://vant.kipt.kharkov.ua/ARTICLE/VANT_2006_1/article_2006_1_145.pdf (in Russian)
[5]   B.A. Kolachev, R.E. Shalin, and A.A. Ilyin, *Hydrogen storage alloys*, Reference edition (Metallurgia, Moscow, 1995). (in Russian).
[6]   B.P. Tarasov, V.V. Burnasheva, M.V. Lototsky, and V.A. Yartys, *Alternative energy and ecology*, **12**(32), 14-37 (2005), (in Russian).
[7]   M.V. Lototskyy, I. Tolj, L. Pickering, C. Sita, F. Barbir, and V. Yartys, Progress in Natural Science: Materials International, **27**(1), 3-20 (2017), https://doi.org/10.1016/j.pnsc.2017.01.008
[8]   G. Sandrock, and R.C. Bowman Jr., J. of Alloys and Compounds, **356-357**, 794-799 (2003), https://doi.org/10.1016/S0925-8388(03)00090-2
[9]   M.V. Lototskyy, V.A. Yartys, B.G. Pollet, and R.C. Bowman Jr, Int. J. of Hydrogen Energy, **39**(11), 5818-5851 (2014), https://doi.org/10.1016/j.ijhydene.2014.01.158
[10] S. Fukada, Y. Toyoshima, and M. Nishikawa, Fusion Engineering and Design, **49-50**, 805 (2000) https://doi.org/10.1016/s0920-3796(00)00192-7
[11] K.J. Maynard, N.P. Kherani, and W.T. Shmayda, Fusion Technology, **28**(3P2), 1546-1551 (1995), https://doi.org/10.13182/FST95-A30632
[12] W.T. Shmayda, N.P. Kherani, and A.G. Heics, J. Vac. Sci. Technol. A, **6**(3), 1259 (1988), https://doi.org/10.1116/1.575685
[13] G.R. Longhurst, R.A. Jalbert, and R.L. Rossmassler, Fusion Technology, **15**(2P2B), 1331-1336 (1989), https://doi.org/10.13182/fst89-a39873

[14] M.V. Lototsky , V.A. Yartys, Ye.V. Klochko, and V.N. Borisko, J. of Alloys and Compound, **404-406**, 724-727 (2005), https://doi.org/10.1016/j.jallcom.2005.02.086

[15] I.N. Sereda, E.V. Klochko, and A.F. Tseluiko, PAST, **4**, 155 (2008), https://vant.kipt.kharkov.ua/ARTICLE/VANT_2008_4/article_2008_4_155.pdf (In Russian).

[16] D.P. Broom *Hydrogen Storage Materials: The Characterisation of Their Storage Properties,* (Springer, London, 2011), https://doi.org/10.1007/978-0-85729-221-6

[17] G.D. Sandrock, and P.D. Goodell, J. Less Common Metals, **73**(1), 161-168 (1980), https://doi.org/10.1016/0022-5088(80)90355-0

[18] G.D. Sandrock, and P.D. Goodell, J. Less-Common Metals, **104**, 159-173 (1984), https://doi.org/10.1016/0022-5088(84)90452-1

[19] J.H.N. van Vucht, F.A. Kuijpers, and H.C.A.M. Bruning, Philips Research Report, **25**(2), 133-140 (1970). OSTI Identifier: 4129528.

[20] L. Schlapbach, A. Seiler, H.C. Siegmann, T.V. Waldkirch, P. Zucher, and C.R. Brundle, Int. J. of Hydrogen Energy, **4**(1), 21-28 (1979), https://doi.org/10.1016/0360-3199(79)90126-5

[21] Th. von Waldkirch, and P. Zurcher, Appl. Phys. Lett. **33**, 689-691 (1978), https://doi.org/10.1063/1.90531

[22] V.T. Cherepin, *Ion probe*, (Naukova Dumka, Kyiv, 1981). (in Russian)

[23] M. Schülke, H. Paulus, M. Lammers, G. Kiss, F. Réti, and K.H. Müller, Annal Bioanal. Chem. **390**(6), 1495-1505 (2008), https://dx.doi.org/10.1007/s00216-007-1797-7

[24] G. Kiss, H. Paulus, O. Krafcsik, F. Réti, K.-H. Müller, and J. Giber, Fresenius J Anal Chem, **365**, 203–207 (1999). https://doi.org/10.1007/s002160051473

[25] M.H. Mintz, I. Jacob, and D. Shaltiel, Topics in Applied Physics, **67**, 285-317 (2002), https://doi.org/10.1007/3-540-54668-5_14

[26] В.Т. Черепин, М.А. Васильев *Методы и приборы для анализа поверхности материалов: Справочник*, (Киев: Наукова думка), (1982). (In Russian).

[27] I.A. McHugh, in: *Secondary Ion Mass Spectrometry*, (Mir, Moscow, 1979), pp. 276-342. (In Russian).

[28] V.I. Veksler, *Secondary ion emission of metals*, (Nauka, Moscow, 1978). (In Russian).

[29] Ya.M. Fogel', International Journal of Mass Spectrometry and Ion Physics, **9**(2), 109-125 (1972), https://doi.org/10.1016/0020-7381(72)80037-8

[30] V.A. Litvinov, V.T. Koppe, and V.V. Bobkov, Bulletin of the Russian Academy of Sciences: Physics, **76**(5), 553–557 (2012), https://doi.org/10.3103/S1062873812050152

[31] P. Dantzer, Materials Science and Engineering, **A329–331**, 313–320 (2002), https://doi.org/10.1016/S0921-5093(01)01590-8

[32] E.E. Shpilrain, S.P. Malyshenko, and G.G. Kuleshov, *Introduction to hydrogen power engineering*, (Energoatomizdat, Moscow, 1984). (In Russian).

[33] S. Luo, J.D. Clewley, T.B. Flanagan, R.C. Bowman Jr., and L.A. Wade, J. Alloys Comp. **267**(1-2), 171-181 (1998), https://doi.org/10.1016/S0925-8388(97)00536-7

[34] H. Züchner, R. Dobrileit, and T. Rauf, Fresenius J Anal Chem. **341**, 219-232 (1991), https://doi.org/10.1007/BF00321552

[35] H. Züchner, P. Kock, T. Bruning, and T. Rauf, J. Less Common Metals, **172-174**(Part A), 95-106 (1991), https://doi.org/10.1016/0022-5088(91)90437-9

[36] H. Zuchner, J. Kintrup, R. Dobrileit, and I. Untiedt, J. Alloys Comp, **293-295**, 202-212 (1999), https://doi.org/10.1016/S0925-8388(99)00420-X

[37] D. Lebiedz, H. Zuchner, and O.A Gutfleisch, J. Alloys Comp, **356-357**, 679-682 (2003), https://doi.org/10.1016/S0925-8388(03)00288-3

[38] R. Dobrileit, and H. Zuchner, Z. Naturforsch, **50**(6), 533 (1995), https://doi.org/10.1515/zna-1995-0604

[39] V.A. Litvinov, I.I. Okseniuk, D.I. Shevchenko, and V.V. Bobkov, J. Surf. Invest. X-ray, Synchrotron and Neutron Techniques, **12**(3), 576-583 (2018), https://doi.org/10.1134/S1027451018030321

[40] V.A. Litvinov, I.I. Okseniuk, D.I. Shevchenko, and V.V. Bobkov, (Interaction of ions with a surface VIP-2017, Moscow), **2**, 52-55 (2017), (In Russian), http://plasma.mephi.ru/ru/uploads/files/conferences/ISI_2017/ISI_2017_Tom_2.pdf

[41] V.A. Litvinov, I.I. Okseniuk, D.I. Shevchenko, and V.V. Bobkov, Ukr. J. Phys, **62**(10), 845-857 (2017), https://doi.org/10.15407/ujpe62.10.0845

[42] V.A. Litvinov, A.G. Koval, and B.M. Fizgeer, Izvestiia AN SSSR: Ser. Phys. **55**(12), 2423-2426 (1991). (In Russian).

[43] B.A. Kolachev, A.A. Ilyin, V.A. Lavrenko, and V. Levinsky, *Hydride Systems: A Handbook*. (Metallurgiia, Moscow, (1992).

[44] A.N. Perevezentsev, B.M. Andreev, V.K. Kapyshev, L.A. Rivkis, M.P. Malek, V.M. Bystritsky, and V.A. Stolupin, Physics of elementary particles and the atomic nucleus, **19**(6), 1386-1439 (1988). (In Russian).

[45] T. Takeshita, S.K. Malik, and W.E. Wallace, J. of Solid-State Chemistry, **23**(3-4), 271-274 (1978), https://doi.org/10.1016/0022-4596(78)90074-9

[46] M.H. Mendelsohn, D.M. Gruen, and A.E. Dwight, J. Less Common Metals, **63**(2), 193-207 (1979), https://doi.org/10.1016/0022-5088(79)90243-1

[47] L.G. Shcherbakova, Yu.M. Solonin, and Ye.N. Severyanina, Carbon Nanomaterials in Clean Energy Hydrogen Systems, **645**, 644-652 (2008), https://doi.org/10.1007/978-1-4020-8898-8_80

[48] H. Diaz, A. Percheron-Guégan, J.C. Achard, C. Chatillon, and J.C. Mathieu, Int. J. of Hydrogen Energy, **4**(5), 445-454 (1979), https://doi.org/10.1016/0360-3199(79)90104-6

[49] P.D. Goodell, J. Less Common Metals, **89**(1), 45-54 (1983). https://doi.org/10.1016/0022-5088(83)90247-3

[50] K. Suzuki, K. Ishikawa, and K. Aoki, Material Transactions JIM, **41**(5), 581-584 (2000), https://doi.org/10.2320/matertrans1989.41.581

[51] J.I. Han, and J.Y. Lee, J. of the Less Common Metals, **152**(2), 329-338 (1989), https://doi.org/10.1016/0022-5088(89)90100-8

[52] P. Dantzer, J. of the Less Common Metals, **131**, 349-363 (1987), https://doi.org/10.1016/0022-5088(87)90534-0

[53] R.C. Bowman, D.M. Gruen, and M.H. Mendelsohn, Solid State Communications, **32**(7), 501-506 (1979), https://doi.org/10.1016/0038-1098(79)90362-4

[54] R.C Bowman Jr., B.D Craft, A. Attalla, M.H. Mendelsohn, and D.M. Gruen, J. of the Less Common Metals, **73**(2), 227-232 (1980), https://doi.org/10.1016/0022-5088(80)90307-0

[55] C.E. Lundin, F.E. Lynch, and C.B. Magee, J. of the Less Common Metals, **56**(1), 19-37 (1977), https://doi.org/10.1016/0022-5088(77)90215-6

[56] W.E. Wallace, E.B. Boltich, J. of Solid State Chemistry, **33**(3), 435-437 (1980), https://doi.org/10.1016/0022-4596(80)90168-1

[57] C. Lartigue, A. Percheron-Guegan, J.C. Achard, J. of the Less Common Metals, **75**, 23-29 (1980), https://doi.org/10.1016/0022-5088(80)90365-3

[58] L. Schlapbach, A. Seiler, F. Stucki, and H.C Siegmann, J. Less Common Metals, **73**, 145-160 (1980), https://doi.org/10.1016/0022-5088(80)90354-9

[59] A.A. Radzig, and B.M. Smirnov, *Handbook of atomic and molecular physics*, (Atomizdat, Moscow, 1980). (In Russian).

[60] V.A. Litvinov, I.I. Okseniuk, D.I. Shevchenko, and V.V. Bobkov, *Ion-Surface Interactions ISI – 2019*, (Moscow, 2019), **2**, pp. 71-74.

[61] V.A. Litvinov, I.I. Okseniuk, D.I. Shevchenko, and V.V. Bobkov, Journal of Surface Investigation: X-ray, Synchrotron and Neutron Techniques, **14**(6), 1358–1365. (2020), https://doi.org/10.1134/S102745102006035X

[62] P. Selvam, B. Viswanathan, C.S. Swamy, and V. Srinivasan, J. Less Common Metals, **163**, 89-108 (1990), https://doi.org/10.1016/0022-5088(90)90088-2

[63] P.D. Goodell, J. Less Common Metals, **89**(1), 45-54 (1983), https://doi.org/10.1016/0022-5088(83)90247-3

[64] H.C. Siegmann, L. Schlapbach, and C.R. Brundle, Phys. Rev. Let. **40**(14), 972-975 (1978), https://doi.org/10.1103/PhysRevLett.40.972

[65] F. Stucki, and L. Schlapbach, J. Less Common Metals, **74**(1), 143-151 (1980), https://doi.org/10.1016/0022-5088(80)90084-3

[66] L. Schlapbach, F. Stucki, A. Seiler, and H.C. Siegmann, Surf. Sci., **106**(1-3**)**, 157-159 (1981), https://doi.org/10.1016/0039-6028(81)90194-1

[67] L. Schlapbach, Solid State Communications, **38**(2), 117-123 (1981), https://doi.org/10.1016/0038-1098(81)90802-4

[68] W.E. Wallace, R.F. Karlicek, and H. Imamura, J. Phys. Chem. **83**(13), 1708-1712 (1979), https://doi.org/10.1021/j100476a006

[69] J.H. Weaver, A. Franciosi, W.E. Wallace, and H.K. Smith, J. App. Phys. **51**, 5847-5851 (1980), https://doi.org/10.1063/1.327544

[70] J.H. Weaver, A. Franciosi, D.J. Peterman, T. Takeshita, and K.A. Gschneidner Jr., J. Less Common Metals, **86**, 195-202 (1982), https://doi.org/10.1016/0022-5088(82)90205-3

[71] P. Selvam, B. Viswanathan, and V. Srinivasan, Jnt. J. Hydrogen Energy, **14**(9), 687-689 (1989), https://doi.org/10.1016/0360-3199(89)90048-7

[72] P. Selvam, B. Viswanathan, C.S. Swamy, and V. Srinivasan, Int. J. Hydrogen Energy, **16**(1), 23-33 (1991), https://doi.org/10.1016/0360-3199(91)90057-P

[73] R. Berish, editor, *Sputtering of solids by ion bombardment. Issue 1, Physical spraying of single-element solids*, (Mir, Moscow, 1984). (In Russian).

[74] S.P. Holland, B.J. Garrison, and N. Winograd, Phys. Rev. Letters, **44**, 756-759 (1980), https://doi.org/10.1103/PhysRevLett.44.756

[75] P. Joyes, J. Physique, **44**, 221-227 (1983), https://doi.org/10.1051/jphys:01983004402022100

[76] N. Winograd, B. J. Garrison, T. Fleisch, W. N. Delgass, D. E. Jr. Harrison, J. Vac. Sci. Technol., **16**, 629-634 (1979), https://doi.org/10.1116/1.570017

[77] B.J. Garrison, N. Winograd, D.E. Jr. Harrison, J. Chem. Phys., **69**, 1440-1444 (1978), https://doi.org/10.1063/1.436767.

[78] V.A Litvinov, I.I. Okseniuk, D.I. Shevchenko, and V.V. Bobkov, East European Journal of Physics, **3**, 30-36 (2021), https://doi.org/10.26565/2312-4334-2021-3-04

РОЛЬ ПОВЕРХНІ У ПРОЦЕСАХ ГІДРИДОУТВОРЕННЯ
Віктор О. Літвінов, Іван І. Оксенюк, Дмитро І. Шевченко, Валентин В. Бобков
Харківський національний університет ім. В.Н. Каразина
61022, Україна, м. Харків, пл. Свободи, 4

Методом вторинної іонної мас-спектрометрії (ВІМС) проведене дослідження змін хімічного складу поверхневих моношарів інтерметалевих сплавів на основі лантану у процесі взаємодії з воднем і киснем. У якості первинних іонів використовувалися іони Ar^+ з енергією 10-18 кеВ. Дослідження початкових стадій процесів взаємодії цих сплавів з воднем в умовах експерименту показало, що на ділянках чистої поверхні водень утворює хімічні сполуки з обома основними компонентами сплаву нікелем і лантаном. У міру накопичення водню на поверхні і в приповерхневій області утворюється водневмісна структура, що характеризується певним стехіометричним співвідношенням компонентів. Нікель у такій структурі має міцні хімічні зв'язки з двома атомами водню, а лантан з двома або більше атомами водню. Поряд із такою сполукою утворюються також структури з меншим вмістом водню. Водневмісна структура, що формується включає обидва основні компоненти сплаву і La і Ni для всіх досліджених зразків, хоча прийнято вважати, що гідридоутворюючим елементом у таких сплавах є лантан. Проведені ВІМС дослідження хімічного складу поверхневих моношарів інтерметалевого сплаву $LaNi_5$ у процесі взаємодії з киснем показали наступне. В результаті взаємодії кисню з об'єктом, що досліджується, на поверхні і у приповерхневій області $LaNi_5$ утворюється комплексна хімічна структура, що включає кисень, лантан і нікель. Кисень у такій структурі як і водень утворює міцні хімічні зв'язки з обома компонентами сплаву. Про це свідчить наявність у мас-спектрах великого набору кисневмісних емісій позитивних, і негативних вторинних іонів з лантаном, з нікелем, а також кластерних кисневмісних лантан-нікелевих вторинних іонів. Оксидні сполуки, що утворюються, мають об'ємну структуру і займають десятки моношарів. Отруєння поверхні гідридоутворюючого сплаву $LaNi_5$ киснем може відбуватися незалежно від того чи була поверхня сплаву від самого початку чистої, або була покрита шаром водневмісних хімічних сполук.
Ключові слова: *ВІМС; поверхня; інтерметалеві сплави на основі лантану; водень; гідриди; кисень; оксиди*

ANISOTROPIC COSMOLOGICAL MODEL IN $f(R,T)$ THEORY OF GRAVITY WITH A QUADRATIC FUNCTION OF $T^{\dagger}$

Chandra Rekha Mahanta[a,#], Shayanika Deka[a,‡], Kankana Pathak[a,*]

aDepartment of Mathematics, Gauhati University, Guwahati-781014, India
#E-mail: crmahanta@gauhati.ac.in, ‡E-mail: shayanikadeka.sd75@gmail.com
*Corresponding Author e-mail: kankanapathak@gauhati.ac.in

In this paper, we study spatially homogeneous and anisotropic Bianchi type-I space-time filled with perfect fluid within the framework of $f(R,T)$ theory of gravity for the functional form $f(R,T) = R + 2f(T)$ with $f(T) = \alpha T + \beta T^2$, where α and β are constants. Exact solutions of the gravitational field equations are obtained by assuming the average scale factor to obey a hybrid expansion law and some cosmological parameters of the model are derived. Two special cases, leading to the power-law expansion and the exponential expansion are also considered. We investigate the physical and geometrical properties of the models by studying the evolution graphs of some relevant cosmological parameters such as the Hubble parameter (H), the deceleration parameter (q) etc.

Keywords: *Bianchi type-I universe; f(R, T) theory of gravity; Hubble parameter; Cosmological constant; Deceleration parameter*
PACS: 04.50.kd, 98.80.-k, 04.20.jb

1. INTRODUCTION

More than two decades have passed since the first observational results from Supernovae Type Ia [1–3] with strong support from a number of astrophysical and cosmological observations such as Cosmic Microwave Background (CMB), Wilkinson Microwave Anisotropy Probe (WMAP), Large Scale Structure (LSS), Baryon Acoustic Oscillation (BAO), Galaxy redshift surveys [4–10] etc. that the universe at present is in a state of accelerated expansion. It is accepted as true that there was also a cosmic acceleration, which occurred at the very early epoch of the universe. The early time cosmic acceleration, called inflation, although there is no known direct detection for this, has theoretical explanations, but the root cause of the late time cosmic acceleration having direct detection is yet to be ascertained. Since matter contributes with force and positive pressure that decelerates the rate of cosmic expansion, therefore, as a resolution to this bizarre issue a substantial amount of energy component apart from the baryonic matter is hypothesized to be present in the universe to speed up the cosmic expansion. It is possible only when an unusual component with large negative pressure, dubbed dark energy, covering nearly 68.3% of the total energy content of the universe is present to counteract the gravitational pressure of the baryonic matter. Within the framework of General Relativity, the most efficient candidate for dark energy is the cosmological constant Λ as it works well with the observational data. But due to its problematic nature with the fine-tuning and the cosmic coincidence problems, various other dark energy models such as quintessence, k-essence, tachyon, phantom, Holographic dark energy, Chaplygin gas models etc. have been proposed in the literature.

The problem of late time cosmic acceleration has also been approached with some alternative theories of gravity, popularly known as modified theories of gravity, which are developed by modifying the geometric part of the Einstein-Hilbert action. Among the various modified theories of gravity, the simplest and the most studied one is the $f(R)$ theory of gravity, the action of which is constructed from the standard Einstein-Hilbert action simply by taking an arbitrary function $f(R)$ in place of R, where R is the Ricci scalar curvature. The other most interesting and viable alternative to General Relativity is the $f(R,T)$ theory of gravity proposed by Harko *et al.* [11] in which the gravitational Lagrangian in Einstein-Hilbert action is given by an arbitrary function $f(R,T)$ of the Ricci scalar R and the trace T of the stress-energy tensor T_{ij}. In their work, they have obtained the gravitational field equations in the $f(R,T)$ gravity in the metric formalism and presented the field equations for the three explicit forms of the functional $f(R,T)$: (i) $f(R,T) = R + 2f(T)$, (ii) $f(R,T) = f_1(R) + f_2(T)$, (iii) $f(R,T) = f_1(R) + f_2(R)f_3(T)$.

Harko *et al.* also derived the equations of motion of test particles together with the Newtonian limits in $f(R,T)$ gravity models. Further, they have investigated the constraints on the magnitude of the extra-acceleration on the precession of the perihelion of the planet Mercury. Houndjo [12] discussed transaction of matter dominated phase to an accelerated expansion phase by developing the cosmological reconstruction of $f(R,T)$ theory of gravity. Since then, many researchers have studied cosmological dynamics in $f(R,T)$ theory of gravity as it takes care of the early time inflation as well as the late time cosmic acceleration. A number of authors have also investigated Bianchi cosmological models in $f(R,T)$ theory of gravity in different contexts as Wilkinson Microwave Anisotropy Probe (WMAP) and some other experimental tests support the existence of an anisotropic phase in the early era which might have been wiped out in the course of cosmic evolution resulting in the present isotropic phase. Adhav [13] investigated LRS

Bianchi Type I cosmological model with perfect fluid, Reddy *et al.* [14] explored Bianchi Type III and Kaluza-Klein cosmological model, Chandel and Ram [15] generated a new class of solutions of field equations from a set of known solutions for a Bianchi Type III cosmological model with perfect fluid, Chaubey and Shukla [16] studied a new class of Bianchi Type III, V, VI$_0$ models in presence of perfect fluid, Sahoo and Mishra [17] investigated Kaluza-Klein dark energy model in the presence of wet dark fluid, Ladke *et al.* [18] constructed higher dimensional Bianchi Type-I cosmological model, Sahoo *et al.* [19] investigated an axially symmetric space-time in presence of perfect fluid source, Agrawal and Pawar [20] investigated plane symmetric cosmological model in the presence of quark and strange quark matter, Bhoyar [21] talked about non-static plane symmetric cosmological model with magnetized anisotropic dark energy, Yadav *et al.* [22] searched the existence of bulk viscous Bianchi-I embedded cosmological model by taking into account the simplest coupling between matter and geometry, Yadav *et al.* [23] investigated a bulk viscous universe and estimated the numerical values of some cosmological parameters with observational Hubble data and SN Ia data. Singh and Beesham [24] explored a plane symmetric Bianchi Type I model by considering a specific Hubble parameter which yields a constant deceleration parameter, Chaubey *et al.* [25] considered general class of anisotropic Bianchi cosmological models in $f(R, T)$ gravity with dark energy in viscous cosmology, Bhattacharjee *et al.* [26] presented modelling of inflationary scenarios, Tiwari *et al.* [27] studied Bianchi type I cosmological model for a specific choice of the function of the trace of the energy momentum tensor. Modifications and generalisations of $f(R, T)$ theory of gravity are also considered in the literature. Singh and Bishi [28] studied Bianchi Type III cosmological model in the presence of cosmological constant Λ. Moraes *et al.* [29] investigated static wormholes in modified $f(R, T)$ gravity. Moraes and Sahoo [31] have proposed a new hybrid shape function for wormhole. Azmat *et al.* [31] studied viscous anisotropic fluid and constructed corresponding dynamical equations and modified field equations in $f(R, T)$ theory of gravity. Tretyakov [32] discussed the possibility of a further generalization of $f(R, T)$ gravity by incorporating higher derivative terms in the action and demonstrated that inflationary scenarios appear quite naturally in the theory. Recently, several authors have studied various other cosmological scenarios in the framework of $f(R, T)$ theory of gravity [33–39].

Motivated by the above-mentioned works, we focus our present work in studying spatially homogeneous and anisotropic Bianchi type-I universe with perfect fluid source in $f(R, T)$ theory of gravity for the functional form $f(R, T) = R + 2(\alpha T + \beta T^2)$, where α and β are constants. The field equations are solved by assuming the average scale factor in the form of hybrid expansion law. We organize the paper as follows: in section 2, we give a brief review of the $f(R, T)$ theory of gravity. In section 3, we derive the gravitational field equations for the Bianchi type-I metric. Exact solutions of the field equations are obtained in section 4. In section 5, some physical and kinematical properties of the model are discussed by graphically representing the evolution of graphs of some parameters of cosmological importance. Two particular scenarios are also examined when the expansion of the universe is governed by power-law expansion and exponential expansion only. We summarize the main results with some concluding remarks in section 6.

2. BRIEF REVIEW OF $f(R, T)$ GRAVITY

In $f(R, T)$ gravity proposed by Harko *et al.* (2011), the action is taken as

$$S = \frac{1}{16\pi} \int f(R, T) \sqrt{-g} d^4 x + \int L_m \sqrt{-g} d^4 x, \tag{1}$$

where $f(R, T)$ is an arbitrary function of the Ricci Scalar R and of the trace T of the stress-energy tensor of matter T_{ij} defined by

$$T_{ij} = \frac{-2}{\sqrt{-g}} \frac{\delta(\sqrt{-g} L_m)}{\delta g^{ij}}. \tag{2}$$

Here, L_m is the matter Lagrangian that generates a specific set of field equations for each choice of L_m.
By assuming the Lagrangian of matter to depend only on the metric tensor components g_{ij} and not on its derivatives, the stress-energy tensor can be obtained as

$$T_{ij} = g_{ij} L_m - 2 \frac{\partial L_m}{\partial g^{ij}}. \tag{3}$$

By varying the action (1) with respect to the metric tensor components g^{ij}, the field equations of $f(R, T)$ theory of gravity in the metric formalism are obtained as

$$f_R(R, T) R_{ij} - \frac{1}{2} f(R, T) g_{ij} + \left(g_{ij} \Box - \nabla_i \nabla_j \right) f_R(R, T) = 8\pi T_{ij} - f_T(R, T) T_{ij} - f_T(R, T) \Theta_{ij}, \tag{4}$$

where, $f_R(R, T)$ and $f_T(R, T)$ are the partial derivatives of $f(R, T)$ with respect to R and T respectively, ∇_i is the covariant derivative, $\Box = \nabla_k \nabla^k$ is the D'Alembert operator and

$$\Theta_{ij} = -2T_{ij} + g_{ij} L_m - 2g^{lk} \frac{\partial^2 L_m}{\partial g^{ij} \partial g^{lk}}. \tag{5}$$

The stress-energy tensor of matter T_{ij} is assumed to take the perfect fluid form so that

$$T_{ij} = (\rho + p) u_i u_j - p g_{ij}. \tag{6}$$

where ρ and p are respectively the density and pressure of the perfect fluid.
For the choice $L_m = -p$, we thus have

$$\Theta_{ij} = -2T_{ij} - pg_{ij}. \tag{7}$$

For the functional form

$$f(R,T) = R + 2f(T). \tag{8}$$

where $f(T)$ is an arbitrary function of T, the gravitational field equations of $f(R,T)$ gravity are obtained from Eq. (4), as

$$R_{ij} - \frac{1}{2}Rg_{ij} = 8\pi T_{ij} - 2f'(T)T_{ij} - 2f'(T)\Theta_{ij} + f(T)g_{ij}, \tag{9}$$

where $f'(T) = \frac{d}{dT}(f(T))$. In view of eq (6), the field equations (9) become

$$R_{ij} - \frac{1}{2}Rg_{ij} = 8\pi T_{ij} + 2f'(T)T_{ij} + [2pf'(T) + f(T)]g_{ij}. \tag{10}$$

For the choice

$$f(T) = \alpha T + \beta T^2, \tag{11}$$

where α and β are constants, the eq.(10), in presence of a time varying cosmological constant Λ, reduces to

$$R_{ij} - \frac{1}{2}Rg_{ij} + \Lambda g_{ij} = [8\pi + 2\alpha + 4\beta T]T_{ij} + [2p\alpha + 4p\beta T + \alpha T + \beta T^2]g_{ij}. \tag{12}$$

3.   THE METRIC AND FIELD EQUATIONS

The spatially homogeneous and anisotropic Bianchi type-I metric is given by

$$ds^2 = dt^2 - A^2 dx^2 - B^2 dy^2 - C^2 dz^2, \tag{13}$$

where the directional scale factors A, B and C are functions of the cosmic time t alone. In comoving coordinates, the field equations (12) take the form

$$\frac{\dot{A}}{A}\frac{\dot{B}}{B} + \frac{\dot{B}}{B}\frac{\dot{C}}{C} + \frac{\dot{C}}{C}\frac{\dot{A}}{A} = (8\pi + 3\alpha)\rho + 5\beta\rho^2 - 3\beta p^2 - 14\beta p\rho - \alpha p - \Lambda, \tag{14}$$

$$\frac{\ddot{B}}{B} + \frac{\ddot{C}}{C} + \frac{\dot{B}}{B}\frac{\dot{C}}{C} = -(8\pi + 3\alpha)p + 9\beta p^2 - 6\beta p\rho + \alpha\rho + \beta\rho^2 - \Lambda, \tag{15}$$

$$\frac{\ddot{A}}{A} + \frac{\ddot{B}}{B} + \frac{\dot{A}}{A}\frac{\dot{B}}{B} = -(8\pi + 3\alpha)p + 9\beta p^2 - 6\beta p\rho + \alpha\rho + \beta\rho^2 - \Lambda, \tag{16}$$

$$\frac{\ddot{A}}{A} + \frac{\ddot{C}}{C} + \frac{\dot{A}}{A}\frac{\dot{C}}{C} = -(8\pi + 3\alpha)p + 9\beta p^2 - 6\beta p\rho + \alpha\rho + \beta\rho^2 - \Lambda, \tag{17}$$

where an overhead dot denotes differentiation with respect to t.

4.   COSMOLOGICAL SOLUTION OF THE FIELD EQUATIONS

Here, we have four field equations with six unknowns A, B, C, ρ, p and Λ. So, in order to obtain a complete solution, we have to consider two extra conditions.

Therefore, we consider the equation of state for perfect fluid as

$$p = \omega\rho, \tag{18}$$

where ω is a constant.
And, the average scale factor a defined by

$$a = (ABC)^{\frac{1}{3}}. \tag{19}$$

to obey the hybrid expansion law proposed by Akarsu *et al.* [40];

$$a = a_0 \left(\frac{t}{t_0}\right)^\gamma e^{\xi\left(\frac{t}{t_0} - 1\right)}, \tag{20}$$

where γ and ξ are non-negative constants and a_0 represents the present value of the scale factor and t_0 represents the present age of the universe.
From equations (15)-(17), we then obtain

$$A = a_0 l_1 \left(\frac{t}{t_0}\right)^\gamma e^{\xi\left(\frac{t}{t_0} - 1\right)} \exp\left[m_1 \int \left\{a_0 \left(\frac{t}{t_0}\right)^\gamma e^{\xi\left(\frac{t}{t_0} - 1\right)}\right\}^{-3} dt\right], \tag{21}$$

$$B = a_0 l_2 \left(\frac{t}{t_0}\right)^\gamma e^{\xi\left(\frac{t}{t_0} - 1\right)} \exp\left[m_2 \int \left\{a_0 \left(\frac{t}{t_0}\right)^\gamma e^{\xi\left(\frac{t}{t_0} - 1\right)}\right\}^{-3} dt\right], \tag{22}$$

$$C = a_0 l_3 \left(\frac{t}{t_0}\right)^\gamma e^{\xi\left(\frac{t}{t_0} - 1\right)} \exp\left[m_3 \int \left\{a_0 \left(\frac{t}{t_0}\right)^\gamma e^{\xi\left(\frac{t}{t_0} - 1\right)}\right\}^{-3} dt\right]. \tag{23}$$

where l_1, l_2, l_3 and m_1, m_2, m_3 are constants of integration satisfying the relations $l_1 l_2 l_3 = 1$ and $m_1 + m_2 + m_3 = 0$.

5. PHYSICAL AND GEOMETRICAL PROPERTIES OF THE MODEL

For our model, some important cosmological parameters are:
The spatial volume

$$V = ABC = a_0{}^3 \left(\frac{t}{t_0}\right)^{3\gamma} e^{3\xi\left(\frac{t}{t_0} - 1\right)}. \tag{24}$$

The mean Hubble parameter is

$$H = \frac{\dot{a}}{a} = \frac{1}{3}\left(\frac{\dot{A}}{A} + \frac{\dot{B}}{B} + \frac{\dot{C}}{C}\right) = \frac{\xi}{t_0} + \frac{\gamma}{t}. \tag{25}$$

The deceleration parameter

$$q = -\frac{a\ddot{a}}{\dot{a}^2} = \frac{\gamma t_0{}^2}{(\xi t + \gamma t_0)^2} - 1. \tag{26}$$

The expansion scalar

$$\theta = 3H = \left(\frac{\dot{A}}{A} + \frac{\dot{B}}{B} + \frac{\dot{C}}{C}\right) = 3\left(\frac{\xi}{t_0} + \frac{\gamma}{t}\right). \tag{27}$$

The shear scalar

$$\sigma^2 = \frac{1}{2}\left(\sum_{i=1}^{3} H_i{}^2 - 3H^2\right) = \frac{m_2{}^2 + m_3{}^2 + m_2 m_3}{a_0{}^6 \left(\frac{t}{t_0}\right)^{6\gamma} e^{6\xi\left(\frac{t}{t_0} - 1\right)}}. \tag{28}$$

The anisotropy parameter

$$A_m = \frac{1}{3}\sum_{i=1}^{3}\left(\frac{H_i - H}{H}\right)^2 = \frac{2(m_2{}^2 + m_3{}^2 + m_2 m_3)}{9 a_0{}^6 \left(\frac{\xi}{t_0} + \frac{\gamma}{t}\right)^2 \left(\frac{t}{t_0}\right)^{6\gamma} e^{6\xi\left(\frac{t}{t_0} - 1\right)}}. \tag{29}$$

where $H_1 = \frac{\dot{A}}{A}, H_2 = \frac{\dot{B}}{B}, H_3 = \frac{\dot{C}}{C}$ are the directional Hubble parameters.
The energy density (ρ), the pressure (p) and the cosmological constant (Λ) are obtained as

$$\rho = \frac{4\pi + \alpha}{4\beta(3\omega - 1)} - \frac{\sqrt{(\omega + 1)\left\{(4\pi + \alpha)^2(\omega + 1)a_0{}^6\left(\frac{t}{t_0}\right)^{6\gamma} e^{6\xi\left(\frac{t}{t_0} - 1\right)} + 8\beta(3\omega - 1)\left(m_2{}^2 + m_3{}^2 + m_2 m_3 - \gamma a_0{}^6 t_0{}^{(-2)}\left(\frac{t}{t_0}\right)^{6\gamma - 2} e^{6\xi\left(\frac{t}{t_0} - 1\right)}\right)\right\}}}{4\beta(\omega + 1)(3\omega - 1)a_0{}^3\left(\frac{t}{t_0}\right)^{3\gamma} e^{3\xi\left(\frac{t}{t_0} - 1\right)}}, \tag{30}$$

$$p = \frac{\omega(4\pi + \alpha)}{4\beta(3\omega - 1)} - \frac{\omega\sqrt{(\omega + 1)\left\{(4\pi + \alpha)^2(\omega + 1)a_0{}^6\left(\frac{t}{t_0}\right)^{6\gamma} e^{6\xi\left(\frac{t}{t_0} - 1\right)} + 8\beta(3\omega - 1)\left(m_2{}^2 + m_3{}^2 + m_2 m_3 - \gamma a_0{}^6 t_0{}^{(-2)}\left(\frac{t}{t_0}\right)^{6\gamma - 2} e^{6\xi\left(\frac{t}{t_0} - 1\right)}\right)\right\}}}{4\beta(\omega + 1)(3\omega - 1)a_0{}^3\left(\frac{t}{t_0}\right)^{3\gamma} e^{3\xi\left(\frac{t}{t_0} - 1\right)}}, \tag{31}$$

$$\Lambda = -\frac{(m_2{}^2 + m_3{}^2 + m_2 m_3)(\omega + 5)}{2(\omega + 1)a_0{}^6\left(\frac{t}{t_0}\right)^{6\gamma} e^{6\xi\left(\frac{t}{t_0} - 1\right)}} + \frac{\gamma\{\omega + 5 - 6\gamma(\omega + 1)\}}{2(\omega + 1)t^2} - \frac{3\xi^2}{t_0{}^2} - \frac{6\gamma\xi}{t t_0} - \frac{(4\pi + \alpha)\{(\omega + 5)(4\pi + \alpha) - 2(8\pi + 3\alpha - \alpha\omega)\}}{8\beta(3\omega - 1)} +$$

$$9\left(\frac{\xi}{t_0} + \frac{\gamma}{t}\right)^2 \frac{(m_2{}^2 + m_3{}^2 + m_2 m_3)}{a_0{}^6\left(\frac{t}{t_0}\right)^{6\gamma} e^{6\xi\left(\frac{t}{t_0} - 1\right)}} + \left\{\frac{\pi}{2\beta(3\omega - 1)} +\right.$$

$$\left.\frac{\alpha}{8\beta(\omega + 1)}\right\}\frac{\sqrt{(\omega + 1)\left\{(4\pi + \alpha)^2(\omega + 1)a_0{}^6\left(\frac{t}{t_0}\right)^{6\gamma} e^{6\xi\left(\frac{t}{t_0} - 1\right)} + 8\beta(3\omega - 1)\left(m_2{}^2 + m_3{}^2 + m_2 m_3 - \gamma a_0{}^6 t_0{}^{(-2)}\left(\frac{t}{t_0}\right)^{6\gamma - 2} e^{6\xi\left(\frac{t}{t_0} - 1\right)}\right)\right\}}}{a_0{}^3\left(\frac{t}{t_0}\right)^{3\gamma} e^{3\xi\left(\frac{t}{t_0} - 1\right)}}. \tag{32}$$
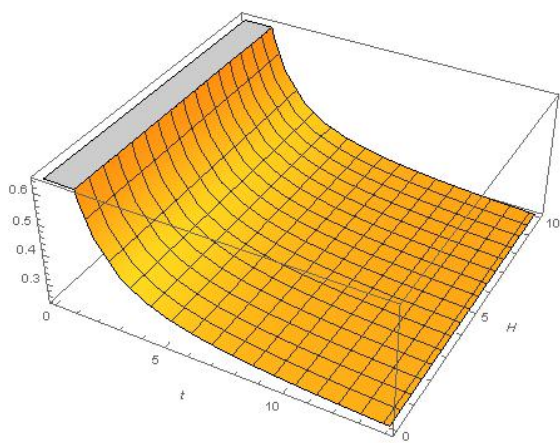
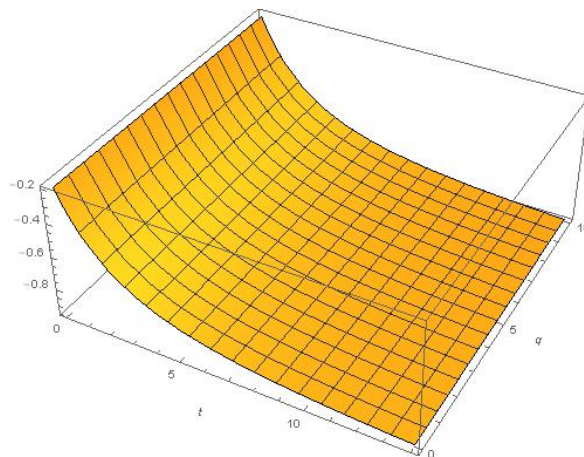**Figure 1.** Variation of the Hubble parameter H v/s cosmic time t

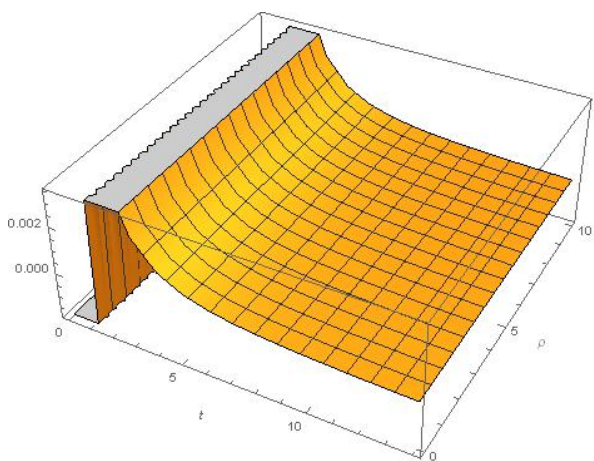**Figure 2.** Variation of the deceleration parameter q v/s cosmic time t

Figure 3. Variation of the energy density ρ v/s cosmic time t
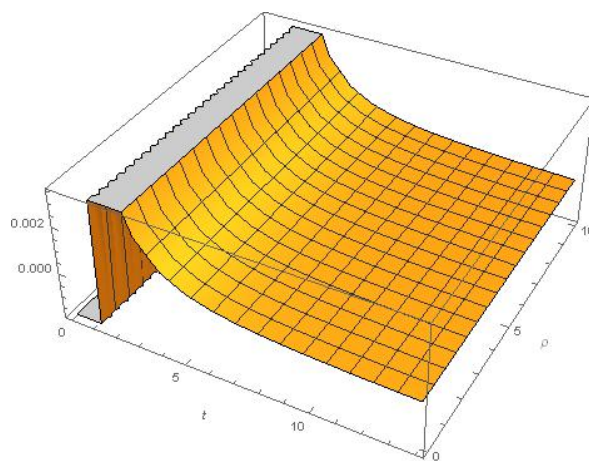

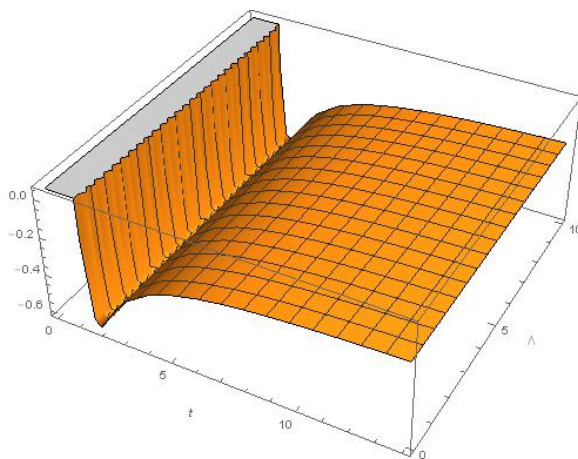**Figure 4.** Variation of the pressure p v/s cosmic time t

Figure 5. Variation of the cosmological constant Λ v/s cosmic time t

To explore the physical and geometrical properties of the model from the evolution graphs of the cosmological parameters, we take $\gamma = 0.6$, $\xi = 0.2$, $a_0 = 1$, $t_0 = 1$, $m_1 = 0.7$, $m_2 = 0.3$, $m_3 = -1$, $\alpha = 0.1$, $\beta = 0.1$, $\omega = 1$. From the graphs, we observe that the Hubble parameter (H) and the deceleration parameter (q) are decreasing functions of cosmic time. The energy density (ρ) and pressure (p) are also decreasing function of cosmic time. Figure 5, shows that the cosmological constant (Λ) decreases rapidly at initial stage and tend to zero in the course of evolution. The hybrid expansion law (20) is a combination of the power law expansion and the exponential expansion. It yields the power law expansion for $\xi = 0$ and the exponential expansion for $\gamma = 0$.

Case (i): When $\xi = 0$, equation (20) reduces to

$$a = a_0 \left(\frac{t}{t_0}\right)^\gamma,$$

which is the power-law of expansion.
Then, equations (21)-(23) yield

$$A = a_0 l_1 \left(\frac{t}{t_0}\right)^\gamma \exp\left[m_1 a_0^{-3} t_0^{3\gamma} \frac{t^{1-3\gamma}}{1-3\gamma}\right], \tag{33}$$

$$B = a_0 l_2 \left(\frac{t}{t_0}\right)^\gamma \exp\left[m_2 a_0^{-3} t_0^{3\gamma} \frac{t^{1-3\gamma}}{1-3\gamma}\right], \tag{34}$$

$$C = a_0 l_3 \left(\frac{t}{t_0}\right)^\gamma \exp\left[m_3 a_0^{-3} t_0^{3\gamma} \frac{t^{1-3\gamma}}{1-3\gamma}\right] \tag{35}$$

Thus, when the expansion of the universe is governed by a power law expansion, then

$$V = a_0^3 \left(\frac{t}{t_0}\right)^{3\gamma}, \tag{36}$$

$$H = \frac{\gamma}{t}, \tag{37}$$

$$q = \frac{1}{\gamma} - 1, \tag{38}$$

$$\theta = \frac{3\gamma}{t}, \tag{39}$$

$$\sigma^2 = \frac{m_2^2 + m_3^2 + m_2 m_3}{a_0^6 \left(\frac{t}{t_0}\right)^{6\gamma}}, \tag{40}$$

$$A_m = \frac{2(m_2^2 + m_3^2 + m_2 m_3)}{9 a_0^6 \left(\frac{\gamma}{t}\right)^2 \left(\frac{t}{t_0}\right)^{6\gamma}}, \tag{41}$$

$$\rho = \frac{4\pi + \alpha}{4\beta(3\omega - 1)} - \frac{\sqrt{(\omega+1)\left\{(4\pi+\alpha)^2(\omega+1)a_0^6\left(\frac{t}{t_0}\right)^{6\gamma} + 8\beta(3\omega-1)\left(m_2^2 + m_3^2 + m_2 m_3 - \gamma a_0^6 t_0^{(-2)}\left(\frac{t}{t_0}\right)^{6\gamma-2}\right)\right\}}}{4\beta(\omega+1)(3\omega-1)a_0^3\left(\frac{t}{t_0}\right)^{3\gamma}}, \tag{42}$$

$$p = \frac{\omega(4\pi+\alpha)}{4\beta(3\omega-1)} - \frac{\omega\sqrt{(\omega+1)\left\{(4\pi+\alpha)^2(\omega+1)a_0^6\left(\frac{t}{t_0}\right)^{6\gamma} + 8\beta(3\omega-1)\left(m_2^2 + m_3^2 + m_2 m_3 - \gamma a_0^6 t_0^{(-2)}\left(\frac{t}{t_0}\right)^{6\gamma-2}\right)\right\}}}{4\beta(\omega+1)(3\omega-1)a_0^3\left(\frac{t}{t_0}\right)^{3\gamma}}, \tag{43}$$

$$\Lambda = -\frac{(m_2^2 + m_3^2 + m_2 m_3)(\omega+5)}{2(\omega+1)a_0^6\left(\frac{t}{t_0}\right)^{6\gamma}} + \frac{\gamma\{\omega+5-6\gamma(\omega+1)\}}{2(\omega+1)t^2} - \frac{(4\pi+\alpha)\{(\omega+5)(4\pi+\alpha)-2(8\pi+3\alpha-\alpha\omega)\}}{8\beta(3\omega-1)} + 9\left(\frac{\gamma}{t}\right)^2 \frac{(m_2^2 + m_3^2 + m_2 m_3)}{a_0^6\left(\frac{t}{t_0}\right)^{6\gamma}} +$$

$$\left\{\frac{\pi}{2\beta(3\omega-1)} + \frac{\alpha}{8\beta(\omega+1)}\right\} \frac{\sqrt{(\omega+1)\left\{(4\pi+\alpha)^2(\omega+1)a_0^6\left(\frac{t}{t_0}\right)^{6\gamma} + 8\beta(3\omega-1)\left(m_2^2 + m_3^2 + m_2 m_3 - \gamma a_0^6 t_0^{(-2)}\left(\frac{t}{t_0}\right)^{6\gamma-2}\right)\right\}}}{a_0^3\left(\frac{t}{t_0}\right)^{3\gamma}}. \tag{44}$$

From the Figures 6, 7, 8 and 9, we see that the Hubble parameter (H), energy density (ρ), pressure (p) are decreasing functions of cosmic time and the cosmological constant (Λ) decreases initially to negative value and then increases tending to zero as time evolves. The deceleration parameter (q) may be positive, negative or zero depending on the values of γ. For $\gamma > 1$, the expansion of the universe corresponding to the constructed model accelerates. For $\gamma < 1$, the expansion decelerates and for $\gamma = 1$, the universe undergoes uniform expansion.

Case (ii): When $\gamma = 0$, equation (21) reduces to

$$a = a_0 e^{\xi\left(\frac{t}{t_0} - 1\right)},$$

which is the exponential law of expansion.

Then, equations (21)-(23) yield

$$A = a_0 l_1 e^{\xi\left(\frac{t}{t_0} - 1\right)} \exp\left[\frac{-m_1 t_0}{3\xi a_0{}^3} e^{-3\xi\left(\frac{t}{t_0} - 1\right)}\right], \tag{45}$$

$$B = a_0 l_2 e^{\xi\left(\frac{t}{t_0} - 1\right)} \exp\left[\frac{-m_2 t_0}{3\xi a_0{}^3} e^{-3\xi\left(\frac{t}{t_0} - 1\right)}\right], \tag{46}$$

$$C = a_0 l_3 e^{\xi\left(\frac{t}{t_0} - 1\right)} \exp\left[\frac{-m_3 t_0}{3\xi a_0{}^3} e^{-3\xi\left(\frac{t}{t_0} - 1\right)}\right]. \tag{47}$$
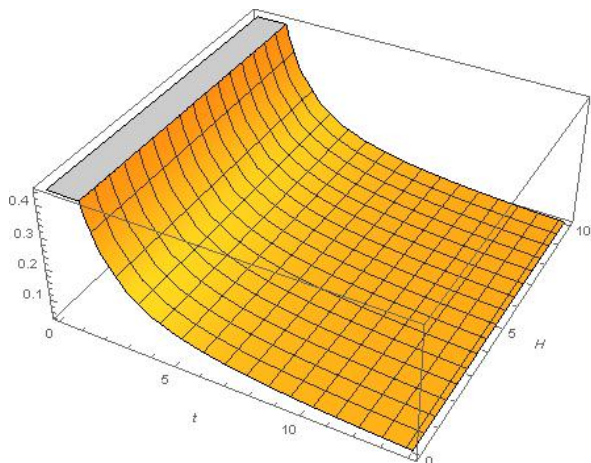

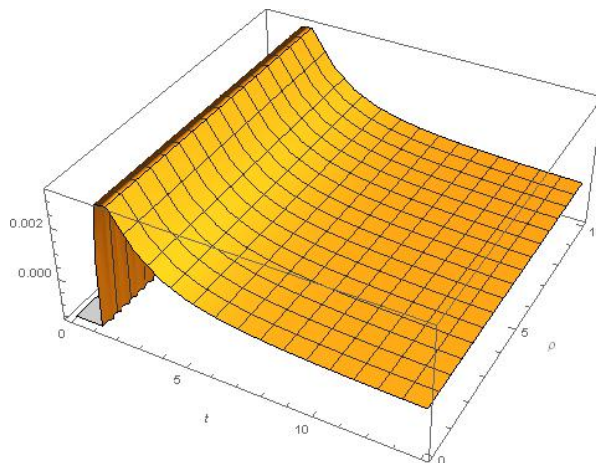**Figure 6.** Variation of the Hubble parameter H v/s cosmic time t

Figure 7. Variation of the energy density ρ v/s cosmic time t
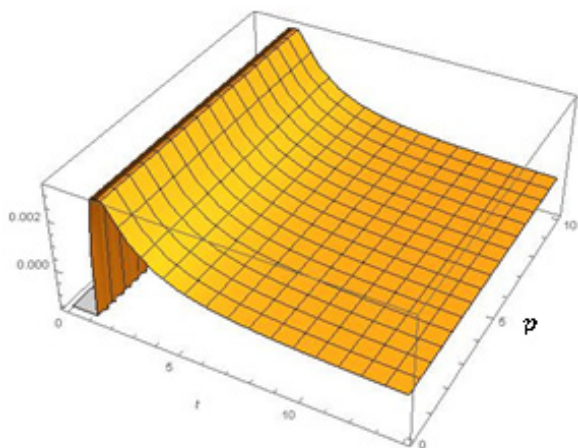

Figure 8. Variation of the pressure p v/s cosmic time t
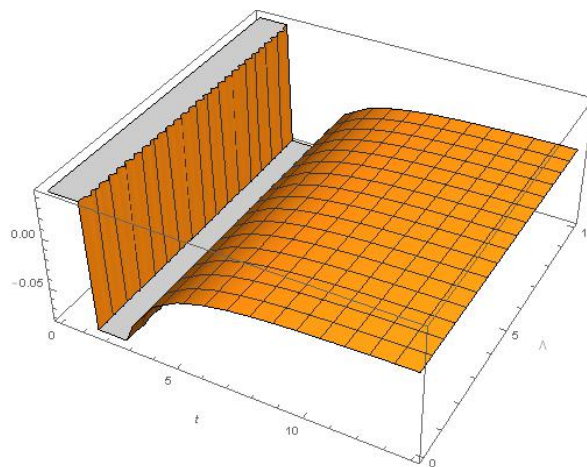

Figure 9. Variation of the cosmological constant Λ v/s cosmic time t

When the expansion of the universe is governed by the exponential law of expansion, then

$$V = a_0{}^3 e^{3\xi\left(\frac{t}{t_0} - 1\right)}, \tag{48}$$

$$H = \frac{\xi}{t_0}, \tag{49}$$

$$q = -1, \tag{50}$$

$$\theta = 3\frac{\xi}{t_0}, \tag{51}$$

$$\sigma^2 = \frac{m_2{}^2 + m_3{}^2 + m_2 m_3}{a_0{}^6 e^{6\xi\left(\frac{t}{t_0} - 1\right)}}, \tag{52}$$

$$A_m = \frac{2(m_2{}^2 + m_3{}^2 + m_2 m_3)}{9a_0{}^6 \left(\frac{\xi}{t_0}\right)^2 e^{6\xi\left(\frac{t}{t_0} - 1\right)}}, \tag{53}$$

$$\rho = \frac{4\pi + \alpha}{4\beta(3\omega - 1)} - \frac{\sqrt{(\omega+1)\left\{(4\pi+\alpha)^2(\omega+1)a_0{}^6 e^{6\xi\left(\frac{t}{t_0}-1\right)} + 8\beta(3\omega-1)(m_2{}^2+m_3{}^2+m_2m_3)\right\}}}{4\beta(\omega+1)(3\omega-1)a_0{}^3 e^{3\xi\left(\frac{t}{t_0}-1\right)}}, \tag{54}$$

$$p = \frac{\omega(4\pi+\alpha)}{4\beta(3\omega-1)} - \frac{\omega\sqrt{(\omega+1)\left\{(4\pi+\alpha)^2(\omega+1)a_0{}^6 e^{6\xi\left(\frac{t}{t_0}-1\right)} + 8\beta(3\omega-1)(m_2{}^2+m_3{}^2+m_2m_3)\right\}}}{4\beta(\omega+1)(3\omega-1)a_0{}^3 e^{3\xi\left(\frac{t}{t_0}-1\right)}}, \tag{55}$$

$$\Lambda = -\frac{(m_2{}^2+m_3{}^2+m_2m_3)(\omega+5)}{2(\omega+1)a_0{}^6 e^{6\xi\left(\frac{t}{t_0}-1\right)}} - \frac{3\xi^2}{t_0{}^2} - \frac{(4\pi+\alpha)\{(\omega+5)(4\pi+\alpha) - 2(8\pi+3\alpha-\alpha\omega)\}}{8\beta(3\omega-1)} + 9\left(\frac{\xi}{t_0}\right)^2 \frac{(m_2{}^2+m_3{}^2+m_2m_3)}{a_0{}^6 e^{6\xi\left(\frac{t}{t_0}-1\right)}} + \left\{\frac{\pi}{2\beta(3\omega-1)} + \right.$$
$$\left. \frac{\alpha}{8\beta(\omega+1)}\right\} \frac{\sqrt{(\omega+1)\left\{(4\pi+\alpha)^2(\omega+1)a_0{}^6 e^{6\xi\left(\frac{t}{t_0}-1\right)} + 8\beta(3\omega-1)(m_2{}^2+m_3{}^2+m_2m_3)\right\}}}{a_0{}^3 e^{3\xi\left(\frac{t}{t_0}-1\right)}}. \tag{56}$$
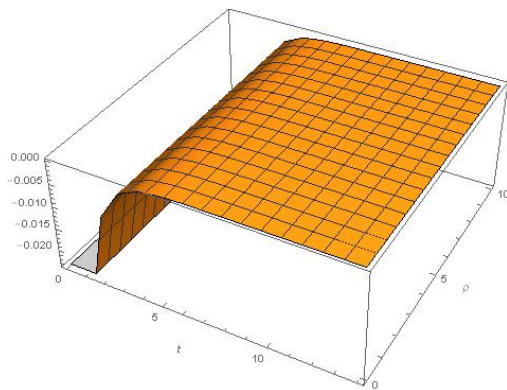

Figure 10. Variation of the energy density ρ v/s cosmic time t
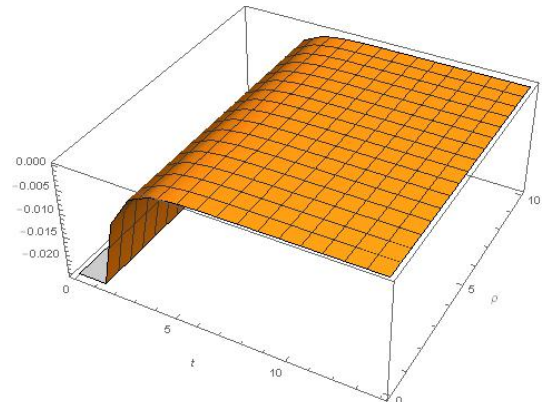

Figure 11. Variation of the pressure p v/s cosmic time t
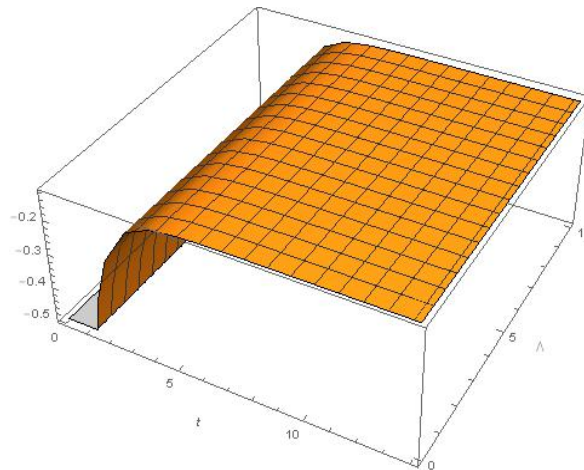

Figure 12. Variation of the cosmological constant Λ v/s cosmic time t

From the graphs, we observe that the energy density, pressure and cosmological constant initially assume negative values and then tend to zero in the course of time.

6. CONCLUDING REMARKS

In this paper, we study Bianchi type-I cosmological model within the framework of $f(R,T)$ theory of gravity considering the functional $f(R,T) = R + 2(\alpha T + \beta T^2)$, where α and β are constants. We consider the expansion of the universe to follow a hybrid expansion law and obtain exact solution of the field equations. Two particular cases are also considered when the expansion of the universe is governed by a power law and an exponential law only. We investigate the physical and kinematical properties of various cosmological parameters in all these three cases and find that

• Both the hybrid expansion law and power law of expansion induce an initial singular model of the universe as the metric coefficients A, B and C vanish at the initial moment. In case of exponential expansion law, the metric coefficients A, B and C become constants at $t = 0$.

• For hybrid law and power law of expansion, the physical parameters H, θ, σ^2, A_m assume very high value at the initial epoch and tend to zero for large t. Also, the volume of the universe is zero at the beginning and increases exponentially with time t. Hence, the universe starts with the Big Bang singularity at $t = 0$ and then expand throughout the evolution. In case of exponential law, the physical parameters H, θ become constants. Volume is initially very low and increases exponentially in the course of time while the other parameters show similar behavior as hybrid law and power law of expansion.

• In hybrid expansion law, the deceleration parameter (q) approaches -1 for large cosmic time. In case of power law of expansion, it may be positive, negative or zero showing thereby that the universe may undergo accelerating expansion, decelerating expansion or uniform expansion. The expression for the deceleration parameter q, in the case of exponential law of expansion, shows that the expansion of the universe is decelerating throughout the evolution without depending on γ.

• For hybrid law and power law of expansion, the energy density and pressure increase rapidly at the beginning but it decreases in the course of evolution and tend to 0 at late time. But in case of exponential expansion law, the energy density and pressure are negative and increase exponentially throughout the evolution of the universe and tend to 0 as time $t \to \infty$.

• The cosmological constant (Λ) decreases initially and then increases and tends to 0 at late times for hybrid law as well as power-law of expansion. In the case of exponential law, cosmological constant is negative and increases in the course of time tending to zero at late times.

ORCID

◉**Chandra Rekha Mahanta,** https://orcid.org/0000-0002-8019-8824; ◉**Shayanika Deka,** https://orcid.org/0009-0007-0771-9535
◉**Kankana Pathak,** https://orcid.org/0009-0004-0353-809X

REFERENCES

[1] A.G. Riess, A.V. Filippenko, P. Challis, A. Clocchiatti, A. Diercks, P.M. Garnavich, R.L. Gilliland, *et al.*, "Observational evidence from supernovae for an accelerating universe and a cosmological constant," Astron. J. **116**, 1009-1038 (1998). https://doi.org/10.1086/300499

[2] S. Perlmutter, G. Aldering, M.D. Valle, S. Deustua, R.S. Ellis, S. Fabbro, A. Fruchter, *et al.*, "Discovery of a supernova explosion at half the age of the Universe," Nature, **391**, 51-54 (1998). https://doi.org/10.1038/34124

[3] S. Perlmutter, G. Aldering, G. Goldhaber, R.A. Knop, P. Nugent, P.G. Castro, S. Deustua, *et al.*, "Measurements of Σ and Λ from 42 High-Redshift Supernovae," Astrophys. J, **517**, 565-589 (1999). https://doi.org/10.1086/307221

[4] C.L. Bennett, M. Halpern, G. Hinshaw, N. Jarosik, A. Kogut, M. Limon, S.S. Meyer, *et al.*, "First-Year Wilkinson Microwave Anisotropy Probe (WMAP) Observations: Preliminary Maps and Basic Results," Astrophys. J. Suppl. Ser. **148**, 1-27 (2003). https://doi.org/10.1086/377253

[5] D.N. Spergel, L. Verde, H.V. Peiris, E. Komatsu, M.R. Nolta, C.L. Bennett, M. Halpern, et al., "First-Year Wilkinson Microwave Anisotropy Probe (WMAP) Observations: Determination of Cosmological Parameters," Astrophys. J. Suppl. Ser. **148**, 175-194 (2003). https://doi.org/10.1086/377226

[6] D.N. Spergel, R. Bean, O. Doré, M.R. Nolta, C.L. Bennett, J. Dunkley, G. Hinshaw, et al., "Three-Year Wilkinson Microwave Anisotropy Probe (WMAP) Observations: Implications for Cosmology," Astrophys. J. Suppl. Ser. **170**, 377-408 (2007). https://doi.org/10.1086/513700

[7] M. Tegmark, D.J. Eisenstein, M.A. Strauss, D.H. Weinberg, M.R. Blanton, J.A. Frieman, M. Fukugita, *et al.*, "Cosmological constraints from the SDSS luminous red galaxies," Phys. Rev. D, **74**, 123507 (2006). https://doi.org/10.1103/PhysRevD.74.123507

[8] D.J. Eisenstein, I. Zehavi, D.W. Hogg, R. Scoccimarro, M.R. Blanton, R.C. Nichol, R. Scranton, *et al.*, "Detection of the baryon acoustic peak in the large-scale correlation function of SDSS luminous red galaxies," Astrophys. J. **633**, 560 (2005). https://doi.org/10.1086/466512

[9] G. Hinshaw, D. Larson, E. Komatsu, D.N. Spergel, C.L. Bennett, J. Dunkley, M.R. Nolta, et al., "Nine-year Wilkinson microwave anisotropy probe (WMAP) observations: cosmological parameter results," Astrophys. J. Suppl. Ser. **208**, 19 (2013). https://doi.org/10.1088/0067-0049/208/2/19

[10] E. Komatsu, K.M. Smith, J. Dunkley, C.L. Bennett, B. Gold, G. Hinshaw, N. Jarosik, et al., "Seven-year Wilkinson microwave anisotropy probe (WMAP) observations," Astrophys J. Suppl. Ser. **192**, 18 (2011). https://doi.org/10.1088/0067-0049/192/2/18

[11] T. Harko, F. Lobo, S. Nojiri, and S.D. Odintsov, " $f(R,T)$ gravity," Phys. Rev. D, **84**, 024020 (2011). https://doi.org/10.1103/PhysRevD.84.024020

[12] M.J.S. Houndjo, "Reconstruction of $f(R,T)$ gravity describing matter dominated and accelerated phases," Int. J. Mod. Phys. D, **21**, 1250003-1250016 (2012). https://doi.org/10.1142/S0218271812500034

[13] K.S. Adhav, "LRS Bianchi Type I Cosmological Model in $f(R,T)$ theory of gravity," Astrophys Space Sci. **339**, 365-369 (2012). https://doi.org/10.1007/s10509-011-0963-8

[14] D.R.K. Reddy, et al., "Bianchi type-III dark energy model in $f(R,T)$ gravity," Int. J. Theor. Phys. **52**, 239-245 (2013). https://doi.org/10.1007/s10773-012-1325-1

[15] S. Chandel, and S. Ram, "Anisotropic Bianchi type III perfect fluid cosmological models in $f(R,T)$ theory of gravity," Indian J. Phys. **87**, 1283-1287 (2013). https://doi.org/10.1007/s12648-013-0362-9

[16] R. Chaubey, and A.K. Shukla, "A new class of Bianchi cosmological model in $f(R,T)$ gravity," Astrophys. Space Sci., **343**, 415-422 (2013). https://doi.org/10.1007/s10509-012-1204-5

[17] P.K. Sahoo, and B. Mishra, "Kaluza-Klein dark energy model in the form of wet dark fluid in $f(R,T)$ gravity," Can. J. Phys. **92**, 1062 (2014). https://doi.org/10.1139/cjp-2014-0235

[18] L.S. Ladke, and R.A. Hiwarkar, and V.K. Jaiswal, "Cosmological Model with Decaying Λ in $f(R,T)$ Theory of Gravity," Int. J. Sci. & Res. **4**, 2245-2249 (2015). https://www.ijsr.net/archive/v4i12/NOV152533.pdf

[19] P.K. Sahoo, B. Mishra, and G.C. Reddy, "Axially symmetric cosmological model in $f(R,T)$ gravity," Eur. Phys. J. Plus, **129**, 49 (2014). https://doi.org/10.1140/epjp/i2014-14049-7

[20] P.K. Agrawal, and D.D. Pawar, "Plane symmetric cosmological model with quark and strange quark matter in $f(R,T)$ theory of gravity," J. Astrophys. Astr. **38**, 2 (2017). https://doi.org/10.1007/s12036-016-9420-y

[21] S. Bhoyar, V. Chirde, and S. Shekh, "Non-static plane symmetric cosmological model with magnetized anisotropic dark energy by hybrid expansion law in $f(R,T)$ gravity," Int. J. of Adv. Research, **3**, 492-500 (2015). https://www.journalijar.com/uploads/478_IJAR-7015.pdf

[22] A.K. Yadav, P.K. Srivastava, and L. Yadav, "Hybrid Expansion Law for Dark Energy Dominated Universe in $f(R,T)$ Gravity," Int. J. Theor. Phys. **54**, 1671-1679 (2015). https://doi.org/10.1007/s10773-014-2368-2

[23] A.K. Yadav, A.T. Ali, "Invariant Bianchi type I models in $f(R,T)$ gravity," Int. J. Geom. Methods in Mod. Phys. **15**, 1850026 (2018). https://doi.org/10.1142/S0219887818500263

[24] V. Singh, and A. Beesham, "Plane Symmetric Model in $f(R,T)$ gravity," Gen Rel Quantum cosmology, **135**, 319-329 (2020). https://doi.org/10.1140/epjp/s13360-020-00314-x

[25] R. Chaubey, A.K. Shukla, and T. Singh, "The general class of Bianchi cosmological models in $f(R,T)$ gravity with dark energy in viscous cosmology," Ind. J. Phys. **90**, 233-242 (2016). https://doi.org/10.1007/s12648-015-0749-x

[26] S. Bhattacharjee, P.K. Sahoo, and S. Arora, "Late-time viscous cosmology in $f(R,T)$ gravity," New Astronomy, **82**, 101452 (2021). https://doi.org/10.1016/j.newast.2020.101452

[27] R.K. Tiwari, A. Beesham, and B.K. Shukla, "Time varying deceleration parameter in $f(R,T)$ gravity: a general case," Afrika Matematika, **32**, 983-994 (2021). https://doi.org/10.1007/s13370-021-00874-w

[28] G.P. Singh, and B.K. Bishi, "Bianchi Type I Universe with Cosmological Constant and Quadratic Equation of State in $f(R,T)$ Modified Gravity," Adv. High Energy Phys. **2015**, 816826 (2015). https://doi.org/10.1155/2015/816826

[29] P.H.R.S. Moraes, R.A.C. Correa, and R.V. Lobato, "Analytical general solutions for static wormholes in $f(R,T)$ gravity," J. Cosmol. Astropart. Phys. **07**, 029 (2017). https://doi.org/10.1088/1475-7516/2017/07/029

[30] P.H.R.S. Moraes, and P.K. Sahoo, "Modelling Wormholes in $f(R,T)$ gravity," Phys. Rev. D. **96**, 044038-044045 (2017). https://doi.org/10.1103/PhysRevD.96.044038

[31] H. Azmat, M. Zubair, I. Noureen, "Dynamics of shearing viscous fluids in $f(R,T)$ gravity," Int. J. Mod. Phys. D, **27**, 1750181 (2018). https://doi.org/10.1142/S0218271817501814

[32] P.V. Tretyakov, "Cosmology in modified $f(R,T)$ gravity," Eur. Phys. J. C, **78**, 896 (2018). https://doi.org/10.1140/epjc/s10052-018-6367-y

[33] P.K. Sahoo, S. Mandal, and S. Arora, "Energy conditions in non-minimally coupled $f(R,T)$ gravity," Astronomische Nachrichten, **342**, 89-95 (2021). https://doi.org/10.1002/asna.202113886

[34] P.K. Sahoo, P. Bhar, and P. Rej, "Phantom energy supported wormhole model in $f(R,T)$ gravity assuming conformal motion," Int. J. Mod. Phys. D, **31**, 2250016 (2022). https://doi.org/10.1142/S021827182250016X

[35] P.K. Sahoo, and S. Bhattacharjee, "Gravitational Baryogenesis in non-minimal coupled $f(R,T)$ gravity," Int. J. Theor. Phys. **59**, 1451-1459 (2020). https://doi.org/10.1007/s10773-020-04414-3

[36] S. Bhattacharjee, P.K. Sahoo, J.R.L. Santos, and P.H.R.S., Moraes, "Inflation in $f(R,T)$ gravity," Eur. Phys. J. Plus, **135**, 576 (2020). https://doi.org/10.1140/epjp/s13360-020-00583-6

[37] P. Sahoo, S. Bhattacharjee, S.K. Tripathy, and P.K. Sahoo, "Bouncing scenario in $f(R,T)$ gravity," Mod. Phys. Lett. A, **35**, 2050095 (2020). https://doi.org/10.1142/S0217732320500959

[38] S. Jokweni, V. Singh, and A. Beesham, "LRS Bianchi I Model with Bulk Viscosity in $f(R,T)$ gravity," Grav. Cosmo. **27**, 169-177 (2021). https://doi.org/10.1134/S0202289321020079

[39] V. Singh, and A. Beesham, "Plane symmetric model in $f(R,T)$ gravity," Eur. Phys. J. Plus, **135**, 1-15 (2020). https://doi.org/10.1140/epjp/s13360-020-00314-x

[40] Ö. Akarsu, S. Kumar, R. Myrzakulov, M. Sami, and Xu. Lixin, "Cosmology with hybrid expansion law: Scalar field reconstruction of cosmic history and observational constraints," Journal of Cosmology and Astroparticle Physics, **01**, 022 (2014). https://doi.org/10.1088/1475-7516/2014/01/022

АНІЗОТРОПНА КОСМОЛОГІЧНА МОДЕЛЬ У $f(R,T)$ ТЕОРІЇ ГРАВІТАЦІЇ
З КВАДРАТИЧНОЮ ФУНКЦІЄЮ ВІД Т
Чандра Рекха Маханта, Шаяніка Дека, Канкана Патхак
Факультет математики, Університет Гаухаті, Гувахаті-781014, Індія

У цій статті ми досліджуємо просторово-однорідний та анізотропний простір-час Біанкі типу I, заповнений ідеальною рідиною, у рамках *f(R,T)* теорії гравітації для функціональної форми *f(R,T)=R+2f(T)* з *f(T)=αT+βT²*, де α і β константи. Точні розв'язки рівнянь гравітаційного поля отримані шляхом припущення, що середній масштабний коефіцієнт підкоряється гібридному закону розширення, і виведено деякі космологічні параметри моделі. Також розглядаються два особливих випадки, що призводять до степеневого розкладу та експоненціального розкладу. Ми досліджуємо фізичні та геометричні властивості моделей, вивчаючи графіки еволюції деяких відповідних космологічних параметрів, таких як параметр Хаббла (*H*), параметр уповільнення (*q*) тощо.
Ключові слова: *Всесвіт Біанкі типу I; f(R,T) теорія гравітації; параметр Хаббла; космологічна стала; параметр уповільнення*

ENERGY CONDITIONS AND STATEFINDER DIAGNOSTIC OF COSMOLOGICAL MODEL WITH SPECIAL LAW OF HUBBLE PARAMETER IN f(R,T) GRAVITY[†]

V.R. Patil[a], P.A. Bolke[b]*, S.K. Waghmare[c], J.L. Pawde[d]

[a]*Department of Mathematics, Arts, Science and Commerce College, Chikhaldara, Dist. Amravati-444807, India*
[b]*Department of Mathematics, Prof. Ram Meghe College of Engineering and Management,*
New Express Highway Bandera, Dist. Amravati-444701, India
[c]*Department of Mathematics, TGPCET Nagpur-441108, India*
[d]*Dadasaheb Gawai Vidyalaya, Malhara, Achalpur, Dist. Amravati-444806, India*
*Corresponding Author: mrpravin.bolke@gmail.com

In this article, we examine the LRS Bianchi type-I cosmological model in the framework of $f(R, T)$ gravity, where R is the Ricci scalar and T is the stress energy momentum tensor in the presence of Domain wall. we used the special law of variation of Hubble's parameter proposed by Berman (1983) to obtained the exact solution of field equation, corresponds to the model of the universe. The Energy conditions and physical behaviour of the universe has been obtained and their evolution has been discussed using some physical parameter and by means of their graphs. Also, we can use the Statefinder parameter for testing the validity of the model.
Keywords: *f(R, T) gravity; Statefinder parameters; LRS Bianchi type -I cosmological model; deceleration parameter*
PACS: 04.20.−q; 04.20.Jb; 04.50.Kd

INTRODUCTION

There are three solutions to the equation of expanding universes, each predicting a different ultimate fate for the entire universe. The ultimate fate of the universe can be determined by measuring the rate at which it is expanding relative to the amount of matter it contains. Open, flat, and closed universes are the three forms of expanding universes that are theoretically possible. The universe would always grow if it were open. If the universe were flat, it would also continue to expand indefinitely, but the rate of growth would eventually reduce to zero. The universe would eventually stop growing and collapse in on itself if it were closed, possibly resulting in another big bang. in all three scenarios gravity is the reason for the slowed expansion.

The universe in which we exist must have gone through a phase of exponential accelerating expansion called inflation. Inflation not only explains the physics of the early universe, but also some conceptual problems in the big bang cosmology such as flatness problems, the horizon problem, etc. Guth [1,2] presented the revolutionized cosmic ideas on this expansion and the beginning of this universe as a result of the big bang. observational data from the Plank collaboration [3], Baryon Oscillation Spectroscopic Survey (BOSS) [4], and Atacama Cosmology Telescope Polarimeter (ACTPol) collaboration [5] provides relevant experimental evidence about the acceleration of our universe. Modern cosmology developed a fresh perspective in the previous century that allowed for significant improvements in the understanding of the universe's current, accelerating expansion. Observations from Supernovae cosmology project [6,7] high red-shift supernova [8], cosmic microwave background (CMB) fluctuations [9,10], large-scale structure (LSS) [11,12], cosmic microwave radiation (CMBR) [13] suggests that present universe is undergoing an accelerated expansion. To explain this acceleration Einstein introduced the simple proposition for Dark energy (DE) known as the cosmological constant to the gravitational field equation. However, this cosmological constant faces some theoretical difficulties such as fine-tuning problems, coincidence, etc. To avoid those cosmological difficulties researchers, approach two different ways to explain the cosmic acceleration. The first approach is to start working on quintessence [14, 15], phantom [16], k-essence [17], tachyons [18], holographic dark energy [19], Chaplygin gas [20], etc.

The second approach is to introduce modified gravity as an alternative to GR and it can describe the late time cosmology as well. In recent years, several theories of modified gravity have been developed corresponding to the modification in Einstein–Hilbert action by a polynomial function of R ($f(R)$ gravity) [21-23], a function of Ricci scalar, and a trace of energy-momentum tensor $f(R,T)$ gravity [24], a function of torsion scalar $f(\tau)$ gravity [25], Gauss-Bonnet scalar $f(G)$ gravity. Among the modified theories of gravitation, $f(R,T)$ gravity become most popular these days to the theoretical cosmologists and astrophysicts as it can explain many cosmological and astrophysical problems.

$f(R,T)$ gravity was proposed by Harko et al. [24] which is the extension of $f(R,T)$ gravity with trace energy momentum tensor T with the modification in Hilbert action principle. This of gravity takes into account the effects of minimal coupling between matter and geometry in the action of gravity. This idea gained popularity when it was first proposed, and researcher used it to explain a variety of other cosmological circumstances scenarios, including thermodynamics [26-28], gravitational waves [29-31], redshift drift [32], big bang nucleosynthesis and entropy evolution

---

[33]. Nisha Godani [34] investigated FRW cosmology in f (R, T) gravity to study the age of universe, apparent magnitude and age of universe. Tiwari et al. [35] studied the quadratically varying parameter in $f(R,T)$ gravity. An anisotropic Tilted Marder's Cosmological Model is investigated by Pawar and Shahare [36] in the framework of $f(R,T)$ gravity and discussed the energy conditions of the model with the help of some physical parameters. Mishra et al [37] analysed cosmological models with an anisotropic variable parameter in $f(R,T)$ gravity. Sahoo et al. [38] discussed the energy conditions in non-minimally coupled in $f(R,T)$ gravity. late-time acceleration for the bulk-viscous fluid in $f(R,T)$ gravity is studied by Arora et al. [39].

The experimental and observations data of microwave background radiation suggest that our present universe is largely homogeneous and isotropic represented by FRW model. Bianchi space-time plays a significant role in modern cosmology to discuss and understand the early phases of the evolution of the universe due to spatial homogeneous and anisotropic behaviour as such cosmological models plays a significant role in describing the large structure and behaviour of the universe. Yadav et al. [40] investigated the existence of bulk viscous universe in $f(R,T)$ gravity. Patil et al. [41] discussed the Bianchi type IX cosmological model in Creation field. Koussour & Bennai [42] discussed Bianchi type I space-time with bulk viscosity in $f(R,T)$ gravity. Recently [43-46] investigated Bianchi type space-time in $f(R,T)$ gravity.

With this motivation, in this paper, we have emphasized to investigate the exact solution of LRS Bianchi type- I model in the framework of modified $f(R,T)$ theory of gravity with domain wall using special law of variation of Hubble's parameter. Also, we discuss energy conditions of the model. The article is organized as follows: In section **2** we briefly review $f(R,T)$ theories, and we present the field equation of gravity. Section **3** is used to find exact solution of LRS Bianchi type- I model, the energy conditions of the model are presented in section **4,** the Statefinder diagnostic are analysed in section **5.** Finally, the results are summarized and concluded in section **6.**

Gravitational field equations of *f (R,T)* gravity

The gravitational field equations of models in $f(R,T)$ theory of gravity is obtained from the Hilbert-Einstein action in variational principle.

The action for $f(R,T)$ modified gravity is given as,

$$S = \int \sqrt{-g} \left(\frac{f(R,T)}{16\pi G} + L_m \right) d^4 x \,, \tag{1}$$

where, $f(R,T)$ is an arbitrary function of the Ricci scalar R and of the trace T of the stress-energy tensor of the matter $T_{\mu\nu}$ and L_m is the usual matter Lagrangian.

The stress-energy tensor of the matter $T_{\mu\nu}$ is defined as

$$T_{\mu\nu} = -\frac{2}{\sqrt{-g}} \frac{\delta\left(\sqrt{-g}\, L_m\right)}{\delta g^{\mu\nu}}, \tag{2}$$

and its trace by $T = g^{\mu\nu} T_{\mu\nu}$

The corresponding field equations of $f(R,T)$ gravity by varying the action (1) with respect to the metric tensor $g_{\mu\nu}$ is given by

$$f_R(R,T) R_{\mu\nu} - \frac{1}{2} f(R,T) g_{\mu\nu} + \left(g_{\mu\nu} \Box - \nabla_\mu \nabla_\nu \right) f_R(R,T) = 8\pi T_{\mu\nu} - f_T(R,T) T_{\mu\nu} - f_T(R,T) \Theta_{\mu\nu} \tag{3}$$

where,

$$f_R \equiv \frac{\partial f(R,T)}{\partial R}, \qquad f_T \equiv \frac{\partial f(R,T)}{\partial T}, \qquad \Box \equiv \nabla^i \nabla_j,$$

∇_i is the covariant derivative and $T_{\mu\nu}$ is the standard matter energy-momentum tensor derived from the Lagrangian L_m.

By contracting equation (3) we get relation between the Ricci scalar R and trace T of stress-energy momentum tensor as,

$$f_R(R,T)R + 3\Box f_R(R,T) - 2f(R,T) = 8\pi T - f_T(R,T)T - f_T(R,T)\Theta, \tag{4}$$

where, $\Theta = g^{\mu\nu}\Theta_{\mu\nu}$

In $f(R,T)$ gravity theory, the function $f(R,T)$ depends on the nature of matter source. Hence, one can obtain several theoretical models corresponding to the different matter models. Harko et al. [24] have considered the following three different classes of $f(R,T)$ gravity models:

$$f(R,T) = \begin{cases} R + 2f(T) \\ f_1(R) + f_2(T) \\ f_1(R) + 2f_2(R)f_3(T) \end{cases}. \tag{5}$$

In this paper, we assume $f(R,T) = R + 2f(T)$, with the particular choice $f(T) = \lambda T$, where λ is constant.

The field equation in $f(R,T)$ theory with the function $f(R,T) = R + 2f(T)$, where the matter source is perfect fluid are given by Harko et al. [24]

$$R_{\mu\nu} - \frac{1}{2}Rg_{\mu\nu} = 8\pi T_{\mu\nu} + 2f'(T)T_{\mu\nu} + [2p\,f'(T) + f(T)]g_{\mu\nu}, \tag{6}$$

where prime denotes the differentiation with respect to argument.

The energy- momentum tensor of domain wall is taken as

$$T_{\mu\nu} = \rho\left(g_{\mu\nu} + w_i w_j\right) + pw_i w_j, \tag{7}$$

where ρ is the energy density , p is the pressure of domain wall and $w^\mu = (1,0,0,0)$ is the four velocity vector in the comoving coordinates which satisfies the condition $w^\mu w_\mu = -1$.

Then we have,

$$T_1^1 = T_2^2 = T_3^3 = \rho, T_4^4 = -p, T = 3\rho - p. \tag{8}$$

Domain walls are cosmologically important due to their appearance in the phase transition of the early universe. Kibble [47] has highlighted that late time evolution of domain walls is governed by their surface tension and their interaction with matter. Different types of domain walls can occur with very different degrees of transparency, but in all cases the size of the overall structure increases over time.

Metric and field equations

We consider the LRS Bianchi type I space-time of the form

$$ds^2 = dt^2 - L(t)^2\,dx^2 - M(t)^2\,(dy^2 + dz^2), \tag{9}$$

where $L(t)$ and $M(t)$ are the scale factor and the function of the cosmic time t only.

The corresponding field equation (6) for the metric (9) for the function $f(R,T) = R + 2f(T)$ with $f(T) = \lambda T$ can be written as

$$\left(\frac{\dot{M}}{M}\right)^2 + 2\frac{\ddot{M}}{M} = -(8\pi + 5\lambda)\rho - \lambda p, \tag{10}$$

$$\frac{\ddot{L}}{L} + \frac{\ddot{M}}{M} + \frac{\dot{L}}{L}\frac{\dot{M}}{M} = -(8\pi + 5\lambda)\rho - \lambda p, \tag{11}$$

$$\left(\frac{\dot{M}}{M}\right)^2 + 2\frac{\dot{L}}{L}\frac{\dot{M}}{M} = (8\pi + \lambda)p - 3\lambda\rho, \tag{12}$$

where dot (.) represents the derivative with respect to t.

Equation (10), (11) and (12) are three linearly equations with four unknowns L, M, ρ and p. In order to solve the system completely we use variation law of Hubble's parameter between H and a proposed by Berman (1983).

$$H = la^{-n} = l(LM^2)^{-n/3}, \tag{13}$$

where $l > 0$ and $n \geq 0$ are constants.

The spatial volume is given by

$$V = a^3 = LM^2, \tag{14}$$

where a the mean scale factor.

The mean Hubble's parameter H for the metric (9) is given by

$$H = \frac{1}{3}\left(H_x + H_y + H_z\right) = \frac{1}{3}\left(\frac{\dot{L}}{L} + 2\frac{\dot{M}}{M}\right) = \frac{\dot{a}}{a} \tag{15}$$

where $H_x = \dfrac{\dot{L}}{L}$ and $H_y = H_z = \dfrac{\dot{M}}{M}$ are the directional Hubble's parameter in the x, y, z respectively.

The volumetric deceleration parameter is

$$q = -1 + \frac{d}{dt}\left(\frac{1}{H}\right) = -\frac{a\ddot{a}}{\dot{a}^2} = n - 1 \tag{16}$$

from equation (13) and (15), on integration we get

$$a = (nlt + k_1)^{\frac{1}{n}}, \quad n \neq 0 \tag{17}$$

Subtracting equation (11) from (10) we get,

$$\frac{d}{dt}\left(\frac{\dot{L}}{L} - \frac{\dot{M}}{M}\right) + \left(\frac{\dot{L}}{L} - \frac{\dot{M}}{M}\right)\left(\frac{\dot{L}}{L} + 2\frac{\dot{M}}{M}\right) = 0 \tag{18}$$

on integrating and using (14), (17) we get

$$L = (c_2)^{\frac{2}{3}}(nlt + k_1)^{\frac{1}{n}}\exp\left(\frac{2c_1}{3l(n-3)}(nlt + k_1)^{\frac{n-3}{n}}\right), n \neq 3 \tag{19}$$

$$M = (c_2)^{-\frac{1}{3}}(nlt + k_1)^{\frac{1}{n}}\exp\left(\frac{-c_1}{3l(n-3)}(nlt + k_1)^{\frac{n-3}{n}}\right), n \neq 3 \tag{20}$$

where c_1 and c_2 are the constant of integration.

using equation (11), (13), (19) and (20) we get,

$$\rho = \frac{1}{\left((8\pi + 3\lambda)^2 - \lambda^2\right)}\left\{\frac{l^2\left[8\pi(2n-3) + 2\lambda(n-3)\right]}{(nlt + k_1)^2} - \frac{2c_1^2(12\pi - \lambda)}{9\left[(nlt + k_1)^{\frac{1}{n}}\right]^6}\right\}, \tag{21}$$

$$p = \frac{-1}{\left((8\pi + 3\lambda)^2 - \lambda^2\right)}\left\{\frac{l^2\left[-6\lambda(1+n) - 24\pi\right]}{(nlt + k_1)^2} + \frac{24c_1^2(\pi + \lambda)}{9\left[(nlt + k_1)^{\frac{1}{n}}\right]^6}\right\} \tag{22}$$

using equation (19) and (20) in equation (9), the model of the universe takes the form

$$ds^2 = dt^2 - (c_2)^{\frac{4}{3}}(nlt + k_1)^{\frac{2}{n}}\exp\left(\frac{4c_1}{3l(n-3)}(nlt + k_1)^{\frac{n-3}{n}}\right)dx^2 - (c_2)^{-\frac{2}{3}}(nlt + k_1)^{\frac{2}{n}}\exp\left(\frac{-2c_1}{3l(n-3)}(nlt + k_1)^{\frac{n-3}{n}}\right)(dy^2 + dz^2), \tag{23}$$

Definition for physical parameter such as, the spatial volume (V), directional Hubble parameter (H_i), mean Hubble's parameter (H), extension scalar (θ), shear scalar (σ) and anisotropy parameter (A_m), deceleration parameter (q) for the universe (23) are given by:

$$V = (nlt + k_1)^{\frac{3}{n}} \tag{24}$$

$$H_x = \frac{2c_1}{3(nlt + k_1)^{\frac{3}{n}}} + \frac{l}{(nlt + k_1)} \tag{25}$$

$$H_y = H_z = \frac{-c_1}{3(nlt + k_1)^{\frac{3}{n}}} + \frac{l}{(nlt + k_1)} \tag{26}$$

$$H = \frac{l}{(nlt + k_1)} \tag{27}$$

$$\theta = \frac{3l}{(nlt + k_1)} \tag{28}$$

$$A_m = \frac{2c_1^{\,2}}{9l^2}\left(nlt + k_1\right)^{\frac{2(n-3)}{n}} \tag{29}$$

$$\sigma^2 = \frac{c_1^{\,2}}{3\left(nlt + k_1\right)^{\frac{6}{n}}} \tag{30}$$

$$q = n - 1 \tag{31}$$

Fig. (1) shows the variation of Hubble parameter (H) with cosmic time (t). From figure we observe that H is decreasing function of cosmic time. Similarly, from **Fig. (4)** the expansion scalar (θ) is the decreasing function of time. Both Hubble's parameter (H) and expansion scalar (θ) starts from a positive value and approaches a small positive value for large value of time (t). Hence the expansion rate is faster at the beginning and slows at later stage. We plotted all the graphs by taking $n, l, k_1, c_1 = 1.5, 2, 1, 1$.

Fig. (2) and (3) shows the variation of spatial volume (V) and shear scalar (σ^2) with cosmic time (t). From the figure we observe that the shear scalar is decreasing positive value function of time and spatial volume of the model is increasing function of cosmic time. Hence the present model is expanding and shearing.
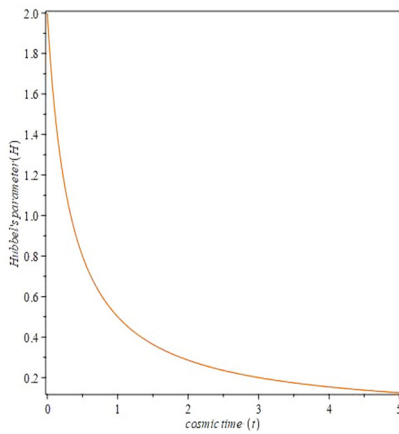

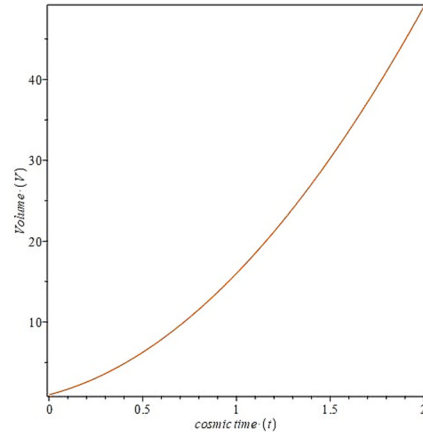**Figure 1.** Plot of variation of Hubbel's parameter (H) vs cosmic time (t)
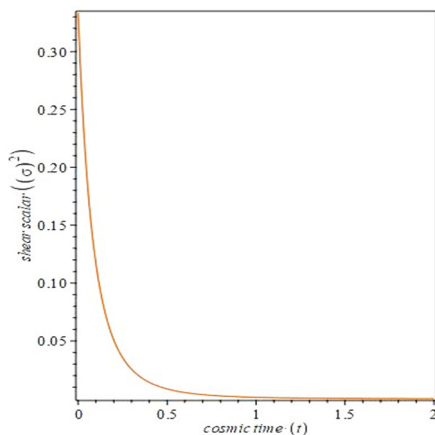

Figure 2. Plot of variation of volumr vs cosmic time (t)

Figure 3. Plot of variation of shear scalar (σ^2) vs cosmic time (t)
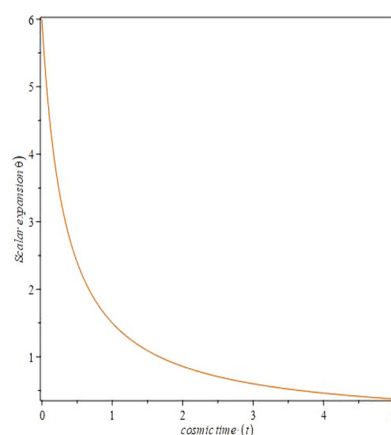

Figure 4. Plot of variation of shear scalar expansion (θ) vs cosmic time (t)

Fig. (5) and (6) represent the plot of pressure and energy density with cosmic time (t) for $\lambda = 0, -1$ and -2 by taking $n, l, k_1, c_1 = 3.2, 0.097, 0.1, 0.2$. The value of pressure approaches to a small negative value close to zero, for large value of time. From the recent observations data and accelerated cosmic expansion of the universe, it is assumed that the Universe is undergoing an accelerating expansion due to the negative pressure called as dark energy. Also, from the graph of energy density (ρ) vs. cosmic time (t), it is observed that, energy density is decreasing positive valued function of time and approaches zero at late time.
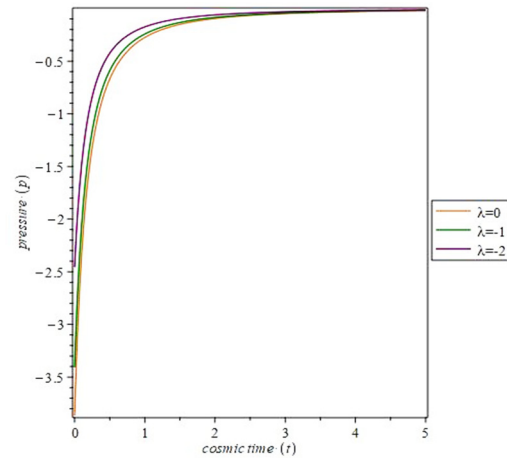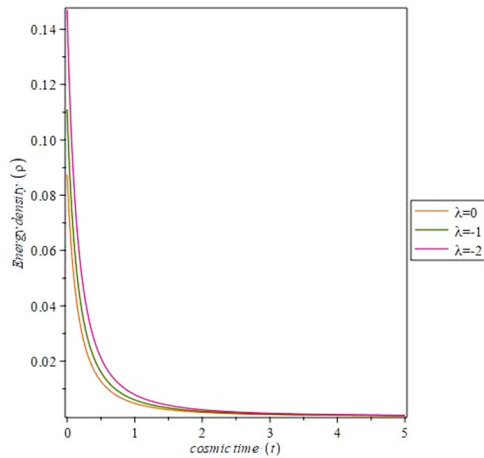
Figure 5. Plot of variation of Energy density (ρ) vs cosmic time (t)

Figure 6. Plot of variation of pressure (p) vs cosmic time (t)

Energy conditions

In this section, we examine the energy condition for our constructed model. Additionally, we examine whether or not our model satisfies the energy conditions.

The energy conditions are:

i) Weak energy conditions (WEC): $\rho \geq 0$ and $\rho + p \geq 0$.

ii) Dominant energy conditions (DEC): $\rho - p \geq 0$.

iii) Strong energy condition (SEC): $\rho + 3p \geq 0$

$$\rho + p = \frac{1}{\left(\left(8\pi + 3\lambda\right)^2 - \lambda^2\right)} \left\{ \frac{l^2 \left(16\pi n + 8\lambda n\right)}{\left(nlt + k_1\right)^2} - \frac{c_1^2 \left(48\pi + 22\lambda\right)}{9\left[\left(nlt + k_1\right)^{\frac{1}{n}}\right]^6} \right\}, \tag{32}$$

$$\rho - p = \frac{1}{\left(\left(8\pi + 3\lambda\right)^2 - \lambda^2\right)} \left\{ \frac{l^2 \left(16\pi n - 6\lambda n - 12\lambda - 48\pi\right)}{\left(nlt + k_1\right)^2} + \frac{26\lambda c_1^2}{9\left[\left(nlt + k_1\right)^{\frac{1}{n}}\right]^6} \right\}, \tag{33}$$

$$\rho + 3p = \frac{1}{\left(\left(8\pi + 3\lambda\right)^2 - \lambda^2\right)} \left\{ \frac{l^2 \left(16\pi n + 20\lambda n + 12\lambda + 48\pi\right)}{\left(nlt + k_1\right)^2} - \frac{\left(70\lambda + 96\pi\right)c_1^2}{9\left[\left(nlt + k_1\right)^{\frac{1}{n}}\right]^6} \right\}, \tag{34}$$
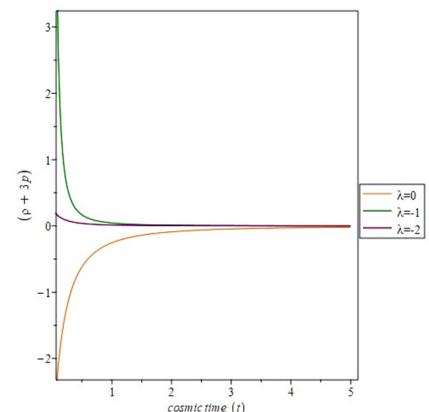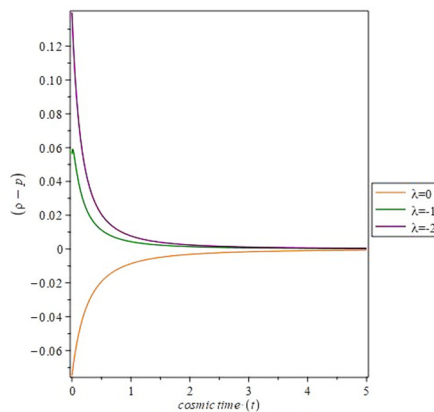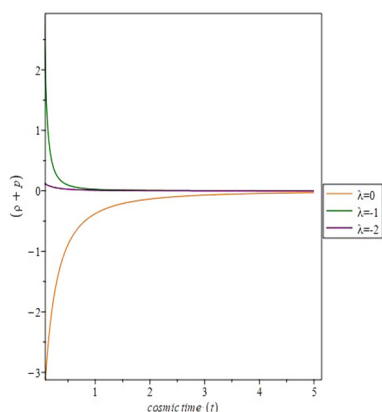

Figure 7. Plot of ($\rho + p$) vs cosmic time (t)

Figure 8. Plot of variation $\rho - p$ vs cosmic time (t)

Figure 9. Plot of variation of ($\rho + 3p$) vs cosmic time (t)

Fig. (7), (8), (9) represents the graph of energy conditions vs. cosmic time with $\lambda = 0, -1$ and -2. From these figures it is observed that all the energy conditions (EC) are satisfies by the model in $f(R,T)$ gravity.

State-finder diagnostic

A cosmological diagnostic parameter set $\{r,s\}$ called State-finder pair was introduced first by Sahni et al. [48] to study a geometric view of the dark energy models. The state finder parameters depend on the scale factor. The important property of state-finder pair is that, the fixed point $\{r,s\} = \{1,0\}$ characterizes the cold dark matter with Λ (ΛCDM) model, while the fixed point $\{r,s\} = \{1,1\}$ characterizes the standard cold dark matter (SCDM) model.

The state finder parameter r and s are defined as follows:

$$r = \frac{\dddot{a}}{aH^3} = (n-1)(2n-1),$$
(35)

$$s = \frac{r-1}{3\left(q - \frac{1}{2}\right)} = \frac{2}{3}n.$$
(36)

From **Fig. (10)**, we can see that our model satisfies SCDM scenario of the universe for $n = 1.5$.
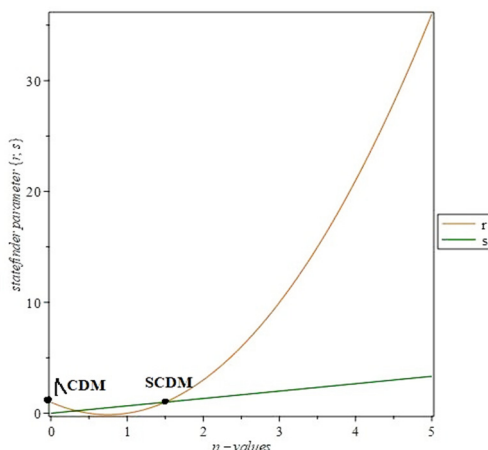

Figure 10. The state finder plane

DISCUSSION AND CONCLUSION

In this paper, we studied the LRS Bianchi -I cosmological model in the framework of $f(R,T)$ theory of gravity with $f(R,T) = R + 2f(T)$ by taking $f(T) = \lambda T$. Exact solution of the field equations is obtained with the help of special law of variation of Hubble's parameter proposed by Berman (1983). We have discussed the geometrical and kinematical properties of various parameters. Also we have studied the behaviour of the model according to graphs of physical parameters such as Hubble's parameter (H), the spatial volume (V), extension scalar (θ), shear scalar (σ), Energy density (ρ) and pressure (p). The Hubble's parameter, shear scalar and expansion scalar are constant as cosmic time tends to zero and this parameter diverges when cosmic time is $-k_1/(n \cdot l)$.

i) Hubble's parameter, shear scalar and expansion scalar are decreasing positive value function of cosmic time. This shows that at the beginning the expansion rate is faster and slows at later stage.

ii) The spatial volume admits constant value at early times of the universe (as cosmic time tends to zero), after that spatial volume start increasing with increase in cosmic time without showing any type of initially singularity and finally diverges to ∞ as $t \to \infty$. This indicates that initially, the evolution of universe starts at the big-bang singularity $t = -k_1/(n \cdot l)$ and then expands approaching to infinite volume.

iii) The positive sign of deceleration parameter (q) corresponds to standard decelerating model whereas the negative sign indicates acceleration. For $n > 1$, deceleration parameter $q > 0$, hence model represents the decelerating model whereas $0 < n < 1$, we get $-1 \leq q < 0$, which describes an accelerating model of the universe.

iv) Energy density (ρ) is positive and decreasing function of cosmic time and also $\rho \to 0$ when $t \to \infty$.

v) It is worth to note that, $f(R,T)$ model reduces to general relativity (GR) for $\lambda=0$. From **Figs. (7-9)**, it is observed that all energy conditions (EC) are satisfied in $f(R,T)$ model but these energy conditions are not satisfied in general relativity $(\lambda=0)$ model.

vi) The Statefinder trajectory **(Fig. 10)**, showing that the model behaves as the SCDM model during the early universe and as the ΛCDM model during the late universe.

ORCID

V.R. Patil, https://orcid.org/0000-0002-0442-3962; **P.A. Bolke**, https://orcid.org/0000-0002-1212-5260
J.L. Pawde, https://orcid.org/0000-0001-8068-6265

REFERENCES

[1] A.H. Guth, and D.I. Kaiser, "Inflationary cosmology: Exploring the universe from the smallest to the largest scales," Science, **307**(5711), 884-890 (2005). https://doi.org/10.1126/science.1107483

[2] A.H. Guth, "Inflation and the new era of high precision cosmology," MIT Physics Annual, 28-39 (2002).

[3] P.A. Ade, N. Aghanim, M. Arnaud, M. Ashdown, J. Aumont, C. Baccigalupi, A.J. Banday *et al.,* "Planck 2015 results-xiii. cosmological parameters. Astronomy and Astrophysics," **594**, A13. (2016). https://doi.org/10.1051/0004-6361/201525830

[4] S. Alam, M. Ata, S. Bailey, F. Beutler, D. Bizyaev, J.A. Blazek, A.S. Bolton, *et al.*, "The clustering of galaxies in the completed SDSS-III Baryon Oscillation Spectroscopic Survey: cosmological analysis of the DR12 galaxy sample," Monthly Notices of the Royal Astronomical Society, **470**(3), 2617-2652 (2017). https://doi.org/10.1093/mnras/stx721

[5] S. Naess, M. Hasselfield, J. McMahon, M.D. Niemack, G.E. Addison, P.A. Ade, R. Allison, *et al.*, "The Atacama cosmology telescope: CMB polarization at 200<ℓ<9000," Journal of Cosmology and Astroparticle Physics, **2014**(10), 007 (2014). https://doi.org/10.1088/1475-7516/2014/10/007

[6] A.G. Riess, A.V. Filippenko, P. Challis, A. Clocchiatti, A. Diercks, P.M. Garnavich, Ron L. Gilliland, *et al.*, "Observational evidence from supernovae for an accelerating universe and a cosmological constant," The astronomical journal, **116**(3), 1009 (1998). https://doi.org/10.1086/300499

[7] S. Perlmutter, G. Aldering, M.D. Valle, S. Deustua, R.S. Ellis, S. Fabbro, A. Fruchter, *et al.*, "Discovery of a supernova explosion at half the age of the Universe," Nature, **391**(6662), 51-54. (1998). https://doi.org/10.1038/34124

[8] S. Perlmutter, G. Aldering, G. Goldhaber, R.A. Knop, P. Nugent, P.G. Castro, S. Deustua, et al., "Measurements of Ω and Λ from 42 high-redshift supernovae," The Astrophysical Journal, **517**(2), 565 (1999). https://doi.org/10.1086/307221

[9] D.N. Spergel, L. Verde, H.V. Peiris, E. Komatsu, M.R. Nolta, C.L. Bennett, M. Halpern, et al., "First-year Wilkinson Microwave Anisotropy Probe (WMAP)*observations: determination of cosmological parameters," The Astrophysical Journal Supplement Series, **148**(1), 175 (2003). https://doi.org/10.1086/377226

[10] D.N. Spergel, R. Bean, O. Doré, M.R. Nolta, C.L. Bennett, J. Dunkley, G. Hinshaw, *et al.*, "Three-year Wilkinson Microwave Anisotropy Probe (WMAP) observations: implications for cosmology," The Astrophysical Journal Supplement Series, **170**(2), 377 (2007). https://doi.org/10.1086/513700

[11] M. Tegmark, M.A. Strauss, M.R. Blanton, K. Abazajian, S. Dodelson, H. Sandvik, X. Wang, *et al.*, "Cosmological parameters from SDSS and WMAP," Physical review D, **69**(10), 103501 (2004). https://doi.org/10.1103/PhysRevD.69.103501

[12] S.F. Daniel, R.R. Caldwell, A. Cooray, and A. Melchiorri, "Large scale Structure as a probe of gravitational slip," Physical Review D, **77**(10), 103513 (2008). https://doi.org/10.1103/PhysRevD.77.103513

[13] Z.Y. Huang, B. Wang, E. Abdalla, and R.K. Su, "Holographic explanation of wide-angle power correlation suppression in the cosmic microwave background radiation," Journal of Cosmology and Astroparticle Physics, **2006**(05), 013 (2006). https://doi.org/10.1088/1475-7516/2006/05/013

[14] S.M. Carroll, "Quintessence and the rest of the world: suppressing long-range interactions," Physical Review Letters, **81**(15), 3067 (1998). https://doi.org/10.1103/PhysRevLett.81.3067

[15] M.S. Turner, "Making sense of the new cosmology," International Journal of Modern Physics A, **17**(supp01), 180-196 (2002). https://doi.org/10.1142/S0217751X02013113

[16] R.R. Caldwell, "A phantom menace? Cosmological consequences of a dark energy component with super-negative equation of state," Physics Letters B, **545**(1-2), 23-29 (2002). https://doi.org/10.1016/S0370-2693(02)02589-3

[17] T. Chiba, T. Okabe, and M. Yamaguchi, "Kinetically driven quintessence," Physical Review D, **62**(2), 023511 (2000). https://doi.org/10.1103/PhysRevD.62.023511

[18] T. Padmanabhan, "Accelerated expansion of the universe driven by tachyonic matter," Physical Review D, **66**(2), 021301 (2002). https://doi.org/10.1103/PhysRevD.66.021301

[19] M. Li, "A model of holographic dark energy," Physics Letters B, **603**(1-2), 1-5 (2004). https://doi.org/10.1016/j.physletb.2004.10.014

[20] A. Kamenshchik, U. Moschella, and V. Pasquier, "An alternative to quintessence," Physics Letters B, **511**(2-4), 265-268. (2001). https://doi.org/10.1016/S0370-2693(01)00571-8

[21] A.D. Dolgov, and M. Kawasaki, "Can modified gravity explain accelerated cosmic expansion?" Physics Letters B, **573**, 1-4 (2003). https://doi.org/10.1016/j.physletb.2003.08.039

[22] S.I. Nojiri, and S.D. Odintsov, "Modified gravity with negative and positive powers of curvature: Unification of inflation and cosmic acceleration," Physical Review D, **68**(12), 123512 (2003). https://doi.org/10.1103/PhysRevD.68.123512

[23] S.I. Nojiri, and S.D. Odintsov, "The minimal curvature of the universe in modified gravity and conformal anomaly resolution of the instabilities," Modern Physics Letters A, **19**(08), 627-638 (2004). https://doi.org/10.1103/PhysRevD.68.123512

[24] T. Harko, F.S. Lobo, S.I. Nojiri, and S.D. Odintsov, "f(R, T) gravity," Physical Review D, **84**(2), 024020 (2011). https://doi.org/10.1103/PhysRevD.84.024020

[25] Y.F Cai, S. Capozziello, M. De Laurentis, and E.N. Saridakis, "f (T) Teleparallel gravity and cosmology," Reports on Progress in Physics, **79**(10), 106901 (2016). https://doi.org/10.1088/0034-4885/79/10/106901

[26] M. Sharif, and M. Zubair, "Thermodynamics in f (R, T) theory of gravity," Journal of Cosmology and Astroparticle Physics, **2012**(03), 028 (2012). https://doi.org/10.1088/1475-7516/2012/03/028

[27] M. Jamil, D. Momeni, and R. Myrzakulov, "Violation of the first law of thermodynamics in f (R, T) gravity," Chinese Physics Letters, **29**(10), 109801 (2012). https://doi.org/10.1088/0256-307X/29/10/109801

[28] D. Momeni, P.H.R.S. Moraes, and R. Myrzakulov, "Generalized second law of thermodynamics in f (R, T) theory of gravity," Astrophysics and Space Science, **361**(7), 228 (2016). https://doi.org/10.1007/s10509-016-2784-2

[29] M.E.S. Alves, P.H.R.S. Moraes, J.C.N. De Araujo, and M. Malheiro, "Gravitational waves in f (R, T) and f (R, T φ) theories of gravity," Physical Review D, **94**(2), 024032 (2016). https://doi.org/10.1103/PhysRevD.94.024032

[30] M. Sharif, and A. Siddiqa, "Propagation of polar gravitational waves in f (R, T) scenario," General Relativity and Gravitation, **51**(6), 74 (2019). https://doi.org/10.1007/s10714-019-2558-6

[31] J. Bora, and U.D. Goswami, "Gravitational wave echoes from compact stars in f (R, T) gravity," Physics of the Dark Universe, **38**, 101132 (2022). https://doi.org/10.1016/j.dark.2022.101132

[32] S. Bhattacharjee, and P.K. Sahoo, "Redshift drift in f (R, T) gravity," New Astronomy, **81**, 101425. (2020). https://doi.org/10.1016/j.newast.2020.101425

[33] S. Bhattacharjee, and P.K. Sahoo, "Big bang nucleosynthesis and entropy evolution in f (R, T) gravity," The European Physical Journal Plus, **135**(4), 350 (2020). https://doi.org/10.1140/epjp/s13360-020-00361-4

[34] N. Godani, "FRW cosmology in f (R, T) gravity," International Journal of Geometric Methods in Modern Physics, **16**(02), 1950024 (2019). https://doi.org/10.1142/S0219887819500245

[35] R.K. Tiwari, and D. Sofuoğlu, "Quadratically varying deceleration parameter in f (R, T) gravity," International Journal of Geometric Methods in Modern Physics, **17**(10), 2030003 (2020). https://doi.org/10.1142/S0219887820300032

[36] D.D. Pawar, and S.P. Shahare, "Anisotropic tilted cosmological model in f (R, T) theory of gravity," New Astronomy, **75**, 101318 (2020). https://doi.org/10.1016/j.newast.2019.101318

[37] B. Mishra, F.M. Esmeili, and S. Ray, "Cosmological models with variable anisotropic parameter in f (R, T) gravity," Indian Journal of Physics, **95**, 2245-2254 (2021). http://dx.doi.org/10.1007/s12648-020-01877-2

[38] P.K. Sahoo, S. Mandal, and S. Arora, "Energy conditions in non-minimally coupled f (R, T) gravity," Astronomische Nachrichten, **342**(1-2), 89-95 (2021). https://doi.org/10.1002/asna.202113886

[39] S. Arora, S. Bhattacharjee, and P.K. Sahoo, "Late-time viscous cosmology in f (R, T) gravity," New Astronomy, **82**, 101452 (2021). https://doi.org/10.1016/j.newast.2020.101452

[40] A.K. Yadav, L.K. Sharma, B.K. Singh, and P.K. Sahoo, "Existence of bulk viscous universe in f (R, T) gravity and confrontation with observational data," New Astronomy, **78**, 101382 (2020). https://doi.org/10.1016/j.newast.2020.101382

[41] V.R. Patil, P.A. Bolke, and N.S. Bayaskar, "Bianchi Type-IX Dust Filled Universe with Ideal Fluid Distribution in Creation Field," International Journal of Theoretical Physics, **53**, 4244-4249 (2014). https://doi.org/10.1007/s10773-014-2175-9

[42] M. Koussour, and M. Bennai, "On a Bianchi type-I space-time with bulk viscosity in f (R, T) gravity," International Journal of Geometric Methods in Modern Physics, **19**(03), 2250038 (2022). https://doi.org/10.1142/S0219887822500384

[43] V.K. Bhardwaj, and A. Dixit, "LRS Bianchi type-I bouncing cosmological models in f (R, T) gravity," International Journal of Geometric Methods in Modern Physics, **17**(13), 2050203 (2020). https://doi.org/10.1142/S0219887820502035

[44] A. Pradhan, A. Dixit, and G. Varshney, "LRS Bianchi type-I cosmological models with periodic time varying deceleration parameter in f (R, T) gravity," International Journal of Modern Physics A, **37**(18), 2250121 (2022). https://doi.org/10.1142/S0217751X22501214

[45] S.N. Gashti, and J. Sadeghi, "Cosmic evolution in the anisotropic space–time from modified f (R, T) gravity," Pramana, **97**(1), 25 (2023). http://dx.doi.org/10.1007/s12043-022-02492-y

[46] S. Jokweni, V. Singh, and A. Beesham, "LRS Bianchi I Cosmological Model with Strange Quark Matter in f (R, T) Gravity," In MDPI. Physical Sciences Forum, **7**(1), 12 (2023). https://doi.org/10.3390/ECU2023-14037

[47] T.W. Kibble, "Topology of cosmic domains and strings," Journal of Physics A: Mathematical and General, **9**(8), 1387 (1976). https://doi.org/10.1088/0305-4470/9/8/029

[48] V. Sahni, T.D. Saini, A.A. Starobinsky, and U. Alam, "Statefinder – a new geometrical diagnostic of dark energy," Journal of Experimental and Theoretical Physics Letters, **77**, 201-206 (2003). https://doi.org/10.1134/1.1574831

**ЕНЕРГЕТИЧНІ УМОВИ ТА ДІАГНОСТИКА ВИЗНАЧНИКА СТАНУ КОСМОЛОГІЧНОЇ МОДЕЛІ
ЗІ СПЕЦІАЛЬНИМ ЗАКОНОМ ПАРАМЕТРІВ ХАББЛА В $f(R,T)$ ГРАВІТАЦІЇ**
В.Р. Патіл[a], П.А. Болке[b], С.К. Вагмаре[c], Дж.Л. Павде[d]
[a]Департамент коледжа математики, мистецтв, науки та торгівлі, Чикхалдара, округ Амраваті-444807, Індія
[b]Кафедра математики, коледж інженерії та управління професора Рама Меге, Амраваті-444701, Індія
[c]Департамент математики, TGPCET Нагпур-441108, Індія
[d]Дадасахеб Гавай Відьялая, Малхара, Ачалпур, округ Амраваті-444806, Індія

У цій статті ми розглядаємо космологічну модель LRS Bianchi типу I в рамках $f(R, T)$ гравітації, де R є скаляр Річчі, а T є тензор імпульсу енергії напруги за наявності доменної стінки. ми використали спеціальний закон зміни параметра Хаббла, запропонований Берманом (1983), щоб отримати точний розв'язок рівняння поля, що відповідає моделі Всесвіту. Були отримані енергетичні умови та фізична поведінка Всесвіту, а їх еволюція обговорювалася за допомогою деяких фізичних параметрів і за допомогою їхніх графіків. Крім того, ми можемо використовувати параметр визначника стану для перевірки валідності моделі.
Ключові слова: *$f(R, T)$ гравітація; параметри вимірювача стану; космологічна модель Б'янкі типу-I; параметр уповільнення*

ENERGY CONDITIONS WITH INTERACTING FIELD IN $f(R)$ GRAVITY[†]

ⓘ **Vasudeo Patil**[a], ⓘ **Jeevan Pawde**[a*], ⓘ **Rahul Mapari**[b], ⓘ **Pravin Bolke**[c]

[a] *Department of Mathematics, Arts, Science and Commerce College, Chikhaldara, Dist. Amravati (MS), India-444807*
[b] *Department of Mathematics, Government Vidarbha Institute of Science & Humanities, Amravati(MS), India-444604*
[c] *Department of Mathematics, Prof. Ram Meghe College of Eng. & Management, New Express Highway,*
Amravati(MS), India-444701
[*] *Corresponding Author e-mail: jeevanpawade@gmail.com*

In the context of current scenario, it is crucial to look beyond Einstein's theory, which opens the door to certain modified theories of gravity. So, present study is devoted to investigate the various energy conditions, particularly, strong energy condition (SEC), weak energy condition (WEC), null energy condition (NEC) and dominant energy condition (DEC) corresponding to different functional forms of $f(R)$ gravity. We have studied for flat, isotropic and homogeneous FLRW cosmological model filled with interacting field i.e., perfect fluid is coupled with mass less scalar field for different models of modified $f(R)$ gravity in which R is the Ricci scalar. We have observed, the accelerated expansion of the Universe which exact match with recent observational evidences.

Keywords: *FLRW cosmological model; $f(R)$ gravity; Interacting field; Hubble's law*

PACS: 04.20.-q; 04.20.Jb; 04.50.Kd

1. INTRODUCTION

During the past few decades, the astrophysical data from cosmic microwave background anisotropy, galaxy clustering and high red-shift supernovae [1, 2, 3] have disclosed large scale structure and accelerated expansion of the Universe caused by a dominated negative pressure fluid termed as dark energy (DE). According to experimental findings, the DE acquires almost 73%, dark matter occupied 23% and baryonic matter served 4% [4, 5, 6] of entire energy density. The vacuum energy (also known as the cosmological constant) with equation of state (EoS) parameter $w = -1$ are the most straightforward and theoretically plausible candidates to explain the existence of DE [7, 8]. But instead of introducing a dark energy it is more sensible to propose theories by modifying the Einstein-Hilbert action with Ricci scalar R and a general function along with matter-geometry coupling. Some of popular and important modified theories are $f(R)$ gravity [9], $f(T)$ gravity [10], $f(G)$ gravity [11], $f(R,T)$ gravity [12] etc.

The $f(R)$ gravity is one of the most powerful and interesting candidates to study the behaviour of DE and is a modification of general relativity that alters the Lagrangian density of the theory by incorporating a function $f(R)$ into the gravitational action [13]. To extend and generalize Einstein's theory of general relativity, there exist different approaches to describe modified gravity theories such as $f(R)$ gravity which approaches aim to expand the understanding of gravitational interactions and their implications. Recent research has focused on $f(R)$ gravity as a potential explanation for the accelerated expansion of the Universe. These theories have limitations such as instability, ghost-like degrees of freedom, and the fine-tuning problem. Despite these limitations, $f(R)$ gravity has been successful in explaining various phenomena, including the structure formation, the unification of cosmic epochs, and the late accelerated expansion of the Universe [14, 15, 16, 17]. Studies in $f(R)$ gravity have supported observations of Type Ia supernovae and WMAP data, which indicate an accelerated expansion of the Universe [18]. After a long period of time, the expansion will cease entirely and the Universe will attain isotropy i.e as $t \to \infty$, $\frac{\sigma^2}{\theta} \to 0$ [19].The Hubble parameter (H) and expansion scalar (θ) have been analyzed, revealing that the expansion rate of the Universe was higher during the Big Bang and has gradually decreased over time [20]. Researchers have also explored the solutions of Bianchi-type cosmology in metric $f(R)$ gravity and compared them with Lematre-Tolman cosmology, which describes inhomogeneity in the Universe on various scales[21]. The influence of magnetism in the early stages of the Universe's evolution has been observed in the investigation of Bianchi type I space-time in $f(R)$ gravity with the presence of string clouds and domain walls containing strange quark matter [22]. Both accelerating and decelerating phases of Bianchi type-I space-time have been studied in $f(R)$ gravity, with the Universe expanding in both phases. The initial expansion rate is much faster than the later rate [23]. The expansion of model begins with zero volume, finite string density as well pressure and continues to expand over time [24]. Fourth-order $f(R)$ extended theories of gravity have been

examined [25], specifically the form $f(R) = R + R^2$, which is in line with theoretical constraints and cosmological data for static and spherically symmetric configurations. In contrast to the expansion scalar, shear scalar, and Hubble's parameter, the spatial volume in $f(R)$ gravity increases exponentially with time, indicating a constant rate of expansion that matches the present-day scenario [26]. Using a special form of the Hubble parameter, researchers [27] have investigated exact solutions of spatially homogeneous Bianchi type-I cosmological models in the context of $f(R)$ theory of gravity. The models depict an expanding Universe following a power law after the Big Bang singularity, with the presence of accelerating or decelerating phases depending on the parameters [28]. Furthermore, the solutions of field equations have been explored for higher dimensional Kaluza-Klein cosmological models using string models in $f(R)$ gravity, resulting in an accelerated expanding Universe [29].

The authors [30] employed a special case proposed by Schwinger and found solutions for the model FRW closed bulk viscous cosmological model with wet dark fluid was examined using the Nordtvedt general scalar-tensor theory. Another investigation focused on two fluid axially symmetric cosmological models in the $f(R,T)$ theory of gravitation. By imposing a supplementary constraint $H_3 = kH_1$, the authors [31] obtained a deterministic model that exhibited an expanding and shearing Universe. Some authors [32] presented a FRW cosmological model which satisfied the principle and considering the most recent research that suggested dark energy is responsible for the Universe's acceleration. The authors [33] selected a specific functional form and explored the cosmological behavior of FRW models in the $f(R,G)$ gravity. They discussed violations of the SEC (strong energy condition) and NEC (null energy condition), which are necessary for bouncing models. In the context of the Big Bang theory, researchers [34] investigated the cosmological behavior within the framework of the $f(R,T)$ gravity. They obtained a solution for the FRW cosmological model, which revealed that the Universe is accelerating and expanding according to current observations. By adopting the fractal parameter $\omega = 0$ and the relationship between p_m and ρ_m, i.e. $p_m = (\gamma - 1)\rho_m$, $1 \le \gamma \le 2$, [35] explored the flat FRW two-fluid cosmological models in fractal theory of gravity and discovered the answers.

By examining the plane-symmetric cosmological model in the presence of a source-free electromagnetic field coupled with mass less scalar field [36, 37] identified an expanding, shearing and non-rotating Universe. It is observed that the closed Universe correspond to quintessence while flat and open Universe corresponding to the phantom model of the Universe [38]. A realistic Universe dominated by matter has been obtained using two-fluid viscous dark energy models for an anisotropic general type of Bianchi space-time that is filled with barotropic and dark fluid in interacting and non-interacting modes with variable EoS parameter [39]. During investigations of the two-fluid Bianchi type-VI_0 anisotropic cosmological model coupled with the zero mass scalar field in Einstein's theory of gravitation, some authors [40] discovered that the cosmological constant decreased over time as the Universe expanded which supported by a recent finding from observations of type Ia supernova explosions (SNIa). Researchers [41] have explored modified $f(T)$ gravity two-fluid cosmological models and observed the expanding and shearing nature of the Universe. Some authors [42] studied both interacting and non-interacting cases while observing the matter and radiation fluids in the scale covariant theory of gravitation for Bianchi type I. Researchers [43] looked at a plane-symmetric cosmological model in $f(R,T)$ gravity with an interacting field as a source of energy and noticed that the pressure and density behaved differently in different models.

Energy conditions are fundamental for understanding concepts like black hole thermodynamics and the singularity theorem. The Raychaudhuri equations [44] provide an excellent model for describing the attractive nature of gravity and the positive energy present in the Universe. There are four different energy conditions: the null energy condition (NEC), weak energy condition (WEC), dominant energy condition (DEC), and strong energy condition (SEC). The weak energy condition states that the energy density measured by any observer should not be negative. It implies that the energy density must be greater than or equal to zero at all points in spacetime. On the other hand, the strong energy condition stipulates that the pressure observed by any observer should be less than or equal to the energy density, and the energy density itself should not be negative. In other words, the pressure should not counteract gravity. The dominant energy condition requires that the energy density measured by any observer must be positive, and the energy flux measurement must not be space-like. This means that the energy flow cannot exceed the speed of light, and the energy density at any point in spacetime must be greater than or equal to zero.

The article follows the following structure. Section II provides an introduction to the formalism of $f(R)$ gravity. Section III examines the field equations for the isotropic, flat, and homogeneous FLRW Universe. In Section IV, the solutions to the field equations for $f(R)$ gravity are obtained and calculations are performed for the Hubble parameter, average scale factor, spatial volume, and Scalar expansion. Section V discusses the energy conditions for various models of $f(R)$ gravity. Finally, Section VI presents a discussion of the findings and concludes the article.

2. FORMALISM OF $f(R)$ GRAVITY

A modification to the general theory of relativity is $f(R)$ gravity. The field equations of $f(R)$ gravity are obtained by varying Hilbert-Einstein action principle which is given by

$$S = \frac{1}{16\pi} \int f(R)\sqrt{-g}d^4x + \int S_m\sqrt{-g}d^4x \tag{1}$$

where $f(R)$ is a general function of Ricci scalar R and g is the determinant of g_{ij} and S_m is Lagrangian of matter.

The Ricci scalar R is obtained by contracting the Ricci tensor R_{ij} as

$$R = g^{ij}R_{ij} \tag{2}$$

Here the formulation of the Ricci tensor is given by

$$R_{ij} = \Gamma^p_{ij},_p - \Gamma^p_{ip},_j + \Gamma^p_{ij}\Gamma^q_{pq} - \Gamma^q_{ip}\Gamma^p_{jq} \tag{3}$$

where $\Gamma^\alpha_{\beta\gamma}$ represents the components of the renowned Levi-Civita connection as described by

$$\Gamma^i_{jk} = \frac{1}{2}g^{im}\left(g_{jm,k} + g_{km,j} - g_{jk,m}\right) \tag{4}$$

The corresponding field equations of $f(R)$ gravity are obtained by varying the action (1) with respect to g_{ij} as,

$$F(R)R_{ij} - \frac{1}{2}f(R)g_{ij} - \nabla_i\nabla_j F(R) + g_{ij}\square F(R) = T_{ij} \tag{5}$$

Where $\quad \square = \nabla_k\nabla^k$ and $F(R) = \frac{df(R)}{dR}$
Here ∇_i is the covariant derivative and T_{ij} is energy momentum tensor derived from the Lagrangian S_m.
The energy momentum tensor T_{ij} is given by

$$T_{ij} = \frac{-2}{\sqrt{-g}}\frac{\partial\left(\sqrt{-g}S_m\right)}{\partial g^{ij}} \tag{6}$$

3. FLRW METRIC AND FIELD EQUATIONS

The observational data from Cosmic Microwave Background (CMB) [45, 46] point out that our Universe is spatially flat at late times, therefore we considered the isotropic, flat and homogeneous FLRW metric as

$$ds^2 = dt^2 - a^2(t)\sum_{i=1}^{3}dx_i^2 \tag{7}$$

Where, a termed as cosmic scale factors used to measure the expansion of Universe, is a functions of time t only.

from equation (3), we obtained the non-zero components of Ricci tensor as

$$R_{00} = -3\frac{\ddot{a}}{a}, \quad R_{11} = R_{22} = R_{33} = -\left(2\dot{a}^2 + a\dot{a}\right) \tag{8}$$

Therefore, the resulting Ricci scalar R for the line element (7) is

$$R = 6\frac{\ddot{a}}{a} + 6\frac{\dot{a}^2}{a^2} = 6\left[\frac{\ddot{a}}{a} + \frac{\dot{a}^2}{a^2}\right] \tag{9}$$

Here $H = \frac{\dot{a}}{a}$ is a Hubble parameter.
We assume the gravitational field's energy source to be an interacting field with dark energy, which is coupling of a perfect fluid and a mass less scalar field for the metric (7) is given by

$$\overline{T_{ij}} = S_{ij} + T_{ij} \tag{10}$$

where S_{ij} represent an energy momentum tensor for perfect fluid distribution given by

$$S_{ij} = (p + \rho)u_iu_j - pg_{ij} \tag{11}$$

Here, p denotes the spatially isotropic pressure, ρ is the matter-energy density, and $u^i = (1, 0, 0, 0)$ represents the time-like four-velocity vector of the cosmic fluid satisfying $u^i u_i = 1$
and

$$T_{ij} = U_{,i} U_{,j} - \frac{1}{2} g_{ij} U_{,s} U^{,s} \tag{12}$$

The mass less scalar field (U) satisfies

$$g^{ij} U_{;ij} = \rho_c \tag{13}$$

where, U and ρ_c are mass less scalar field and charge density respectively depends on cosmic time (t) alone. Also semicolon (;) and comma (,) denotes covariant and partial derivative respectively
The Einstein field equations (5) for the cosmological model (7) using equation (10) are given by

$$\left[2\left(\frac{\dot{a}^2}{a}\right) + \frac{\ddot{a}}{a} \right] F(R) - \frac{1}{2} f(R) + 2\frac{\dot{a}}{a}\dot{F} + \ddot{F} = -p + \frac{\dot{U}^2}{2} \tag{14}$$

$$3\frac{\ddot{a}}{a} F(R) - \frac{1}{2} f(R) + 3\frac{\dot{a}}{a}\dot{F} = \rho - \frac{\dot{U}^2}{2} \tag{15}$$

An over-dot (.) denotes an ordinary derivative with respect to cosmic time t.

4. SOLUTIONS TO FIELD EQUATIONS

There are two linearly independent equations with four unknowns H, p, ρ and $\dot{U}$. Therefore to find above unknowns we have to use following plausible condition; The Hubble's parameter variation Bermann proposed in 1983, which provides the relationship between Hubble parameter and the average scale factor as,

$$H = ba^{-n} \tag{16}$$

where b is positive and $n \geq 0$ are constants.
from above equation we have

$$q = -a\frac{\ddot{a}}{\dot{a}^2} = n - 1 \tag{17}$$

where q is deceleration parameter.
Using equation (17) and equation (18) we obtained
Average scale factor as,

$$a(t) = (ct + d)^{\frac{1}{n}} \tag{18}$$

The Volume (V) is

$$V = a^3(t)$$

$$V = (ct + d)^{\frac{3}{n}} \tag{19}$$

The Hubble Parameter (H) is

$$H = \frac{\dot{a}}{a}$$

$$H = \frac{c}{n(ct + d)} \tag{20}$$

The Scalar expansion (θ) is

$$\theta = 3H$$

$$\theta = \frac{3c}{n(ct + d)} \tag{21}$$

where c and d are the constants of integration.
We have consider charge density $\rho_c = 0$
Therefore, the mass less scalar field is given by

$$U = c_1 \frac{a^4}{4} + c_2 = c_1 \frac{(ct + d)^{\frac{4}{n}}}{4} + c_2 \tag{22}$$

5. ENERGY CONDITIONS

To understanding geodesics of the Universe it is necessary to know the energy conditions (ECs), which are linear combinations of energy density and pressure. The well-known Raychaudhuri equations provide the foundation for energy conditions (ECs) which are of the form [43, 44, 45, 46]

$$\frac{d\theta}{d\tau} = -\frac{1}{3}\theta^2 - \sigma_{ij}\sigma^{ij} + \omega_{ij}\omega^{ij} - R_{ij}u^iu^j \tag{23}$$

$$\frac{d\theta}{d\tau} = -\frac{1}{2}\theta^2 - \sigma_{ij}\sigma^{ij} + \omega_{ij}\omega^{ij} - R_{ij}\eta^i\eta^j \tag{24}$$

where θ is the expansion factor, n^i is the null vector and σ^{ij} and ω_{ij} are shear and rotation respectively for the vector field u^i.

For attractive gravity, equations (23) & (24) satisfy the following conditions

$$R_{ij}u^iu^j \geq 0 \tag{25}$$

$$R_{ij}\eta^i\eta^j \geq 0 \tag{26}$$

Hence, the energy conditions derived from standard GR for perfect fluid matter distribution are

- Strong Energy Conditions (SEC) : $p + 3\rho \geq 0$

- Weak Energy Conditions (WEC) : $\rho \geq 0$, $p + \rho \geq 0$

- Null Energy Conditions (NEC) : $p + \rho \geq 0$

- Dominant Energy Conditions (DEC) : If $\rho \geq 0$, $|p| \leq \rho$

We have discussed the viability of energy conditions in two model.

5.1. $f(R) = R$

To illustrate how the aforementioned conditions can be employed to establish limits on $f(R)$ theories, we will present a specific example. In this case, we will focus on a particular family of theories characterized by the form of $f(R)$

$$f(R) = R \tag{27}$$

With choice of above functional form of $f(R)$ gravity, equation (5) reduced to field equation of G. R. Therefore, equation (14) & (15) are reduced to

$$p = -\frac{c^2}{n^2}\frac{(2n-3)}{(ct+d)^2} + \frac{c_1^2}{2}(ct+d)^{\frac{6}{n}} \tag{28}$$

$$\rho = \frac{1}{2}c_1^2(ct+d)^{\frac{6}{n}} - \frac{3c^2}{n^2}\frac{1}{(ct+d)^2} \tag{29}$$

SEC :

$$\rho + 3p = 2c_1^2(ct+d)^{\frac{6}{n}} + 6(1-n)\frac{c^2}{n^2}\frac{1}{(ct+d)^2} \geq 0 \tag{30}$$

WEC :

$$\rho + p = c_1^2(ct+d)^{\frac{6}{n}} - 2n\frac{c^2}{n^2}\frac{1}{(ct+d)^2} \geq 0$$

$$\rho = \frac{1}{2}c_1^2(ct+d)^{\frac{6}{n}} - \frac{3c^2}{n^2}\frac{1}{(ct+d)^2} \geq 0 \tag{31}$$

NEC :

$$\rho + p = c_1^2(ct+d)^{\frac{6}{n}} - 2n\frac{c^2}{n^2}\frac{1}{(ct+d)^2} \geq 0 \tag{32}$$

DEC :

$$\rho - p = 2(n-3)\frac{c^2}{n^2}\frac{1}{(ct+d)^2} \geq 0 \tag{33}$$

5.2. $f(R) = R + bR^m$

where m is an integer and b is a constant that can assume positive or negative values. To illustrate the energy conditions, we will assume in this subsection that the function $f(R)$ is an algebraic polynomial of R with the independent parameters b and m.

Using above functional form of $f(R)$ gravity, equation (14) & (15) yields,

$$
\begin{aligned}
p = & -\frac{c^2}{n^2}\frac{(2n-3)}{(ct+d)^2} + \frac{c_1^2}{2}(ct+d)^{\frac{6}{n}} \\
& - b(7-n)^{m-1}\left\{(2m-3)(2-n) + \frac{4c}{n(ct+d)}n^2 m(m-1)(2m-1)\right\}\left[\frac{c}{n(ct+d)}\right]^{2m}
\end{aligned}
\tag{34}
$$

$$
\rho = \frac{c^2}{n^2}\frac{3(1-n)}{(ct+d)^2} + \frac{c_1^2}{2}(ct+d)^{\frac{6}{n}} - 9mb6^{m-1}(2-n)^m(1+n+nm)\left[\frac{c}{n(ct+d)}\right]^{2(m+1)}
\tag{35}
$$

SEC :

$$
\begin{aligned}
\rho + 3p = & \frac{c^2}{n^2}\frac{3(4-3n)}{(ct+d)^2} + 2c_1^2(ct+d)^{\frac{6}{n}} - 9mb6^{m-1}(2-n)^m(1+n+nm)\left[\frac{c}{n(ct+d)}\right]^{2(m+1)} \\
& - 3b(7-n)^{m-1}\left\{(2m-3)(2-n) + \frac{4c}{n(ct+d)}n^2 m(m-1)(2m-1)\right\}\left[\frac{c}{n(ct+d)}\right]^{2m} \\
& \geq 0
\end{aligned}
\tag{36}
$$

WEC :

$$
\begin{aligned}
p + \rho = & \frac{c^2}{n^2}\frac{(6-5n)}{(ct+d)^2} + c_1^2(ct+d)^{\frac{6}{n}} - 9mb6^{m-1}(2-n)^m(1+n+nm)\left[\frac{c}{n(ct+d)}\right]^{2(m+1)} \\
& - b(7-n)^{m-1}\left\{(2m-3)(2-n) + \frac{4c}{n(ct+d)}n^2 m(m-1)(2m-1)\right\}\left[\frac{c}{n(ct+d)}\right]^{2m} \\
& \geq 0
\end{aligned}
$$

$$
\rho = \frac{c^2}{n^2}\frac{3(1-n)}{(ct+d)^2} + \frac{c_1^2}{2}(ct+d)^{\frac{6}{n}} - 9mb6^{m-1}(2-n)^m(1+n+nm)\left[\frac{c}{n(ct+d)}\right]^{2(m+1)} \geq 0
\tag{37}
$$

NEC :

$$
\begin{aligned}
p + \rho = & \frac{c^2}{n^2}\frac{(6-5n)}{(ct+d)^2} + c_1^2(ct+d)^{\frac{6}{n}} - 9mb6^{m-1}(2-n)^m(1+n+nm)\left[\frac{c}{n(ct+d)}\right]^{2(m+1)} \\
& - b(7-n)^{m-1}\left\{(2m-3)(2-n) + \frac{4c}{n(ct+d)}n^2 m(m-1)(2m-1)\right\}\left[\frac{c}{n(ct+d)}\right]^{2m} \\
& \geq 0
\end{aligned}
\tag{38}
$$

DEC :

$$
\begin{aligned}
\rho - p = & \frac{-c^2}{n}\frac{1}{(ct+d)^2} + c_1^2(ct+d)^{\frac{6}{n}} - 9mb6^{m-1}(2-n)^m(1+n+nm)\left[\frac{c}{n(ct+d)}\right]^{2(m+1)} \\
& + b(7-n)^{m-1}\left\{(2m-3)(2-n) + \frac{4c}{n(ct+d)}n^2 m(m-1)(2m-1)\right\}\left[\frac{c}{n(ct+d)}\right]^{2m} \\
& \geq 0
\end{aligned}
\tag{39}
$$

From the figure we have observed that,

- The physical characteristics, such as the mean scale factor, spatial volume, Hubble parameter, expansion scalar, pressure, and energy density, exhibit a dependence on cosmic time. As we approach the limit of $t \to 0$, these parameters assume constant values without variation.

- In present described model, the spatial volume (V) undergoes a remarkable transformation, commencing with a small value at the inception of Universe and progressively stretching towards an immeasurable magnitude as shown in Figure 1.This conspicuous phenomenon unequivocally signifies the extraordinary expansion of the Universe.
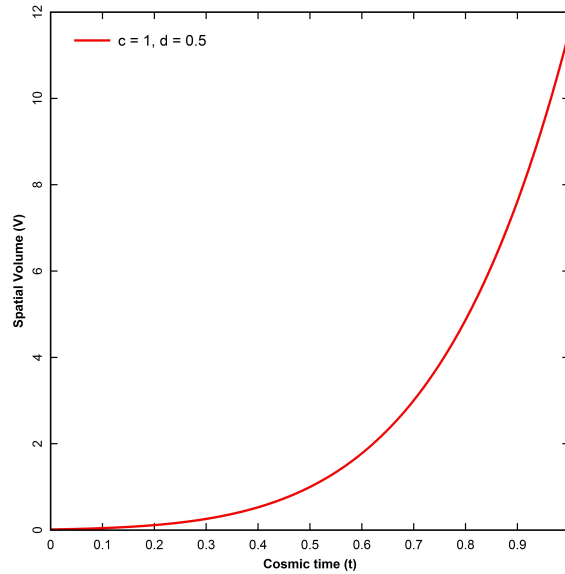
Figure 1. The behavior of Spatial Volume (V) against Cosmic Time (t) for the proper choice of constants: $c = 1$ & $d = 0.5$
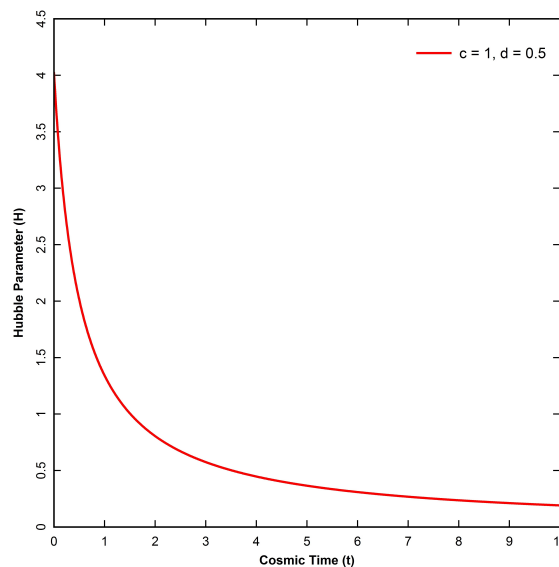

Figure 2. The behavior of Hubble parameter (H) against Cosmic Time (t) for the proper choice of constants: $c = 1$ & $d = 0.5$

- The Hubble parameter (H) represents the pace at which the Universe is expanding, signifying the fractional growth in its scale over a given unit of time. It possesses a positive value and exhibits a decreasing trend as time progresses. The expansion scalar offers insights into the expansion rate, revealing that it was more rapid during the initial stages and gradually decelerates in later phases, as depicted in Figure 2

- From Figure 3, it is observed that as time progresses, the mass less scalar field (U) also increases leading to expansion of the Universe. As time progresses, the scalar field gradually gains energy, resulting in an increasing mass which is responsible for the expansion rate of the Universe and overall cosmological evolution.

- The pressure exhibits a range of variation, shifting from significantly negative values to slightly negative values (as depicted in Figure 4 & 7). Furthermore, as time progresses towards infinity ($t \rightarrow \infty$), the pressure tends to approach zero. These observations hold true for both functional forms of $f(R)$ gravity, namely $f(R) = R$ & $f(R) = R + bR^m$, respectively. The negative nature of the pressure serves as an indicates presence of dark energy and energy density for both functional form of $f(R)$ models are increasing
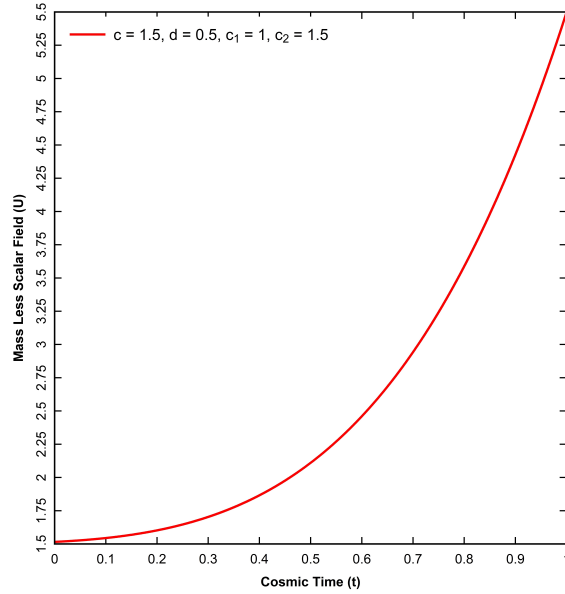
Figure 3. The behavior of Mass Less Scalar Field (U) against Cosmic Time (t) for the proper choice of constants: $c = 1, d = 0.5, c_1 = 1$ & $c_2 = 1.5$
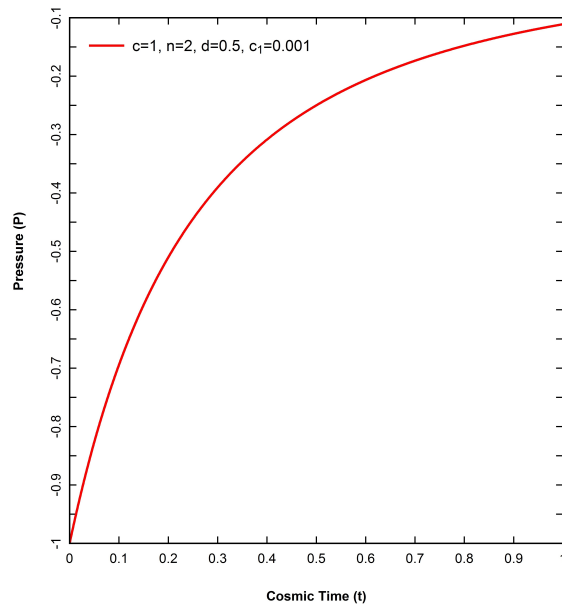

Figure 4. The behavior of energy pressure (p) for $f(R) = R$ against Cosmic Time (t) for the proper choice of constants: $c = 1, n = 2, d = 0.5$ & $c_1 = 0.01$

function of cosmic time (t) (Figure 5 & 8).

6. DISCUSSION & CONCLUSION

The $f(R)$ gravity offers an alternative explanation for the recent cosmic acceleration, by eliminating additional spatial dimensions or introducing exotic dark energy term. Also, different functional forms for $f(R)$ introduces a challenge in constraining the numerous theories of $f(R)$ gravity from a physical perspective.

In this this article we explored the FRW cosmological model in the presence of an interacting field. Specifically, we consider a scalar field that modifies the energy-matter content and influences the dynamics of Universe. We found that the expansion of Universe starts with a steady state and increases gradually. At a specific time, the Universe suddenly exploded and expanded to a large extent, which is consistent with the Big Bang scenario and agreed with recent observational data [1, 2]. It is observed that the Hubble parameter (H) initiates with a fixed value and gradually approaches zero as $t \to \infty$. Consequently, under such conditions, the Universe demon-
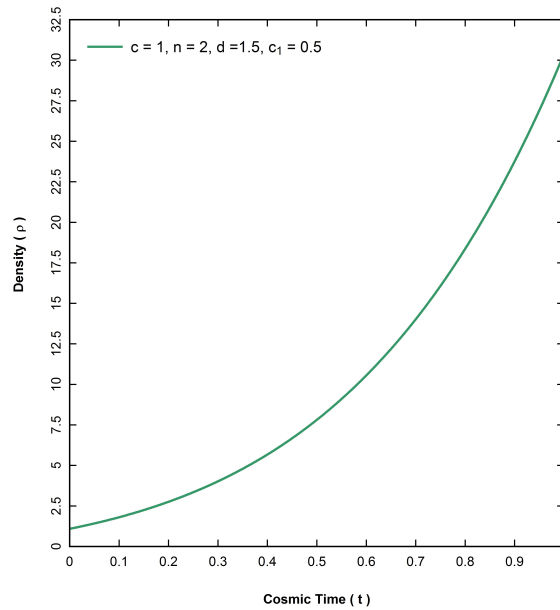
Figure 5. The behavior of energy Density (ρ) for for $f(R) = R$ against Cosmic Time (t) for the proper choice of constants: $c = 1, n = 2, d = 1$ & $c_1 = 0.5$
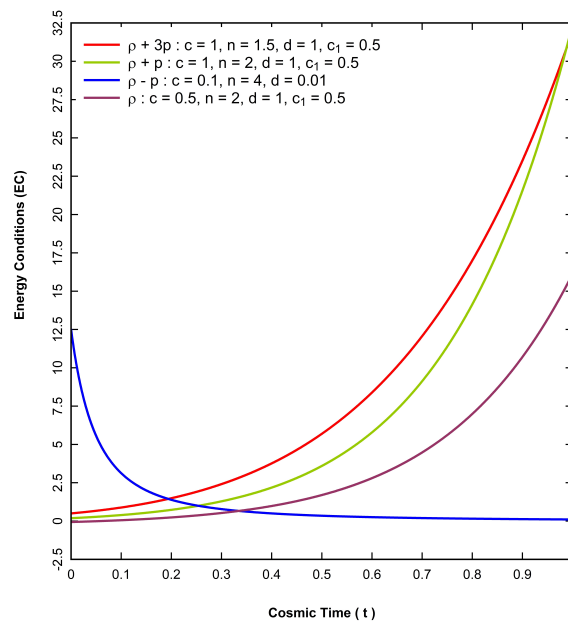

Figure 6. The behavior of Energy Conditions for $f(R) = R$ against Cosmic Time (t) for the proper choice of constants: c, n, d & c_1

strates a tendency towards de-Sitter space in an asymptotic manner. Concurrently, the deceleration parameter (q) remains constant, acquire negative value when $0 < n < 1$ which value signifies the accelerated expansion of the Universe. The energy density remains consistently positive and exhibits an upward trend as cosmic time progresses while the pressure associated with dark energy is increases negatively as time passes.Investigating energy conditions based on the behaviour of matter and energy under gravitational theories allows researchers to study the characteristics, evolution, and future of the Universe. These circumstances are strong tools for exploring basic physics ideas and understanding the intricate dynamics of our cosmos.

In this article, we have provided insights into a particular inquiry by exploring various limitations imposed on general $f(R)$ gravity, focusing on the energy conditions. By utilizing Raychaudhuri's equation and the essential criterion of gravitational attraction, we establish the SEC, WEC, NEC and DEC within the framework of $f(R)$ gravity. Our findings reveal that while these conditions bear resemblance to those derived in the general relativity.Based on our observations, in the present study, we find that the strong energy condition (SEC),
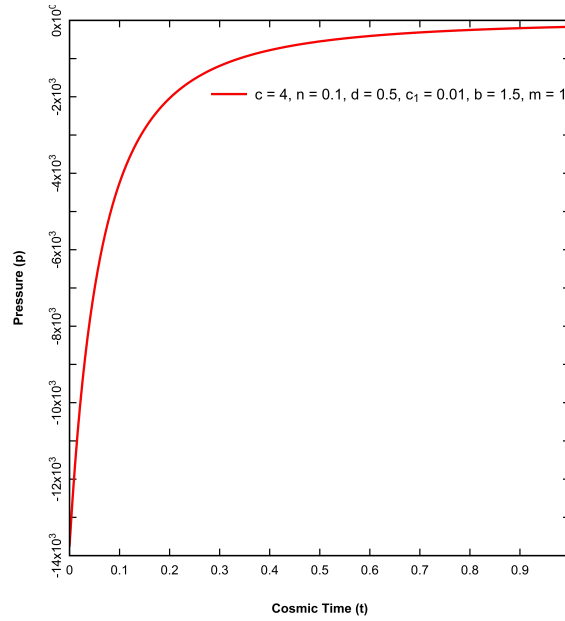
Figure 7. The behavior of energy pressure (p) for $f(R) = R + bR^m$ against Cosmic Time (t) for the proper choice of constants: $c = 4, n = 0.1, d = 0.5, c_1 = 0.01, b = 1.5$ & $m = 1$
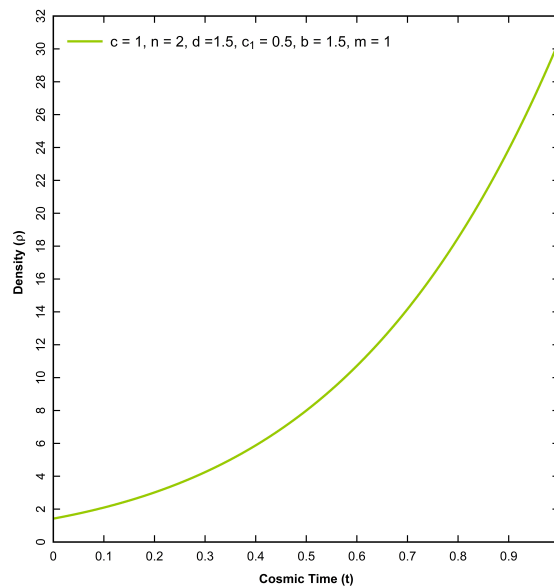

Figure 8. The behavior of energy Density (ρ) for $f(R) = R + bR^m$ against Cosmic Time (t) for the proper choice of constants: $c = 1, n = 2, d = 1.5, c_1 = 0.5, b = 1.5$ & $m = 1$

represented by the inequality $\rho + 3p \geq 0$, is satisfied for both the functional forms of $f(R)$. This result indicates that the model under consideration is non-singular, as the SEC imposes restrictions on the energy density ρ with the pressure p to ensure non-negative values.

Furthermore, our analysis reveals that the weak energy condition (WEC), given by the inequality $\rho \geq 0$, is also satisfied. This condition indicates that the energy density is non-negative, confirming the physical viability of the model. These conclusions can be observed from equations (29) and (35), which provide further evidence for the fulfillment of the WEC in the present study.

Moreover, we investigate the null energy condition (NEC), expressed as $\rho + p \geq 0$. Our findings demonstrate that the NEC is preserved for both functional forms of $f(R)$. This preservation of the NEC is evident from equations (32) and (37), reinforcing the consistency of the model with regard to the NEC. Additionally, our study reveals that the dominant energy condition (DEC), defined as $\rho - p \geq 0$, is also preserved. The preservation of the DEC, as indicated by equations (33) and (39), suggests an accelerated expansion of the Universe. In summary, our observations (from Figure 6 & Figure 9) shows that the present model satisfies the SEC, WEC,
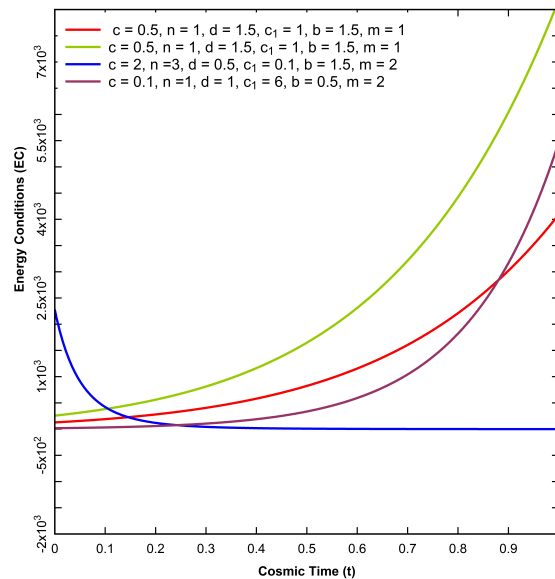
Figure 9. The behavior of Energy Conditions for $f(R) = R + bR^m$ against Cosmic Time (t) for the proper choice of constants: c, n, d, c_1, b & m

NEC and DEC also agreed with results of [47, 48, 49] for WEC, NEC and DEC . This indicates the non-singular nature of the model, ensures non-negative energy densities, confirms the preservation of the NEC, and suggests an accelerated expansion of the Universe. These results contribute to our understanding of the energy conditions in the context of $f(R)$ gravity and provide valuable insights into the behavior of matter and evolution of the Universe within this modified gravitational framework.

ORCID

🆔 **Vasudeo Patil**, https://orcid.org/0000-0002-0442-3962; 🆔 **Jeevan Pawde**, https://orcid.org/0000-0001-8068-6265; 🆔 **Rahul Mapari**, https://orcid.org/0000-0002-5724-9734; 🆔 **Pravin Bolke**, https://orcid.org/0000-0002-1212-5260

REFERENCES

[1] A.G. Riess, et al., Astron. J. **116**, 1009 (1998). https://doi.org/10.1086/300499

[2] S. Perlmutter, et al., Astrophys. J. **517**, 565 (1999). https://doi.org/10.1086/307221

[3] C.L. Bennet, et al., Astrophys. J. Suppl. **148**, 1 (2003). https://doi.org/10.1086/377253

[4] A.G. Riess, et al., Astrophys. J. **607**, 665 (2004). https://doi.org/10.1086/383612

[5] D.J. Eisenstein, et al. Astrophys. J. **633**, 560 (2005). https://doi.org/10.1103/RevModPhys.75.559

[6] P. Astier, et al., Astron. Astrophys. **447**, 31 (2006). https://doi.org/10.1051/0004-6361:20054185

[7] T. Padmanabhan, Phys. Rept. **380**, 235 (2003). https://doi.org/10.1016/S0370-1573

[8] P.J.E. Peebles, and B. Ratra, Rev. Mod. Phys. **75**, 559 (2003). https://doi.org/10.1103/RevModPhys.75.559

[9] S. Nojiri, and S. Odintsov, Phys. Rev. D, **68**, 123512 (2003). https://doi.org/10.1103/PhysRevD.68.123512

[10] R. Femaro, and F. Fiorini, Phys. Rev. D, **75**, 084031 (2007). https://doi.org/10.1103/PhysRevD.75.084031

[11] S. Nojiri, S. Odinstov, and P. Tretyakov, Prog. Theor. Phys. Suppl. **172**, 81 (2008). https://doi.org/10.1143/PTPS.172.81

[12] T. Harko, F.S.N. Lobo, S. Nojiri, and S.D. Odintsov, Phys. Rev. D, **84**, 024020 (2011). https://doi.org/10.1103/PhysRevD.84.024020

[13] H.A. Buchadahl, Mon. Not. Roy. Astron. Soc. **150**, 1 (1970). https://doi.org/10.1093/mnras/150.1.1

[14] S. Nojiri, and S.D. Odintsov, Int. J. Geom. Meth. Mod. Phys. **4**, 115 (2007). https://doi.org/10.1142/S0219887807001928

[15] T. Multamaki, and I. Vilja, Phys. Rev. D, **74**, 064022 (2006). https://doi.org/10.1103/PhysRevD.74.064022

[16] T. Multamaki, and I. Vilja, Phys. Rev. D, **76**, 064021 (2007). https://doi.org/10.1103/PhysRevD.76.064021

[17] M.F. Shamir, Astrophys. Space Sci, **330**, 183 (2010). https://doi.org/10.1007/s10509-010-0371-5

[18] M. Sharif, and H.R. Kausar, Phys. Lett. B, **697**, 1 (2011). https://doi.org/10.1016/j.physletb.2011.01.027

[19] M.F. Shamir, Int. J. Theor. Phys. **50**, 637 (2011). https://doi.org/10.1007/s10773-010-0587-8

[20] K.S. Adhav, Bulg. J. Phys. **39**, 197 (2012). https://www.bjp-bg.com/papers/bjp2012_3_197-206.pdf

[21] M.F. Shamir, and Z. Raza, Can. J. Phys. **93**, 1 (2015). https://doi.org/10.1139/cjp-2014-0338

[22] S.D. Katore, S.P. Hatkar, and R.J. Baxi, Found. of Phys. **46**, 409 (2016). https://doi.org/10.1007/s10701-015-9970-x

[23] S.R. Bhoyar, V.R. Chirde, and S.H. Shekh, Prespacetime J. **7**(3), 456 (2016). https://prespacetime.com/index.php/pst/article/viewFile/915/907

[24] M.V. Santhi, V.U.M. Rao and Y. Aditya, Can. J. Phys. **96**, 1 (2017). https://doi.org/10.1139/cjp-2017-0256

[25] A.V. Astashenok, S.D. Odintsov, and A. Cruz-Dombriz, Class. Quantum Grav. **34**, 205008 (2017). https://doi.org/10.1088/1361-6382/aa8971

[26] M.V. Santhi, Y. Sobhanbabu, and B.J.M. Raoz, J. Phys.: Conf. Ser. **1344**, 012038 (2019). https://doi.org/1088/1742-6596/1344/1/012038

[27] A.H. Hasmani, and A.M. Al-Haysah, Appl. Appl. Math, **14**, 334 (2019). https://digitalcommons.pvamu.edu/cgi/viewcontent.cgi?article=1717andcontext=aam

[28] S.D. Katore, and S.V. Gore, J. Astrophys. Astr. **41**, 12 (2020). https://doi.org/10.1007/s12036-020-09632-z

[29] A.M. Al-Haysah, and A.H. Hasmani, Heliyon, **7**(9), e08063 (2021). https://doi.org/10.1016/j.heliyon.2021.e08063

[30] V.U.M. Rao, M.V. Santhi, and Y. Aditya, Prespacetime J. **6**(6), 531-539 (2015). https://prespacetime.com/index.php/pst/article/download/749/752

[31] D.D. Pawar, V.J. Dagwal, and P.K. Agrawal, Malaya J. Mat. **4**(1), 111 (2016). https://www.malayajournal.org/articles/MJM16_14.pdf

[32] G.K. Goswami, A. Pradhan, M. Mishra, and A. Beesham, New Astronomy, **73**, 101284 (2019). https://doi.org/10.1016/j.newast.2019.101284

[33] S.V. Lohakare, F. Tello-Ortiz, S.K. Tripathy, and B. Mishra, Universe, **8**(12), 636 (2022). https://doi.org/10.3390/universe8120636

[34] V.R. Patil, J.L. Pawde, and R.V. Mapari, IJIERT, **9**, 4 (2022). https://dx.doi.org/10.17605/OSF.IO/QABKV

[35] D.D. Pawar, D.K. Raut, and W.D. Patil, Pramana J. Phys. **96**, 133 (2022). https://doi.org/10.1007/s12043-022-02364-5

[36] S.N. Bayskar, D.D. Pawar, and A.G. Deshmukh, Rom. Journ. Phys. **54**, 763 (2009). http://www.nipne.ro/rjp/2009_54_7-8.html

[37] D.D. Pawar, and R.V. Mapari, J. Dyn. Systems and Geom. Theories, **20**(1), 115-136 (2022). https://doi.org/10.1080/1726037X.2022.2079268

[38] B. Saha, H. Amirhashchi, and A. Pradhan, Astrophys. Space Sci. **342**, 257 (2012). https://doi.org/10.1007/s10509-012-1155-x

[39] V.R. Chirde, and S.H. Shekh, The African Rev. Phys. **9**, 0050 (2014). http://lamp.ictp.it/index.php/aphysrev/article/view/971/393

[40] J. Satish, and R. Venkateswarlu, Bulg. J. Phys. **46**, 67 (2019). https://www.bjp-bg.com/papers/bjp2019_1_067-079.pdf

[41] V.J. Dagwal, and D.D. Pawar, Mod. Phys. Lett. A, **35**(04), 1950357 (2020). https://doi.org/10.1142/S0217732319503577

[42] S.P. Hatkar, P. Agre, and S.D. Katore, Ann. Appl. Sci. **1**, 659 (2022). https://doi.org/10.55085/aas.2022.659

[43] A. Raychaudhuri, Phys. Rev. **98**, 1123 (1955). https://doi.org/10.1103/PhysRev.98.1123

[44] S. Nojiri, and S.D. Odintsov, Int. J. Geom. Methods Mod. Phys. **4**, 115 (2007). https://doi.org/10.1142/S0219887807001928

[45] N.W. Halverson, E.M. Leitch, and Pryke et. al., Astrophys. J. **568**, 38 (2002). https://doi.org/10.1086/338879

[46] J. Ehlers, Int. J. Mod. Phys. D, **15**, 1573 (2006). https://doi.org/10.1142/S0218271806008966

[47] S. Mandal, P.K. Sahoo, and J.R.L. Santos, Physical Review D, **102**(2), 024057 (2020). https://doi.org/10.1103/PhysRevD.102.024057

[48] P.K. Sahoo, S. Mandal, and S. Arora, Astron. Nachr. **342**, 89 (2021). https://doi.org/10.1002/asna.202113886

[49] S.H. Shekh, V.R. Chirde, and P.K. Sahoo, Commun. Theor. Phys. **72**, 085402 (2020). https://doi.org/10.1088/1572-9494/ab95fd

ЕНЕРГЕТИЧНІ УМОВИ З ПОЛЕМ ВЗАЄМОДІЇ В f(R) ГРАВІТАЦІЇ

Васудео Патіл[a], **Дживан Павде**[a], **Рахул Мапарі**[b], **Правін Болке**[c]

[a] *Кафедра математики, мистецтв, науки та торгівлі коледжу, Чикхалдара, округ Амраваті (MS), Індія*

[b] *Кафедра математики, Державний інститут науки та гуманітарних наук Відарбха, Амраваті (MS), Індія*

[c] *Кафедра математики, Коледж інженерії та управління проф. Рама Меге, Амраваті (MS), Індія*

У поточному контексті сценарію вкрай важливо дивитися за межі теорії Ейнштейна, яка відкриває двері до спеціально модифікованих теорій гравітації. Отже, дане дослідження присвячене дослідженню різних енергетичних умов, зокрема сильних енергетичних умов (SEC), слабких енергетичних умов (WEC), нульових енергетичних умов (NEC) і домінуючих енергетичних умов (DEC), що відповідають різним функціональним формам f(R) сила тяжіння. Ми досліджували плоскі, ізотропні та однорідні космологічні моделі FLRW, заповнені полем взаємодії, тобто; ідеальна рідина поєднується з безмасовим скалярним полем для різних моделей модифікованої f(R) гравітації, в якій R є скаляром Річчі. Ми спостерігали прискорене розширення Всесвіту, що відповідає останнім даним спостережень.

Ключові слова: *космологічна модель FLRW; гравітація f(R); взаємодіюче поле; закон Хаббла*

A STUDY OF EVOLUTION OF COSMOLOGICAL PARAMETERS BASED ON DARK ENERGY MODELS IN KALUZA-KLEIN FRAMEWORK†

Sudipto Roy[a,*], **Asmita Das**[b,†], **Anwesha Dey**[b,§], **Debolina Biswas**[b,#], **Sudipto Saha Roy**[b,‡]

[a]Department of Physics, St. Xavier's College, Kolkata, West Bengal, India
[b]M.Sc. Student (2020-2022), Subject: Physics, St. Xavier's College, Kolkata, India
[†]e-mail: asmita.das.0098@gmail.com, [§]e-mail: anwesha230798@gmail.com,
[#]e-mail: debolinabiswas699@gmail.com; [‡]e-mail: sudiptosaharoy1997@gmail.com
Corresponding Author e-mail: roy.sudipto@sxccal.edu
Received June 25, 2023; revised July 11, 2023; accepted July 12, 2023

The purpose of the present study is to determine the characteristics of time evolution of various cosmological quantities, based on four models constructed for a universe undergoing accelerated expansion. This formulation is done in the framework of Kaluza-Klein space-time, for zero spatial curvature. To solve the field equations, an ansatz is chosen for each model in such a way that it leads to a signature flip of the deceleration parameter, to ensure its consistency with recent astrophysical observations indicating a change from a decelerated expansion to an accelerated expansion of the universe. Based on these four models, time evolutions of several cosmological parameters are obtained and their variations are shown graphically against time. The arbitrary constants, associated with each model, are so tuned that the model correctly predicts the values of the Hubble parameter, deceleration parameter, energy density and gravitational constant at the present time. The findings from these models are consistent with each other, and they are in agreement with the observed features. The gravitational constant (G) shows a rapid fall in the early universe, followed by an extremely slow rise which continues at the present time. Taking (G) as a constant in two of the four models, the cosmological constant is found to be independent of time. A significant finding is that the signature flip of the deceleration parameter almost coincides with the signature flip of the cosmological constant (Λ), pointing towards a relation between the accelerated expansion and the dark energy which is represented by Λ. Other plots with respect to Λ also depict dark energy's role in governing cosmic evolution. Considering its dynamical nature, Λ is referred to as cosmological term (instead of cosmological constant) in the text. Contrary to the common trend of using arbitrary units, the SI units for all measurable quantities are used.

Keywords: *Kaluza-Klein Cosmology; Dark Energy; Cosmological constant; Gravitational constant; Cosmic Acceleration*
PACS: 04.20.−q; 04.50.+h; 04.50.−h; 98.80.Es; 98.80.−k

1. INTRODUCTION

Worldwide research in recent years, based on observational data, has proved beyond doubt that the universe is expanding with acceleration. It has caused a remarkable shift of the focus of research interests from a mere expansion to the mysteries of acceleration in the expansion process. Had gravitation been the only controlling force, which is attractive, the expansion would surely have been a decelerated one. An energy of an exotic form, designated as Dark Energy (DE), generating a negative pressure, is considered to be responsible for the cosmic acceleration, based on the experimental observations from supernova 1a [1, 2]. Extensive research is going on to find the characteristics of DE which remains a cosmological mystery. Based on recent research using supernova data, it has been found that the universe had changed its mode of expansion in the past, from deceleration to acceleration, causing a signature flip of the deceleration parameter from positive to negative [3-5]. One finds mainly two approaches of studying this field in the scientific literature to unravel the mysteries of the accelerated expansion of the universe. One of these approaches is to formulate models for dark energy and study their dynamics. Another approach is to construct cosmological models under the framework of modified theories of gravity (modified version of Einstein's theory) and study their dynamics. The cosmological constant (Λ) is regarded as the simplest candidate representing dark energy. There are other models like quintessence, phantom, k-essence and quintom which are known to account for dark energy [6-9]. Although Λ was used in the field equations by Einstein as a constant [10], it is presently regarded as a dynamical quantity due to certain limitations pertaining to Cosmological Problem and Coincidence Problem [11]. Einstein's theory of gravitation has undergone several modifications resulting in the birth new theories like f(R) and f(R,T) theories of gravity [12-14], and scalar tensor theories of gravitations such as Brans-Dicke (BD) and Saez-Ballester (SB) [15, 16]. Investigations of various types have been carried out in recent times by constructing DE cosmological models based on the above-mentioned theories [17-20].

Kaluza and Klein made an attempt to unify gravitational force with electro-magnetic force in the third decade of the twentieth century resulting into the formulation of Kaluza-Klein (KK) theory [21, 22]. There is an extra dimension, namely the fifth dimension, in the KK theory which was required to unify the two forces mentioned earlier. In the five dimensional model constructed by Chodos and Detweiler, it was shown that there is a contraction of the extra dimension due to cosmic evolution [23]. The present four-dimensional form of the universe is considered theoretically to be preceded by an era that required a multidimensional description. As time goes on, the extra dimensions shrink in

such a way that they no longer remain detectable by the experimental facilities at our disposal. This phenomenon has motivated many researchers to work in the field of cosmological models in higher dimensions. KK theory is essentially the theory of general relativity in five dimensions. Some of the authors who have carried out significant studies in five-dimensional space-time are Chodos & Detweller [23], Witten [24], Appelquist et al. [25], Appelquist & Chodos [26] and Marchiano [27]. One of the articles that attracted our attention to the formulation of DE models, based on Kaluza-Klein theory, is an investigation by Mukhopadhyay *et al.* [28].

To ensure the authenticity of predictions based on a theoretical formulation, one must construct more than one model (under the same framework) and validate them using some standard results obtained from observational data. An objective of the present work is to carry out a theoretical study, to determine the time dependence of some cosmological quantities, by constructing models with sufficient inter-model consistency. Another objective is to determine the dependence of cosmic evolution upon dark energy, represented here by the cosmological term (Λ). In order to fulfill the second objective, we aim to formulate expressions relating Λ with some parameters and also to examine graphically the variation of some parameters as functions of Λ.

For the present study, we have chosen the framework of the Kaluza-Klein space-time (with zero spatial curvature). The main theoretical formulation (described in Section 2) of our study is divided into two parts (A & B). The third part (Part-C) uses the results of the preceding parts to derive expressions involving Λ. Part-A has two models based on the assumption that the equation of state (EoS) parameter has a constant value (as in ref. no. 28). Part-B consists of two models formulated on an assumption that the gravitational term (G) is a constant quantity. Using these four models, we have determined the nature of time dependence of several cosmological quantities such as, scale factor (a), Hubble parameter (H), deceleration parameter (q), energy density (ρ), EoS parameter (ω), cosmological term (Λ), gravitational term (G) and $\dot{G}/G$. Part-A is based on two empirical expressions for Λ (for Models 1 & 2) and Part-B is based on two empirical expressions for H (for Models 3 & 4). Results of the studies, using these four models, are mostly in agreement with astrophysical observations regarding a universe expanding with acceleration. To ensure the authenticity or theoretical validity of each model, we have tuned the constant parameters (associated with each model) in a way such that the values of H_0, q_0, ρ_0 and G_0 obtained from the model are consistent with their presently accepted values. The symbols H_0, q_0, ρ_0 and G_0 denote respectively the values of H, q, ρ and G at the present time, i.e. $t = t_0$, where t_0 is the present age of the universe. Time dependence of several cosmological quantities has been shown graphically and they are consistent with the findings of other recent investigations, some of whom are based on theoretical frameworks or models different from ours.

An important feature of this study is that, unlike many other contemporary studies, we have used proper units (SI) for all measurable quantities (H, ρ, G), instead of plotting them in arbitrary units. To depict the time dependence of a parameter pictorially, we have plotted it graphically against t/t_0 (where t_0 is the present age of the universe, about 13.7×10^9 years). This way of graphical depiction is expected to give the readers a concrete picture of how a cosmological parameter evolves with time. A significant and unique finding of our study is that the change of sign of the deceleration parameter (indicating transition from deceleration to acceleration) occurs almost simultaneously with the signature flip of the cosmological term Λ (which represents dark energy) from negative to positive.

2. FIELD EQUATIONS AND MODELS

The metric of Kaluza-Klein space-time is given by,

$$ds^2 = dt^2 - a^2(t)\left[\frac{dr^2}{1-kr^2} + r^2 d\Omega^2 + (1 - kr^2)d\psi^2\right] \tag{1}$$

Here, $d\Omega^2 = d\theta^2 + sin^2\theta\, d\phi^2$ and $a(t)$ stands for the scale factor. The symbol k stands for the curvature parameter where we have $k = -1, 0, 1$ respectively for spatially open, flat and closed universe.

For a universe, which is constituted by a perfect fluid, the energy-momentum tensor is expressed as,

$$T_{\mu\nu} = (p + \rho)u_\mu u_\nu - p g_{\mu\nu} \tag{2}$$

Here, $\mu, \nu = 0,1,2,3,4$ and u_μ (five-velocity) satisfies the relation $u^\nu u_\nu = 1$. The symbols p and ρ denote, respectively, the pressure of the cosmic fluid and the energy density of the universe.

Einstein's field equations are expressed as,

$$R_{\mu\nu} - \frac{1}{2}R\, g_{\mu\nu} + \Lambda\, g_{\mu\nu} = 8\pi G\, T_{\mu\nu} \tag{3}$$

In equation (3), $R_{\mu\nu}$ and R denote the Ricci curvature tensor and Ricci scalar respectively. The symbol Λ denotes what was initially introduced by Einstein as cosmological constant. The symbol $g_{\mu\nu}$ denotes the metric tensor for general relativity and G stands for the gravitational constant. Considering their dynamical nature in Models 1 & 2, Λ and G have been referred to as the cosmological term and the gravitational term respectively in the present article.

Based on equations (1), (2) and (3), we obtain the following two equations from which the time dependence of the scale factor (a) can be determined.

$$8\pi G\rho + \Lambda = 6\left(\frac{\dot{a}^2}{a^2} + \frac{k}{a^2}\right) \tag{4}$$

$$8\pi Gp - \Lambda = -3\left(\frac{\ddot{a}}{a} + \frac{\dot{a}^2}{a^2} + \frac{k}{a^2}\right) \tag{5}$$

For a universe with zero spatial curvature (i.e., $k = 0$), equations (4) and (5) can be expressed as the following two equations respectively.

$$8\pi G\rho + \Lambda = 6\frac{\dot{a}^2}{a^2} = 6H^2 \tag{6}$$

$$8\pi Gp - \Lambda = -3\dot{H} - 6H^2 \tag{7}$$

We have used the expression for the Hubble parameter (H), i.e., $H = \frac{\dot{a}}{a}$, to obtain equations (6) and (7) from equations (4) and (5) respectively.

The continuity equation is given by,

$$\dot{\rho} + 4H(p + \rho) = 0 \tag{8}$$

For a barotropic equation of state, we have the following relation between pressure and density.

$$p = \omega\rho \tag{9}$$

Here ω is called the equation of state (EoS) parameter.
Using equation (9) in equation (7) we obtain,

$$8\pi G\omega\rho - \Lambda = -3\dot{H} - 6H^2 \tag{10}$$

Using equation (9) in equation (8) we obtain,

$$\dot{\rho} + 4H\rho(\omega + 1) = 0 \tag{11}$$

Combining equation (6) with equation (10) we obtain,

$$\dot{H} = \frac{(\omega+1)(\Lambda - 6H^2)}{3} \tag{12}$$

2.1. PART-A

In this part of our study, we assume the EoS parameter (ω) to be independent of time, as has been done in many recent studies, such as the one by Mukhopadhyay *et al*. [28]. Here we formulate two models (Models 1 & 2) based on two different empirical expressions for the cosmological parameter (Λ).

Solving equation (11) by integration we obtain the following expression for energy density (ρ).

$$\rho = C_1 a^{-4(\omega+1)} \tag{13}$$

where C_1 is the constant of integration. Its value can be determined by using the values of energy density (ρ) and the scale factor (a) at present time ($t = t_0$). Choosing a scale factor with $a(t_0) = 1$ we get $C_1 = \rho_0$ where ρ_0 denotes the value of ρ at $t = t_0$.

2.1.1. Model-1

Here we use the following ansatz for the cosmological term (Λ).

$$\Lambda = 6H^2 - \beta t^m \tag{14}$$

where β and m are constants.
Substituting equation (14) into equation (12) and integrating we obtain,

$$H = \frac{\dot{a}}{a} = -\frac{(1+\omega)\beta}{3}\frac{t^{m+1}}{m+1} \tag{15}$$

Integrating equation (15), the scale factor (a) is obtained as.

$$a = C_2 \exp\left[-\frac{\beta(1+\omega)}{3(m+1)(m+2)}t^{m+2}\right] \tag{16}$$

where C_2 is the constant of integration.
Using equation (16), the expression for the deceleration parameter is obtained as,

$$q = -\frac{a\ddot{a}}{\dot{a}^2} = -1 + \frac{3(m+1)^2}{\beta(1+\omega)} t^{-(m+2)} \tag{17}$$

Substituting equation (16) into equation (13) we obtain the following expression for the energy density (ρ).

$$\rho = D_1 \, exp\left[\frac{4\,\beta\,(1+\omega)^2}{3\,(m+1)\,(m+2)} t^{(m+2)}\right] \tag{18}$$

where $D_1 = C_1 C_2^{-4(\omega+1)}$.

Substituting equation (15) into equation (14), we get the following expression for the cosmological term (Λ).

$$\Lambda = 6\left[\frac{\beta\,(1+\omega)}{3\,(m+1)}\right]^2 t^{2\,(m+1)} - \beta t^m \tag{19}$$

Using equations (15), (18) and (19) in equation (6), we get the following expression for the gravitational term (G).

$$G = \frac{\beta}{8\pi D_1} t^m exp\left[-\frac{4\beta(1+\omega)^2}{3(m+1)(m+2)} t^{m+2}\right] \tag{20}$$

Using equation (20) we get the following expression for $\dot{G}/G$,

$$\frac{\dot{G}}{G} = mt^{-1} - \frac{4\beta(1+\omega)^2}{3(m+1)} t^{m+1} \tag{21}$$

2.1.2. Model-2

Here we use the following ansatz for the cosmological term (Λ).

$$\Lambda = 6H^2(1 + \alpha t^n) \tag{22}$$

where α and n are constants.

Substituting equation (22) in equation (12) and integrating we get,

$$H = \frac{\dot{a}}{a} = -\frac{(n+1)}{2\alpha(1+\omega)} t^{-(n+1)} \tag{23}$$

Integrating equation (23), the expression of the scale factor (a) is obtained as,

$$a = C_3 \, exp\left[\frac{n+1}{2\,\alpha\,n\,(1+\omega)} t^{-n}\right] \tag{24}$$

where the constant of integration is C_3.

Using equation (24), the deceleration parameter (q) is obtained as,

$$q = -1 - 2\alpha(1 + \omega)t^n \tag{25}$$

Substituting equation (24) into equation (13), we get the following expression for the energy density (ρ).

$$\rho = D_2 \, exp\left[-\frac{2(n+1)}{\alpha\,n} t^{-n}\right] \tag{26}$$

Here $D_2 = C_1 C_3^{-4(\omega+1)}$.

Substituting equation (23) into equation (22), the cosmological constant (Λ) is obtained as,

$$\Lambda = 6\left[\frac{(n+1)}{2\alpha(1+\omega)}\right]^2 t^{-2(n+1)}(1 + \alpha t^n) \tag{27}$$

Using equations (23), (26) and (27), in equation (6), the following expression is obtained for the gravitational term (G).

$$G = -\frac{3(n+1)^2}{16\pi D_2(1+\omega)^2\alpha} t^{-(n+2)} exp\left[\frac{2(n+1)}{\alpha n} t^{-n}\right] \tag{28}$$

Using equation (28), we get the following expression for $\dot{G}/G$.

$$\frac{\dot{G}}{G} = -(n+2)t^{-1} - \frac{2(n+1)}{\alpha} t^{-(n+1)} \tag{29}$$

2.2. PART-B

In this part of our study, we assume G to be independent of time, having a value of $G = 6.67 \times 10^{-11} \, Nm^2 Kg^{-2}$ (i.e., the value of the gravitational constant). This assumption is logically valid because the value of $\dot{G}/G$ is very small ($\approx 10^{-11} \, Yr^{-1}$ at $t = t_0$, as obtained from Models 1 & 2). Here we formulate two models based on two different empirical expressions for the Hubble parameter (H).

Using equations (6) and (10) we get,

$$\omega = -1 - \frac{3}{8\pi G\rho}\dot{H} \tag{30}$$

Substituting equation (30) into equation (11) we get,

$$\dot{\rho} = \frac{3H}{2\pi G}\dot{H} \tag{31}$$

Solving equation (31) for ρ by integration we obtain,

$$\rho = \rho_0 + \frac{3}{4\pi G}(H^2 - H_0^2) \tag{32}$$

In obtaining equation (32) from the solution of equation (31), we have used the fact that $H = H_0$ and $\rho = \rho_0$ at $t = t_0$ (the present time).

Substituting equation (32) into equation (6) we obtain the following expression for Λ.

$$\Lambda = 6H_0^2 - 8\pi G\rho_0 \tag{33}$$

Equation (33) shows that Λ is time independent.

Using the values of the parameters G, H_0 and ρ_0 in equation (33), we get $\Lambda = 1.768 \times 10^{-35}$. The values of different cosmological parameters (at $t = t_0$) used in this article are given in Section-3.

2.2.1. Model-3

In this model, we use the following ansatz for the Hubble parameter (H).

$$H = H_0 \left(\frac{t}{t_0}\right)^k \tag{34}$$

Here, k is a constant.

At $t = t_0$, the ansatz yields $H = H_0$.

Using equation (34), we get the following expression for the deceleration parameter.

$$q = -1 - \frac{\dot{H}}{H^2} = -1 - \frac{k}{H_0 t_0}\left(\frac{t}{t_0}\right)^{-(k+1)} \tag{35}$$

Using the fact that $q = q_0$ at $t = t_0$, we get,

$$k = -H_0 t_0 (1 + q_0) \tag{36}$$

Substituting equation (34) into equation (32) we get the following expression for the energy density.

$$\rho = \rho_0 + \frac{3H_0^2}{4\pi G}\left[\left(\frac{t}{t_0}\right)^{2k} - 1\right] \tag{37}$$

Using equations (34) and (37) in equation (30), we get the EoS parameter (ω) as,

$$\omega = -1 - k\,\frac{3H_0}{8\pi G}\left(\frac{t^{k-1}}{t_0^k}\right)\left[\frac{1}{\rho_0 + \frac{3H_0^2}{4\pi G}\left[\left(\frac{t}{t_0}\right)^{2k} - 1\right]}\right] \tag{38}$$

Using the relation $H = \frac{\dot{a}}{a}$, equation (34) can be rewritten as,

$$\frac{\dot{a}}{a} = H_0 \left(\frac{t}{t_0}\right)^k \tag{39}$$

Solving the above equation by integration and taking $a = 1$ at $t = t_0$, we get,

$$a = Exp\left[\frac{H_0 t_0}{(k+1)}\left(\left(\frac{t}{t_0}\right)^{k+1} - 1\right)\right] \tag{40}$$

2.2.2 Model-4

In this model, we choose an ansatz for the Hubble parameter (H), which is given by,

$$H = \frac{\mu}{t} + \gamma \tag{41}$$

where γ and μ are arbitrary constants.

Using equation (41) we obtain the following expression for the deceleration parameter.

$$q = -1 + \frac{\mu}{(\mu + \gamma t)^2} \tag{42}$$

Using the fact that, $H = H_0$, $q = q_0$ at $t = t_0$, we obtain the following values of the parameters μ and γ (based on eqns. 41 and 42).

$$\mu = H_0^2 t_0^2 (1 + q_0) \tag{43}$$

$$\gamma = H_0 - \frac{H_0^2 t_0^2 (1 + q_0)}{t_0} \tag{44}$$

Substituting equation (41) into equation (32) we obtain the following expression for the energy density (ρ).

$$\rho = \rho_0 + \frac{3}{4\pi G}\left[\left(\gamma + \frac{\mu}{t}\right)^2 - H_0^2\right] \tag{45}$$

Substituting equation (41) and (45) into equation (30), we obtain the following expression for the EoS parameter (ω).

$$\omega = -1 + \frac{3\mu}{8\pi G t^2}\left[\frac{1}{\rho_0 + \frac{3}{4\pi G}\left[\left(\gamma + \frac{\mu}{t}\right)^2 - H_0^2\right]}\right] \tag{46}$$

Using the relation $H = \frac{\dot{a}}{a}$, equation (41) can be written in the following way,

$$\frac{\dot{a}}{a} = \frac{\mu}{t} + \gamma \tag{47}$$

Solving equation (47) by integration and using $a = 1$ for $t = t_0$, we get,

$$a = e^{\gamma(t - t_0)}\left(\frac{t}{t_0}\right)^{\mu} \tag{48}$$

2.3 PART-C
Expressions relating Λ with q and ρ based on Models 1 & 2

We know that Λ represents dark energy and its value is related with dark energy density [46]. In this part of the study we find relations connecting Λ to q and ρ, based on Part-A.

Combining equation (19) with equations (17) and (18), we get the following two equations relating Λ with q and ρ respectively.

$$\Lambda = 6\left[\frac{\beta(1+\omega)}{3(m+1)}\right]^2\left(\left[(q+1)\frac{\beta(1+\omega)}{3(m+1)^2}\right]^{\frac{-1}{m+2}}\right)^{2(m+1)} - \beta\left(\left[(q+1)\frac{\beta(1+\omega)}{3(m+1)^2}\right]^{\frac{-1}{m+2}}\right)^m \tag{49}$$

$$\Lambda = 6\left[\frac{\beta(1+\omega)}{3(m+1)}\right]^2\left(\left[\left(ln\left(\frac{\rho}{D_1}\right)\right)\left(\frac{3(m+1)(m+2)}{4\beta(1+\omega)^2}\right)\right]^{\frac{1}{m+2}}\right)^{2(m+1)} - \beta\left(\left[\left(ln\left(\frac{\rho}{D_1}\right)\right)\left(\frac{3(m+1)(m+2)}{4\beta(1+\omega)^2}\right)\right]^{\frac{1}{m+2}}\right)^m \tag{50}$$

Combining equation (27) with equations (25) and (26), we get the following two equations relating Λ with q and ρ respectively.

$$\Lambda = 6\left[\frac{(n+1)}{2\alpha(1+\omega)}\right]^2\left(\left(\frac{q+1}{-2\alpha(1+\omega)}\right)^{\frac{1}{n}}\right)^{-2(n+1)}\left(1 + \alpha\left(\left(\frac{q+1}{-2\alpha(1+\omega)}\right)^{\frac{1}{n}}\right)^n\right) \tag{51}$$

$$\Lambda = 6\left[\frac{(n+1)}{2\alpha(1+\omega)}\right]^2\left(\left[\left(ln\left(\frac{\rho}{D_2}\right)\right)\left(\frac{\alpha n}{-2(n+1)}\right)\right]^{-\frac{1}{n}}\right)^{-2(n+1)}\left(1 + \alpha\left(\left[\left(ln\left(\frac{\rho}{D_2}\right)\right)\left(\frac{\alpha n}{-2(n+1)}\right)\right]^{-\frac{1}{n}}\right)^n\right) \tag{52}$$

Equations (49) and (51) are expressions for the cosmological term (Λ) in terms of deceleration parameter (q), based on Models 1 and 2 respectively. Equations (50) and (52) are expressions for the cosmological term (Λ) in terms of energy density (ρ), based on Models 1 and 2 respectively.

3. RESULTS AND DISCUSSION
To find the time dependence of various cosmological quantities (a, H, q, ρ, G, Λ, ω, $\dot{G}/G$), one needs to know the values (or the permissible ranges of values) of the constant parameters associated with each of the four models constructed here. These values can be estimated from the considerations of the following requirements.
1) $a > 0$ by definition. Here we have chosen $a = 1$ at $t = t_0$,
2) $H > 0$ since the universe is expanding,
3) $\rho > 0$ by definition,

4) the values of H_0, q_0, ρ_0, G_0, which are obtained from the models, should be consistent with their currently accepted values obtained from observational data,

5) the time-variation of q, as obtained from these models, must be such that it undergoes a change of sign from positive to negative, to be consistent with the fact that the present accelerated expansion of the universe was preceded by a phase of deceleration [3-5].

The currently accepted values (in SI units) of some cosmological parameters, used in the present study are given below [29-31].

$$H_0 = 2.39 \times 10^{-18} \, sec^{-1}, q_0 = -0.55, \rho_0 = 9.90 \times 10^{-27} Kg \, m^{-3}, G_0 = 6.67 \times 10^{-11} N \, m^2 \, Kg^{-2}, t_0 = 4.34 \times 10^{17} \, sec.$$

Based on the five requirements, mentioned above, we have obtained the following set of values for the constant parameters associated with Models 1 & 2.

$$\alpha = -1.230 \times 10^{9}, \beta = 1.230 \times 10^{-9}, m = -1.467, n = -0.533, \omega = -0.535, C_1 = 9.9 \times 10^{-27}, C_2 = C_3 = 0.143.$$

Following values have been obtained for the constant parameters associated with the Models 3 & 4, using equations (36), (43) and (44).

$$k = -0.467, \mu = 0.484, \gamma = 1.274 \times 10^{-18}, \Lambda = 1.768 \times 10^{-35}$$

Figure 1 shows the time dependence of the scale factor (a), as obtained from Models 1, 2, 3, 4 respectively. These graphs manifest almost the same behavior for a, indicating clearly that it increases monotonically with time, which is appropriate for an expanding universe and it is found to be consistent with the findings of a recent study based on a different model in Kaluza-Klein framework [28].

Figure 2 shows the time dependence of the Hubble parameter (H), as obtained from Models 1, 2, 3, 4. These graphs are almost in agreement with each other, indicating a fall in the value of H with time, at a gradually decreasing rate. It is quite similar to the nature of time dependence of H as obtained from some other recent studies [28, 30, 31].
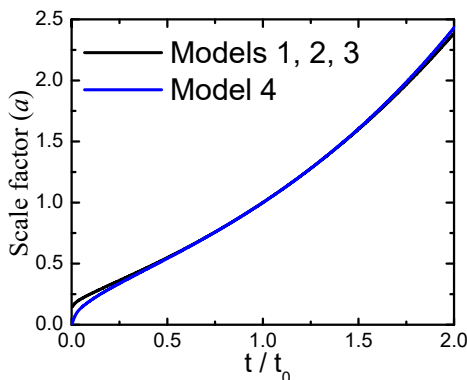

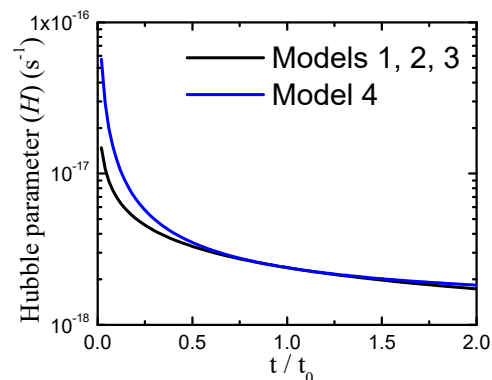**Figure 1.** Variation of scale factor (a) as a function of time for Models 1-4

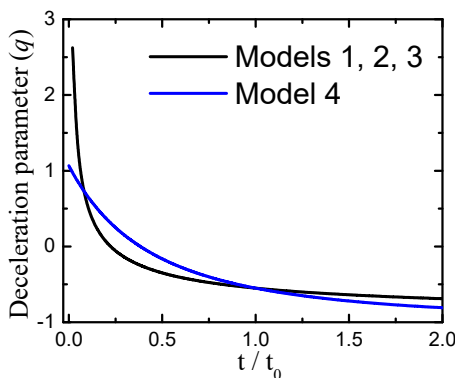**Figure 2.** Variation of Hubble parameter (H) as a function of time for Models 1-4

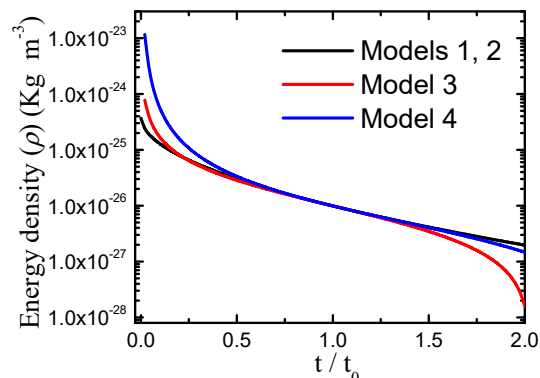**Figure 3.** Variation of deceleration parameter (q) as a function of time for Models 1-4

Figure 4. Variation of energy density (ρ) as a function of time for Models 1-4

Figure 3 shows the time variation of the deceleration parameter (q) for Models 1, 2, 3 and 4. Each of these graphs shows that q undergoes a signature flip from positive to negative, implying a change from a decelerated expansion to an

accelerated expansion, in absolute agreement with the results based on observational data [3-5]. It is observed that q is a monotonically decreasing function of time, with a gradually decreasing rate of change. These characteristics of q are similar to the results of some recent investigations based on various theoretical formulations [28, 30-32].

Figure 4 depicts the time evolution of the energy density (ρ) as obtained from Models 1, 2, 3 and 4. For a greater visual clarity of data, ρ has been plotted in the logarithmic scale. These plots show that it decreases with time with a decreasing rate of change. This behavior of ρ is in agreement with the results of some recent studies carried out by methods different from ours [28, 31, 32].

Figure 5 shows the time variation of the cosmological term (Λ), based on Models 1 and 2. It is observed that Λ is negative in the early universe. It increases very steeply with time initially, becoming asymptotic to a positive value which is nearly 1.59×10^{-35}. Here, the rate of increase of Λ is found to be very high in the early universe but it gradually decreases to a much smaller value. This observation is consistent with the results of some recent studies carried out by various methods [33-37].

According to the Models 3 & 4, Λ is independent of time (eqn. 33), with a value of 1.77×10^{-35}. It is important to note that the value of Λ at present time (i.e., $t = t_0$), obtained from Models 1 & 2, is 1.77×10^{-35}, which is the same as the value obtained from Models 3 & 4.
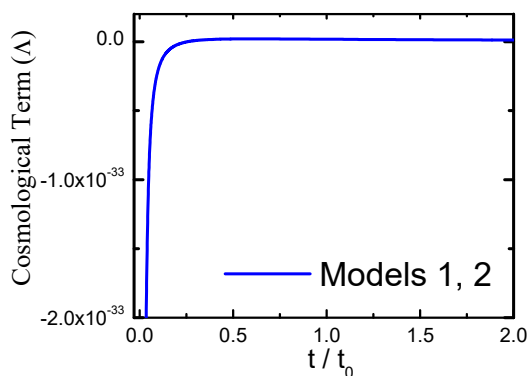

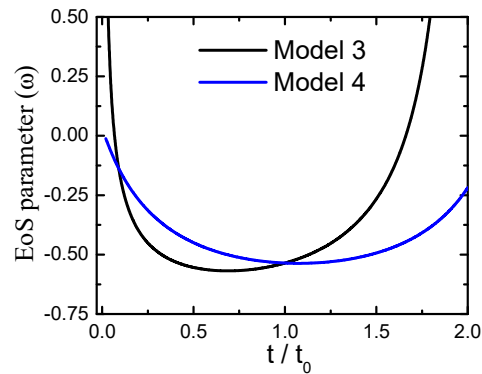**Figure 5.** Variation of cosmological term (Λ) as a function of time for Models 1 and 2

Figure 6. Variation of EoS parameter (ω) as a function of time for Models 3 and 4

Figure 6 shows the time variation of the EoS parameter (ω), as obtained from Models 3 and 4. It is observed that ω initially decreases and later increases with time for both models. This nature of time evolution is found to be close to the findings of some recent investigations based on models of various types [38-40]. These figures show that its values are in the quintessence ($\omega > -1$) region over almost the entire span of time shown in these plots. According to these plots we have, $\omega_0 = -0.535$. It is observed that this value is the same as the one that we must set for ω, for Models 1 & 2 (where ω is a constant quantity), to ensure that the predictions from these models are in agreement with the observed features of the universe.
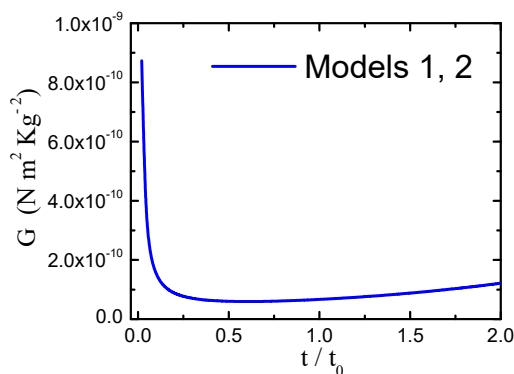

Figure 7. Variation of gravitational term (G) as a function of time for Models 1 and 2
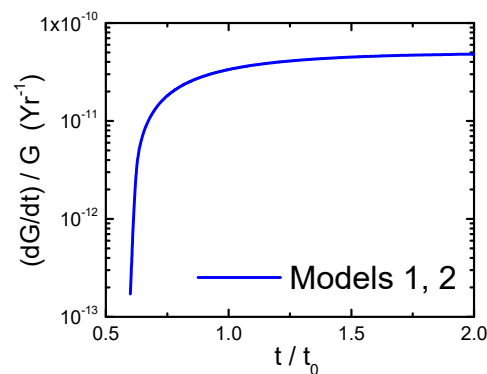

Figure 8. Variation of $\dot{G}/G$ as a function of time for Models 1 and 2

Figure 7 depicts the time variation of the gravitational term (G) based on Models 1 & 2. Each of these plots shows a steep fall in G in the early universe, followed by a slow rise. G is found to be increasing with time for almost the entire span of time shown in these plots. It is observed that G has a rising trend at the present time ($t = t_0$). There are several studies, conducted by different methods, where the gravitational term is found to increase with time [28, 41-44].

Figure 8 shows the time dependence of $\dot{G}/G$ as obtained from Models 1 and 2. In both plots, $\dot{G}/G$ is found to be increasing very steeply with time in the early universe, from negative to smaller negative values, at a gradually decreasing rate. Nearly at $t = 0.59t_0$, its sign changes from negative to positive. The value of $(\dot{G}/G)_{t=t_0}$ is $3.35 \times 10^{-11} \ Yr^{-1}$ for

both models. These values are consistent with those obtained from recent observations [45]. The positive sign of $(\dot{G}/G)_{t=t_0}$ corresponds to the fact that G is presently increasing with time, which is shown by Figure 7. It is evident from the values of $\dot{G}/G$ that we have an extremely slow change of G with time, where dG/dt is of the order of 10^{-21} (in $N\ m^2\ Kg^{-2}\ Yr^{-1}$) at the present time (i.e., $t = t_0$). Its smallness implies that the change of G is extremely slow. This observation justifies our decision to consider G to be independent of time for the calculations in Part-B of the present article.

The equation of state parameter (ω) is a very important tool to find the characteristics of the accelerated expansion of the universe. The values of ω, used in many studies, are 0, 1/3, 1 and −1, for respectively the pressure-less dust, radiation, stiff-fluid and vacuum-fluid dominated universe [46]. The ranges of values of ω, obtained from galaxy clustering statistics [47] and the observational results from SN 1a data [48], are $-1.33 < \omega < -0.79$ and $-1.67 < \omega < -0.62$ respectively. However, one does not necessarily have to regard ω to have a constant value. It can be regarded as a function of time [49, 50]. On account of the unavailability of observational results, one often uses a constant value of ω for calculations [51, 52], as we have done in Models 1 & 2 of this article.

Figure 9 depicts the variation of deceleration parameter (q) as a function of cosmological term (Λ). Here, a significant observation is that the time at which q changes its sign from positive to negative is almost the same as the time at which Λ changes its sign from negative to positive. This plot is based on the data generated by equations (49) and (51). This observation indicates that the transition from the phase of deceleration to the phase of acceleration is somehow connected to some phenomena involving dark energy which is regarded here as being represented by Λ.

Figure 10 shows the variation of energy density (ρ) with respect to the cosmological term (Λ). It is based on the data generated by equations (50) and (52). Here, we find that ρ decreases very rapidly after Λ changes its sign from negative to positive. It means that the rate of decrease of ρ with time is much greater than the rate of change of Λ at that stage of cosmic evolution, indicating a considerably faster expansion of the universe compared to the era of negative Λ. Like Figure 9, this figure also indicates a relation between the accelerated expansion and dark energy whose density is estimated in terms of the value of Λ [46].
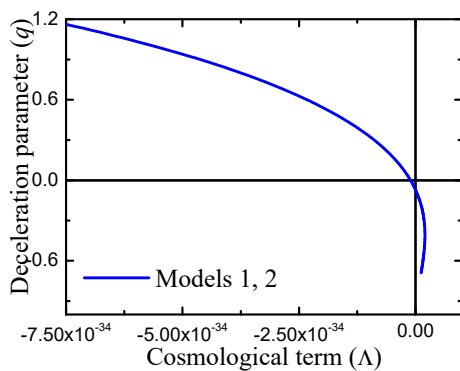

Figure 9. Variation of deceleration parameter (q) as a function of cosmological term (Λ) for Models 1, 2
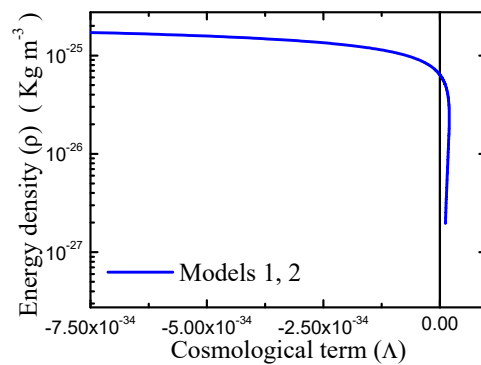

Figure 10. Variation of energy density (ρ) as a function of cosmological term (Λ) for Models 1, 2

Figures 11 and 12 show, respectively, the variations of Hubble parameter (H) and the cosmic expansion rate ($da/dt \equiv aH$) with respect to the cosmological term (Λ). In each of these two figures, it is observed that, the evolution of the dependent variable becomes much faster as the cosmological term (Λ) undergoes a signature flip from negative to positive. This behaviour may be regarded as a manifestation of acceleration in the expansion process controlled by dark energy (represented here by Λ). Quite significantly, the signature flip of Λ is found to be almost coincident with the signature flip of the deceleration parameter, as depicted by Figure 9.

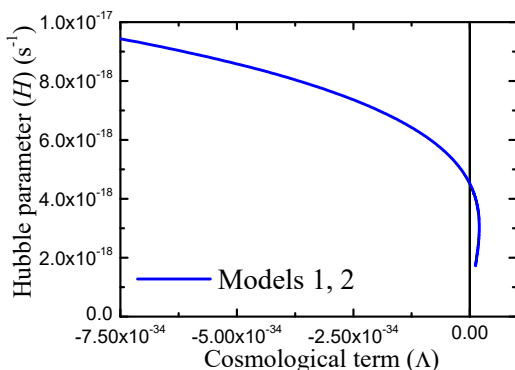**Figure 11.** Variation of Hubble parameter (H) as a function of cosmological term (Λ) for Models 1, 2
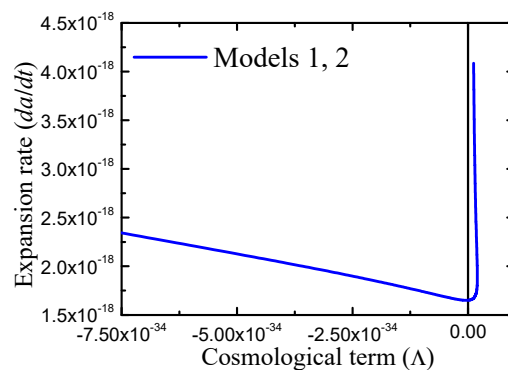

Figure 12. Variation of cosmic expansion rate ($\dot{a} \equiv aH$) as a function of cosmological term (Λ) for Models 1, 2

4. CONCLUSIONS

In the framework of Kaluza-Klein space-time, with zero spatial curvature, we have constructed four theoretical models based on four different ansatzes, and the results of this investigation have been depicted graphically. According to each of these four models, the deceleration parameter is a function of time and it changes sign from positive to negative, implying a change from a phase of decelerated expansion to a phase of acceleration, which is consistent with the conclusions drawn from recent astrophysical observations [3-5]. These four models are consistent with each other in terms of the predictions made by them regarding the characteristics of time evolution of different cosmological quantities. The results of the present investigation are also consistent with the findings of several other studies, carried out under theoretical frameworks different from ours, as discussed in the previous section. In Models 1 & 2, the EoS parameter (ω) is regarded as a constant and its value is determined from the requirement that the models should account for the observed features of the universe with sufficient accuracy. These two models enabled us to determine the time dependence of the cosmological term (Λ) and the gravitational term (G) among other parameters. It is interesting to note that, Λ has come out to be independent of time in Models 3 & 4, where we have regarded G as a constant quantity. The value of Λ obtained here is the same as the value of Λ_0 (i.e., the value of the dynamical Λ term at $t = t_0$) obtained from the Models 1 & 2. Time dependence of ω has been obtained from Models 3 & 4. The value of ω_0 obtained here is the same as the value of constant ω estimated by Models 1 & 2. All these aspects show an inter-model consistency, confirming the authenticity of predictions based on these models. A notable finding is that the signature flip of the deceleration parameter happens simultaneously with the signature flip of the dynamical Λ term. Through the plots in Figures 9-12, we have made an attempt to demonstrate, in a simple way, the role played by dark energy (represented here by Λ) in controlling the evolution of various parameters that characterize an expanding universe. A unique feature of the present article is that we have shown graphically the time evolution of $\dot{G}/G$, whose value at $t = t_0$ has been obtained from observations in several ways, as discussed in details in an article by Ray et. al. [45]. The present work can be regarded as a mathematical exercise aimed at determining the characteristics of time dependence of various cosmological quantities, under the framework of Kaluza-Klein space-time and our findings are in accordance with the observed features of the expanding universe. These findings are based on four models which are mathematically simpler than many other studies we have come across. Unlike a common convention, our graphical depiction of time evolution of every parameter is with respect to t/t_0 (instead of just t in arbitrary units) which enables the reader to get the exact time at which the parameter attains a certain value. A limitation of the present work is that we have not been able assume any ansatz using which the time evolution of both ω and G can be determined from the same model. As a future extension of this study, we have plans to work with some new ansatzes in this regard and compare the results of investigations with those obtained observationally and also with those obtained here, making thereby an attempt to achieve an improvement over the present work. The present work might be helpful to other researchers for studying cosmic evolution under various other theoretical frameworks.

ORCID IDs
Sudipto Roy, https://orcid.org/0000-0002-8811-2511; **Asmita Das**, https://orcid.org/0009-0004-5235-6479
Anwesha Dey, https://orcid.org/0009-0005-3160-0150; **Debolina Biswas**, https://orcid.org/0009-0001-5184-812X
Sudipto Saha Roy, https://orcid.org/0009-0009-6809-5601

REFERENCES
[1] A. G. Riess, A. V. Filippenko, P. Challis, A. Clocchiatti, A. Diercks, P. M. Garnavich, R. L. Gilliland, et al., "Observational Evidence from Supernovae for an Accelerating Universe and a Cosmological Constant," Astron. J. **116**(3), 1009–1038 (1998). https://doi.org/10.1086/300499
[2] S. Perlmutter, G. Aldering, G. Goldhaber, R. A. Knop, P. Nugent, P. G. Castro, S. Deustua, et al., "Measurements of Ω and Λ from 42 High-Redshift Supernovae," Astrophys. J. **517**(2), 565–586 (1999). https://doi.org/10.1086/307221
[3] A. G. Riess, P. E. Nugent, R. L. Gilliland, B. P. Schmidt, J. Tonry, M. Dickinson, R. I. Thompson, et al., "The Farthest Known Supernova: Support for an Accelerating Universe and a Glimpse of the Epoch of Deceleration," Astrophys. J. **560**(1), 49–71 (2001). https://doi.org/10.1086/322348
[4] T. Padmanabhan and T. R. Choudhury, "A theoretician's analysis of the supernova data and the limitations in determining the nature of dark energy," Mon. Not. R. Astron. Soc. **344**(3), 823–834 (2003). https://doi.org/10.1046/j.1365-8711.2003.06873.x
[5] L. Amendola, "Acceleration at z > 1?" Mon. Not. R. Astron. Soc. **342**(1), 221–226 (2003). https://doi.org/10.1046/j.1365-8711.2003.06540.x
[6] B. Ratra, and P. J. E. Peebles, "Cosmological consequences of a rolling homogeneous scalar field," Phys. Rev. D **37**(12), 3406-3427 (1988). https://doi.org/10.1103/physrevd.37.3406
[7] T. Chiba, T. Okabe, and M. Yamaguchi, "Kinetically driven quintessence," Phys. Rev. D **62**(2) (2000). https://doi.org/10.1103/physrevd.62.023511
[8] E. Elizalde, S. Nojiri, and S. D. Odintsov, "Late-time cosmology in a (phantom) scalar-tensor theory: Dark energy and the cosmic speed-up," Phys. Rev. D **70**(4) (2004). https://doi.org/10.1103/physrevd.70.043539
[9] R. R. Caldwell, "A phantom menace? Cosmological consequences of a dark energy component with super-negative equation of state," Phys. Lett. B **545**(1-2), 23–29 (2002). https://doi.org/10.1016/s0370-2693(02)02589-3
[10] D. Janzen, "Einstein's cosmological considerations," (2014). https://arxiv.org/pdf/1402.3212.pdf
[11] J. M. Overduin and F. I. Cooperstock, "Evolution of the scale factor with a variable cosmological term," Phys. Rev. D **58**(4) (1998). https://doi.org/10.1103/physrevd.58.043506

[12] S. Nojiri, S. D. Odintsov, and S. Tsujikawa, "Properties of singularities in the (phantom) dark energy universe," Phys. Rev. D **71**(6) (2005). https://doi.org/10.1103/physrevd.71.063004

[13] S. Nojiri, S. D. Odintsov, and M. Sasaki, "Gauss-Bonnet dark energy," Phys. Rev. D **71**(12) (2005). https://doi.org/10.1103/physrevd.71.123509

[14] T. Harko, F. S. N. Lobo, S. Nojiri, and S. D. Odintsov, "f(R,T)gravity," Phys. Rev. D **84**(2) (2011). https://doi.org/10.1103/physrevd.84.024020

[15] C. Brans and R. H. Dicke, "Mach's Principle and a Relativistic Theory of Gravitation," Phys. Rev. **124**(3), 925–935 (1961). https://doi.org/10.1103/physrev.124.925

[16] D. Sáez and V. J. Ballester, "A simple coupling with cosmological implications," Phys. Lett. A **113**(9), 467–470 (1986). https://doi.org/10.1016/0375-9601(86)90121-0

[17] M. Kiran, D. R. K. Reddy, and V. U. M. Rao, "Minimally interacting holographic dark energy model in a scalar- tensor theory of gravitation," Astrophys. Space Sci. **354**(2), 577–581 (2014). https://doi.org/10.1007/s10509-014-2099-0

[18] Y. Aditya, V. U. M. Rao, and M. Vijaya Santhi, "Bianchi type-II, VIII and IX cosmological models in a modified theory of gravity with variable Λ," Astrophys. Space Sci. **361**(2) (2016). https://doi.org/10.1007/s10509-015-2617-8

[19] V. U. M. Rao, U. Y. D. Prasanthi, and Y. Aditya, "Plane symmetric modified holographic Ricci dark energy model in Saez-Ballester theory of gravitation," Results Phys. **10**, 469–475 (2018). https://doi.org/10.1016/j.rinp.2018.06.027

[20] Y. Aditya and D. R. K. Reddy, "FRW type Kaluza–Klein modified holographic Ricci dark energy models in Brans–Dicke theory of gravitation," Eur. Phys. J. C **78**(8) (2018). https://doi.org/10.1140/epjc/s10052-018-6074-8

[21] T. Kaluza, "On the Unification Problem in Physics," Int. J. Mod. Phys. D **27**(14), 1870001 (2018). https://doi.org/10.1142/s0218271818700017

[22] O. Klein, "Quantentheorie und fünfdimensionale Relativitätstheorie," Z. Für Phys. **37**(12), 895–906 (1926). https://doi.org/10.1007/bf01397481

[23] A. Chodos, and S. Detweiler, "Where has the fifth dimension gone?" Phys. Rev. D **21**(8), 2167–2170 (1980). https://doi.org/10.1103/physrevd.21.2167

[24] E. Witten, "Some properties of O(32) superstrings," Phys. Lett. B **149**(4-5), 351–356 (1984). https://doi.org/10.1016/0370-2693(84)90422-2

[25] A. Thomas, C. Alan, and P.G.O. Freund, 1936, editors, *Modern Kaluza-Klein theories,* (Addison-Wesley Pub. Co., Menlo Park, Calif, 1987). http://pi.lib.uchicago.edu/1001/cat/bib/719574

[26] T. Appelquist and A. Chodos, "Quantum Effects in Kaluza-Klein Theories," Phys. Rev. Lett. **50**(3), 141–145 (1983). https://doi.org/10.1103/physrevlett.50.141

[27] W. J. Marciano, "Time Variation of the Fundamental "Constants" and Kaluza-Klein Theories," Phys. Rev. Lett. **52**(7), 489–491 (1984). https://doi.org/10.1103/physrevlett.52.489

[28] U. Mukhopadhyay, I. Chakraborty, S. Ray, and A. A. Usmani, "A Dark Energy Model in Kaluza-Klein Cosmology," Int. J. Theor. Phys. **55**(1), 388–395 (2015). https://doi.org/10.1007/s10773-015-2672-5

[29] P. B. Pal, "Determination of cosmological parameters: An introduction for non-specialists," Pramana **54**(1), 79–91 (2000). https://doi.org/10.1007/s12043-000-0008-2

[30] G. K. Goswami, "Cosmological parameters for spatially flat dust filled Universe in Brans-Dicke theory," Res. Astron. Astrophys. **17**(3), 27 (2017). https://doi.org/10.1088/1674-4527/17/3/27

[31] A. Pradhan, G. Goswami, and A. Beesham, "The reconstruction of constant jerk parameter with f(R,T) gravity," J. High Energy Astrophys. **2023**. https://doi.org/10.1016/j.jheap.2023.03.001

[32] A. Pradhan, P. Garg, and A. Dixit, "FRW cosmological models with cosmological constant in f(R, T) theory of gravity," Can. J. Phys. **99**(9), 741–753 (2021). https://doi.org/10.1139/cjp-2020-0282

[33] G. P. Singh, A. Y. Kale, and J. Tripathi, "Dynamic cosmological 'constant'in brans dicke theory," Rom. Journ. Phys. **58**(1-2), 23-35 (2013). https://rjp.nipne.ro/2013_58_1-2/0023_0035.pdf

[34] A.K. Yadav, "Bianchi type V matter filled universe with varying Lambda term in general relativity," (2009). https://arxiv.org/abs/0911.0177

[35] M. Moksud Alam, "Kaluza-Klein Cosmological Models with Barotropic Fluid Distribution," Phys. & Astron. Int. J. **1**(3) (2017). https://doi.org/10.15406/paij.2017.01.00018

[36] G. P. Singh, B. K. Bishi, and P. K. Sahoo, "Scalar field and time varying cosmological constant in f (R, T) gravity for Bianchi type-I universe," Chin. J. Phys. **54**(2), 244–255 (2016). https://doi.org/10.1016/j.cjph.2016.04.010

[37] R. K. Tiwari, F. Rahaman, and S. Ray, "Five Dimensional Cosmological Models in General Relativity," Int. J. Theor. Phys. **49**(10), 2348–2357 (2010). https://doi.org/10.1007/s10773-010-0421-3

[38] S. K. Tripathy, B. Mishra, S. Ray, and R. Sengupta, "Bouncing universe models in an extended gravity theory," Chin. J. Phys. **71**, 610–622 (2021). https://doi.org/10.1016/j.cjph.2021.03.026

[39] H. Farajollahi, M. Setare, F. Milani, and F. Tayebi, "Cosmic dynamics in F(R,ϕ) gravity," Gen. Relativ. Gravit. **43**(6), 1657–1669 (2011). https://doi.org/10.1007/s10714-011-1148-z

[40] E. Aydiner, I. Basaran-Öz, T. Dereli, and M. Sarisaman, "Late time transition of Universe and the hybrid scale factor," Eur. Phys. J. C **82**(1) (2022). https://doi.org/10.1140/epjc/s10052-022-09996-2

[41] A. Pradhan, B. Saha, and V. Rikhvitsky, "Bianchi type-I transit cosmological models with time dependent gravitational and cosmological constants: reexamined," Indian J. Phys. **89**(5), 503–513 (2014). https://doi.org/10.1007/s12648-014-0612-5

[42] S. Kotambkar, G. P. Singh, and R. Kelkar, "Bulk Viscous Anisotropic Cosmological Models with Dynamical Cosmological Parameters G and Λ," Nat. Sci. **07**(04), 179–189 (2015). https://doi.org/10.4236/ns.2015.74021

[43] A. Pradhan, A. K. Pandey, and R. K. Mishra, "Bianchi type-I transit cosmological models with time dependent gravitational and cosmological constants," Indian J. Phys. **88**(7), 757–765 (2014). https://doi.org/10.1007/s12648-014-0472-z

[44] B. Saha, V. Rikhvitsky, and A. Pradhan, "Bianchi type-I cosmological models with time dependent gravitational and cosmological constants: An alternative approach," Rom. Journ. Phys. **60**(1-2), 3-14 (2015). https://rjp.nipne.ro/2015_60_1-2/RomJPhys.60.p3.pdf

[45] S. Ray, U. Mukhopadhyay, and S.B.D. Choudhury, "Dark energy models with a time-dependent gravitational constant," Int. J. Mod. Phys. D **16**(11), 1791–1802 (2007). https://doi.org/10.1142/s0218271807011097

[46] S. Ray, F. Rahaman, U. Mukhopadhyay, and R. Sarkar, "Variable Equation of State for Generalized Dark Energy Model," Int. J. Theor. Phys. **50**(9), 2687–2696 (2011). https://doi.org/10.1007/s10773-011-0766-2

[47] M. Tegmark, M. R. Blanton, M. A. Strauss, F. Hoyle, D. Schlegel, R. Scoccimarro, M. S. Vogeley, et al., "The Three-Dimensional Power Spectrum of Galaxies from the Sloan Digital Sky Survey," Astrophys. J. **606**(2), 702–740 (2004). https://doi.org/10.1086/382125

[48] A. Pradhan, and H. Amirhashchi, "Dark energy model in anisotropic Bianchi type-III space-time with variable EoS parameter," Astrophys. Space Sci. **332**(2), 441-448 (2010). https://doi.org/10.1007/s10509-010-0539-z

[49] V. M. Zhuravlev, "Two-component cosmological models with a variable equation of state of matter and with thermal equilibrium of components," J. Exp. Theor. Phys. **93**(5), 903-919 (2001). https://doi.org/10.1134/1.1427102

[50] P. J. E. Peebles, and B. Ratra, "The cosmological constant and dark energy," Rev. Mod. Phys. **75**(2), 559–606 (2003). https://doi.org/10.1103/revmodphys.75.559

[51] J. Kujat, A. M. Linn, R. J. Scherrer, and D. H. Weinberg, "Prospects for Determining the Equation of State of the Dark Energy: What Can Be Learned from Multiple Observables?" Astrophys. J. **572**(1), 1-14 (2002). https://doi.org/10.1086/340230

[52] M. Bartelmann, K. Dolag, F. Perrotta, C. Baccigalupi, L. Moscardini, M. Meneghetti, and G. Tormen, "Evolution of dark-matter haloes in a variety of dark-energy cosmologies," New Astron. Rev. **49**(2-6), 199-203 (2005). https://doi.org/10.1016/j.newar.2005.01.014

ДОСЛІДЖЕННЯ ЕВОЛЮЦІЇ КОСМОЛОГІЧНИХ ПАРАМЕТРІВ НА ОСНОВІ МОДЕЛЕЙ ТЕМНОЇ ЕНЕРГІЇ В ТЕОРІЇ КАЛУЦИ-КЛЯЙНА

Судіпто Рой[a], Асміта Дас[b], Анвеша Дей[b], Деболіна Бісвас[b], Судіпто Саха Рой[b]
[a]Кафедра фізики, коледж Св. Ксав'єра, Колката, Західна Бенгалія, Індія
[b]Магістр, студент (2020-2022), фізика, коледж Св. Ксав'єра, Колката, Індія

Метою цього дослідження є визначення характеристик часової еволюції різних космологічних величин на основі чотирьох моделей, побудованих для Всесвіту, що зазнає прискореного розширення. Це формулювання виконано в рамках простору-часу Калуци-Клейна для нульової просторової кривизни. Щоб розв'язати рівняння поля, для кожної моделі вибирається підхід таким чином, щоб це призвело до характерного перевороту параметра уповільнення, щоб забезпечити його узгодженість з нещодавніми астрофізичними спостереженнями, які вказують на зміну від уповільненого розширення до прискореного розширення Всесвіту. На основі цих чотирьох моделей отримані часові еволюції кількох космологічних параметрів і їх варіації показані графічно в залежності від часу. Довільні константи, пов'язані з кожною моделлю, налаштовані так, що модель правильно прогнозує значення параметра Хаббла, параметра уповільнення, щільності енергії та гравітаційної постійної в даний час. Висновки цих моделей узгоджуються один з одним, і вони узгоджуються з спостережуваними особливостями. Гравітаційна постійна (G) показує швидке падіння в ранньому Всесвіті, а потім надзвичайно повільне зростання, яке триває в даний час. Взявши G за константу в двох із чотирьох моделей, космологічна стала не залежить від часу. Важливим відкриттям є те, що характерний переворот параметра уповільнення майже збігається з характерним переворотом космологічної постійної (Λ), що вказує на зв'язок між прискореним розширенням і темною енергією, яка представлена Λ. Інші сюжети щодо Λ також зображають роль темної енергії в управлінні космічною еволюцією. Враховуючи його динамічну природу, Λ у тексті згадується як космологічний термін (замість космологічної постійної). Всупереч поширеній тенденції використання довільних одиниць, для всіх вимірних величин використовуються одиниці СІ.

Ключові слова: *космологія Калуци-Клейна; темна енергія; космологічна стала; гравітаційна стала; космічне прискорення*

RENYI HOLOGRAPHIC DARK ENERGY MODEL IN *f(R)* GRAVITY WITH HUBBLE'S IR CUT-OFF[†]

Kishor S. Wankhade[a#], Alfred Y. Shaikh[b$], Siraj N. Khan[c*]

aDepartment of Mathematics, Yashwantrao Chavan Arts and Science Mahavidyalaya, Mangrulpir Dist. Washim - 444403, India
bDepartment of Mathematics, Indira Gandhi Mahavidyalaya, Ralegaon - 445402, India
cProf. Ram Meghe College of Engineering and Management, Badnera, Amravati - 444701, India
#E-mail: wankhade.kishor@rediffmail.com; $E-mail: shaikh_2324ay@yahoo.com
*Corresponding Author e-mail: sirajnk2311@gmail.com
Received July 12, 2023; revised August 1, 2023; accepted August 1, 2023

In the present study, a homogeneous and anisotropic LRS Bianchi type-I universe model is considered with an interacting dark matter and Renyi holographic dark energy model (RHDE) in $f(R)$ gravity. The deceleration parameter (DP) shows a signature flipping for a universe which was decelerating in past and accelerating at present epoch. Therefore, the DP is a most physically justified parameter to analyze the solution of cosmological model. In order to find an exact solution of the field equations of the model, the shear scalar is considered to be proportional to the expansion scalar. We have considered $f(R) = bR^n$, the depiction model of $f(R)$ which is the function of Ricci scalar R. The physical and geometrical characteristics of the universe model have been studied.
Keywords: *f(R) Gravity; RHDE; dark matter; Cosmology; Bianchi type-I space-time*
PACS: 04.50.Kd; 95.35.+d; 95.36.+x; 98.80.-k

INTRODUCTION

Observational cosmic data show that our Universe is currently expanding at a faster rate [1–5]. Dark energy (DE), which has negative pressure and accounts for 70% of the exotic component, is what propels the universe's cosmic expansion [6–9]. To investigate the universe and its accelerated expansion, modified theories of gravity provide an alternative approach. Some appropriate characteristics of modified theories of gravity are found in [10]. In the literature, several modified theories, including $f(R)$ gravity [11–15], $f(T)$ gravity [16–20], and $f(G)$ gravity [21–23] have been proposed with the changes of the Einstein–Hilbert action. Many researchers have worked on modified theories of gravity in recent past on different aspects of Cosmology [24-34]. In fact, the Ricci scalar $f(R)$ theory uses a conventional Einstein-Hilbert action that contains an arbitrary function R. The authors of Nojiri et al. [35] provided a comprehensive overview of modified theories of gravitation. Theoretical models of workable dark energy are described in [36]. The Noether symmetry technique is used to show spherically symmetric solutions in [37]. The exact solutions of static spherically symmetric space-times in $f(R)$ gravity coupled to nonlinear electrodynamics have been studied by Hollenstein and Lobo [38]. $f(R)$ gravity has been studied by a number of researchers in various cosmological contexts [39–53].

Holographic dark energy (HDE) has a variety of characteristics that have been studied in [54–58]. In [59–61], the holographic concept serves as the foundation for the potential of HDE. The HDE theory is also a helpful approach for addressing the DE conundrum in [62]. It was put forth based on the quantum characteristics of black holes (BH), which have been thoroughly studied in the literature to research quantum gravity. Studying the cosmic ramifications of holographic dark energy is more natural because Newton's gravitational constant is made dynamical in the Scalar Tensor Theory. According to [63], the holographic principle refers to a system's entropy, which is determined by its surrounding surface area rather than its volume. If we assume that the infrared (IR) cutoff is equal to the size of the universe, then the holographic energy density is rather near to the dark energy density. We can discover the cosmological characteristics of the vacuum energy with the aid of the HDE theory. The decreased Planck mass $M_p^2 = 8\pi G$ and the numerical constant d are used to calculate the HDE energy density $\rho_{de} = 3d^2 M_p^2 L^{-2}$. Numerous investigations have examined the interaction of holographic dark energy with matter using various IR cutoffs, including particle horizons, future horizons, and Hubble horizons. The authors of [64] suggested an IR cut-off made up of local Hubble scale values and temporal derivative Hubble scales. Sheykhi et al. in [65] explore the astrophysical implications of New Holographic DE (NHDE) by using the Hubble radius $L = H^{-1}$ as the system's IR cutoff. Many extended entropy formalisms have been used to investigate cosmological and gravitational events, but Tsallis and Renyi entropies offer the most accurate universe model. Sharma-Mittal HDE is compatible with the expansion of the universe and it is stable whenever it dominates the cosmos. The horizon is assigned to the Tsallis and Renyi entropies to investigate the cosmic ramifications. The generalized entropies

have been used to develop three HDE models: the Tsallis HDE (THDE) [66], the Renyi HDE (RHDE) [67] and the Sharma-Mittal HDE (SMHDE) [68]. Jawad and colleagues studied the THDE, RHDE and SMHDE models [69]. Maity and Debnath have examined all the aforementioned HDE models as well as New Agegraphic DE (NADE) in the context of flat D-dimensional fractal Universe in loop quantum cosmology [70]. The same authors analysis of THDE, RHDE, and SMHDE in [71] used the Nojiri- Odinstov (NO) cut-off as the IR cut-off. In [72], Sharma and Dubey looked at the RHDE in relation to Brans-Dicke cosmology. An interacting model of the Renyi holographic dark energy in the Brans-Dicke theory of gravity was built by the authors in [73]. Numerous relativists have recently worked on RHDE in various cosmological contexts, as seen in [74-83].

The main goal for this work is to illuminate the cosmic expansion for a homogeneous and anisotropic LRS Bianchi type I universe model with an interacting dark matter and RHDE within the framework of $f(R)$ gravity by taking the Hubble horizon as a candidate for the IR-cutoff i.e., $L = 1/H$. The deceleration parameter (DP) shows a signature flipping for a universe which was decelerating in past and accelerating at present epoch. Therefore, the DP is a most physically justified parameter to analyze the solution of cosmological model. In order to find an exact solution of the field equations of the model, the shear scalar is considered to be proportional to the expansion scalar. We have considered $f(R) = bR^n$, the depiction model of $f(R)$ which is the function of Ricci scalar R.

$f(R)$ **GRAVITY FORMALISM**

The $f(R)$ gravity is one of the generalizations of the general theory of relativity. The three primary approaches to $f(R)$ gravity are "affine gravity", "Palatini formalism" and "metric approach". The action is varied with regard to the metric tensor and the connection used in the metric approach is a Levi-Civita connection. While in Palatini formalism, the metric and the connection are independent of one another and the two aforementioned parameters can vary on their own. In metric-affine $f(R)$ gravity, the metric tensor and connection both operate independently, with the assumption that the matter action also depends on the connection. Action in this theory is provided by

$$S = \int \sqrt{-g} \left(f(R) + L_m \right) d^4 x . \tag{1}$$

Here, g the metric determinant, L_m the matter Lagrangian and a general function $f(R)$ of the Ricci scalar are present. It should be noted that this action can be obtained simply by replacing R by $f(R)$ in the default Einstein-Hilbert action. From this action, the associated field equations are discovered as

$$F(R) R_{\mu\nu} - \frac{1}{2} f(R) g_{\mu\nu} - \nabla_\mu \nabla_\nu F(R) + g_{\mu\nu} \Box F(R) = -T_{\mu\nu} , \tag{2}$$

where $\Box \equiv \nabla^\mu \nabla_\mu$, $F(R) \equiv df(R)/dR$, $T_{\mu\nu}$ the standard matter energy momentum tensor is obtained from the Lagrangian L_m, and ∇_μ is the covariant derivative.

METRIC AND FIELD EQUATION COMPONENTS

Cosmologies with anisotropic models are being investigated in recent times. The spatially homogeneous and anisotropic Bianchi type models are more interesting because of their ability to explain the cosmic evolution in early phase of universe. More ever, Bianchi type models have simple mathematical forms. In this work, we are interested to explore $f(R)$ gravity using Locally Rotationally Symmetric (LRS) Bianchi type-I space-time. The line element is of the form

$$ds^2 = -dt^2 + A^2(t) dx^2 + B^2(t) \left[dy^2 + dz^2 \right], \tag{3}$$

where A and B are functions of cosmic time t only.
Consider the stress energy momentum tensor for interacting two fluid as

$$T_{\mu\nu} = \overline{T}_{\mu\nu} + \hat{T}_{\mu\nu} \tag{4}$$

where, $\overline{T}_{\mu\nu} = \rho_m u_\mu u_\nu$ and $\hat{T}_{\mu\nu} = (\rho_r + p_r) u_\mu u_\nu + p_r g_{\mu\nu}$, with comoving coordinates $u^\mu = (0,0,0,1)$ and $u^\mu u_\nu = -1$, where u^μ is the four velocity vector of the fluid, p_r is pressure of RHDE, ρ_m and ρ_r are energy densities of dark matter and RHDE respectively. Now we define some kinematical quantities of the space-time such as average scale factor and volume respectively as

$$a^3 = V = AB^2 . \tag{5}$$

The mean Hubble parameter, which expresses the volumetric expansion rate of the universe is

$$H = \frac{1}{3}\left(H_1 + H_2 + H_3\right),$$ (6)

where H_1, H_2 and H_3 are the directional Hubble parameters in the directions of x, y and z axes respectively. Anisotropy parameter, for discussing whether universe approach isotropy or not, is defined as

$$A_m = \frac{1}{3}\sum_{i=1}^{3}\left(\frac{H_i - H}{H}\right)^2.$$ (7)

The expansion scalar and shear scalar are respectively defined as

$$\theta = \frac{\dot{A}}{A} + 2\frac{\dot{B}}{B},$$ (8)

$$\sigma^2 = \frac{3}{2}H^2 A_m.$$ (9)

Here dot indicates a derivative with regard to time.
Using equations (2), (3), and (4), the field equations can be expressed as follows

$$\left(\frac{\ddot{A}}{A} + 2\frac{\dot{A}}{A}\frac{\dot{B}}{B}\right)F(R) + \frac{1}{2}f(R) + 2\frac{\dot{B}}{B}\dot{F} + \ddot{F} = p_r,$$ (10)

$$\left(\frac{\ddot{B}}{B} + \frac{\dot{B}^2}{B^2} + \frac{\dot{A}}{A}\frac{\dot{B}}{B}\right)F(R) + \frac{1}{2}f(R) + \left(\frac{\dot{A}}{A} + \frac{\dot{B}}{B}\right)\dot{F} + \ddot{F} = p_r,$$ (11)

$$\left(\frac{\ddot{A}}{A} + 2\frac{\ddot{B}}{B}\right)F(R) + \frac{1}{2}f(R) + \left(\frac{\dot{A}}{A} + 2\frac{\dot{B}}{B}\right)\dot{F} = -\left(\rho_m + \rho_r\right).$$ (12)

SOLUTION OF THE FIELD EQUATIONS

The deceleration parameter is defined in terms of the scale factor and scale factor is a function of time. So, it always motives the researchers to investigate the time dependent deceleration parameter rather than the constant deceleration parameter. Thus, we have interested to investigate the time dependent deceleration parameter. The deceleration parameter is defined as $q = -a\ddot{a}/\dot{a}^2$, where a is the average scale factor. We have considered the special form of time varying deceleration parameter $q = -1 + \beta/1 + a^\beta$, where $\beta > 0$ is a constant. Consequently, the Hubble's parameter is

$$H = 1 + a^{-\beta}.$$ (13)

Again, integrating the above equation, we have

$$a = \left(e^{\beta t + c} - 1\right)^{1/\beta}.$$ (14)

Using equation (5), we get $AB^2 = \left(e^{\beta t + c} - 1\right)^{3/\beta}$. Now, in order to solve the field equations, we take into account that expansion scalar is proportional to shear scalar [84-85] which results as $A = B^m$ where $m > 1$ is an arbitrary constant. Hence, we get

$$A = \left(e^{\beta t + c} - 1\right)^{\frac{3m}{\beta(m+2)}},$$ (15)

$$B = \left(e^{\beta t + c} - 1\right)^{\frac{3}{\beta(m+2)}},$$ (16)

Using equations (15) and (16), the metric in (3) filled with the fluid in (4) in the framework of $f(R)$ gravity becomes

$$ds^2 = -dt^2 + \left(e^{\beta t + c} - 1\right)^{\frac{6m}{\beta(m+2)}}dx^2 + \left(e^{\beta t + c} - 1\right)^{\frac{6}{\beta(m+2)}}\left[dy^2 + dz^2\right].$$ (17)

TWO FLUIDS INTERACTING MODEL

When dark matter and holographic Renyi dark energy interact, the overall energy density fulfils the continuity equation as $(\dot{\rho}_m) + (\dot{\rho}_r) + 3H(\rho_m + \rho_r + p_r) = 0$. However, when their individual energy densities do not conserve, the equation for the continuity of matter becomes [86],

$$(\dot{\rho}_m) + 3H(\rho_m) = Q, \tag{18}$$

$$(\dot{\rho}_r) + 3H(\rho_r + p_r) = -Q. \tag{19}$$

The quantity $Q \geq 0$, expresses the interaction (for $Q > 0$) and non-interaction ($Q = 0$) term between RHDE and dark matter components. Since we are interested in investigating the interaction between RHDE and dark matter, it should be noted that an ideal interaction term must be motivated from the theory of quantum gravity. In the absence of such a theory, we rely on pure dimensional basis for choosing an interaction Q. In our work, we consider the interacting term as $Q = 3\kappa H \rho_m$, where κ is the coupling constant to determine its appropriateness.

DYNAMICAL PROPERTIES OF THE MODEL

The average scale factor and spatial volume are respectively obtained as

$$a = \left(e^{\beta t + c} - 1\right)^{1/\beta}, \tag{20}$$

$$V = a^3 = \left(e^{\beta t + c} - 1\right)^{3/\beta}. \tag{21}$$

The mean Hubble parameter and expansion scalar yield as

$$H = \frac{1}{\left(1 - e^{-(\beta t + c)}\right)}, \tag{22}$$

$$\theta = \frac{3}{\left(1 - e^{-(\beta t + c)}\right)}. \tag{23}$$

The anisotropy parameter is

$$A_m = \frac{2(m-1)^2}{(m+2)^2}. \tag{24}$$

The shear scalar is determined as

$$\sigma^2 = \frac{3(m-1)^2}{(m+2)^2} \frac{1}{\left(1 - e^{-(\beta t + c)}\right)^2}. \tag{25}$$
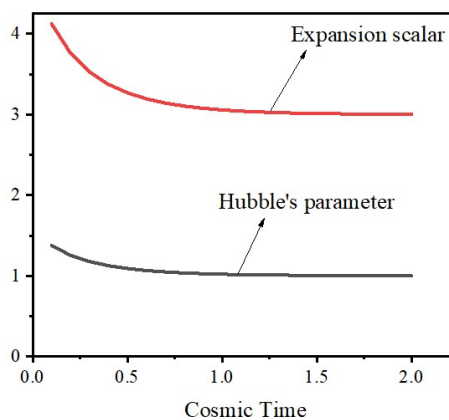

Figure 1. Hubble parameter and Expansion scalar versus cosmic time for $c = 1$, $m = 2$ and $\beta = 3$

It can be shown that the universe is expanding as cosmic time advances because both the average scale factor and spatial volume are rising. It is depicted from Figure 1 that the mean Hubble parameter is acting as a constant throughout the universe's expansion and that the expansion scalar gets less as cosmic time grows. Expansion scalar is constant because of $t \to \infty$. It implies that the universe's expansion is initially more rapid and then it slows down over time. Anisotropy

parameter is observed to be constant during the expansion of the universe and does not depend on cosmic time t in contrast to shear scalar, which is observed to depend on cosmic time and change over the course of the universe's evolution.

The deceleration parameter is obtained as

$$q = -1 + \beta e^{-(\beta t + c)} \tag{26}$$

The DP shows a transition of universe for $\beta > 1$ and again lies at an accelerating phase for $\beta \leq 1$. Summing up the results, it can be concluded that, the deceleration parameter plays a vital role in account of accelerated expansion of the universe. The model with time varying deceleration parameter represents an expanding universe in accelerated phase. From Figure 2, it is noted that the deceleration parameter, which reflects the typical accelerating expansion, $q \rightarrow -1$ is negative throughout the expansion of the universe. As cosmic time lengthens, recent theoretical observations are consistent with this scenario.
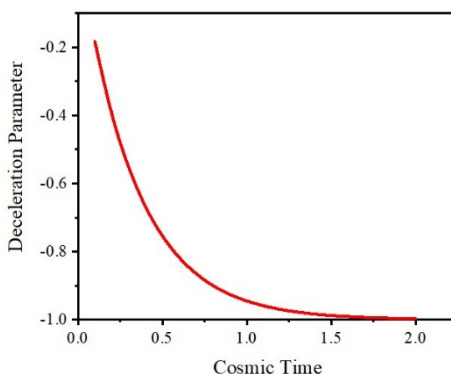

Figure 2. Deceleration parameter versus cosmic time for $c = 1$ and $\beta = 3$.

The Ricci scalar R is obtained as

$$R = \frac{(-6)}{M_1\left(1 - e^{-(\beta t + c)}\right)}\left(\beta M_1 + \frac{M_2}{\left(1 - e^{-(\beta t + c)}\right)}\right), \tag{27}$$

where $M_1 = (m + 2)^2$ and $M_2 = 3(m^2 + 2m + 3) - \beta(m + 2)^2$.

The depiction model of $f(R)$ is

$$f(R) = b\left\{\frac{(-6)}{M_1\left(1 - e^{-(\beta t + c)}\right)}\left(\beta M_1 + \frac{M_2}{\left(1 - e^{-(\beta t + c)}\right)}\right)\right\}^n. \tag{28}$$

Also,

$$F(R) = bn\left\{\frac{(-6)}{M_1\left(1 - e^{-(\beta t + c)}\right)}\left(\beta M_1 + \frac{M_2}{\left(1 - e^{-(\beta t + c)}\right)}\right)\right\}^{n-1}. \tag{29}$$

Energy density for RHDE has the form

$$\rho_r = \frac{3d^2}{8\pi L^2}\left(1 + \pi \delta L^2\right)^{-1},$$

with d and δ being constants [67], [69]. Here, by considering the Hubble horizon as a candidate for the IR-cutoff, i.e., $L = 1/H$, the energy density for RHDE from above equation is obtained as

$$\rho_r = \frac{3d^2}{8\pi}\frac{1}{\tau^2\left(1 + \pi \delta \tau^2\right)}, \tag{30}$$

where, $\tau = 1 - e^{-(\beta t + c)}$.

The isotropic pressure is

$$p_r = \frac{3}{(m+2)\tau}\left\{\left[\beta m + \frac{m(3m - \beta(m+2)+6)}{(m+2)\tau}\right]F + 2\dot{F}\right\} + \frac{1}{2}f + \ddot{F},$$ (31)

where

$$\dot{F} = -bn(n-1)\beta\left(\frac{-6}{M_1}\right)^{n-1}\left(\frac{1-\tau}{\tau}\right)\left(\beta M_1 + \frac{2M_2}{\tau}\right)\left(\beta M_1 + \frac{M_2}{\tau}\right)^{n-2},$$

and

$$\ddot{F} = \left\{\begin{array}{l} bn(n-1)\left(\frac{-6}{M_1}\right)^{n-1}\left(\frac{1-\tau}{\tau^n}\right)\left(\beta M_1 + \frac{M_2}{\tau}\right)^{n-3} \\ \left\{\left[\left(\beta M_1 + \frac{M_2}{\tau}\right)\left[2M_2\left(\frac{1-\tau}{\tau^2}\right) + \left(\beta M_1 + \frac{2M_2}{\tau}\right)\left(1 + 2\frac{(1-\tau)}{\tau}\right)\right] + (n-2)\left(\frac{1-\tau}{\tau}\right)\left(\beta M_1 + \frac{2M_2}{\tau}\right)^2\right]\right\} \end{array}\right\}$$

The RHDE equation of state parameter is found to be

$$\omega_r = \frac{8\pi}{3d^2}\tau^2\left(1 + \pi\delta\tau^2\right)\left\{\frac{3}{(m+2)\tau}\left\{\left[\beta m + \frac{m(3m-\beta(m+2)+6)}{(m+2)\tau}\right]F + 2\dot{F}\right\} + \frac{1}{2}f + \ddot{F}\right\}.$$ (32)

The RHDE energy density is always positive and decreases with cosmic time t as depicted in Figure 3. As the cosmos expands, its energy density drops until it reaches zero at a massive expansion. In Figure 4, RHDE pressure versus cosmic time t is depicted graphically.
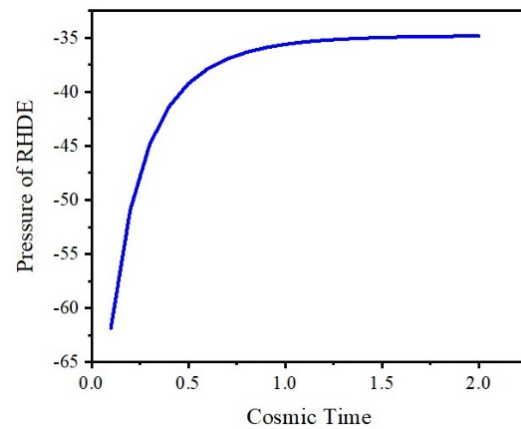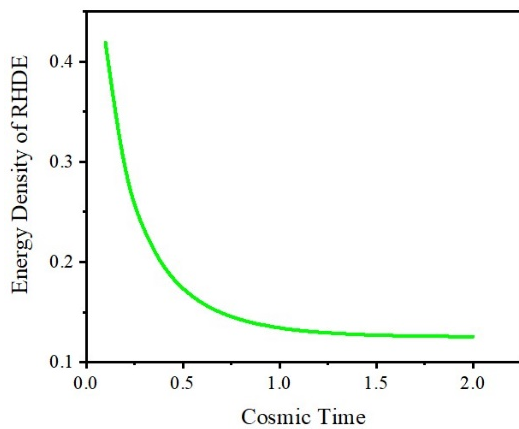

Figure 3. Energy density of RHDE versus cosmic time for $\beta = 3$, $c = 1$, $d = 1.2$ and $\delta = 4$

Figure 4. Pressure of RHDE versus cosmic time for $\beta = 3$, $c = 1$, $m = 2$, $n = 2$ and $b = 1$.

It is evident that RHDE exerts a negative pressure throughout the universe's expansion. The year 2009 saw a result that limits the dark energy equation of state parameter to $-1.44 < \omega_r < -0.92$ by combining cosmic data sets from galaxy clustering, CMBR anisotropy, and luminosity distances of high redshift SNe-Ia.
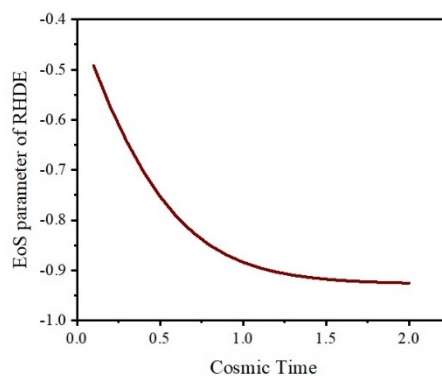

Figure 5. EoS parameter of RHDE versus cosmic time for $\beta = 3$, $c = 1$, $d = 1.2$, $\delta = 4$, $m = 2$, $n = 2$ and $b = 1$.

In Figure 5, it is shown that the equation of state parameter initially reflects the quintessence region and that as time goes on, it evolves around the ΛCDM model. The equation of state parameter behaves like a cosmological constant $\omega_r = -1$ as the universe expands, which is consistent with recent theoretical results.

Stability factor is

$$
\vartheta_r^2 = -\frac{8\pi}{3d^2\beta}\left(\frac{\tau^2}{1-\tau}\right)\frac{\left(1+\pi\delta\tau^2\right)}{\left[\frac{\pi\delta}{\left(1+\pi\delta\tau^2\right)}+\frac{2}{\tau}\right]}\left\{\frac{1}{2}f+\ddot{F}+\frac{3}{(m+2)\tau}\left\{\begin{array}{l}-\beta\left(\dfrac{1-\tau}{\tau}\right)\left\{\left[\beta m+\dfrac{2m\left(3m-\beta(m+2)+6\right)}{(m+2)\tau}\right]F+2\dot{F}\right\}\\[2ex]+\left[\beta m+\dfrac{m\left(3m-\beta(m+2)+6\right)}{(m+2)\tau}\right]\dot{F}+2\ddot{F}\end{array}\right\}\right\}
$$

(33)

where

$$
\ddot{F}=\left\{\begin{array}{l}-bn(n-1)\beta\left(\dfrac{-6}{M_1}\right)^{n-1}\left(\tau_1\right)^{n-3}\left(\dfrac{1-\tau}{\tau^n}\right)\\[3ex]\left[\left(\dfrac{1-\tau}{\tau^2}\right)\left\{2\tau_2\tau_3+\dfrac{M_2}{\tau}\left[2M_2\left(\dfrac{3-2\tau}{\tau}\right)+\beta M_1(2-\tau)\right]+(n-2)\tau_1\tau_3\right\}\right.\\[3ex]\left.+\left\{\tau_1\left[2M_2\left(\dfrac{1-\tau}{\tau^2}\right)+\tau_2\left(\dfrac{2-\tau}{\tau}\right)\right]+(n-2)\left(\dfrac{1-\tau}{\tau}\right)\tau_2^{\;2}\right\}\left\{(n-3)M_2\left(\dfrac{1-\tau}{\tau^2\tau_1}\right)+\left(1+n\left(\dfrac{1-\tau}{\tau}\right)\right)\right\}\right]\end{array}\right\},
$$

and

$$
\tau_1=\left(\beta M_1+\frac{M_2}{\tau}\right),\ \tau_2=\left(\beta M_1+\frac{2M_2}{\tau}\right),\ \tau_3=\left[2M_2\left(\frac{3-\tau}{\tau}\right)+\beta M_1\right].
$$

From Figure 6, it is clear that the universe is unstable because RHDE has a negative stability factor during the universe's expansion.
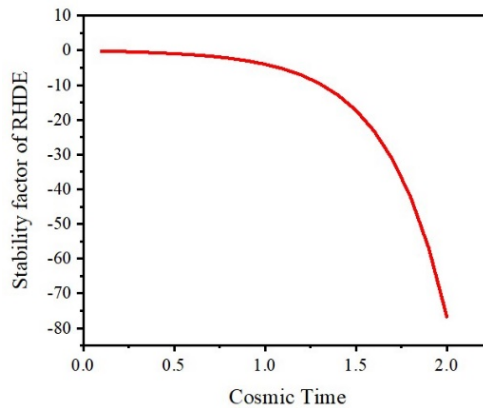

Figure 6. Stability factor of RHDE versus cosmic time for $\beta=3$, $c=1$, $d=1.2$, $\delta=4$, $m=2$, $n=2$ and $b=1$.

CONCLUSION

In the present study, a homogeneous and anisotropic LRS Bianchi type I universe model is considered with an interacting dark matter and RHDE in $f(R)$ gravity.

- It is found that the energy density of RHDE is always positive and decreases as a function of cosmic time t.
- As time goes on, the equation of state parameter evolves around the ΛCDM model, which is familiar from the universe's current accelerated expansion. The equation of state parameter initially represents the quintessence area [87-88].
- The average scale factor and the spatial volume increase with increasing cosmic time.
- Expansion scalar is constant because of $t \to \infty$. It implies that the universe expands more quickly initially and then less quickly as time goes on.
- The deceleration parameter is negative during the entire universe's expansion, which is consistent with the usual accelerating expansion [89-90].
- The stability factor has been negative during the universe's expansion, indicating that the cosmos is unstable.
- As cosmic time lengthens, recent theoretical observations are consistent with this scenario.

ORCID

Alfred Y. Shaikh, https://orcid.org/0000-0001-5315-559X; **Siraj N. Khan,** https://orcid.org/0000-0003-2246-7050

REFERENCES
[1] A.G. Riess, *et al*., (Supernova Search Team): Astron. J. **116**, 1009 (1998). https://doi.org/10.1086/300499
[2] A.G. Riess *et al*., (Supernova Search Team): Astron. J. **607**, 665 (2004). https://doi.org/10.1086/383612
[3] D.N. Spergel *et al*., Astrophys. J. Suppl. Ser. **148**, 175 (2003). https://doi.org/10.1086/377226
[4] D.N. Spergel *et al*., Astrophys. J. Suppl. Ser. **170**, 377 (2007). https://doi.org/10.1086/513700
[5] M. Tegmark *et al*., Phys. Rev. D, **69**, 103501 (2004). https://doi.org/10.1103/PhysRevD.69.103501
[6] P. Astier, and R. Pain, Comptes Rendus Physique, **13**(6), 521 (2012). https://doi.org/10.1016/j.crhy.2012.04.009
[7] E.J. Copeland, M. Sami, and S. Tsujikawa, Int. J. of Mod. Phys. D, **15**, 1753 (2006). http://dx.doi.org/10.1142/S021827180600942X
[8] R.R. Caldwell, and M. Kamionkowski, Ann. Rev. Nucl. Part. Sci. **59**, 397 (2009). https://doi.org/10.1146/annurev-nucl-010709-151330
[9] A. Silvestri, and M. Trodden, Rep. Prog. Phys. **72**, 096901 (2009). 10.1088/0034-4885/72/9/096901
[10] S. Nojiri, and S.D. Odintsov, Int. J. Geom. Meth. Mod. Phys. **115**, 4 (2007). https://doi.org/10.1142/S0219887807001928
[11] S. Capozziello, Int. J. Mod. Phys. D, **11**, 483 (2002). https://doi.org/10.1142/S0218271802002025
[12] S. Nojiri, and S.D. Odintsov, Phys. Rev. D, **74**(8), 086005 (2006). https://doi.org/10.1103/PhysRevD.74.086005
[13] S. Nojiri, and S.D. Odintsov, Phys. Lett. B, **657**(4), 238 (2007). https://doi.org/10.1016/j.physletb.2007.10.027
[14] S. Nojiri, and S.D. Odintsov, Phys. Rept., **505**, 59 (2011). https://doi.org/10.1016/j.physrep.2011.04.001
[15] S.K. Tripathy, and B. Mishra, The Eur. Phys. J. Plus, **131**, 273 (2016). https://doi.org/10.1140/epjp/i2016-16273-5
[16] E.V. Linder, Phys. Rev. D, **81**, 127301 (2010). https://doi.org/10.1103/PhysRevD.81.127301
[17] R. Myrzakulov, The Eur. Phys. J. C, **71**(9), 1752 (2011). https://doi.org/10.1140/epjc/s10052-011-1752-9
[18] S.H. Chen, J.B. Dent, S. Dutta, and E.N. Saridakis, Phys. Rev. D, **83**(2), 023508 (2011). https://doi.org/10.1103/PhysRevD.83.023508
[19] J.B. Dent, S. Dutta, and E.N. Saridakis, J. of Cosm. and Astroparticle Phys., **2011**, 009 (2011). https://doi.org/10.1088/1475-7516/2011/01/009
[20] T. Harko, F.S. Lobo, G. Otalora, and E.N. Saridakis, Phys. Rev. D, **89**(12), 124036 (2014). https://doi.org/10.1103/PhysRevD.89.124036
[21] S. Nojiri, and S.D. Odintsov, Phys. Lett. B, **631**(1), 1 (2005). https://doi.org/10.1016/j.physletb.2005.10.010
[22] B. Li, J.D. Barrow, and D.F. Mota, Phys. Lett. B, **76**(4), 044027 (2007). https://doi.org/10.1103/PhysRevD.76.044027
[23] G. Konas, and E.N. Saridakis, Phys. Rev. D, **90**, 084044 (2014). https://doi.org/10.1103/PhysRevD.90.084044
[24] V.J. Dagwal, Can. J. Phys., **98**, 636 (2020). https://doi.org/10.1139/cjp-2019-0226
[25] V.J. Dagwal, D.D. Pawar, Ind. J. of Phys., **95**, 1923 (2021). https://doi.org/10.1007/s12648-020-01830-3
[26] A.Y. Shaikh, A.S. Shaikh, and K.S. Wankhade, (2020). https://arxiv.org/abs/2006.12300
[27] V.J. Dagwal, and D.D. Pawar, Ind. J. of Phys., **95**, 177 (2021). https://doi.org/10.1007/s12648-020-01691-w
[28] V.J. Dagwal, and D.D. Pawar, Mod. Phys. Lett. A, **35**, 1950357 (2020). https://doi.org/10.1142/S0217732319503577
[29] D.D. Pawar, R.V. Mapari, and J.L. Pawade, Pramana – J. of Phys., **95**, 1 (2021). https://doi.org/10.1007/s12043-020-02058-w
[30] A.Y. Shaikh, and K.S. Wankhade, Theoretical Physics, **2**(1), 34-43 (2017). https://dx.doi.org/10.22606/tp.2017.21006
[31] V.J. Dagwal, Ind. J. of Phys. **96**, 3361 (2022). https://doi.org/10.1007/s12648-021-02256-1
[32] V.J. Dagwal, D.D. Pawar, and Y.S. Solanke, Mod. Phys. Lett. A, **35**, 2050316 (2020). https://doi.org/10.1142/S0217732320503162
[33] D.D. Pawar, and R.V. Mapari, J. of Dyn. Sys. and Geom. Theories, **20**, 115 (2022). https://doi.org/10.1080/1726037X.2022.2079268
[34] D.D. Pawar, R.V. Mapari, and P.K. Agrawal, J. Astrophys. Astron. **40**, 1 (2019). https://doi.org/10.1007/s12036-019-9582-5
[35] S. Nojiri, S.D. Odintsov, and V.K. Oikonomou, Phys. Rep. **692**, 1 (2017). https://doi.org/10.1016/j.physrep.2017.06.001
[36] S. Nojiri, and S.D. Odintsov, (2008). https://arxiv.org/abs/0807.0685v1
[37] S. Capozziello, A. Stabile, and A. Troisi, Class. Quantum Grav. **24**, 2153 (2007). https://doi.org/10.1088/0264-9381/24/8/013
[38] L. Hollenstein, and F.S.N. Lobo, Phys. Rev. D, **78**, 124007 (2008). https://doi.org/10.1103/PhysRevD.78.124007
[39] M.J. Reboucas, and J. Santos, Phys. Rev. D, **80**, 063009 (2009). https://doi.org/10.1103/PhysRevD.80.063009
[40] M. Sharif, and M.F. Shamir, Class. Quantum Grav. **26**, 235020 (2009). https://doi.org/10.1088/0264-9381/26/23/235020
[41] M. Sharif, and M.F. Shamir, Gen. Relativ. Gravit. **42**, 2643 (2010). https://doi.org/10.1007/s10714-010-1005-5
[42] S. Capozziello, A. Stabile, and A. Troisi, Int. J. Theor. Phys. **49**, 1251 (2010). https://doi.org/10.1007/s10773-010-0307-4
[43] K. Bamba, S. Nojiri, and S.D. Odintsov, Phys. Lett. B, **698**, 451 (2011). https://doi.org/10.1016/j.physletb.2011.03.038
[44] Y.B. Wu, Y.Y. Zhao, R.G. Cai, J.B. Lu, J.W. Lu, and X.J. Gao, Phys. Lett. B, **717**, 323 (2012). https://doi.org/10.1016/j.physletb.2012.10.008
[45] S. Capozziello, and M. De Laurentis, Ann. Phys. **524**, 545 (2012). https://doi.org/10.1002/andp.201200109
[46] M. Sharif, and Z. Yousaf, Mon. Not. R. Astron. Soc. **440**, 3479 (2014). https://doi.org/10.1093/mnras/stu533
[47] S.D. Odintsov, V.K. Oikonomou, Phys. Rev. D, **92**, 124024 (2015). https://doi.org/10.1103/PhysRevD.92.124024
[48] S. Capozziello, and M. De Laurentis, Phys. Rep., **509**, 167 (2017). https://doi.org/10.1016/j.physrep.2011.09.003
[49] M.Z. Bhatti, Z. Yousaf, and M. Ilyas, J. Astrophys. Astr. **39**, 69 (2018). https://doi.org/10.1007/s12036-018-9559-9
[50] Z. Yousaf, K. Bamba, M.Z. Bhatti, and U. Ghafoor, Phys. Rev. D, **100**, 024062 (2019). https://doi.org/10.1103/PhysRevD.100.024062
[51] Z. Yousaf, A. Ikram, and M.Z. Bhatti, Can. J. Phys., **98**, 474 (2020). https://doi.org/10.1139/cjp-2019-0360
[52] A.S. Agrawal, S.K. Tripathy, and B. Mishra, Chin. J. of Phys. **71**, 333 (2021). https://doi.org/10.1016/j.cjph.2021.03.004
[53] K.S. Wankhade, A.Y. Shaikh, and S.N. Khan, Prespacetime Journal, **13**(3), 365, 379 (2022). https://prespacetime.com/index.php/pst/article/download/1852/1734
[54] A.G. Cohen, D.B. Kaplan, and A.E. Nelson, Phys. Rev. Lett. **82**, 4971 (1999). https://doi.org/10.1103/PhysRevLett.82.4971
[55] S.D.H. Hsu, Phys. Lett. B, **594**(1-2), 13 (2004). https://doi.org/10.1016/j.physletb.2004.05.020
[56] M. Li, Phys. Lett. B, **603**(1-2), 1 (2004). https://doi.org/10.1016/j.physletb.2004.10.014
[57] S.H. Shekh, Physics of the Dark Universe, **33**, 100850 (2021). https://doi.org/10.1016/j.dark.2021.100850

[58] M.R. Setare, and E.N. Saridakis, J. Cosm. Astropart. Phys., **2009**, 002 (2009). https://doi.org/10.1088/1475-7516/2009/03/002

[59] L. Susskind, J. Math. Phys. **36**, 6377 (1995). https://doi.org/10.1063/1.531249

[60] P. Horova, and D. Minic, Phys. Rev. Lett., **85**, 1610 (2000). https://doi.org/10.1103/PhysRevLett.85.1610

[61] M.R. Setare, Phys. Lett. B, **644**(2-3), 99 (2007). https://doi.org/10.1016/j.physletb.2006.11.033

[62] S. Ghaffari, M.H. Dehghani, and A. Sheykhi, Phys. Rev. D, **89**, 123009 (2014). https://doi.org/10.1103/PhysRevD.89.123009

[63] S. Nojiri, and S.D. Odintsov, Gen. Relativ. Gravit. **38**, 1285 (2006). https://doi.org/10.1007/s10714-006-0301-6

[64] L.N. Granda, and A. Oliveros, Phys. Lett. B, **669**, 275 (2008). https://doi.org/10.1016/j.physletb.2008.10.017

[65] A. Sheykhi, M.H. Dehghani, and S. Ghaffari, Int. J. Mod. Phys. D, **25**, 1650018 (2016). https://doi.org/10.1142/S0218271816500188

[66] M. Tavayef, A. Sheykhi, K. Bamba, and H. Moradpour, Phys. Lett. B, **781**, 195 (2018). https://doi.org/10.1016/j.physletb.2018.04.001

[67] H. Moradpour, S.A. Moosavi, I.P. Lobo, J.P.M. Graca, A. Jawad, and I.G. Salako, Eur. Phys. J. C, **78**, 829 (2018). https://doi.org/10.1140/epjc/s10052-018-6309-8

[68] A.S. Jahromi, S.A. Moosavi, H. Moradpour, J.P.M. Grac, I.P. Lobo, I.G. Salako, and A. Jawad, Phys. Lett. B, **780**, 21 (2018). https://doi.org/10.1016/j.physletb.2018.02.052

[69] A. Jawad, K. Bamba, M. Younas, S. Qummer, and S. Rani, Symmetry, **10**, 635 (2018). https://doi.org/10.3390/sym10110635

[70] S. Maity, and U. Debnath, Eur. Phys. J. Plus, **134**, 514 (2019). https://doi.org/10.1140/epjp/i2019-12884-6

[71] S. Maity, and U. Debnath, Int. J. of Geom. Methods in Mod. Phys. **17**(11), 2050170 (2020). https://doi.org/10.1142/S0219887820501704

[72] U.K. Sharma, and V.C. Dubey, Modern Physics Letters A, **35**(34), 2050281 (2020). https://doi.org/10.1142/S0217732320502818

[73] V.C. Dubey, U.K. Sharma, and A. Al Mamon, Adv. in High Energy Phys. **2021**, 6658862 (2021). https://doi.org/10.1155/2021/6658862

[74] S. Nojiri, and S.D. Odintsov, Eur. Phys. J. C, **77**, 528 (2017). https://doi.org/10.1140/epjc/s10052-017-5097-x

[75] A. Iqbal, and A. Jawad, Physics of the Dark Universe, **26**, 100349 (2019). https://doi.org/10.1016/j.dark.2019.100349

[76] S. Ghaffari, A.H. Ziaie, V.B. Bezerra, and H. Moradpour, Modern Phys. Lett. A, **35**, 1, 1950341 (2019). https://doi.org/10.1142/S0217732319503413

[77] U.K. Sharma, and V.C. Dubey, New Astronomy, **80**, 101419 (2020). https://doi.org/10.1016/j.newast.2020.101419

[78] A. Dixit, V.K. Bhardwaj, and A. Pradhan, (2020). https://arxiv.org/abs/2010.10847v1

[79] S. Chunlen, and P. Rangdee, (2020). https://arxiv.org/abs/2008.13730v2

[80] S. Ali, S. Khan, S. Sattar, and A. Abebe, (2020). https://arxiv.org/abs/2011.10046v2

[81] V.C. Dubey, A.K. Mishra, and U.K. Sharma, Astrophys. Space Sci. **365**, 129 (2020). https://doi.org/10.1007/s10509-020-03846-x

[82] A. Saha, S. Ghose, A. Chanda, and B.C. Paul, (2021). https://arxiv.org/abs/2101.04060

[83] A.Y. Shaikh, (2021). https://arxiv.org/abs/2105.04411v1

[84] M.F. Shamir, J. Exp. Theor. Phys. **123**, 607 (2016). https://doi.org/10.1134/S1063776116110182

[85] C.B. Collins, J. Math. Phys. **18**, 2116 (1977). https://doi.org/10.1063/1.523191

[86] H. Wei, and R.G. Cai, Eur. Phys. J. C, **59**, 99 (2009). https://doi.org/10.1140/epjc/s10052-008-0799-8

[87] A.Y. Shaikh, and B. Mishra, Int. J. of Geom. Methods in Mod. **17**(11), 2050158 (2020). https://doi.org/10.1142/S0219887820501583

[88] A.Y. Shaikh, S.V. Gore, and S.D. Katore, New Astronomy, **80**, 101420 (2020). https://doi.org/10.1016/j.newast.2020.101420

[89] A.Y. Shaikh, A.S. Shaikh, and K.S. Wankhade, Pramana – J. Phys., **95**, 19 (2021). https://doi.org/10.1007/s12043-020-02047-z

[90] A.Y. Shaikh, and B. Mishra, Commun. Theor. Phys. **73** ,025401 (2021). https://doi.org/10.1088/1572-9494/abcfb2

ГОЛОГРАФІЧНА МОДЕЛЬ ТЕМНОЇ ЕНЕРГІЇ РЕНЬЇ У f(R) ГРАВІТАЦІЇ З ІЧ-ОБРІЗАННЯМ ХАББЛА

Кішор С. Ванкхаде^a, Альфред Ю. Шейх^b, Сірадж Н. Хан^c

^aДепартамент математики, Махавідьялая, округ Мангрулпір. Васим - 444403, Індія
^bДепартамент математики, Індіра Ганді Махавідьялая, Ралегаон - 445402, Індія
^cКоледж інженерії та менеджменту професора Рама Меге, Баднера, Амраваті - 444701, Індія

У цьому дослідженні розглядається однорідна та анізотропна модель Всесвіту LRS Bianchi типу I із взаємодіючою темною матерією та голографічною моделлю темної енергії Реньї (RHDE) у *f*(*R*) гравітації. Параметр уповільнення (DP) показує характерне перевертання для Всесвіту, який уповільнювався в минулому та прискорювався в нинішню епоху. Таким чином, DP є найбільш фізично виправданим параметром для аналізу рішення космологічної моделі. Щоб знайти точний розв'язок польових рівнянь моделі, скаляр зсуву вважається пропорційним скаляру розширення. Ми розглянули *f*(*R*) = *bR*ⁿ, моделлю зображення *f*(*R*) якої є функція скаляра Річчі *R*. Досліджено фізико-геометричні характеристики моделі Всесвіту.

Ключові слова: *f*(*R*) *гравітація; RHDE; темна матерія; космологія; простір-час Бьянкі типу I*